CONTROL OF BURIAL AND SUBSURFACE LOCOMOTION IN PARTICULATE SUBSTRATES

A Thesis
Presented to
The Academic Faculty

by

Sarah S. Sharpe

In Partial Fulfillment
of the Requirements for the Degree
Doctor of Philosophy in the
Interdisciplinary Bioengineering Graduate Program
Department of Biomedical Engineering

Georgia Institute of Technology
December 2013

CONTROL OF BURIAL AND SUBSURFACE LOCOMOTION IN PARTICULATE SUBSTRATES

Approved by:

Dr. Daniel I. Goldman, Advisor
School of Physics
Georgia Institute of Technology

Dr. Stephen P. DeWeerth
Department of Biomedical Engineering
Georgia Institute of Technology

Dr. T. Richard Nichols
School of Applied Physiology
Georgia Institute of Technology

Dr. David Hu
Department of Mechanical Engineering
Georgia Institute of Technology

Dr. Kurt Wiesenfeld
School of Physics
Georgia Institute of Technology

Date Approved: October 30, 2013

To my family,

for their love, support and constant belief in me.

ACKNOWLEDGEMENTS

This work was made possible by a number of people and organizations who have provided intellectual, technical, emotional and financial support.

First, I would like to thank my advisor, Dr. Daniel I. Goldman, whose passion for science and wide breadth of research interests have allowed students with diverse backgrounds to come together and conduct interdisciplinary research. Dr. Goldman put faith in my abilities as a young graduate student and allowed me to pursue both my neuroscience and biomechanics interests. His excitement for cutting edge research as well as new techniques and tools have made the complex rheology and biomechanics (CRAB) lab a fun place to work. He has always known how to apply the right amount of 'pressure' to motivate his students to progress and excel. Finally, my oral and written communication skills have advanced dramatically over my time in the lab primarily due to Dr. Goldman's influence. Dr. Goldman not only emphasizes conducting good research but has taught his students that communicating that good research to others is equally important.

Thanks to my committee members Dr. Stephen P. DeWeerth, Dr. David Hu, Dr. T. Richard Nichols, and Dr. Kurt Wiesenfeld. Working in Dr. DeWeerth's lab during a summer research experience for undergraduates (REU) directly influenced my decision to go to graduate school and pursue a PhD at Georgia Tech. In addition, his influence in my first two years as my co-advisor was extremely valuable and helped to advance not only my neuroengineering knowledge but also my ability to look at the 'big picture'. I'd like to thank Dr. Nichols who brought me to my first (and one of the most fun) international conference, the Alberta Motor Control Neurohike Meeting. Thanks to Dr. Wiesenfeld for his intellectual input and advice regarding neuromechanical phase lags computations and explanations. I'd like to thank Dr. Hu, whose diverse research and always amazing talks have inspired me in my own research interests. Finally, I'd like to thank all of the members for their intellectual input on this research before and during my proposal and also for

reading and giving comments on this dissertation.

I'd like to thank my family, which is so large that I cannot list all of their names for fear of doubling the size of this dissertation. Thanks especially to my father Daniel Steinmetz. Every step that I've made is a step in which I hope to become closer to the wonderful example he has set for me. I'd like to thank my mother, Karen Steinmetz, who told me I was brilliant all of my life (even when I didn't believe her) and gave me the confidence to pursue any field of my choosing. Thanks also to my mother, Debra Jahns-Nelsen, whose caring nature has been a source of emotional support. I am very grateful for my siblings who have always been there for me in anyway I needed. In particular, I want to thank my sister Kelly, who has talked and listened to me throughout my undergraduate and graduate career and has always known what to say in order to give me the confidence to move forward. Finally, I'd like to thank my husband, Jeffrey Sharpe. Even as freshmen in college, he was never upset when I placed my priorities on my academics. His support has enabled me to pursue my passions and he has certainly provided balance in my life.

I'd like to thank all of my colleagues in the lab, both graduate and undergraduate. I'd like to thank Ryan Maladen and Yang Ding (the sandfish team) for their helpful discussions and intellectual contributions especially early in my graduate career. Thanks to Chen Li, Nicole Mazouchova and Nick Gravish, whom I could always go to in order to bounce around ideas. I'd like to thank the undergraduates whom I worked closely with to develop my dissertation topics which include Robyn Kuckuk, Andrew Masse, Humaira Taz, Tamunodiepriye George, Kevin Daffon, Baris Yildirim, and Andras Karsai. Thanks Mateo Garcia and Andrei Savu for help in particular with building and setting up apparatus. Thanks also to lab members Feifei Qian, Daria Monaenkova, Tingnan Zhang, Jeff Aguilar, Mark Kingsbury, Will Savoie and Perrin Schiebel. Finally, thanks to the members of the DeWeerth lab for providing neuro-related advice especially in my early graduate years.

I would like to thank my undergraduate research advisor, Dr. Alexander Leonessa, who convinced me to leave my Mechanical Engineering co-op and conduct research with him instead (which proved to be much more interesting). Dr. Leonessa taught me how to begin a research project and influenced my decision to attend graduate school. Thanks to Dr.

Tonia Hseih for help with biological statistics principles and also Dr. Paul Umbanhowar for helpful discussions over my graduate career and for providing advice on the shovel-nosed snake Chapter. I am grateful for Dr. Stephan A. Koehler who has provided helpful discussions and ideas about the shovel-nosed snake research and for running calculations that have helped to explain the data. I would also like to thank Miguel Serrano for providing tracking code and B-spline fitting analysis code to analyze ocellated skink and shovel-nosed snake data. Thanks to Dr. Joseph Mendelson for providing assistance in the acquisition of shovel-nosed snake and providing guidance in how to maintain them in capativity. Thanks to Dr. Thomas J. Burkholder for assistance with sandfish dissection and thanks to Dr. Robert E. Gulberg's lab for assistance with CT scans of sandfish morphology. Thanks to Dr. Elizabeth A. Gozal for providing EMG analysis code (SpinalMOD). I am also appreciative of the people that have made working with research animals possible, in particular Physiolgical Research Laboratory (PRL) veterinarian Laura O'Farrell, PRL lab manager Kim Benjamin, and IACUC research associate at the Office of Research Integrity Assurance, Anna Marie Lee. Thanks to the radiation safety associates, Christina Tabor, Gary Spichiger, and Nazia Zakir.

I'd like to thank my funding sources: the National Science Foundation Integrative Graduate Education and Research Traineeship Fellowship, the Burroughs Wellcome Fund, the National Science Foundation Physics of Living Systems Grant, the Army Research Laboratory Micro Autonomous System Technologies Collective Technology Alliance, and the Army Research Office Grant.

TABLE OF CONTENTS

IV LIMB USE IN THE SANDFISH LIZARD DURING RAPID BURIAL 109

LIST OF TABLES

LIST OF FIGURES

GLOSSARY

A: wave amplitude

A/λ: a dimensionless parameter which characterizes the spatial of the sandfish kinematics

AB: experimental condition in which all of sandfish limbs were bound

c: viscous damping coefficient

CFL: contralateral forelimb

CHL: contralateral hindlimb

CoT: mechanical cost of transport $= \frac{power}{mass \times speed}$

CoM: center of mass

CONT: experimental control condition in which the sandfish had two pieces of tape wrapped around two body locations and limbs were unbound

CPG: central pattern generator

CP: closely packed

d_{CoM}: distance from rotation point on sandfish to center of mass

E_{loss}: area enclosed by the hysteresis loop

EMG: electromyogram / electromyography

f: undulation frequency

$\vec{f}$: granular force per unit length (Chapter 3)

$\vec{F}$: granular force on a segment

FB: experimental condition in which sandfish forelimbs were bound

FL: forelimb

fps: frames per second

GM: granular media / granular medium

h: structural damping coefficient

HB: experimental condition in which sandfish hindlimbs were bound

HL: hindlimb

I: EMG intensity - the ratio of the EMG burst integrated area to the

EMG burst duration

I_{rel}: relative EMG intensity - EMG intensity normalized to the average intensity during undulation 3 for a single experiment

K: body stiffness

L/r: body length to body radius ratio

LF: left forelimb

LH: left hindlimb

L_{Eff}: Effective length = 0.87 × STL

L_M: normalized muscle length estimated from the angle between segments

LP: loosely packed

m: mass

M_{wet}: mass of wet media = mass of dry media + mass of water

MUAPs: motor unit action potentials

NB: experimental condition which sandfish had no limb (or body) bindings

NMR: nuclear magnetic resonance

NPL: neuromechanical phase lags

$\overrightarrow{R}$ center of mass velocity

Re: Reynold's number

RF: right forelimb

RFT: resistive force theory

RH: right hindlimb

$\bar{S}$: slip – average angle between velocity and tangent vectors along the body

s.d.: standard deviation

STL: snout-to-tail length

SVL: snout-to-vent length

t: time

T: period of undulation

$\widehat{t}$: unit tangent vector (Chapter 5)

$\widehat{v}$: unit velocity vector

v_c: speed of the traveling curvature wave

v_{EMG}: average speed of traveling EMG wave

v_{for}: forward speed - speed of the 0.5 SVL marker in the average forward direction of movement

v_{lat}: lateral speed - speed of the 0.5 SVL marker in the lateral direction of movement

v_{seg}: segmental speed - speed of a marker in the direction of movement

v_w: speed of the traveling wave, where $v_w = f\lambda$

v_x: forward speed

V_p volume of particles

V volume of occupied space

W: water content = mass of liquid / mass of dry media

x_b: distance along a line parallel to the direction of the traveling wave measured from the tail tip

y_b: lateral displacement from the midline of a straight animal

η: wave efficiency - the ratio of the average forward speed of the animal to the speed of the kinematic traveling wave

η_{loss}: loss factor due to structural damping where $\eta_{loss} = h/K$

θ_d: angle of descent - angle between horizontal and the best linear fit to the positions of all tracked dorsal markers during the subsurface descent

κ: curvature

$\kappa\lambda_s$: relative curvature- local curvature multiplied by twice the the arc length of a half wave

λ: wavelength of the sinusoidal wave

λ_s: arc length of one wave

μ_s: body-particle coefficient of friction

ξ: number of waves along the body

ρ_{GM}: density of the granular media

τ_v: viscous torque

τ_{rms}: root mean square torque

ϕ: volume fraction - the ratio of the solid volume of the grains to the total occupied volume

ψ: angle between a segment axis and its velocity direction

SUMMARY

A diversity of animals move on and within granular media, a material that can display both solid and fluid-like features. Dry granular media such as that found in sandy deserts and coastal dunes, are collections of particles that interact through dissipative, repulsive contact forces. Cohesive wet granular media make up an even larger proportion of the planet, occurring in rainforest soils, beaches, agricultural land and even at the bottom of oceans. Despite the numerous animals that move on and within these substrates, little is known about the biomechanics and neural control strategies used to move within these complex terrains. Burial and subsurface locomotion provides a particularly interesting behavior in which to study principles of interaction because the entire body becomes surrounded by the granular environment. Understanding the morphological adaptations, kinematics, and neural strategies that animals use to move into and underneath the ground will advance our understanding of locomotion principles on granular substrates and may lead to the development of robotic devices capable of moving in complex terrains.

In this dissertation, we used three model organisms to understand control principles of movement within granular substrates: the sand-specialist sandfish lizard (*Scincus scincus*) which dives into dry sand using limb-ground interactions and swims subsurface using body undulations; the long-slender sand-specialist shovel-nosed snake (*Chionactis occipitalis*) which undulates subsurface with low slip; and the ocellated skink (*Chalcides ocellatus*), a desert generalist which buries into both wet and dry substrates. Using muscle activation measurements we discovered that the sandfish targeted a kinematic template which maximized forward speed and minimized the mechanical cost of transport. In addition, the simplicity of the sandfish revealed the fundamental mechanism responsible for neuromechanical phase lags, a general timing phenomenon between muscle activation and curvature along the body that has been observed in all undulatory animals swimming in fluids. Kinematic experiments revealed that the snake moved subsurface using a similar

locomotion strategy as the sandfish but its long body and low skin friction allowed it to move with higher performance (lower slip). The ocellated skink used a different locomotor pattern than observed in the sandfish and snake but that was sufficient for burial into both wet and dry media. Furthermore, the ocellated skink could only reach shallow burial depths in wet compared to dry granular media. We attribute this difference to the higher resistance forces in wet media and hypothesize that the burial efficacy is force-limited. These studies revealed basic locomotor principles of burial and subsurface movement in granular media and demonstrate the impact of environmental interaction in dictating locomotor behavior.

CHAPTER I

INTRODUCTION

Numerous animals live and move in complex terrains, like dry sand, wet soil, snow and debris, which can display both fluid and solid-like features. These environments are dominated by friction and can flow and deform in response to stress, or maintain a static configuration [1, 2]. Despite the abundance of these deformable substrates in the natural world, our understanding of how to effectively locomote in these environments are limited. A case in point is the Mar rover, Spirit, which used ribbed wheels to traverse the surface of Mars and is currently stuck in Martian granular media [3] (Fig. 1.1). Animals, however, can walk, run, jump, burrow and even swim through these substrates with relative ease. We seek to discover principles of locomotion in complex environments by observing biological organisms in particulate substrates and quantifying morphology, kinematics, and neural strategy. We will focus on movement in monodispersed granular media (GM), defined as a collection of particles that interact through dissipative contact forces [2].

Several challenges have made quantitative locomotion studies in GM difficult. First, no well established theories exist for movement in GM. In most studies of terrestrial movement, the ground is assumed to be flat, undeformable and frictional such that no slip occurs, making ground reaction forces possible to calculate. While movement in fluids, such as in air or water, is more complex, the Navier-Stokes hydrodynamic equations exist and dictate how the fluid contributes to drag and lift [4, 5]. Second, limbs and bodies often penetrate into the opaque ground obstructing observations of kinematics. Furthermore, visualization of material flow can be difficult as techniques like Particle Image Velocimetry (PIV) for fluids [6] are nearly non-existent for GM. For these reasons, reports on subsurface movement patterns are often anecdotal and not quantitative.

Recently, a frictional fluid model (called granular resistive force theory) [7, 8] which uses empirical data from rod drag experiments, has shown predictive ability for movement in

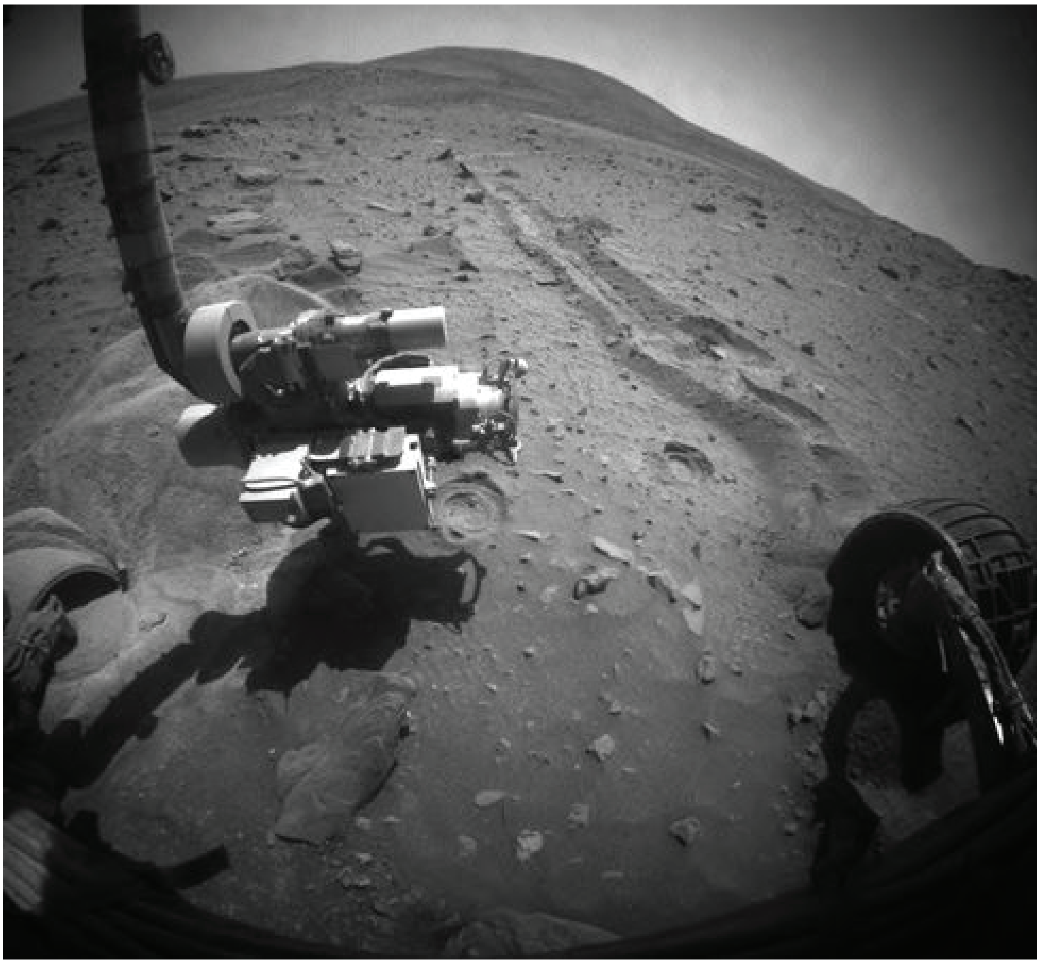

Figure 1.1: Self portrait of the Mars rover, Spirit, stuck in Martian granular media on December 26, 2009. Photo courtsey of NASA/JPL-Caltech

granular substrates. Also molecular dynamic simulations which model individual grain-grain interactions are now possible for a large amount of particles due to advances in computer processing time [7, 9, 10]. These newly developed tools can be used to test and generate hypotheses regarding locomotion in sand. Additionally, more accessibility to technology, such as x-ray [11–14] and nMRI [15] machines, enables visualization through opaque material and quantification of subsurface animal kinematics.

In this dissertation, we will focus on burial and subsurface locomotion in which the animal becomes surrounded by the substrate (Fig. 1.2). The above tools will be used to characterize and understand how movement is influenced by granular media properties. Our objective is to discover control principles used by animals that help improve the efficacy of subsurface locomotion. These findings could lead to the development of novel robotic devices that are capable of traversing and maneuvering within complex ground.

1.1 Background and significance

Successful locomotion in a diversity of environments [16–19] emerges from the interplay between neuromechanical [20] systems (the combined action of the nervous and mechanical systems) with the physical environment. The numerous studies of animal locomotion in water, air and on hard ground have enhanced our understanding of general movement principles [17–19]. While movement on and within granular media (GM) is common in nature, the biomechanics of the many animals that live on and within these substrates are relatively unexplored [21–25]. Even less is known about the neuromechanical strategies used by animals to move in granular substrates [26]. Understanding how animals move on and within ground could have both evolutionary and ecological implications, could lead to the development of bioinspired robotics, and provides a broader biological perspective.

1.1.1 Biological Perspective

Leonardo da Vinci stated, “We know more about the movement of celestial bodies than about the soil underfoot”. This statement is as true today as it was 500 years ago [40]. The view-point that subterranean ecosystems are extreme environments in which only a few highly specialized animals can survive is shifting and scientists now recognize the extensive

Figure 1.2: A diversity of animals burrow and move within granular media from arthropods such as woodlice [27] and ants [28], mammals like the Namib desert mole [13, 29], worms including the polychaete [30], earthworm [31, 32] and nematode [33], desert dwelling reptiles like the sandfish lizard [11, 34] and sand viper [35, 36], and aquatic animals like the razor clam [37, 38] and sand lance [39]. Credits- Woodlice: Small-Farm-Permaculture-and-Sustainable-Living.com/Meg Howe/ Graeme Young; Mole: Stewart Rushton; Fire Ant: Nick Gravish; Sand lance: NOAA/NMFS/AKFSC/Mandy Lindeberg; Earthworm: iStockphoto/Alasdair Thomson; Polychaete: Claude Nozres; Sand viper: Dr. Zoltan Takacs copyrighted; Razor Clam: Turtle Emily on vimeo.com

biodiversity of subterranean organisms [41]. Studies by soil ecologists suggest that the total biomass underneath the ground is greater than that above the surface [40]. In both terrestrial and aquatic environments, many animals transition from above surface movement to subsurface movement where their bodies become surrounded by the substrate [32]. Animals burrow to avoid extreme climate, evade predators, or to feed on soil flora or fauna (Fig. 1.2).

A large proportion of subterranean animals are small, occuring on the mm-scale, and include arthropods like the fire ant (*Solenopsis invicta*) [28], cave-beetle (*Cytodromus dapsoides*) [42], and woodlouse (Isopoda: Oniscidea) [27] and worms like the nematode (*Caenorhabditis elegans*) [33], earthworm (*Lumbricus terrestris*) [31,32] and polychaete (*Nereis virens*) [30]. Many of these animals must move particles which are large compared to their body width.

Many larger animals also readily bury into the surrounding substrate. Desert dwelling reptiles, like the viper snake (*Cerastes vipera*) [35,36], sandfish lizard (*Scincus scincus*) [11], Mojave fringed-toed lizard (*Uma scoparia*) [22] and shovel-nosed snake (*Chionactis occipitalis*) [21], possess the ability to bury in order to escape hot temperatures and remain covered in a habit often devoid of shrubs. In these substrates, creating open burrows is difficult as the dry media often collapses, forcing animals to displace media continuously during movement subsurface.

Numerous large animals bury into wet soil. These include the more than 160 species of caecillians, a type of amphibian found in tropical regions [43] that spends most, if not all, of their life subsurface. These species are highly adapted to burrowing and subterranean life and are limbless, girdleless and have reduced eyes. Other amphibians which readily bury include the many types of salamanders [44, 45] and some frogs (such as the giant burrowing frog (*Heleioporus australiacus*)) [46]. Burial into moist soil is often vital for these animals' survival in order to prevent desiccation. Worm lizards (suborder Amphisbaenians) are fossorial squamates which also inhabit tropical habitats in the Neotropics, Caribbean Islands, Florida, Baja California, parts of the Mediterranean and Middle East, and sub-Saharan Africa [47]. There are over 150 extant species, yet worm lizards have been minimally studied. Worm lizards enter soil using head-first burrowing. Most species are limbless but a few, such as in the genus *Bipes*, have robust forelimbs which are used for digging. Many snakes also live in soil but remain unstudied because they attract less attention as they are typically small, nocturnal and fossorial [48]. In areas of the Western Piedmont of North Carolina, small fossorial snakes are among the most abundant vertebrates present, and found in both dry and wet soil [49]. How [48] found that the *Simoselaps* snake species on the Swan Coastal Plain of Western Australia shows morphologically convergent features associated with other sand-swimming snakes in distant desert areas like the American *Chionactis* and the African *Elapsoidea.* Little information is available on the burrowing kinematics of these snakes.

Subterranean mammals fall into three orders: rodents, insectivores, and marsupials and comprise 144 of the 4060 mammalian species (known as of 1979) [50]. These animals include many types of moles (such as the Namib Desert Golden mole (*Eremitalpa granti namibensis*) [13, 29]), rats, and gophers. Although burrowers typically consist of small animals, even some large mammals such as coyotes (*Canis latrans*) and badgers (*Taxidea taxus*) dig into the media and construct dens within ground [51].

Aquatic subterranean burrowing is also common and has been studied in organisms such as the razor clam (*Ensis directis*) [37,38], burrowing mud shrimp (*Upogebia pugettensis*) [52], sand lance fish (*Ammodytidae*) [39], and eel (*Pisodonophis boro*) [24]. These animals often bury into the media using similar strategies as terrestrial animals [32]. Adult female sea turtles, which spend the majority of their lives swimming in water [53], occasionally return to land and use their aquatically adapted flippers to dig nests in beach sand.

Moving within a granular media can be challenging as the substrates are highly resistive and animals must displace the surrounding sediments in order to move through the environment. Mechanisms for burial are diverse; these strategies include the use of limbs to dig within the substrate and create burrows, the use of high frequency body undulations to 'loosen' the surrounding soil, ploughing with the head, using expansion and contraction of the body to anchor and pull themselves through the media, and ingestion of the surrounding particles [22, 30, 32]. Once subsurface, there is limited understanding about how animals move. Often experiments attempt to "planarize" the view by having animals construct burrows near a transparent wall such that part of the burrow and animal can be viewed [14, 28]. While these experiments provide valuable information about substrate excavation and tunneling, natural conditions have been modified due to the presence of a rigid wall. Only a few studies have used x-ray or nMRI to observe movement strategies in a more natural 3-D environment [11–15, 54].

Subterranean activity typically falls into three categories: (1) burrowers that create open cavities in firm soil (like the Amphisbaenians and moles), (2) quiescent burial, which consists of many cursorial species that bury into sand and remain stationary underground (*Uma*, *Meroles*, and *Callisaurus*), and (3) subarenaceous animals that consist of sand-swimmers that move long distances in loose sand [55–57]. In this dissertation we will study two subarenaceous animals, the sandfish lizard (*Scincus scincus*) and shovel-nosed snake (*Chionactis occipitalis*), and one desert generalist, the ocellated skink (*Chalcides ocellatus*) which may be a mix between a quiescent burrower and firm soil burrower.

1.1.2 Evolutionary Perspective

Darwin suggested that the origin of life was in a “warm little pond”; however, some soil ecologists speculate that a subterranean environment may be a more likely candidate [40]. These sediments may have provided protection from Earth’s harsh climate in the first billion years. Studying small organisms within ground may give us a look back in time at some of the first creatures to exist. Furthermore, for larger animals like snakes and lizards, sub-surface movement may be enabled by ancestral traits from prehistoric times when animals swam in water and moved without limbs.

Movement in sand presents many mechanical and physiological challenges for animals. Moving from the surface to a terrestrial or aquatic subterranean habitat requires specialized adaptations to the absence of light, scarcity of food, constant temperatures, lack of oxygen, habitat fragmentation, and other ecological pressures [42]. Typical convergent features for unrelated burrowing animals include, but are not limited to, smooth bodies, limblessness, elongation, eye loss, pigmentation loss, and decrease in respiratory metabolism [41,50]. The burial strategies and morphological features of animals could also represent an exaptation, or trait that evolved in a linneage previously that presents a ready-made solution to a new selective pressure (such as escape into dry media) [22]. These ancestral traits could act to promote (or limit) an animal's adaptive capacity. For example, the lateral undulations used during subsurface sand-swimming in the *Scincus scincus* and *Angolosaurus skoogi* are present in many Scincidae (skink) species during movement through grass, rubble, and debris, implying that this trait may be an exaptation used by a common ancestor and co-opted many times due to environmental pressure [22].

1.1.3 Ecological Perspective

Meysman et al. [32] postulated that "burrowing organisms affect most, if not all, of the surface of the Earth" in both the terrestrial and aquatic regimes. The importance of bioturbation, or the biological reworking of soil and sediments by biological processes, was first recognized by Darwin [31] in his study on earthworms. He found that these tiny creatures could have large-scale impacts on their environment, such as in landscape formation. For example, burrowing often acts to loosen the soil which counteracts the natural process of consolidation. This activity promotes soil creep and erosion, which in the long-term may lead to landscape flattening.

The importance of bioturbation is exemplified by the Oceanic Cambrian explosion [32], when a large number of aquatic animals appear in the fossil record over a short period of time. As animals appeared with skeletons and other "hard parts", digging into ground was used to escape predation which attracted other bottom-feeding animals to the ocean floor. This resulted in an extreme change in both the ecological and geochemical functioning of the ocean floor as the once dominant microbial mats disappeared due to soil tunneling and deposit-feeders.

Furthermore, bioturbation by animal movement can result in the redistribution of food, viruses, bacteria, and eggs [32, 54]. In the desert, burrowing animals have been shown to have a strong influence on the development and survival of plant life by disrupting hard soil, facilitating deeper water penetration and retention, and cycling nutrients within soil [58]. Understanding constraints which influence subsurface movement depth, distance, speed, and even ability could have important implications for these ecological processes.

1.1.4 Robotic Models

Our understanding of movement on hard ground and within water and air is illustrated by the numerous robotic devices that move effectively within these environments. Cars, boats, submarines and planes are built based on principles of body-medium interactions. Recently, a surge of interest in bio-inspiration and biomimetics has instigated the building of smaller, light-weight robots with animal-like control strategies and sensing abilities (Fig. 1.3). Studying animal morphology, physiology and control strategies and their interaction with the environment may lead to novel robotic designs with advanced capabilities. For example, studies on gecko climbing (Fig. 1.4) have revealed that their feet contain hundreds of satae, small hair-like structures, that interact with a surface through van der Waals forces [59–61]. These van der Waals forces provide dry adhesion that depend on the contact angle between the satae and the surface. The gecko places its feet of the surface in such a way as to maximize adhesion, while lifting off using a different orientation and minimizing adhesion. These studies have led to a gecko inspired robot which uses a bio-inspired synthetic adhesive pad made of small fibrils that have directionality [62, 63]. The robot is capable of climbing up smooth surfaces with a high payload using a gecko-like movement strategy. On the other end, robots can be used to gain insight about biological function and design. Parameters such as foot contact angle, body morphology, and stiffness can be adjusted in the robotic design and the resulting movement can be observed. Marras et al. [64] used a biomimetic robotic fish to study social behavior in live animals. He found other fish were more attracted to a robotic model when it was beating its tail compared to when it was stationary.

Our understanding of movement on soft materials, such as sand and debris, is limited, and this is reflected in the lack of locomotor devices that move effectively on granular substrates. The Mar's robotic rover, Spirit, which used wheels to move of the surface of Mars, is currently stuck in Martian granular media, and despite the efforts of scientists, cannot be "wiggled" out [3] (Fig. 1.1). Studying biological organisms that move on these soft substrates effectively could lead to discoveries about the animal-medium interactions and aid in robotic design. Such robots are needed for search and rescue missions in disaster

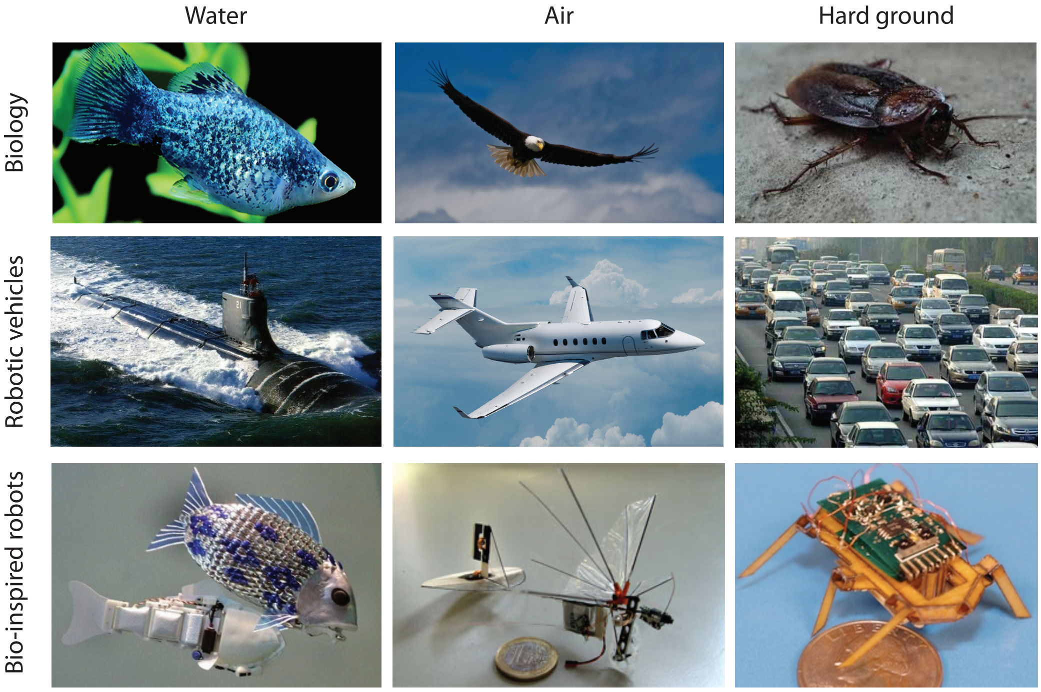

Figure 1.3: Like animals, many devices possess the ability to move through water, air and on hard ground. Recently, robotic efforts have been focused on creating robots more similar to their animal counterparts. These efforts may lead not only to better robotic designs but also allow scientists to test hypotheses about animal movement. Credits (from top-left to bottom-right): fish- Dr. Tom Bailey; eagle- animalpictureplace.com; cockroach- unknown source; submarine- submarinehistory.com; plane- copterplane.net; cars- china.org.cn; robotic fish: Dr. Huosheng Hu, University of Essex [65]; DelFly robot- Delft University of Technology [66]- RoACH robot- Dr. Ronald Fearing, Biomemetic Millisystems Lab, Berkeley [67].

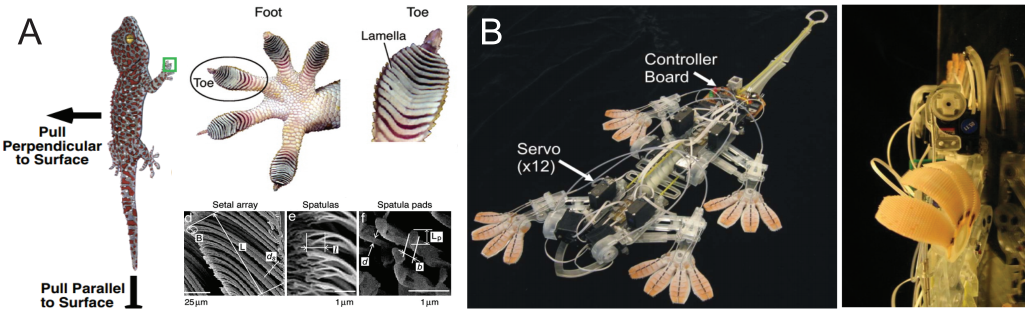

Figure 1.4: Studies on gecko feet and satae have inspired the design of a robot which uses adhesive pads and movement strategies similar to the animal. (A) Gecko, feet and microscopy images of the satae. Figures reproduced from [59, 61]. (B) Stickybot inspired by the gecko. Figure reproduced from [68].

zones, exploration, military operations, and drilling.

Recent studies have begun to explore movement on complex terrains. Li et al. [69] used a RHex class robot, SandBot (Fig. 1.5), to show that leg rotation parameters that enabled the robot to move swiftly on hard ground resulted in low performance (speed) on a granular substrate. By changing limb frequency during stance and swing, robot performance could be returned. Experimental studies on the Atlantic razor clam, *Ensis directus*, (Fig. 1.2) revealed that it burrows within aquatic granular media using an anchoring system [38]. Contraction of its valve caused local fluidization around the clam and decreased drag forces with depth. A bio-inspired robot, RoboClam (Fig. 1.5), was developed that uses this valve mechanism to decrease energy expenditure during burial.

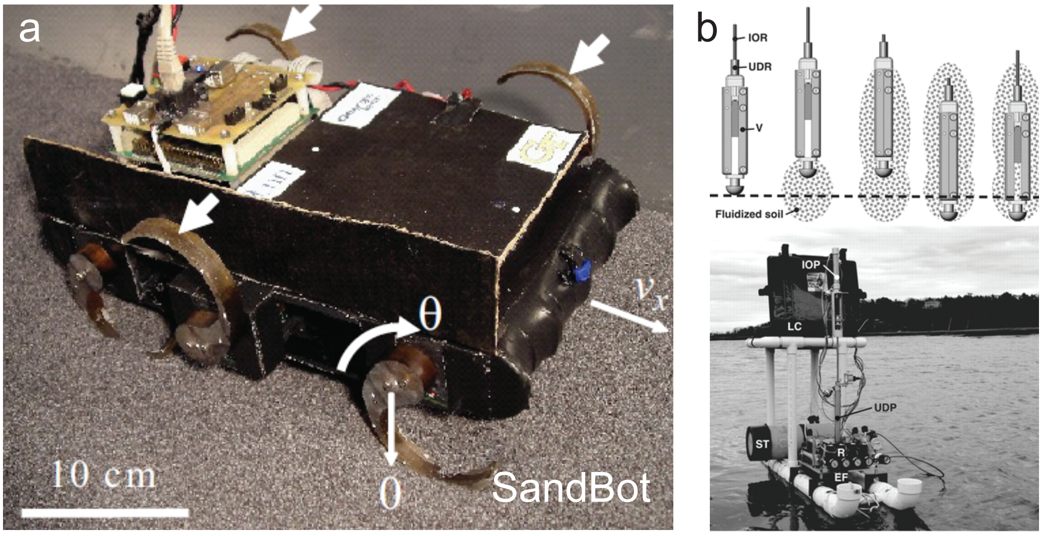

Figure 1.5: Bio-inspired robotic devices that move within granular media. (A) Inspired from the running cockroach, SandBot, is a RHex class robot that uses a tripod gait and compliant c-shaped legs to locomote. Performance of this robot on granular media depends sensitively on leg frequency parameters and media compaction. Reproduced from [69]. (B) RoboClam, inspired from the locomotion of the Atlantic Razor clam, uses it valve motion in saturated wet soils to cause local fluidization and decrease digging energy. Reproduced from [38].

Although these studies have helped to advance this field, robotic locomotors that move effectively on granular media are limited. Robot burial and movement *within* substrate is even more challenging as the entire robot becomes surrounded by the resistive and abrasive media. Studying adaptations and locomotion strategies of animals that are specialized for movement within granular substrates could reveal the biomechanics and control principles necessary for subsurface movement and could be used in developing better robots. Furthermore, robotic models could be used to test hypotheses about animal locomotion and allow systematic variation of parameters.

1.2 Model Organisms

To uncover principles of subsurface locomotion within granular substrates we focus om three different animals: the sandfish lizard (*Scincus scincus*), the shovel-nosed snake (*Chionactis occipitalis*), and the ocellated skink (*Chalcides ocellatus*). The sandfish and the shovel-nosed snake are both considered sand-specialists; they are found exclusively in dry sandy habitats. In addition, they are both subarenaceous species, spending most of their day subsurface and possessing the ability to move underground. Despite their similarities, these animals are distantly related (Fig. 1.6) and live in different regions of the world (sandfish in northern Africa and shovel-nosed snake in southwest North America). While featuring some similar morphological features, like a wedge-shaped head and flat belly, they also have many morphological differences. The snake has a long-slender body, while the sandfish is relatively shorter, greater in width, and has large limbs. We will use these animals as model organisms to study locomotion in possibly the simplest particulate substrate: dry, monodispered granular media. In the sandfish, we will build on previous kinematic work and investigate its neural control strategy during subsurface movement and its entry kinematics. We will also investigate how the snake's and sandfish's subsurface swimming performance is influenced by body morphology and body properties. The third animal, the ocellated skink, is found in the same dry desert regions of Northern Africa as the sandfish, but also inhabits the costal regions of northern Africa, southern Europe and the Middle East. Due to the diversity of environments it inhabits, it is known as a desert generalist [70]. It also possesses the ability to burrow in both wet soil and dry sand. We will use the ocellated skink to investigate how burrowing strategy and performance change between these wet and dry substrates.

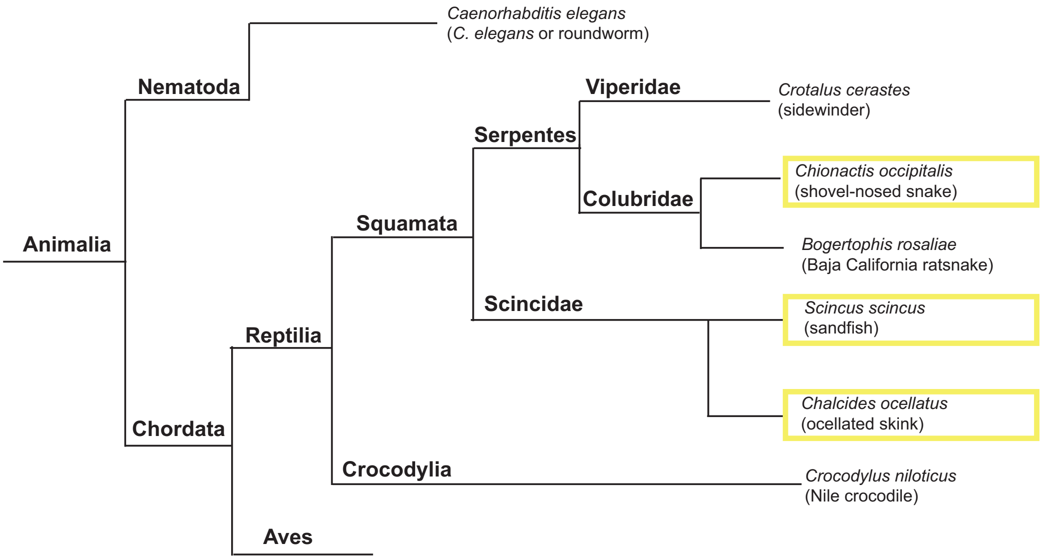

Figure 1.6: Phylogenetic tree showing relationships between model organisms: *Scincus scincus*, *Chalcides ocellatus* and *Chionactis occipitalis*. Bar length does not reflect evolutionary time. See [71] for a more in depth phylogeny of the Scincidae family.

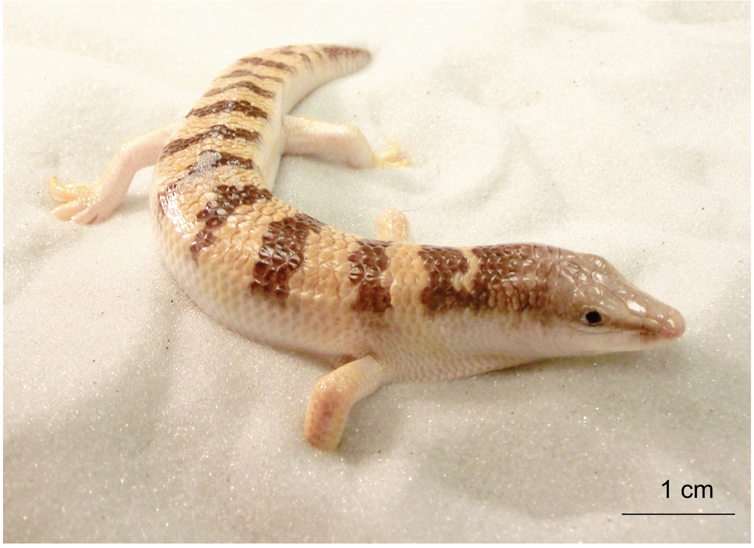

Figure 1.7: Sandfish lizard, *Scincus scincus*, resting on dry 0.3 mm diameter glass particles.

1.2.1 Sandfish Lizard

The Egyptian sandfish lizard (or just sandfish), *Scincus scincus* (scientific names also used in literature: *Scincus officinalis* and *Lacerta scincus*), was first recognized by Linnaeus in 1758 [72]. Since then many reports have briefly mentioned the subterranean behavior of the *Scincus scincus* and closely related *Scincus mitranis* (the Eastern sandfish lizard) [36,55,56]. Arnold et al. [22] provided the first detailed description of the burial behavior. He observed that this lizard targeted loose sand for burial in nature, and used limbs and body undulations during the initial burial. After half of its body was buried, the hindlimbs were placed by its sides and large amplitude traveling wave body undulations were used to propel the animal forward into the media (Fig. 1.8). This burial process took between 1-2 seconds.

Figure 1.8: Diagrammatic representation of *Scincus mitranis*'s subsurface burial strategy. Arnold reported that *Scincus* used high amplitude sinusoidal undulations with its limbs folded by its sides during final burial. Figure reproduced from [22].

In recent years, the sandfish has been the focus of many different research groups. Studies have investigated its seasonal immunological variations [73], its sensing abilities in localizing and capturing prey [74, 75], and its low friction, abrasion resistant skin [15, 76]. In the last 5 years, the subsurface locomotion has been studied with techniques which allow visualization through opaque material. Baumgartner et al. [77] used fast nuclear magnetic resonance (NMR) imaging to visualize sandfish movement patterns. He found a similar locomotion strategy as described by Arnold [22] in which sandfish use high amplitude traveling serpentine waves. He also concluded that sandfish used limbs subsurface. However, the imaging was subject to substantial noise (Fig. 1.9, A). Maladen et al. [11] used x-ray to achieve clearer images of the sandfish subsurface movement (Fig. 1.9, B & C). He found that the sandfish swim with a wave efficiency (η, defined as the ratio of forward speed to the speed of the traveling wave) of ≈ 0.5 during movement in both a closely packed and loosely packed granular medium. In contrast to Baumgartner's work, he found that the distance between the limbs became smaller subsurface, as compared to the sprawled orientation used above surface and during burial. Maladen et al. postulated that sandfish were not using limbs subsurface and used a resistive force theory model to show that a similar η could be achieved when incorporating body-medium interactions only (i.e. no limbs). A separate work corroborated this finding using a discrete element method simulation, which coupled a sandfish-like body to a model of the granular medium, and showed that body undulations would be sufficient to move the sandfish forward with $\eta = 0.5$ [7]. These studies also reported that sandfish used a consistent amplitude to wavelength ratio (A/λ) of ≈ 0.2, which simulation, theory and robotic models predicted were optimal for producing the fastest forward swimming speed [7, 78].

Maladen's work found highly stereotyped kinematics regardless of changes in resistance force from the granular media. It is unknown whether this kinematic pattern is a result of a tuned open-loop control pattern, or if the animal actively modulates muscle activation based on sensing of the environment. In this dissertation, we expand on the work of Maladen and investigate the muscle activation strategy in the sandfish. We hypothesize that the sandfish actively modulates muscle activation to maintain this optimal waveform with changing resistive force conditions.

The sandfish also presents an opportunity to study undulatory locomotion in a medium dominated by frictional interactions where inertial forces are negligible. Undulatory locomotion is a primitive form of movement used by many phylogenetically diverse animals,

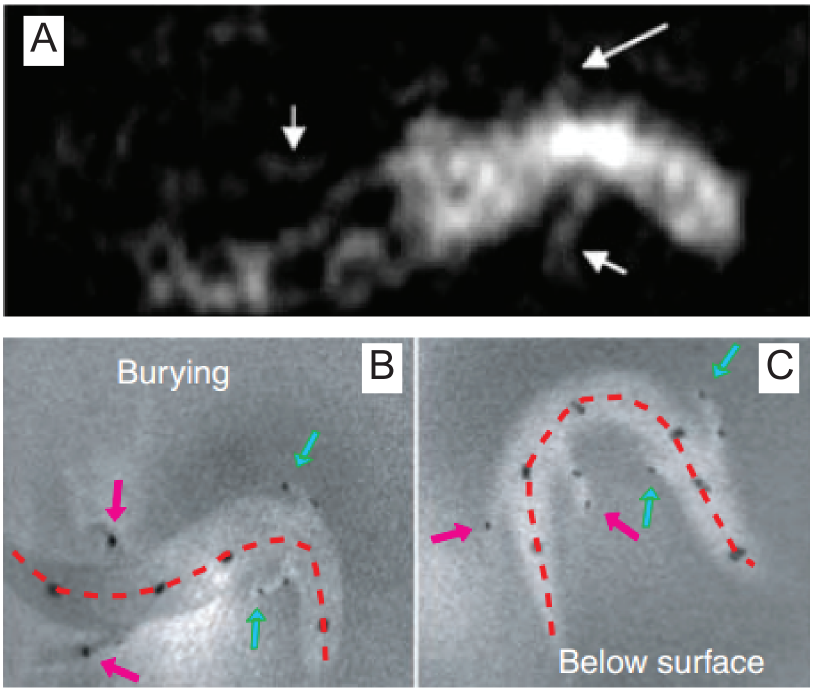

Figure 1.9: Comparison between (A) NMR imaging used by Baumgartner and (B & C) x-ray imaging used by Maladen. Arrows point to limbs. Figure reproduced from [77] and [78].

but has mainly been studied in fluid environments or on hard ground. We will compare the control strategy used by the sandfish and investigate similarities and differences with animals moving in other environments.

Finally, we will investigate the role of the limbs during entry into the medium, which Baumgartner and Arnold speculate are critical for submergence.

1.2.2 Shovel-Nosed Snake

The shovel-nosed snake, *Chionactis occipitalis* (name also used in literature: *Sonora occipitalis*), is commonly found in the Mojave and Sonoran deserts of southern California, southern Nevada, Arizona and in Northern Mexico [79] (Fig. 5.3). This snake is largely nocturnal, but can occasionally be found moving on the surface of the media near sundown [80]. Like the sandfish, the shovel-nosed snake spends most of its time subsurface and in the winter, these animals are found anywhere from 2.5 cm to 60 cm beneath the ground [81]. When it emerges, the shovel-nosed snake moves using lateral undulations and has little slippage [81]. The shovel-nosed snake moves only short distance on the surface of sand, in comparison to other snakes, and buries "effortlessly" into the granular media [21,55,82,83]. Many reports have briefly mentioned that shovel-nosed snakes use lateral body undulations to bury themselves and can move far distances beneath the surface. Yet, no studies exist which quantify kinematics during burial or that capture subsurface movement using x-ray or NMR imaging. For the first time, we will investigate the subsurface locomotion strategy of the shovel-nosed snake using x-ray imaging.

Interestingly, the snake shares many convergent morphological features with the sandfish: it has a countersunk lower jaw, smooth polished scales, and observations of the snake moving on glass has shown that it has a slightly concave ventral surface [55]. However, the snake also has a long-slender body where the longest body length observed in literature was 37.5 cm [81], compared to the sandfish which usually has a body length of approximately 14 cm. Previous work using models to simulate undulatory swimmers moving subsurface within granular media posited that having a longer-slender body would improve swimming performance (η) [8]. The model showed that to swim forward, the thrust from the body must exceed the drag on the head and body, and so the overall locomotor ability depends on the ratio between body and head areas. Therefore, a more long slender animal, with a smaller relative head area, could have a higher swimming speed for a given undulation frequency. We will investigate these claims by comparing the subsurface locomotion performance of the snake with that of the sandfish.

1.2.2.1 Collection of Shovel-nosed snakes

Shovel-nosed snakes were collected in the field by Daniel I. Goldman, Georgia Tech Associate Professor of Physics, Joseph R. Mendelson III, curator of herpetology at Zoo Atlanta, and by Sarah S. Sharpe, Georgia Tech graduate student, near Antelope Valley in southern California. The snakes were caught by 'night driving', in which snakes were found crossing roads. When found on the road, snakes typically appeared active as opposed to other snakes which were lying in the road stationary. Shovel-nosed snakes were primarily found between the hours of 8:00 pm and 11:00 pm. No snakes were found in the day-time. These animals were approved for capture by the California Department of Fish and Game (#SC- 11713).

Figure 1.10: Shovel-nosed snake, *Chionactis occipitalis*, found in the Mojave desert. Photo courtesy of drakeinteractive.com.

In the more recent years, our collaborators in Arizona have collected shovel-nosed snakes during their field studies in Arizona in accordance with the scientific collection permit (#SP-591773) approved by the Arizona Game and Fish Department. Snakes were acquired from Maricopa, Pima and Yuma counties in the Sonoran desert and shipped to the Georgia Tech Physiological Research Laboratory (PRL).

1.2.3 Ocellated Skink

The ocellated skink, *Chalcides ocellatus* (Fig. 1.11), is considered semi-fossorial and is native to northern Africa, southwest Europe and the Middle East [71, 84]. The *Chalcides ocellatus* inhabits a wider geographical distribution than any other Genus *Chalcides*, having crossed water twice during its radiation. The ocellated skink is considered a habitat generalist occupying loose sandy deserts, gravel deserts, coastal regions, agricultural land, and debris [36].

A study by Attum [70] found that ocellated skink and sandfish lizards coexists in the sand dunes of North Sinai, Egypt, although the ocellated skink occupies a different micro-habit. The sandfish is found in loose dry sand while the ocellated skink often lives closer to vegetation and ‘harder’ soil. Unlike the sandfish and shovel-nosed snake, the ocellated skink has a rounded snout, unmodified lower jaw, and cylindrical body [55].

The ocellated skink also commonly buries into the surrounding substrate. However, in a study on escape tactics, Attum [70] found that when the ocellated skink was threatened, it ran to surrounding vegetation to hide in ≈85% of the trials instead of burrowing into sand.

The ocellated skink possesses the ability to bury within a variety of substrates like loose sand, wet soil and debris. Also, this animal is commonly found using similar undulatory waves as the sandfish with limbs laid by its sides during above surface movement through rocks and debris [22]. Because of its ability to bury in soils of varying conditions, we used the ocellated skink as a model organism to study burrowing behavior in granular media with varying water content. Kinematics in wet and dry substrates were quantified using x-ray imaging. This was one of the few, if not the first, locomotion study that controls for media compaction and water content.

Figure 1.11: Ocellated skink, *Chalcides ocellatus*, resting on wet 0.3 mm diameter glass particles.

1.3 Physics of Granular Media

A granular medium (GM) is a collection of macroscopic particles greater than 10 μm in diameter [85] that interact through dissipative, repulsive contact forces. Below 1 μm the material is subject to thermal fluctuations causing Brownian motion whereas a granular media is athermal [85]. Over the last century, granular media has drawn the attention of many physicists and engineers. The medium behavior in bulk is complicated and not well characterized. Unlike a fluid, a granular pile maintains its shape despite stress at the boundary. However, when the pile is tilted beyond a critical angle (called the angle of stability), the grains start to flow [86]. Not only is the physics of GM complex, exhibiting both solid and fluid-like features, but the interaction of GM with intruders is even more involved and not well understood. For example, during locomotion on sand, limbs and bodies of animals can intrude at different depths, speeds, and orientations which may elicit different responses from the medium. Recent experimental studies exploring impact [87, 88], penetration [89], and drag forces [11, 90, 91] within a simple granular medium (monodispersed, spherical glass particles) have helped to reveal some general GM characteristics. In addition, resistive force measurements and computational simulations using the Discrete Element Method (DEM) have enabled the development of a general force model for limbs interacting with dry GM, called 'terradynamics', which may have predictive ability in a large range of dry substrates [89].

Below we review some of the physical principles important to consider when studying locomotion within a granular substrate.

1.3.1 Dry Granular Media

Dry granular media is composed of particles that interact through frictional, repulsive forces only and therefore cannot support any tensile loading [1, 2]. They also flow at the boundary when the angle of stability is exceeded. Consequently, permanent burrows are difficult, if not impossible, to construct in dry sand because the sand caves in easily. Dry sand dunes appear on much of the earth's surface, typically near rivers and oceans or in the desert [92]. Dry sand is estimated to cover as much as 6-10% of all terrestrial surfaces [93]. Grains found in deserts are typically composed of silica and can have a variety of shapes and sizes which may depend on chemical and mechanical factors. Older sands, for example, are typically rounder due to increased abrasion and chemical actions [94]. In the Namib desert, grains range in size between 120 and 490 μm [95]. Larger particles (>400μm) have an increased probability of fracture due to increased probability of imperfections [94].

Numerous physics studies have been conducted using monodispersed, spherical particles

(Fig. 1.12, B & E). This medium may be a good approximation to natural sand found in vast, eolian deserts like the Sahara. GM that are non-spherical (e.g. poppy seeds in Fig. 1.12, A & D, and 'new' sand) and polydispersed, may give a different force response. However, general relationships like rate independence (described below) hold for both materials.

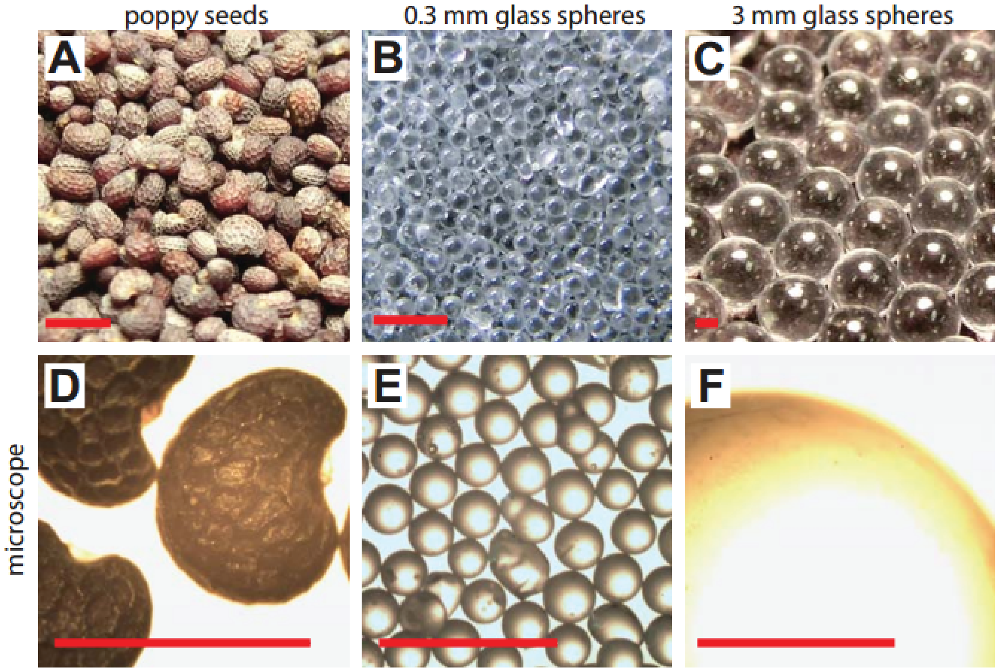

Figure 1.12: Example of granular media. Pictures of (A & D) poppy seeds, (B & E) 0.3 mm diameter spherical glass particles used as experimental granular media, and (C & F) 3 mm diameter spherical glass particles. The length of each scale bar is 1 mm. Figure reproduced from [89].

1.3.1.1 Volume Fraction

In nature, granular media can be found with differing compactions. Loose eolian sand at the top of dunes displays a different behavior than the closely packed grains found on heavily treaded paths. Compaction is characterized by volume fraction, $\phi = \frac{V_p}{V}$, the fraction of the volume of particles, V_p, to the volume of total occupied space, V. Therefore, ϕ represents the fraction of filled space. In the Namib desert, the compaction of sands in different locations range from $\phi = 0.55$ to 0.63 [95]. The compaction varies due to environmental influences (i.e. recently deposited sand at the top of dunes by wind occurs in a more loosely packed state) and due to animal interactions (sand under heavily treaded paths are more closely packed and depending on the medium's initial state, animal burial can act to loosen or consolidate the granular substrate).

Similarly, mechanically stable collections of monodispersed spheres are found in a range between $\phi = 0.55$ (random loose packed) and 0.64 (random close packed) [96]. The term 'random' refers to the fact that these particles are not ordered. For ordered uniform spheres, compaction can be as high as $\phi = 0.74$ which occurs with a face-centered cubic (fcc) lattice arrangement, and can be as low as $\phi = 0.52$ when the arrangement is a simple-square lattice. However, these compactions have never been reported for dry granular media found in nature. Moving objects through a granular media will tend to shear grains, causing a closely packed medium (CP or high ϕ) to dilate, and a loosely packed medium (LP or low ϕ) to consolidate [97]. A material at the critical packing state (ϕ_c) will neither dilate nor consolidate under shear, and this is the compaction at which GM dynamics between LP or CP states shift.

Experimental Technique to Control ϕ: In the laboratory, ϕ can be systematically varied using a fluidized bed and mechanical vibrations [11, 69, 90, 98]. An air flow induces a fluidized state (when particles move relative to each other) and a slow decrease in air flow to zero results in a LP state. CP states can be created by applying a slight air flow below the onset of fluidization and subsequently vibrating the granular media. Another method of creating a CP state is to apply quick pulses of air creating impulses through the media and causing the medium to compact [69].

1.3.1.2 Resistive Forces in a GM

In the absence of theoretical equations, studies have experimentally investigated the forces exerted on intruders (such as a rod) moving through granular media [11, 89–91, 99–102]. These studies have increased our understanding about principles of movement within a GM.

Horizontal Drag:

The majority of horizontal drag studies have been conducted with slow drag speeds ($v < 0.5$ m/s) [11, 91, 102]. In this regime, drag force is independent of speed because grain-grain interactions are dominated by rate independent friction forces(Fig. 1.13, C). However, a recent study revealed that resistive forces increase when moving at higher speeds ($v > 0.5$ m/s); at these high speeds rate dependent inertial forces are no longer negligible [103]. Animal burial and subsurface movement usually occurs at $v < 0.5$ m/s where resistance force is independent of speed. However, for animals such as the *Callisaurus draconoides* that rapidly run on sand, inertial effects may become important during foot impact [104].

Because grain friction force depends on pressure, drag force (F) on an object scales linearly with depth such that $F \propto k|z|A$ for drag speeds less than 0.5 cm/s, where $|z|$ is the depth beneath the surface, A is the projected area of the object, and k is a parameter dependent on material properties [11,91,104] (Fig. 1.13, B).

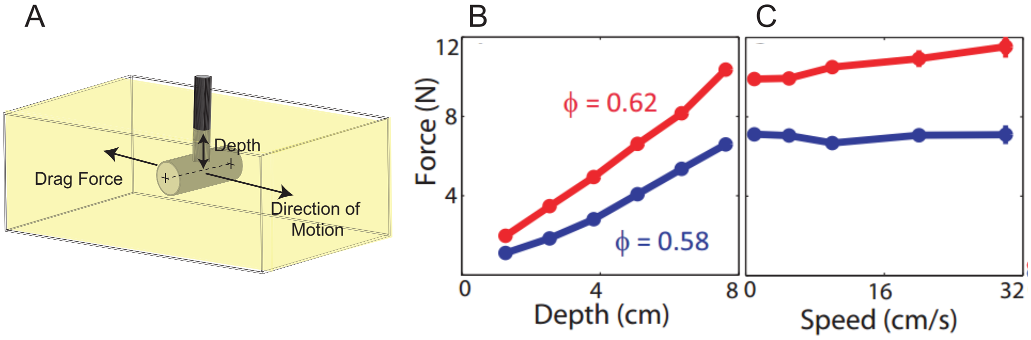

Figure 1.13: Rod drag experiments in granular media. A cylindrical steel intruder (diameter 1.6 cm, length 3.81 cm) is dragged through 0.3 mm diameter glass particles with an attached force sensor which measures resistance force. The drag force acting on the cylinder alone (in B & C) is obtained by subtracting the force acting on the support rod. (B) Resistance force scales linearly with depth and (B) is insensitive to speed. Red points correspond to measurements in a closely packed (CP) granular media and blue are for measurements in a loosely packed (LP) granular media. B and C reproduced from [11].

Tangential forces on a cylindrical rod moving through monodispersed glass particles are approximately proportional to $\cos(\psi)$, where ψ is the angle between the rod and direction of motion (Fig. 1.14, B). This relation is similar to movement through a fluid. However, unlike movement through a fluid, the normal forces are not proportional to $\sin(\psi)$. At low angles the forces increase from zero more rapidly (see Fig. 1.14, A) [8,11].

Shape of the intruder has little effect on the magnitude of drag force for depths less than 14 cm if the projected area of the intruder remains constant ($\leq$30% difference) [101]. However, the lift force on two objects with the same projected area but differing shapes can

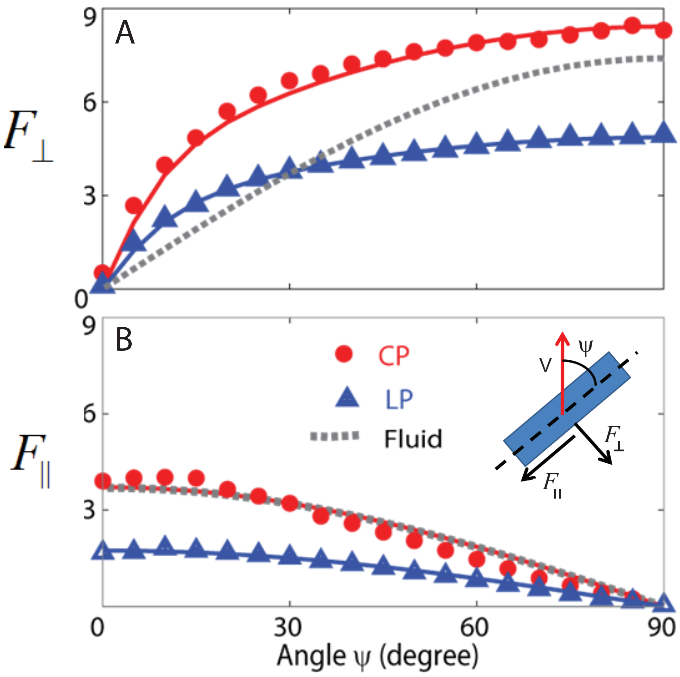

Figure 1.14: Resistance force vs rod angle. (A) Perpendicular and (B) parallel forces on a rod oriented at different angles, ψ, with respect to the drag direction. The red and blue points are experimentally measured drag in CP and LP granular media, respectively. Gray dashed curves are drag in a fluid where the forces have been scaled such that the parallel drag in the fluid matches the parallel drag in a CP granular media. Reproduced from [11].

substantially differ (100% increase between cylinder vs. square shape) at shallow depths [9, 105]. Furthermore, bars with cylindrical or rectangular cross-sections have a positive lift force during drag which would make these object rise during movement. In contrast, a bar with a flat bottom and semicircular top would experience a negative lift force causing the object to submerge deeper into the material.

Penetration:

Like horizontal drag, penetration resistance is insensitive to speed below 0.5 cm/s, increases linearly with depth, and increases with projected area of the object [100,103]. These results suggests than an animal with a bigger foot and/or body may have more resistance to overcome during burial and that some animals may not be able to move beyond a certain depth due to the increased force requirement.

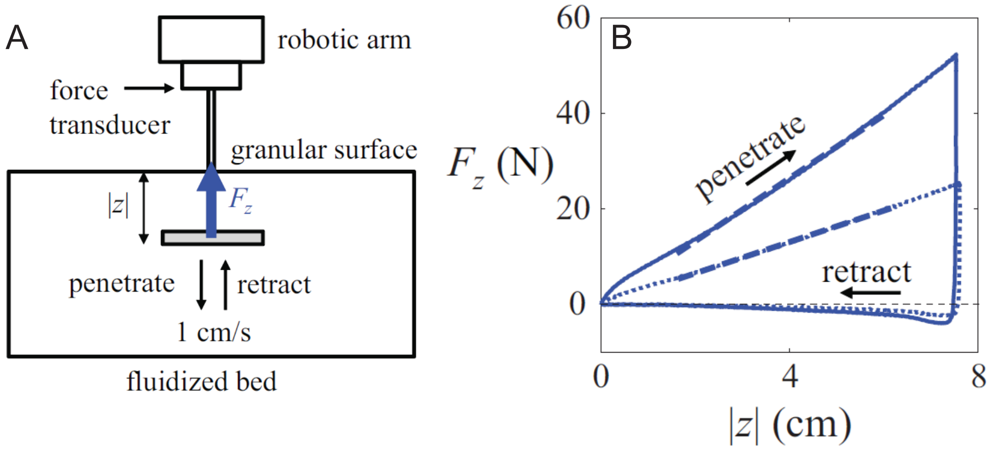

Figure 1.15: Penetration in granular media. (A) Robotic arm is used to penetrate a plate in 0.3 mm glass particles. The arm penetrates into the media to a depth of 7.6 cm at a speed of 1 cm/s, pauses, then retracts at the same speed. (B) Penetration force as a function of depth. The solid curve is the force on a plate of area 7.6 × 2.5 cm^2. The dotted curve is the force on a plate of half the area (3.8 × 2.5 cm^2). Figure reproduced from [103].

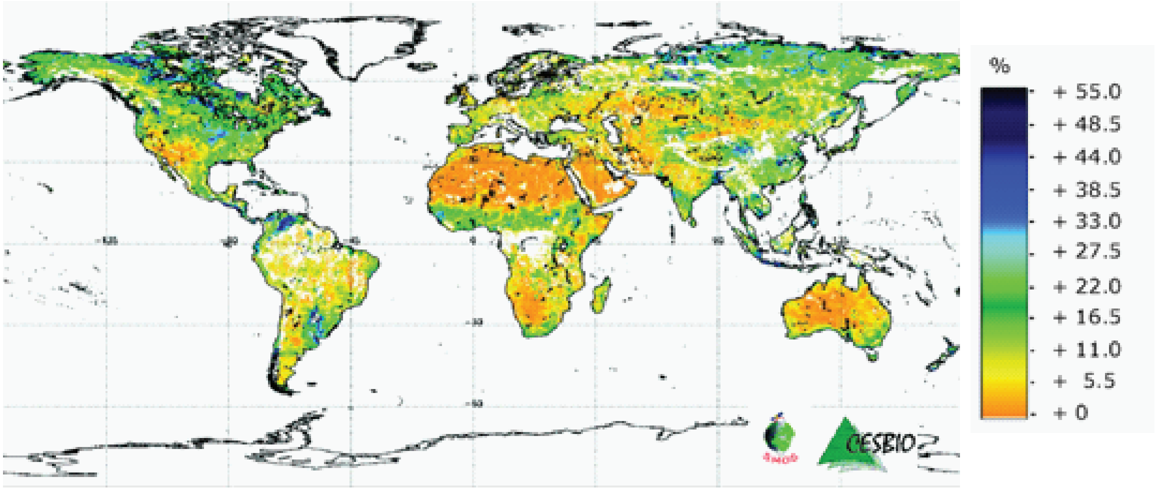

Figure 1.16: Surface soil moisture content (defined as a percentage of saturation) for terrestrial terrain as estimated by remote sensing data from June 8-15, 2010. Orange colors denote dry soils while blue colors denote wetter conditions. Soil moisture levels are given to an accuracy of 4% at a spatial resolution of 50 km. Credit: Image courtesy of the European Environment Agency and data was obtained from the Soil Moisture and Ocean Salinity (SMOS) satellite.

1.3.2 Wet Granular Media

Wet granular media comprises an even larger proportion of terrestrial surfaces than dry media (Fig. 1.16). Numerous animals such as worms, caecilians, snakes and moles burrow into wet ground. The addition of small amounts of water to granular media can have have large changes in the physics of the substrates [106]. For example, mixing water with dry media enables the creation of tunnels and sand-castle structures that are mechanically stable. This increased stability arises due to cohesion from liquid bridges that form between grains. Fluorescence microscope images have enabled visualization of liquid bridge formation. Depending on wetness content (W, mass of liquid/ mass of dry media), wet granular media is grouped into four states: pendular, funicular, capillary and slurry (Fig. 1.17). In the pendular state liquid bridges form between two particle contacts and this occurs when a small amount of liquid is added. As more liquid is added the wet media enters the funicular state where the fluid fills the pore-space spanning multiple particle but some air-filled voids remain. The capillary state occurs where all pores are filled with the liquid. The slurry state occurs when particles are completely immersed in the liquid and no capillary action occurs at the surface. This happens after saturation is reached [106, 107].

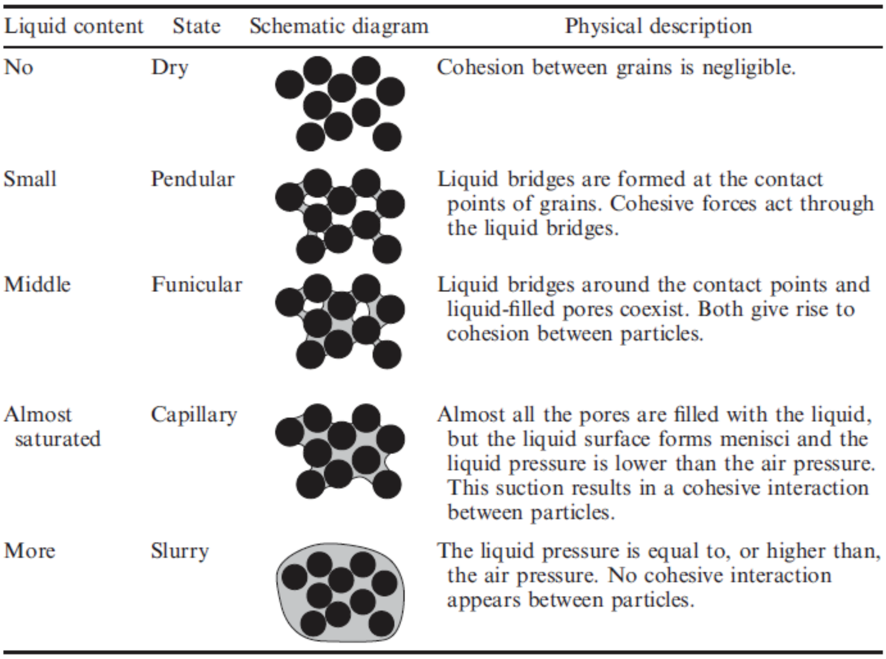

Liquid content	State	Schematic diagram	Physical description
No	Dry		Cohesion between grains is negligible.
Small	Pendular		Liquid bridges are formed at the contact points of grains. Cohesive forces act through the liquid bridges.
Middle	Funicular		Liquid bridges around the contact points and liquid-filled pores coexist. Both give rise to cohesion between particles.
Almost saturated	Capillary		Almost all the pores are filled with the liquid, but the liquid surface forms menisci and the liquid pressure is lower than the air pressure. This suction results in a cohesive interaction between particles.
More	Slurry		The liquid pressure is equal to, or higher than, the air pressure. No cohesive interaction appears between particles.

Figure 1.17: Granular media with varying wetness contents. Black circles are grains and gray regions represent water. Figure reproduced from [106].

The top layer of soil found on the majority of earth's land masses are in the pendular or funicular state (according to soil moisture data from the European Environment Agency, Fig. 1.16). Although liquid formation and the resulting force have been studied extensively between two particles, the physics of a wet collection of grains is still not well understood. Some physics studies have explored cohesion, strength and stability in wet granular media. Most studies have been conducted in the pendular regime. For the few studies that have explored mechanical properties in the funicular regime, differing results have been shown. This could be due to the use of differing dry granular materials between experiments [106] or due to different preparation techniques [108]. The forces exerted on an animal by wet granular media and how these forces differ with depth [109], speed, and grain properties like size and mass are largely unknown [106]. Preparing large, repeatable wet substrates to test animals on and within can be difficult. Below we review some of the studies which have characterized the mechanical properties of wet substrates.

1.3.2.1 Cohesion

Cohesion in wet granular media is induced by the surface tension of the wetting fluid and capillary effects [106]. The presence of liquid between two grains results in a suction force. As water is added to granular media, the number of liquid bridges on each particle rises quickly to 6. As more water is added the number of bridges per particle stays the same [107] but the water volume spanning each particle increases. The number of liquid bridges formed in a closely packed wet granular media is approximately 10% higher than for loosely packed wet media. Eventually these bridges coalesce into clusters. In the pendular state, mechanical properties change quickly with the addition of small amounts of water then remain similar as more water is added. This relationship is attributed to the number of liquid bridges on each particle, which rise sharply then plateau. For example, in the pendular regime Coulomb cohesion (shear strength at zero confining stress) [110] and tensile strength [111] both rise as W increases initially, then saturate.

Cohesion also results in a higher angle of stability and repose in wet granular media. The angle of repose is the steepest angle at which a granular media can be formed relative to the horizontal. The angle of stability (also called the critical angle) is the largest angle a material can be tilted without avalanching. In dry sand, the angle of repose is approximately 30° and varies with material properties. Studies found that angle of repose increased with liquid content indicating an increase in cohesion [86]. The increased angle of repose allows animals to create tunnels within granular materials that are not possible for dry granular media which collapse easily. These tunnels could allow animals to move underground using pre-made burrows and without having to deform substrates continuously during movement. However, initially creating the tunnels within undisturbed wet media may be more difficult due to increased resistance force from the increased cohesion. For larger liquid contents where agglomerates form, the angle of repose is less understood and changes for different experimental preparations. However, studies have shown that the distribution width of the repose angles becomes larger for higher liquid contents [112].

1.3.2.2 Compaction

Wet granular media can reach lower volume fractions than possible in a dry granular media due to the stabilizing effect of the liquid bridges [106]. Depending on the liquid used as the wetting fluid and particle type, ϕ can be as low as 0.43 in a wet granular medium [113]. This low ϕ is most likely due to large voids that are formed within the medium. Experimental studies have attempted to reproduce consistent preparations using a variety of techniques: (1) Mixing the liquid and dry media, followed by slow pouring into a container [114]; (2) Vigorously shaking of the liquid-sand preparation to homogenously distribute the water [107, 110]; (3) Constructing thin (2.5-5mm thick) layers of sand where a fine jet sprays a known quantity of water onto each layer before another is added [115]; (4) Imbibition (a wetting process) in which water is allowed to percolate through the media [108]; (5) Use of a humidifier to introduce water into the substrate [116] and; (5) Drainage (a drying process) [108]. These techniques often result in different compactions with small changes in preparation. Studies that have attempted to control or alter the compaction or wet GM do so by using a ram [117] or by tapping the material [107, 113, 116] to achieve higher compactions. Fiscina [113] found that the compaction dynamics of a wet medium obeys an inverse logarithmic law, like most dry GM. However, the characteristic relaxation times changed when liquids of different surface tensions were used. Currently, no techniques exist which create homogenous loosely packed states without large voids in quantities sufficient for locomotion experiments.

1.4 Neural Control of Movement

Movement results from the complex interplay among an animal's nervous system, biomechanics, and the surrounding environment. Understanding how animals actuate their muscles in order to produce joint torques is a critical aspect in understanding how successful locomotion is produced and/or stabilized. Movement can occur passively, due to external influences, or actively, due to forces generated by muscle contractions. For example, passive dynamics walkers are mechanical devices which 'walk' downhill without actuation under the influence of gravity [118]. These robots are an excellent example of how passive mechanics alone can produce long-distance motion. However, these passive robots cannot walk uphill and often become unstable with the slightest perturbation. Sensing and control from the nervous system can allow animals to do work against their environment, maintain a kinematic control target as external parameters change, and provide stability by effectively tuning passive properties (like stiffness). Understanding how animals use neural control during locomotion in different environments not only provides a more complete picture about how successful locomotion is generated but also has implications for robotic design and control.

A multitude of studies have investigated the neural control of undulatory swimming, a simple and primitive form of locomotion used by a diversity of organisms to move in a range of environments. These studies, for example, have led to the discovery and characterization of Central Pattern Generators (CPGs), neural networks that endogenously produce rhythmic patterned outputs [119]. These rhythmic oscillations are involved in many biological processes that occur in both vertebrates and invertebrates [120]. For example, the leech is an invertebrate that moves forward using dorso-ventral undulations. Each ganglion of its neural cord possesses a CPG that drives antagonistic muscles 180° out of phase [121, 122]. These CPGs have intersegmental connections that project in the rostral (head) and caudal (tail) direction and produce a phase lag between the onset of activation of rostral muscle groups. This coordination between activation timing results in a rostral-caudal traveling wave of muscle contractions that produces a single period traveling kinematic wave and enables forward locomotion. In addition, numerous studies have investigated neural activation and control in lampreys. For example, *in vitro* studies on the lamprey have induced fictive locomotion by stimulating the brainstem [123], spinal cord [124] or by applying excitatory drugs [125]. These studies have helped to identify how neural networks interact to generate locomotion. Other studies have enhanced our understanding about neural control by measuring the activation of muscles using electromyography (EMG) (see below). This less invasive technique records neural activation *in vivo*. In 1989, Williams et al. [126] used EMG and found that the wave of muscle activation propagates faster than the wave of curvature during lamprey and trout swimming, a phenomenon that was later found to be general in undulatory animals and thought to help stiffen rostral body segments during swimming to generate additional power. This topic will be explored more in Chapter 3 using EMG measurements in the sandfish. The *Caenorhabditis elegans* worm is another animal that has been used extensively as a model organism to study locomotion due to its "simple" structure (relative to mammals and other larger animals) and transparent body. *C. elegans* are composed of 302 neurons and the connections have been fully mapped by scientists [127]. This animal has been used to study chemotaxis, mating behavior, sensing and movement. However, even with this "simple" nervous system we still do not understand its entire complexity.

Fewer studies have investigated neural control in complex environments such as within sand. Jayne et al. [26] used EMG to investigate muscle activation in the *Uma* lizard during sand diving. He found that temperature influenced both neural activation and performance. However, a general understanding about how animals control muscle contractions to generate subsurface movement in granular media is lacking. We hypothesize that muscle activation changes with changing resistive force in order to maintain subsurface performance. Muscle activation recordings could also be used to compare and contrast movement within granular media to movement through water.

1.4.1 EMG Experiments

EMG is a technique which measures the electrical activity produced in muscle. EMG recordings can be used as a means of observing neural control of muscles during contraction while minimally interfering with the behavior of the system [128]. Although EMG is not directly proportional to muscle tension, it can give some indication about force generation when techniques (such as tendon buckles) that measure tension cannot be implemented.

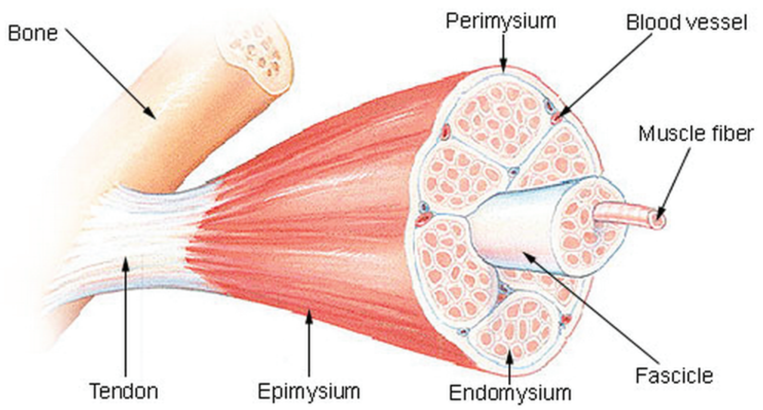

Figure 1.18: Structure of skeletal muscle. Credit: Wikimedia Commons.

Muscles are made up of parallel bundles of string-like fascicles, which are themselves made up of string-like multinucleated cells called muscle fibers [129] (Fig. 1.18). Motor neurons synapse onto muscle fibers at motor endplates (usually located near the middle of the fiber). An action potential within the neuron's axon triggers the release of a neurotransmitter called acetylcholine. The acetylcholine binds to ion channels within the muscle causing these channels to open. The resting membrane potential in vertebrate skeletal muscle is usually between -70 and -90 mV. The opening of the channels causes an influx of current that depolarizes the muscle cell. This depolarization opens more voltage gated sodium channels and leads to further current influx. Eventually potassium channels open and K^+ ions flow outward along their concentration gradient repolarizing the cell. This depolarization and repolarization event is referred to as an action potential. The action potential propagates down the muscle fiber at 2-5 m/s. The change in potential across a muscle cell triggers the release of calcium ions from the sarcoplasmic reticulum within a muscle fiber. The presence of these calcium ions cause globular heads on myosin (thick) filaments to interact with and move actin (thin) filaments such that the overlapping region between the filaments increases and the muscle shortens (see Fig. 1.19 for a description of how myosin interacts and moves actin filaments). In this way, electrical activity is converted to mechanical tension [128].

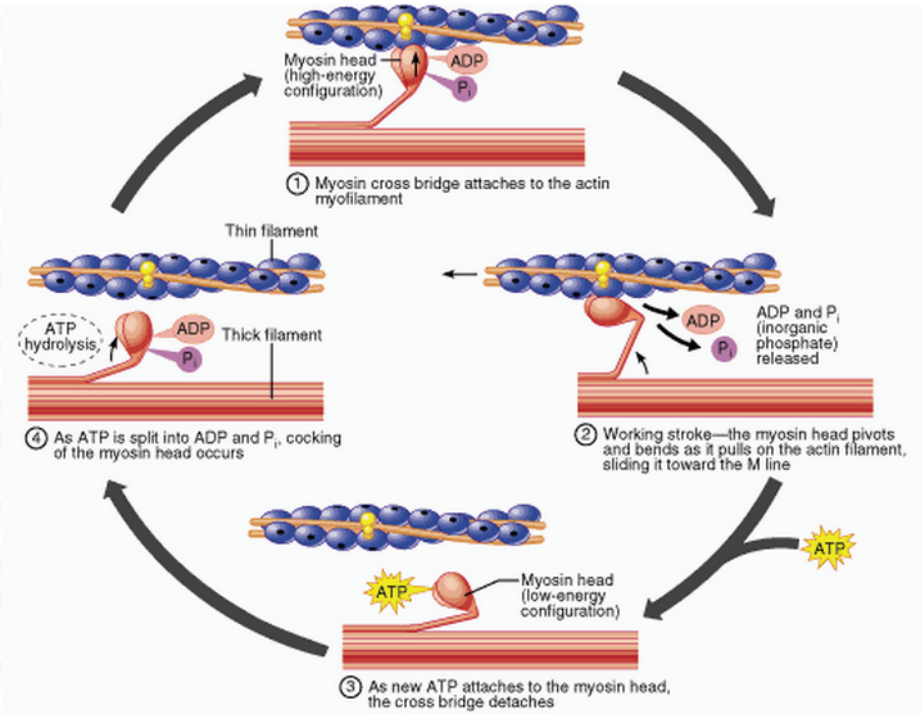

Figure 1.19: Sliding filament theory of contracting muscle. In step 1, the myosin head attaches to actin in the presense of calcium. In step 2, the myosin head pivots and pulls the actin filament. In step 3, ATP (Adenosine triphosphate) binds to the myosin head and causes the cross-bridge to detach. In step 4, ATP hydrolysis occurs (the ATP splits into ADP (Adenosine diphosphate) and P (orthophosphate)), and causes the myosin head to cock. This process is repeated until Ca^{++} ions are removed from the cytoplasm and binding sites on actin filaments are blocked. Credit: Benjamin Cummings, 2001, Addison Wesley Longman, Inc.

A muscle is typically controlled by approximately 100 motor neurons. Each motor neuron innervates 100 to 1000 muscle fibers. A motor unit is defined by a motor neuron and all of the muscle fibers it innervates. EMG wires inserted within or on the surface of muscle measures the aggregate motor unit action potentials (MUAPs) from surrounding fibers. In some small animals, such as the cockroach (*Blaberus discoidali*), a single motor neuron innervates a single muscle structure. Therefore, individual action potentials can be measured using EMG [130]. However, for most animals EMG measures the sum of many MUAPs. Individual action potentials can be identified for these EMG signals using decomposition techniques such as wavelet analysis [131]. However, these techniques were not used in this work.

Typically EMG electrodes are constructed from stainless steel, platinum alloys, copper or gold wire, and are wrapped in an insulation sheath. A small portion of the insulation is removed during construction such that the metal comes into contact with the muscle at a desired location. Monopolar (one contact), bipolar (two-contacts), or multipolar (many contacts) electrodes can be constructed to measure EMG signals, and the choice of electrode may vary with the application [128]. Typically a ground electrode is implanted in adipose tissue, skin or fascia to establish a reference voltage in passive tissue. Bipolar electrodes are commonly used in animal experiments because they give an indication of muscle activation timing and amplitude. The differential voltage output is generally on the order of 100μV. Relative movement between the wires can cause cross-talk and noise, so typically wires are wound around each other to prevent movement before amplification. Skin surface electrodes are often used as a noninvasive method to record EMGs and have been used extensively in human studies. However, the quality of these recordings depend on the skin through which they must detect potentials and thus can vary with preparation and skin type. In addition, surface electrodes typically have less spatial selectivity. A more invasive technique used in many animal studies are percutaneous electrodes implanted *in* muscle via a hypodermic needle or sutured into the muscle. These electrodes have more spatial selectivity and can record from deeper muscle groups.

There is a delay between EMG onset and force production within the muscle (> 2 ms). Despite this, EMG timing and duration can give an indication about when muscles actively produce force. As a muscle produces more force, additional motor units are recruited which will result in a stronger contraction. As such, when more MUAPs are detected by the electrode, the effect will be a larger amplitude EMG. However, inferences about EMG amplitude and/or intensity (the ratio of rectified integrated area of the EMG burst to burst duration) and their correlation with muscle force must be made with caution for a multitude of reasons. (1) The intensity can change between electrode implantation sites and with small changes in electrode construction. (2) Due to the force-velocity, force-length relation in muscle, the same EMG intensity detected during contraction at different speeds or different muscle lengths could correspond to different muscle forces (or vice-versa). (3) Muscle has a history dependent force response. Furthermore, as a muscle fatigues from use, more motor units are recruited to maintained the same muscle force. As a result, EMG may detect an increasing level of activation in a fatigued muscle while force is held constant or even declining.

Even with these caveats, EMG provides a good, minimally invasive method to gain measure the output of the central nervous system understanding about neural control during locomotion and how environments may influence the activation strategy. In this dissertation, we implant bipolar hook electrodes made from ≈ 50 μm diameter stainless steel wire into the epaxial musculature of the sandfish. We hypothesize that the sandfish targets an optimal kinematic wave which maximizes speed and minimizes cost of transport. Therefore we predict the neural activation changes with changing resistive force conditions to maintain an optimal shape during swimming.

1.5 Resistive Force Theory

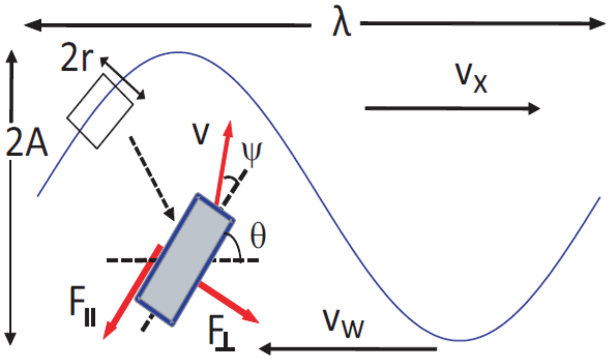

Figure 1.20: Diagram explaining resistive force theory and the forces on a segment of the body. The blue curve is the modeled body. A is the amplitude of the wave and λ is the wavelength. v_x is the forward velocity and v_w is the velocity of the traveling wave down the modeled body. ψ is the angle between the velocity direction and orientation of the segment. $F_{||}$ and $F_{\perp}$ were found from rod drag experiments (see Fig. 1.14). Figure reproduced from [11, 132].

Resistive force theory (RFT) was a theory developed in 1955 to explain features of undulatory swimming for organisms (such as spermatozoa) that move in low Reynold's number (Re) fluids [133]. At these low Re, viscous forces dominate and inertia is negligible. In the RFT model, the body is partitioned into small segments (Fig 1.20). Each segment experiences a thrust and drag which is related to the velocity and orientation of the segment through the Stokes equations. The net forward force on an element is

$$\delta F_x = \delta F_\perp \sin\theta - \delta F_{||} \cos\theta, \tag{1.1}$$

where θ is the angle between the forward direction of the animal and the instantaneous orientation of a segment. Stokes equations do not apply for movement through granular media. Consequently, empirically measured normal and parallel forces were obtained by dragging a small cylindrical intruder through the granular media at different angles relative to the velocity direction [7,11] (Fig. 1.14) and used in the granular RFT model. These forces were independent of speed below ≈50 cm/s. This model assumes that there is no interaction between segments. In a low Re number fluid, this simplifying assumption may lead to error between model predictions and experiment, but in a granular media, where forces dissipate quickly with increasing distance from the segment, the error is small (≤20%) [7]. The net force on the body is obtained by integrating the forces on each segment along the entire wave. The average forward (steady-state) speed was calculated by summing the forces on the body and the head and setting the sum equal to zero. The total time-averaged force in the forward direction is described by:

$$\bar{F}_x = \int_0^\lambda (P_\perp \sin\theta - P_{||} \cos\theta)\sqrt{1+\tan^2\theta}\, b \, \mathrm{d}x + \bar{F}_{\mathrm{head}}, \tag{1.2}$$

where $P_\perp$ and $P_{||}$ are stresses perpendicular and parallel to the axis of each element, b is the height of each element, and $\sqrt{1+\tan^2\theta}\mathrm{d}x$ is the arc length of an element.

In collaboration with Yang Ding, we used RFT to predict subsurface sandfish speed, wave efficiency (η, forward speed divided by the speed of the wave), and mechanical cost of transport (Chapter 2) as a function of sandfish shape (quantified by amplitude of the wave divided by the wavelength (A/λ)). RFT was also used to predict wave efficiency as function of the portion of the body interacting with the media to understand how limbs are needed during the beginning of burial (Chapter 4). In collaboration with Stephan A. Koehler, we again use RFT to predict the wave efficiency for an undulatory swimmer moving within granular media with changing A/λ, waves along the body, body shape (body-length to body radius ratio), and particle-skin friction (Chapter 5). These predictions helped to explain experimental observations and develop additional hypotheses. For more details, see [7, 8, 132].

1.6 Specific Aims

The overall goal of this dissertation is to (1) gain insight into how animal morphology, kinematics, and neural strategy can be leveraged to achieve effective locomotion in granular substrates and (2) to understand how animals compensate for changing resistive force conditions with changing environmental parameters, like media compaction, wetness or depth of penetration (Fig. 1.21). To do this we use x-ray imaging to visualize the kinematics of several animals which are commonly found in granular environments and readily burrow and move subsurface. In addition, we record muscle activation patterns from a sand-specialist lizard to investigate neural control strategies. Resistive force measurements in GM and theoretical analysis which couples animal movement to a model of the environment are used to generate and test hypotheses about these locomotion strategies. This work introduces the first proposed "template" for control in dry granular media, and suggests the importance of considering environmental condition when examining movement patterns.

Specific Aim 1: Characterize neural control strategy used by the sandfish lizard during subsurface locomotion in dry GM.

Study 1A- Investigate the neural activation in the sandfish during subsurface movement at different depths, speeds and in varying media compaction.

Study 1B- Investigate the activation timing patterns in the sandfish during sand-swimming

---

All RFT work in this dissertation was developed and run by Yang Ding in Chapter 2, 3, and 4. RFT was conducted by Stephan A. Koehler for comparison between sandfish and snake in Chapter 5.

and compare to the resistive force theory model.

Specific Aim 2: Investigate the role of limbs during rapid sandfish burial.

Study 2A- Characterize the sandfish limb pattern used during burial into GM.

Study 2B- Restrain limb-use and observe effect on sandfish burial performance.

Specific Aim 3: Compare subsurface swimming of the sandfish lizard and shovel-nosed snake.

Study 3A- Quantify body morphology, body friction, kinematics, and slip in the shovel-nosed snake and compare to the sandfish.

Study 3B- Use resistive force theory to investigate how body morphology influences slip in a GM.

Specific Aim 4: Investigate the effect of GM water content on resistive force and ocellated skink locomotion.

Study 4A- Develop a method to produce repeatable, homogenous wet granular media preparations.

Study 4B- Quantify and compare the burial strategy of the desert-generalist ocellated skink in wet and dry media.

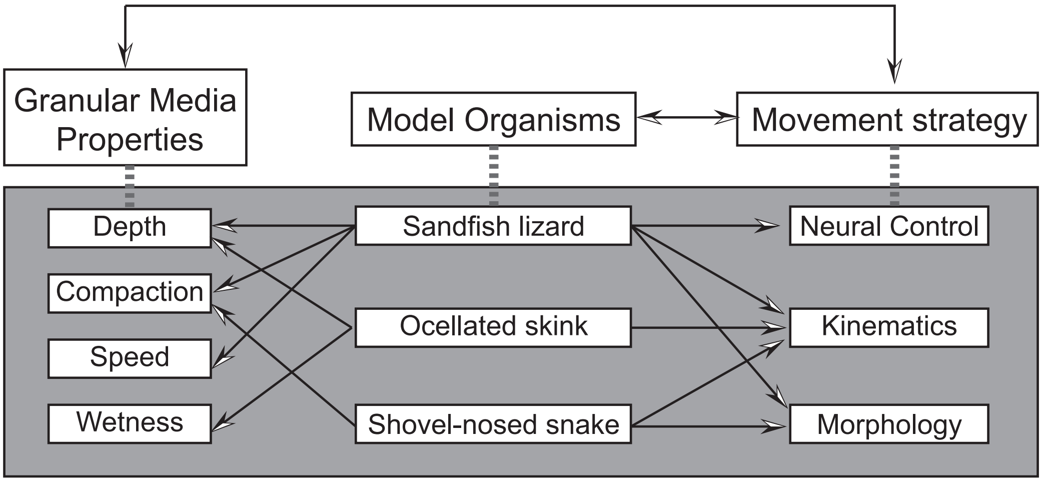

Figure 1.21: This dissertation will focus on the interplay between locomotion strategies and environment for a group of model organisms. The gray box displays the animals and corresponding aspects that were studied for each.

CHAPTER II

NEUROMECHANICS OF SAND-SWIMMING: EVIDENCE OF A TEMPLATE FOR CONTROL

2.1 Summary

Animals like the sandfish lizard (*Scincus scincus*) that live in desert sand locomote on and within a granular medium whose resistance to intrusion is dominated by frictional forces. Recent kinematic studies revealed that the sandfish utilizes a wave of body undulation during swimming. Models predict that a particular combination of wave amplitude and wavelength yields maximum speed for a given frequency, and experiments have suggested that the sandfish targets this kinematic waveform. To investigate the neuromechanical strategy of the sandfish during walking, burial and swimming, here we use high-speed x-ray and visible light imaging with synchronized electromyogram (EMG) recordings of epaxial muscle activity. While moving on the surface, body undulation was not observed and EMG showed no muscle activation. During subsurface sand-swimming, EMG revealed an anterior-to-posterior traveling wave of muscle activation which traveled faster than the kinematic wave. Muscle activation intensity increased as the animal swam deeper into the material but was insensitive to undulation frequency. These findings were in accord with empirical force measurements, which showed that resistance force increased with depth but was independent of speed. The change in EMG intensity with depth indicates that the sandfish targets a kinematic waveform (a template) that models predict maximizes swimming speed and minimizes the mechanical cost of transport as the animal descends into granular media. The differences in the EMG pattern compared with EMG of undulatory swimmers in fluids can be attributed to the friction-dominated intrusion forces of granular media.

This chapter is a published paper by Sarah S. Sharpe, Yang Ding and Daniel I. Goldman, *The Journal of Experimental Biology*, 2012 [34]

2.2 Introduction

Successful locomotion in a diversity of environments [16–19] emerges from the interplay between neuromechanical [20] systems (the combined action of the nervous and mechanical systems) and the physical environment. The central nervous system (CNS), musculoskeletal system and sensory system constitute a feedback system that accepts inputs from internal and external sensors and generates appropriate muscular action to generate forces that act on the environment. At one extreme, locomotion can be generated with a feed-forward control strategy in which activation patterns are dictated by commands from the CNS. This motor control may be insensitive to perturbations [129]. In this situation, mechanical feedback can be used to passively stabilize movement with changing external forces [130, 134, 135]. At another extreme, motor control can be actively modulated by sensory input to generate specific kinematic patterns that are tuned in response to environmental changes [136, 137].

The surrounding physical environment plays a significant role in determining animal kinematics, neuromuscular strategy and the efficacy of the locomotion strategy. Many recent studies [39, 136, 138–144] have investigated how these factors change with either changing substrate mechanics or changes in the rate of movement through the material. For example, some animals move between environments like water and land that present different mechanical responses to limb and body movement [136, 136, 141, 145]. These different force conditions are correlated with different movement strategies. For example, on hard ground, salamanders generate propulsion with limbground interactions [146] and use standing waves of axial bending [147]; however, in water, salamanders generate propulsive thrust forces using traveling wave axial body undulations while limbs are placed along their sides. Lungfish, which commonly move in muddy conditions in the wild, change kinematics and muscle activation when they encounter fluids of varying viscosity [143]. During steady-state swimming, lungfish increase lateral bending and use a higher amplitude of muscle activity as fluid viscosity increases. Similarly, the American eel [138] uses a different pattern of muscle activation and kinematics while swimming in water at faster speeds. Only posterior musculature is employed during slow swimming while anterior muscle groups are recruited as the eel increases its speed.

Modulating neural control strategies with changing conditions can allow an animal to maintain stability, reduce energy, enhance speed or operate at some other locomotion control target. These control targets can be analyzed in more detail by establishing a 'template' for a locomotion pattern. Templates are low-order models [148] that capture the basic features of a locomotor behavior for example, an inverted pendulum model for walking [149] and a spring-loaded inverted pendulum (SLIP) model for running [148,150] and these models have demonstrated predictive ability for stability [151] and energy savings [149, 152]. Templates can also be used to advance hypotheses concerning neuromechanical control strategies that enable a targeted behavior [148].

The biomechanics of the many animals that live on and within granular media, a material that can display both solid and fluid-like features, are relatively unexplored [21–25] and even less is known about the neuromechanical strategies used by animals that move in granular substrates [26]. Granular media are defined as collections of particles that interact through dissipative, repulsive contact forces. The animals encounter external resistive force conditions that depend on the location of the movement (above or below the surface), and also on granular media compaction and depth beneath the surface. Compaction is characterized by volume fraction (ϕ; the ratio of the solid volume of the grains to the total occupied volume) [2] and is influenced by wind and animal digging, with ϕ ranging from 0.55 to 0.63 in natural dry sands [95].

In the laboratory, ϕ can be systematically varied *via* an air-fluidized bed [11, 69, 90] (Fig. 2.1, B), and provides a controlled method to test the effects of compaction on locomotion. A less compact granular medium (low ϕ, loosely packed or LP) generates smaller forces on a rod intruder moving at constant speed than does a more compact granular medium (high ϕ, closely packed or CP) [11,90] (Fig. 2.1, C & D). Unlike fluids, the average force acting on an object moving at low speed (typically less than 0.5 m/s) through granular media increases proportionally with depth (Fig. 2.1, C) and is approximately independent of speed (Fig. 2.1, D) [11, 91]. This is because frictional interactions dominate the forces between grains and intruders.

Recent work [7, 11] used high-speed (up to 1000 frames per second (fps)) x-ray imaging

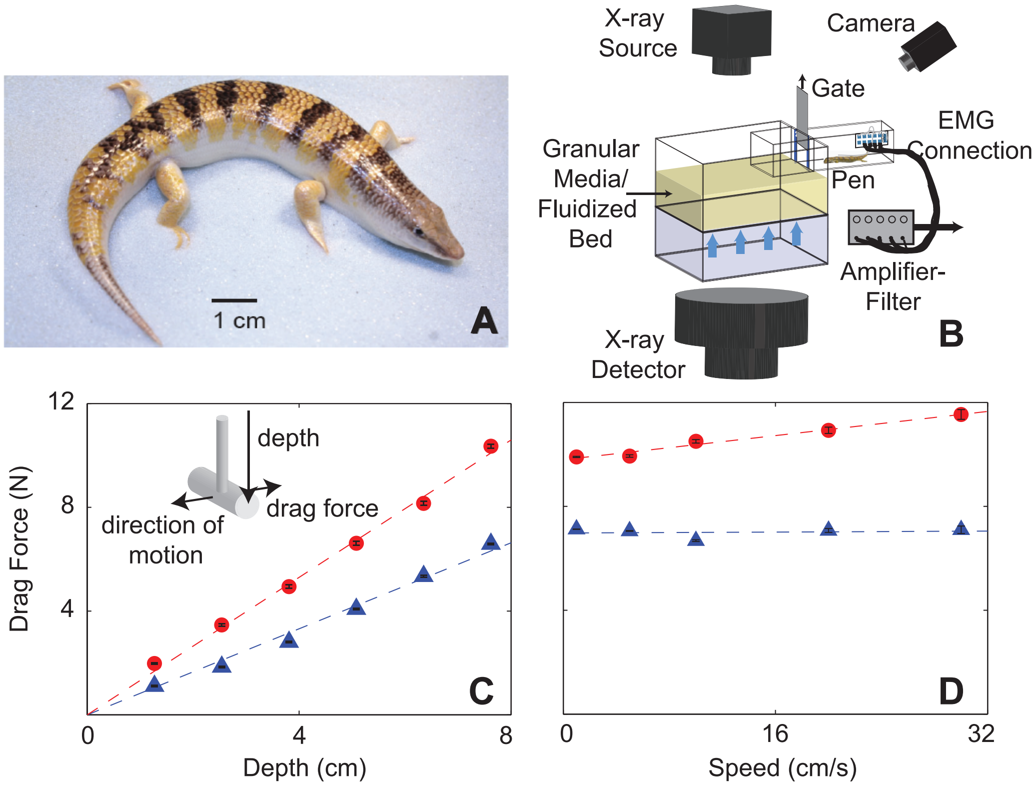

Figure 2.1: The sandfish lizard (*Scincus scincus*), experimental setup and granular drag force. (A) Image of the sandfish lizard resting on 0.27 ± 0.04 mm diameter glass particles. (B) The experimental setup consists of a fluidized bed for preparing granular media into different volume fractions ϕ, x-ray imaging equipment and high-speed cameras. Electromyogram (EMG) wires from the sandfish body run to an amplifier-filter and then to the data acquisition (DAQ) device. (C,D) Drag force on a stainless steel cylindrical rod (diameter 1.6 cm, length 3.81 cm) dragged at different (C) depths and (D) speeds in a loosely (blue triangles) and closely (red circles) packed granular medium (ϕ=0.58 and ϕ=0.62, respectively). Note that the s.d. bars are smaller than the marker size. The orientation of the rod is perpendicular to the direction of motion (C, inset). Drag velocity is 10 cm/s in C and depth is 7.62 cm in D. Dashed lines are best linear fits. Data are re-plotted from supplementary material in Maladen et al. [11].

to investigate the kinematics of the sandfish (*Scincus scincus*), a sand-specialist lizard [22, 36, 55, 70] native to the Sahara desert (Fig. 2.1). The sandfish is subarenaceous, spending most of its time subsurface and moving while fully buried beneath the sand [11,22,55]. The x-ray studies showed that the sandfish uses its limbs in a diagonal gait pattern to generate forward propulsion when moving above the surface and, unlike other lizards, the trunk undergoes little undulation [11]. As the sandfish dives into the surrounding sand, it executes a stereotyped swimming pattern making it an excellent animal model for studying how the physics of granular media influences movement strategies. During subsurface movement, the sandfish propagates an anterior-to-posterior traveling and approximately sinusoidal wave of axial body undulations to propel itself through the media while its legs remain by its sides [11]. Remarkably, the animal uses a similar spatial form (the ratio of wave amplitude, A, to wavelength, λ) of $\approx$0.2, and wave efficiency (η, the ratio of the average forward speed of the animal to the speed of the kinematic traveling wave) of $\approx$0.5 regardless of media ϕ or swimming speed; for a single period sinusoidal wave, A/λ characterizes the shape of the animal. Models reveal that the sandfish propels itself by swimming through a self-generated localized 'frictional fluid' within the media [7].

We hypothesized that the sandfish uses a neural strategy that targets these kinematics and we propose that the observed waveform is a template for optimal sand-swimming. In support of this hypothesis, we note that recent theory, numerical simulation and robotic models of the sandfish interacting with granular media have revealed that forward velocity is maximized at $A/\lambda = 0.2$ [7, 78]. In this paper, to determine whether the sandfish actively modulates its muscle activation strategy to achieve this control target, we measured the kinematics and the axial neuromuscular strategy during above surface movement and subsurface swimming using high-speed x-ray and visible light imaging with synchronized electromyogram (EMG) recordings of epaxial musculature. Based on above-ground kinematics we predict that there will be little axial muscle activation during walking on the surface. Subsurface, we predict that the sandfish will develop a traveling wave of muscle activation to drive the traveling kinematic wave. Considering the general features of granular forces described above, during subsurface movement we predict that resistive forces in granular media should dominate the muscle activity. Further, if the animal seeks to maintain spatial form in the face of a changing environment, it will have to modify muscle force and potentially its activation pattern. Therefore, as it moves within a frictional fluid we predict a change in EMG magnitude with both depth and ϕ but not with undulation frequency.

2.3 Materials and Methods

2.3.1 Animals

Sandfish lizards, *Scincus scincus* [72](Fig. 2.1, A) were purchased from commercial vendors (LLL Reptile, Vista, CA, USA and Ocean Pro Aquatics, Chino Hills, CA, USA). The nine animals used for the EMG and kinematic study had a snoutvent length (SVL) of 8.9 ± 0.4 cm and a mass of 16.6 ± 1.8 g. We did not use sandfish with regenerated tails. Two sandfish were dissected to facilitate understanding of axial musculature (Fig. 2.2, A) and electrode placement (Fig. 2.2, B). The skeletal structure of a live anesthetized sandfish was observed using micro-computed tomography (micro-CT). All animals were housed individually in large containers (21 cm × 43 cm × 28 cm) filled with sand to a depth of ≈15cm. Animals were fed mealworms coated in a supplemental calcium powder. The holding room was maintained on a 12h:12h light:dark cycle and the average temperature was 28°C during the day and 24°C during the night. Animals were provided with a heat lamp and a water dish to facilitate thermoregulation. All experimental procedures were conducted in accordance with the Georgia Institute of Technology IACUC protocol number (A08012) and Radiation Safety protocol (X–272).

2.3.2 Media Preparation

Granular media compaction varies in nature and influences the resistive force experienced by a burrowing animal. A few percent increase in ϕ can substantially increase resistive force on an intruder moving through the substrate [11] (Fig. 2.1, D). Further, when an intruder moves through a LP granular medium, drag forces are approximately constant; however, drag forces in CP states can oscillate during the movement through periodic yielding along transiently stable shear planes [11, 90]. LP and CP states are distinguished by ϕ of less

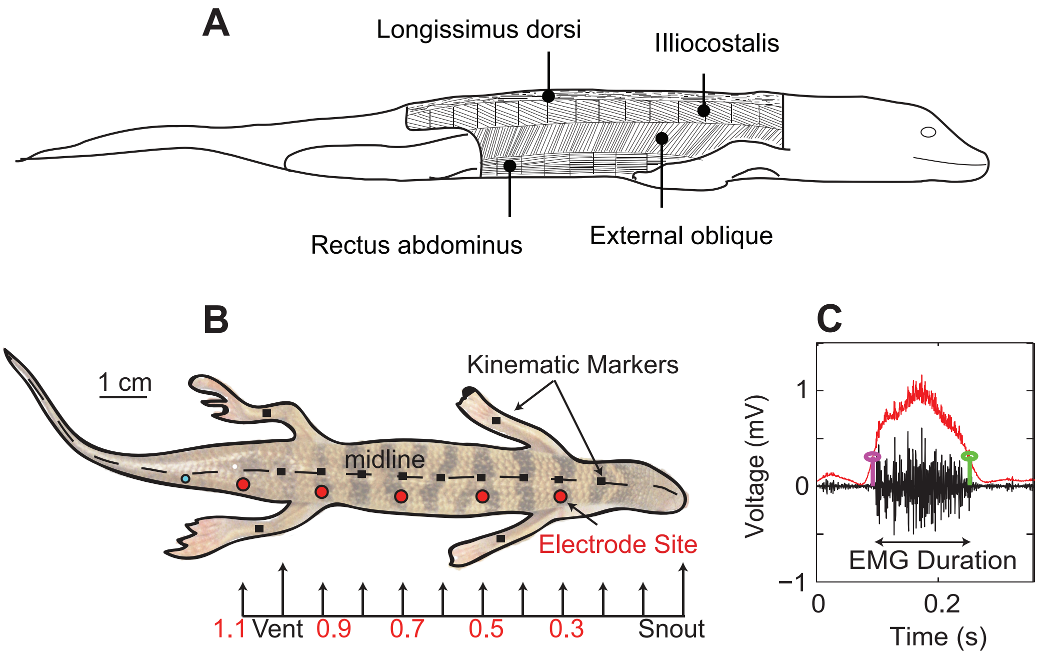

Figure 2.2: Sandfish superficial axial musculature and EMG recording during sand-swimming. (A) Diagrammatic representation of some superficial axial musculature in the sandfish. The iliocostalis muscles are targeted for EMG recordings. (B) Location of the EMG electrode implantation sites (red circles) in the right dorsal side and x-ray opaque markers (black squares) attached to the exterior midline and limbs. (C) A typical EMG recording at 0.5 SVL during subsurface locomotion. The red trace was generated by rectifying the EMG signal, filtering with a second-order Chebyshev filter, and then scaling by 5 for visibility. Burst onset (magenta circle) and burst offset (green circle) are determined by when the red trace crosses a specified threshold (see Materials and methods for details).

than or greater than a critical volume fraction [90,153], $\phi = 0.605$ in 0.3 mm diameter glass particles.

To control the compaction of the substrate, an air-fluidized bed [11] (Fig. 2.1, B) was used to create repeatable initial ϕ states. The bed was filled with spherical glass beads that were similar in size (diameter 0.27 ± 0.04 mm) and density ($\rho = 2.5\ g/cm^3$) to particles found in sand dunes [95]. An air flow created a fluidized state and a slow decrease in air flow to zero resulted in a LP state ($\phi = 0.584 \pm 0.013$). CP states ($\phi = 0.635 \pm 0.013$) were created by applying a slight air flow below the onset of fluidization and subsequently vibrating the granular media using a motor with an off-axis mass that was attached to the side of the bed. The difference in compaction resulted in an $\approx 50\%$ increase in the average resistive force between LP and CP preparations (Fig. 2.1, C). Air flow was off during all animal trials and ϕ was determined by measuring the height of the granular media before each sandfish swim.

The ambient air temperature during experiments was 34°C. Heat lamps over the sand were turned on at least 1 h prior to recording the first animal trial, resulting in a minimum internal sand temperature of 30°C. The sand bed was fluidized periodically, allowing mixing of the grains, which produced a more uniform temperature distribution within the media. The temperature of the granular media continued to rise during the course of the experiment to a maximum of 38°C. As temperature was measured at the beginning and end of experiments, we used the time stamp on each trial in order to estimate the temperature of the sand and correlate it with speed and EMG (see Results). We estimate that the majority of the experiments (>75%) were conducted between 34 and 38°C. Previous studies on the burial performance of Uma scoparia [26] within granular media at low (23°C), moderate (32°C) and high (39°C) temperatures revealed that low temperature increased burial time while middle to high temperatures showed similar performance.

2.4 Above Surface Video Recording

Above surface visible light video was taken at 250 frames per second (fps) using a high-speed camera (AOS Technologies AG X-PRI, Baden Daettwil, Switzerland) to characterize general features of above surface movement in the sandfish such as axial bending and speed. Lizards were initially placed in a holding pen (Fig. 2.1, B) separated from the sand-filled container by a gate (4.5 cm wide). Sandpaper bonded to the holding pen floor increased traction during above surface movement. Two holding pens were used depending on the goal of the study. One had a rectangular area (6.3 cm × 18 cm × 11 cm) that did not extend over the sand [11] and thus did not interfere with subsurface video recording. In the other holding pen (4.2 cm × 11 cm × 6.5 cm), the gate was farther from the sand area to induce more above surface strides before burial took place. In addition, the bottom of this holding pen extended over the sand bed area so that above surface movement was captured on both the visible light video and subsurface x-ray images. The different holding pens did not affect the subsurface performance of the sandfish. The visible light camera was suspended above the holding pens so that the dorsal view of the sandfish was visible and the midline position could be tracked.

2.4.1 Subsurface Video Recording

Visualization of subsurface movement in optically opaque material has been accomplished with x-ray [12–14] and nuclear magnetic resonance imaging (NMRI) [77]. In our experiments, sandfish kinematics were recorded using x-ray systems (OEC 9000, Radiological Imaging Systems, Hamburg, PA, USA top-view recording; and Philips, Andover, MA, USA side-view recording) coupled to high-speed cameras (Fastcam 1024 PCI, Photron, San Diego, CA, USA and Phantom v210, Vision Research Inc., Wayne, NJ, USA, respectively) which recorded at 250 fps. The top-view x-ray system was set to an energy level of 85 kV and 20 mA and the side-view was set to 85 kV and 75 mA. During side-view recordings, the sandfish burial began near the outside edge of the x-ray image intensifier, which had significant distortion. To account for this distortion, a calibration grid with known dimensions was used to transform distorted images using a custom-written image processing code (Matlab, Mathworks, Natick, MA, USA). Because the motion for the top-view recording occurred near the middle of the x-ray image intensifier and camera lens, only a small amount of camera distortion occurred. However, objects closer to the image intensifier appear smaller than objects farther from the image intensifier (i.e. closer to the source). Therefore, in top-view recordings as the animal moved deeper into the material, the sandfish appeared smaller. To correct for this, we calculated a calibration value for depth (where a calibration value of 1 was used for an object at the surface of the sand) by moving an object with known dimensions closer to the image intensifier. We approximated the depth of the sandfish during a particular undulation and used the calibration value to correct calculated distances (i.e. distances and speeds at undulation 2, 3, 4 and 5 were increased by 2%, 5%, 7% and 10%, respectively).

For enhanced contrast, in both visible light and x-ray videos, a maximum of 12 small opaque markers ($\approx 1\ mm^2$ each, total mass < 0.5 g) made from lead were bonded to the midline of the sandfish using cyanoacrylate glue between 0.2 and 1.1SVL, where the vent is at $\approx$0.75 of the total body length (snouttail length, STL) of the animal (Fig. 2.2, B, black squares). A maximum of two markers were placed on each limb (one distal and one proximal). These opaque markers were used for tracking during both surface and subsurface movement.

X-ray imaging of the sandfish in the horizontal plane (top-view recording) was used to characterize subsurface kinematic parameters such as spatial form (A/λ), wave efficiency (η), segmental speed (v_{seg}) and the phase of the cycle (N=5 animals; Table 2.1). X-ray imaging from the side view was used to characterize the angle of descent (θ_d) under different packing conditions (N=3 animals; Table 2.2). During subsurface movement, sandfish swam in a 10 cm deep granular bed of glass beads held in a container (with area 22.9 cm × 40.6 cm for top-view recordings, and 11.3 cm × 40.6 cm for side-view recordings). The bed width was reduced during side-view recordings because x-ray recordings through glass particles beyond 12 cm gave low contrast images. EMG experiments were conducted in the larger bed with the top-view x-ray imaging (Fig. 2.1, B).

2.4.2 EMG

To examine neural control commands and changes in muscle actuation we used EMG, which records voltage gradients in muscle. Although it is not directly proportional to

Table 2.1: Summary of EMG implantation locations and the number of subsurface undulation cycles that were considered for each sandfish at each compaction.

Sandfish #	SVL (cm)	Side Implanted	EMG Locations	CP	LP
1	9.2	Left	0.5, 0.7, 0.9, 1.1	4	6
2	9.2	Right	0.3, 0.5, 0.7, 0.9	11	10
3	8.7	Left	0.3, 0.5, 0.7	5	2
4	8.6	Right	0.3, 0.5, 1.1	3	7
5	8.5	Left	0.5, 0.7, 0.9	3	3

EMG implantation locations are given as a fraction of SVL

Table 2.2: Number of runs for each treatment for side view kinematics experiment.

Sandfish #	SVL (cm)	CP	LP
6	8.3	4	5
7	9.3	9	8
8	9.2	2	4

tension in muscle, it can be used as a proxy for muscle force development [128, 154]. Also, EMG minimally interferes with movement and can be obtained in muscles that cannot be instrumented with tendon buckles [128, 155].

The sandfish was sedated by gas induction with 5% isoflurane in medical grade oxygen and then anesthetized with an intramuscular injection of ketamine hydrochloride (200 mg/kg body mass). Anesthesia was maintained during electrode implantation by continuous administration of 2% isoflurane gas solution. Sandfish were implanted with bipolar hook electrodes [128] constructed from two Teflon-insulated, single-stranded, stainless steel fine wires (50 μm diameter, A-M Systems, Carlsborg, WA, USA) which were $\approx$ 1 m in length. Insulation was removed from the last 0.5 mm of the wire, and the ends of the two wires were separated by $\approx$ 1 mm. The electrodes were inserted percutaneously using a 26 gauge hypodermic needle into the epaxial musculature located $\approx$ 4 mm away from the midline (or halfway between the midline and lateral edge, Fig. 2.2, B, red markers) on one side of the sandfish body; the side implanted was chosen randomly between experiments and each side showed similar patterns. For the five animals that were euthanized or did not survive surgery, the implantation sites were verified to be located in the iliocostalis muscle group with longitudinal position varying approximately ± 0.05 SVL. However, because animals were not always euthanized following experimentation, the muscle group implanted and longitudinal position could not be verified for all experiments. Five bipolar electrodes were implanted at 0.3, 0.5, 0.7, 0.9 and 1.1 SVL. However, because of electrodes pulling out or shifting, we usually recorded from three to four of these implanted electrode sites that showed a clear EMG burst during burial. Hook ground electrodes were constructed from a single wire and insulation was removed at one end. Five ground electrodes were implanted in the posterior portion of the tail after the 1.1 SVL electrode site (Fig. 2.2, B, blue marker), where adipose tissue was abundant. These electrodes were wound around each bipolar electrode and connected to ground to minimize noise. All wires were strain relieved at multiple dorsal locations by application of cyanoacrylate glue, which adheres strongly to their keratinous skin and minimally affects body movement; 1–3 weeks after implantation, the glue detached from the skin as a result of shedding, and electrodes were easily removed. See Table 2.1 for a summary of EMG experiments and location of electrodes.

EMG recordings were amplified by 1000 and bandpass filtered between 300 and 1000 Hz using a differential AC amplifier (A-M Systems, Model 1700, Sequim, WA, USA). The signals were recorded at a sampling rate of 2 kHz (National Instruments, USB– 6008, Austin, TX, USA) and analyzed through custom-written programs (LabVIEW, National Instruments, Austin, TX, USA). The bandpass filter frequencies and sampling rate were initially determined to reduce movement artifact and increase the number of channels that could be recorded. Analysis with a wider bandpass (10-5000 Hz) and higher sampling rate (10 kHz) revealed power below 300 Hz. Applying a 300-1000 Hz filter and downsampling this EMG signal in software showed EMG intensity decreased by 59 ± 2 % but the functional form of the signal and EMG trends did not change, nor were our conclusions affected.

2.4.3 Data Analysis

Kinematics were obtained by tracking the opaque markers along the midline of the sandfish body in both above surface and below surface video recordings using custom-written software (Matlab) to obtain positions with time. Above surface sequences were included in the study for analysis only when animals moved farther than two stride lengths forward and used a diagonal gait. Subsurface trials selected for analysis were those in which the mean sinusoidal positions followed a straight path and occurred at least 2 cm away from the edge of the container. The trials in which the sandfish completed less than two undulation cycles or when the sandfish stopped and started swimming while subsurface were not considered. A single period sinusoid was fitted to the sandfish midline markers and those with fits with $r^2 < 0.8$ were discarded. We accepted undulations in which sandfish completed the full undulation and continued swimming for at least a quarter of a cycle. The sandfish was considered to be subsurface when the animal body and legs were covered by the granular medium. We included EMG bursts in our subsurface analysis with the tail visible (undulation 2) if limbs were no longer in the sprawled posture and appeared to be passive and placed along the sides of the animal. If the legs were used or limbs and body were visible above the surface, the animal was considered to be in the burial phase and these movements were excluded from the subsurface analysis.

The instantaneous forward, lateral and segmental speeds of the animal were calculated between consecutive video frames as the displacement of the 0.5 SVL marker in the forward (v_{for}), lateral (v_{lat}) and overall direction of motion (v_{seg}), respectively, divided by the elapsed time between frames. We used v_{seg} in the subsurface analysis to characterize the overall speed and we compared this parameter with EMG characteristics. If the 0.5 SVL marker detached from the animal, the 0.3 SVL marker was used instead and gave similar results. In order to minimize the effects from the contralateral muscle activation, the mean segmental speed (v_{seg}) was calculated as the average segmental speed for approximately half of the total cycle (during the time the muscle at the 0.5 SVL location was shortening). Assuming the sandfish is moving in a perfect sine wave, when $v_{lat} > 0$ there is a change in the configuration of that segment from maximally convex to maximally concave; thus, muscle shortening coincides with positive lateral speed.

As in Maladen et al. [11], the midline positions fit well to a single period sinusoidal wave $y = A\sin(\frac{2\pi}{\lambda}(x + v_w t))$ during subsurface swimming, where A is the amplitude, λ is the wavelength, v_w is the speed of the traveling kinematic wave, x is the position in the forward direction and t is time. A/λ and wave efficiency, $\eta = \frac{v_x}{v_w}$, were calculated for each undulation cycle. v_x is the average forward speed and $v_w = f\lambda$, where f is the undulation frequency. For top-view x-ray trials, where a direct measurement of depth by side-view x-ray was lacking, the estimated depth was binned according to undulation number using both above surface video with top-view x-ray images. Undulation 1 was defined as when the head of the animal was covered by granular media but hindlimbs remained visible. Undulation 2 was defined as when only part of the tail was visible and the rest of the body and legs were subsurface. Undulations 3, 4 and 5 were defined as the first, second and third burst when the sandfish was undulating fully subsurface. Only EMG bursts during undulations 2-5 were considered in the depth and ϕ analysis, while undulation 1 was ignored because a significant proportion of the body was above the surface and use of hindlimbs was evident. In the sideview x-ray recordings, depth was measured directly as the vertical distance from the surface of the media to the 0.5 SVL marker position. θ_d was measured for side-view recordings as the angle between horizontal and the best linear fit to the positions of all tracked dorsal markers during the subsurface descent.

EMG signals were analyzed using SpinalMOD, a custom-written Matlab program [156]. For burst detection, the EMG signal was rectified and filtered using a second-order Chebyshev filter (Fig. 2.2, C, red trace) with a stopband ripple of 10 dB and stopband edge frequency of 30 Hz. The 'filtfilt' function in Matlab was used to remove phase distortion. A threshold equal to the mean of this filtered-amplified EMG trace was set to detect EMG burst. Burst onset was defined as the time when the filtered EMG signal exceeded the threshold and afterwards remained above it for a minimum of 0.04s (Fig. 2.2, C, magenta marker). EMG burst offset was defined as when the filtered EMG signal became lower than the threshold and remained below for at least 0.08 s [156, 157] (Fig. 2.2, C, green marker).

Threshold and timing parameters were changed when necessary by visual observation because of the occasional occurrence of spikes that did not constitute an EMG burst or missed detection of EMG onset. EMG duration was calculated as the time between the onset and offset of the EMG burst (Fig. 2.2, C), and the EMG duty cycle was determined as the ratio of EMG duration to EMG period (time between sequential EMG bursts). The frequency of bursting was defined as the inverse of the EMG period.

The rectified integrated area was found for each EMG burst using the original EMG signal (filtered once in hardware). Because the area was influenced by burst duration and swimming speed, the EMG intensity (I), defined as the ratio of the EMG integrated area to the EMG duration, was calculated to characterize the differences in activation between different ϕ, undulation numbers and speeds. To reduce variation associated with averaging intensities across multiple recording sites, EMG intensities were only considered for the 0.5 SVL location. Because of the differences in electrode construction, I was compared across individuals only after standardization (see [138]). After observing correlation between undulation number and I, a standardization was performed by using the best-fit line for I versus undulation number for a single implantation site. We used the calculated I at undulation 3 to normalize all other EMG intensities at that site. This undulation number was used because all animals tested consistently undulated at least 3 times during burial. We refer to the normalized EMG signal as the relative EMG intensity, I_{rel}.

The activation timing was compared with the estimated muscle strain cycle at a segment by calculating the angle between adjacent kinematic markers on the dorsal midline. Using this sinusoidal trajectory of angle with time, the normalized muscle length (L_M) and total cycle duration were estimated. L_M of 0 represents when the muscle is at resting length and the local segments (i.e. axial body positions at 0.1 SVL increments) are aligned. L_M of 1 is when the segment is at maximal convexity and L_M of -1 is maximal concavity. Therefore, moving from $L_M = 1$ to -1 (phase between 90 and 270°) represents muscle shortening. The difference between the time at which L_M was maximal and the EMG onset time was divided by the cycle period to calculate relative phasing, which will be referred to as neuromechanical phase lags. Comparing EMG onset with the estimated muscle strain cycle is a common measure among undulatory swimmers [138], and it can be used as a means of comparing muscle activation timing in water to activation timing in granular media. We calculated the ratio of the average wave speed of activation to the average wave speed of curvature ($\frac{v_{EMG}}{v_c}$). v_{EMG} was calculated by fitting a line between the longitudinal distance between EMG recording locations along the body and EMG onset time. v_c was calculated by fitting a line between distance and time at which maximal convexity occurs at those locations. Note that v_w, the wave of lateral displacement, is 0.68 ± 0.18 of v_c calculated from curvature speed. A ratio of $\frac{v_w}{v_c}$ <1 is expected as the wave of curvature must travel faster than the wave of lateral displacement. This is because the curvature propagates along the entire body (STL) while the lateral wave propagates a distance λ, which is always less than the STL for an inextensible animal. Theoretically, for A/λ of 0.22 this ratio should equal to 0.73.

2.4.4 Resistive Force Theory Model

We used a previously developed granular resistive force theory (RFT) model (see [7, 11]) to explain some features of sand-swimming. The RFT model used a simplified model of the sandfish kinematics and empirical force laws of granular media as inputs. The modeled sandfish was assumed to have a uniform body and moved in 0.3 mm diameter glass particles. The body of the model sandfish was divided into infinitesimal segments. By prescribing the different orientation of segments as a function of time, waves with different A/λ could be produced. For each segment, forces were calculated as functions of segment velocity and orientation using empirical force laws [see Chapter 1, Section 1.5 and [7, 11] for functional forms of the force laws]. The forward speed of the body was then obtained from the balance of thrust and drag in the forward direction. The weight-specific mechanical cost of transport (CoT) was calculated as by summing the power output of all segments to the external media and dividing by the forward speed and sandfish body weight:

$$CoT = \frac{power}{weight \times speed}. \tag{2.1}$$

The RFT model generated predictions of the dependence of η, mechanical CoT and swimming speed on A/λ for a given undulation frequency, f. By increasing the drag force on the head, the RFT allowed simulation of sandfish movement under different drag conditions, important to bound the effects of drag induced by the EMG wires.

2.4.5 Statistical Analysis

We used analysis of variance (ANOVA) to determine whether spatial form (A/λ) varied with ϕ (LP or CP), undulation number (2, 3, 4) or individual. Next, three multivariate analyses were performed to resolve which factors affected the kinematic variable wave efficiency, η. In the first, analysis of covariance (ANCOVA) was used with A/λ as the continuous variable, ϕ (LP or CP) and undulation number (2, 3, 4) as fixed variables and individual as the random variable. We used ANOVA to test whether η and A/λ in our data set differed from previous data [11] and included ϕ as a factor. To test the effect of wire drag on the response variable, η, we used ANOVA and included the factors of A/λ (continuous), individual and whether the trial did or did not have wires glued to the animals dorsal surface (fixed).

The temperature effect on animal speed and EMG intensity was characterized by using two ANCOVA analyses. For the first, we tested whether the factors of estimated temperature (continuous), undulation number and individual influenced animal speed. We did this for both LP and CP trials separately. For the second, estimated temperature, speed, ϕ and individual were tested against EMG intensity. In this analysis, we examined statistical results at each undulation number.

A paired t-test was used to determine whether EMG intensity during walking above surface was statistically different from that when remaining still. To see how the parameters of undulation number, ϕ, speed and individual affected EMG intensity during subsurface movement we performed two ANCOVA. In the first we included the interaction term of speed × ϕ and grouped by undulation number. In the second we included the interaction term of speed × undulation number and grouped by ϕ. We repeated the first test but also included the continuous variable A/λ to see whether this affected results. To understand timing characteristics, we calculated the phase lag between EMG onset relative to the time at which that site was maximally convex and the EMG offset relative to maximal concavity

(N=4 animals). We used ANCOVA to test whether the response variable, phase (onset and offset), changed with the position along the body (fixed), ϕ and speed. Only cycles during undulation 3 were included in the analysis. Statistical tests were conducted for each of the four individuals separately. Animal 5 (see Table 2.1) was excluded from the statistical test because of the overall low number of trials collected and, thus, low degrees of freedom. We tested whether the duty cycle of the EMG changed with the factors of undulation number, position along the body and individual using ANOVA. We conducted this test for both LP and CP states. Lastly, ANOVA was used to determine whether undulation number, ϕ or individual affected the ratio between the speed of the EMG wave to the speed of curvature ($\frac{v_{EMG}}{v_c}$).

In the side-view experiments, we tested whether ϕ and individual influenced the angle of burial using ANOVA. For all above tests, ϕ and undulation number were fixed variables, individual was a random variable and speed was a continuous variable. Statistics were performed using the software package JMP (SAS Institute, Cary, NC, USA). The results were considered significant if the P-value was smaller than 0.05. Values are shown as means ± s.d.

2.5 Results

2.5.1 Morphology

A micro-CT scan of a single sandfish revealed 26 vertebrae in the trunk and 13 anterior caudal vertebrae in the tail; individual posterior caudal vertebrae could not be distinguished. Dissection revealed qualitatively similar muscle morphology to that described for *Iguana iguana* [158,159]. The iliocostalis musculature (targeted for implantation) is located on the dorso-lateral portion of the trunk (Fig. 2.2, A).

2.5.2 Kinematics (Dorsal View)

Figure 2.3A shows the qualitative difference in trunk trajectories between above surface walking (green), burial (pink) and subsurface swimming (blue). On a hard surface before burial, the sandfish moved with a diagonal gait (each front limb moved in synchrony with the contralateral hindlimb) and showed little lateral bending of the body (when speed <3

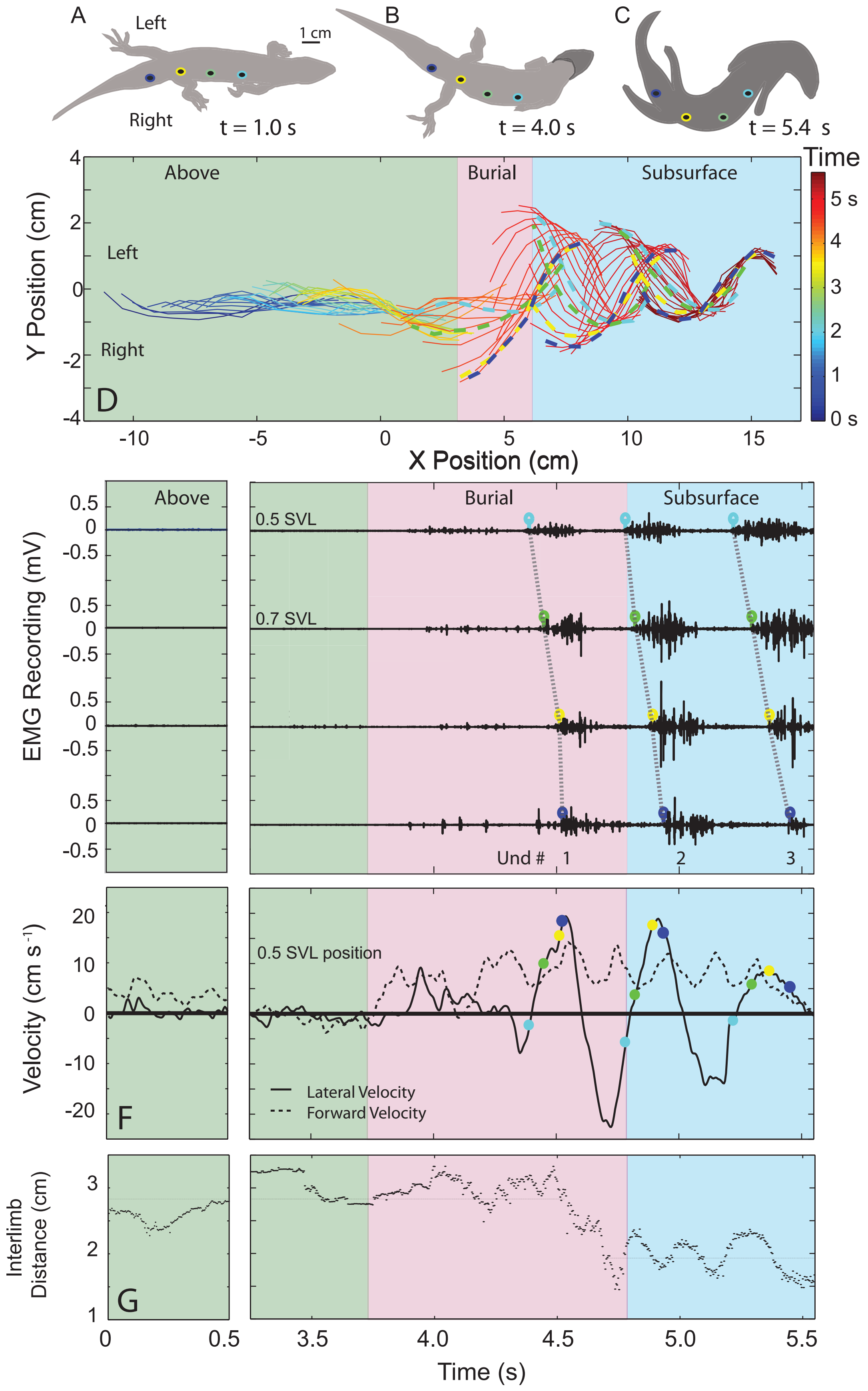
A
Left
1 cm
Right
t = 1.0 s
B
t = 4.0 s
C
t = 5.4 s
Above
Burial
Subsurface
Time
5 s
4
3
2
1
0 s
Y Position (cm)
4
2
0
-2
-4
Left
Right
D
-10
-5
0
5
10
15
X Position (cm)
EMG Recording (mV)
0.5
0
-0.5
0.5 SVL
0.7 SVL
Und #
1
2
3
Velocity (cm s^{-1})
20
10
0
-10
-20
F
0.5 SVL position
Lateral Velocity
Forward Velocity
Interlimb Distance (cm)
3
2
1
G
0
0.5
3.5
4.0
4.5
5.0
5.5
Time (s)

SVL/s) (Fig. 2.3, A & D, Above region). For a sandfish that was unconstrained (i.e. moved at least 5 cm away from walls and had no wires attached to its body), the maximum lateral deviation of an axial segment from its mean position during walking on a hard surface was 0.61 ± 0.17 cm (n=6). The sandfish with EMG wires showed a slightly greater deviation due to a curved tail from the wire attachment and also tended to turn more as a result of container narrowing. During walking above surface on hard ground, most sandfish moved at slow speeds (relative to subsurface movement) with a median average speed of 0.49 SVL/s (n=17 trials, N=4 animals) and a mean speed of 1.25 SVL/s (n=17 trials, N=4 animals). All trials had an average speed less than 3.0 SVL/s except for one, which had an average speed of 5.8 SVL/s. For this outlier, lateral bending was larger. After reaching the granular bed, the sandfish paused for 0.8 ± 0.7 s on the surface of the media before beginning burial.

The forward and lateral velocities are shown for a representative trial (Fig. 2.3, F). Lateral velocity was small and the mean forward walking speed was 2.7 cm/s (or 0.3 SVL/s). Forward velocity decreased to zero as the sandfish paused for 0.6 s before entry. The sandfish then tilted its head downwards and thrust itself into the media using its limbs. During

---

Figure 2.3 *(preceding page)*: Kinematics and muscle activation of the sandfish during transition from above surface to subsurface movement during a representative trial. A sketch of the animal posture (light gray indicates above surface, dark gray is below-surface) for three different instants showing (A) above surface walking (at t = 1 s), (B) burial (at t = 4 s), (C) and subsurface swimming (at t = 5.4 s) phases. Electrodes are implanted in the right side of the animal with locations at 0.5, 0.7, 0.9 and 1.1 SVL segments shown by colored markers on the back. (D)Tracked midline positions of the sandfish when moving above the surface (green region), during burial (pink region), and during subsurface movement (blue region). The color of midline traces indicates time progression from 0 (dark blue) to 6 s (dark red). Dashed midline tracks show the position of the animal at the onset of the EMG burst (light blue, 0.5 SVL onset; green, 0.7 SVL onset; yellow, 0.9 SVL onset; dark blue, 1.1 SVL onset). Both lens and depth distortion were removed in this representative sandfish trial at each frame by multiplying by a factor that kept the overall length of the animal constant. (E) EMG recordings from epaxial muscles where colored stems indicate the onset of the EMG burst. Dashed gray lines display a traveling wave of activation (i.e. onset of bursts propagates from anterior to posterior segments). (F) Lateral (solid) and forward (dashed) velocity of the sandfish measured at 0.5 SVL. The convention chosen for positive lateral velocity was that the marker was moving toward the left side. Colored circles show the velocity of the animal at the onset of the EMG burst. (G) Distance between the hindlimbs measured from markers located near the ankle joint. This sandfish has a SVL of 9.2 cm.

burial, the sandfish also increased the curvature of its trunk (Fig. 2.3, B & D, 'Burial' region). It accelerated from rest and buried itself in 1.0 ± 0.3 s (n=17, N=4). In accord with previous findings [11], the hindlimbs were in a sprawled position during above surface movement and most of burial (distance between the hindlimb distal markers on ankles was 2.8 cm, Fig. 2.3, G). After half of the body was buried, the hindlimbs simultaneously adducted and the distance between limbs decreased. During subsurface locomotion the distance between limbs oscillated around a mean distance of 1.9 cm (Fig. 2.3, G). We attribute the changing limb distance to external forces, as the limbs were closest to the midline when the body location was maximally convex. Forelimbs show a similar trend [11].

During subsurface movement the animal propagated a traveling wave of undulation down its body to move forward (Fig. 2.3, C & D, 'Subsurface' region). Sandfish segmental speed was between 1 and 3.5 SVL/s during subsurface movement and higher than forward walking speed. Sandfish decelerated during subsurface movement by 0.64 ± 0.4 SVL/s (n=21, N=5) for each undulation cycle. Most trials were conducted in a temperature range between 34 and 38°C. However, a few trials were recorded at temperatures as low as 30°C. We found no significant effects of temperature on animal speed.

Average spatial form, A/λ, for animals with EMG electrodes was 0.18 ± 0.04. In accord with our hypothesis, spatial form did not vary with ϕ (ANOVA, $F(1,42) = 2.3, P = 0.14$), or undulation number ($F(3,42) = 1.4, P = 0.26$) (supplementary material Fig. 2.10). However, we did find that spatial form varied between animals tested ($F(4,42) = 3.7, P = 0.01$). Similarly, wave efficiency, η, was independent of ϕ (ANCOVA, $F(1,24) = 1.4, P = 0.25$) and undulation number ($F(2,24) = 0.9, P = 0.42$) (supplementary material Fig. 2.10), but varied among different animals tested (ANCOVA, $F(5,24) = 5.4, P < 0.01$). In addition, η was positively correlated with A/λ (ANCOVA, $F(1,24) = 6.5, P = 0.02$) which is in accord with RFT model predictions [11] (see supplementary material Fig. 2.11). All data were in a range where η was sensitive to A/λ (e.g. a 30% increase in A/λ led to a 75% increase in η).

Overall, subsurface sandfish kinematic results were in accord with those found previously [11] and suggested that the EMG wires did not impede the performance of the sandfish.

η and A/λ were compared with previously collected data [11] in which no electrodes were inserted into the animal. η and A/λ were higher for the animals in the previous study ($\eta = 0.51 \pm 0.10$, $A/\lambda = 0.21 \pm 0.04$) than for the animals with implanted electrodes ($\eta = 0.36 \pm 0.08$, $P < 0.01$, and $A/\lambda = 0.18 \pm 0.04$, $P < 0.01$) (supplementary material Fig. 2.11). To test whether drag from the electrode wires affected η, we tested sandfish with (n=11 trials, N=2 animals) and without (n=15 trials, N=4 animals) electrode wires attached to their dorsal surface (no electrodes were implanted). For the animals used during this experiment, we found that η did not significantly vary with individual. We found that there were small but significant differences in η with and without wires (ANCOVA,$F(1, 20) = 6.6, P = 0.02$) but that all η were within the range of η for EMG-implanted sandfish. In addition, best-fit slopes between η and A/λ were similar for sandfish with and without wires (see supplementary material Fig. 2.10). These experiments were conducted in LP treatments, and undulation number was not characterized because previous findings showed that it did not influence η or A/λ. The increased drag resulted in a lower η ($\approx$ 19% decrease) for a similar A/λ. This decrease in η was in accord with the RFT prediction (supplementary material Fig. 2.11) that the extra drag from the wires (estimated to be 40% of the head drag by dragging the wires through the granular medium) leads to an $\approx$15% decrease in η in the range of A/λ used by the sandfish ($A/\lambda = 0.2$). The animals implanted with EMG wires used in this study displayed a larger range of η than in the previous study; our animals also operated at a lower average η (supplementary material Fig. 2.11).

2.5.3 Muscle Activation

EMG recordings were taken from five different sandfish. A total of 33 subsurface top-view trials with EMG were considered (14 CP, 19 LP) from all recorded trials. Within the top-view trials, 54 fully subsurface, straight undulations were recorded and analyzed. We found no significant effects of temperature on EMG intensity.

During above surface movement, no muscle activity was detected (Fig. 2.3, E, 'Above' region). I during above surface movement (4.1 ± 1.3 μV) did not differ from the noise produced when the wires were moved but the animal remained stationary (5.4 ± 4.8 μV,$P >$

0.05). During the first half of burial, the tracked segments moved forward with small lateral velocity and minimal activation (Fig. 2.3, E & F, first half of 'Burial' region). As the animal entered the medium, lateral oscillation increased and EMG bursts were detected (Fig. 2.3, E, F, second half of 'Burial' region). During subsurface movement, the sandfish produced an anterior to posterior traveling wave of muscle activation, which coincided with the traveling wave of curvature. The sandfish body shape was similar at the onset of each EMG burst. Muscle activity onset (colored circles) is plotted against lateral velocity at the 0.5 SVL segment in Figure 2.3F ('Burial' and 'Subsurface' region). Near the 0.5 SVL EMG onset (cyan circle), the lateral velocity of the 0.5 SVL segment became positive; a positive lateral velocity indicates muscle shortening, assuming the sandfish is moving in a sine wave.

Typically, EMG bursts became larger as the sandfish descended into the granular medium; this can be seen in a representative trial in Figure 2.4A. EMG intensity, I, increased with undulation number for most animals (the slope of I versus undulation number was significantly higher than zero, $P < 0.05$, for the individuals shown; Fig. 2.4, B, C & D). For combined data (N=5 animals), in which speed, undulation number and individual are factors and the data are grouped by ϕ, we found that relative intensity (I_{rel}) increased significantly with undulation number ($F(2, 18) = 3.7, P = 0.04$ for LP and $F(3, 13) = 5.2 and P = 0.01$ for CP, Fig. 2.4, E). I_{rel} increased by 0.26 per undulation in CP and by 0.2 per undulation in LP, but these slopes were not significantly different. Individual, speed and interactions did not significantly change I_{rel}.

The mean intensity of CP data was higher on average than LP data for every undulation number in the combined data set. These differences were small, with a 13% increase in I_{rel} from LP to CP during undulation 2 and 3 and a 19% increase during undulation 4. In a test in which speed, individual and ϕ were factors, we found that this intensity was not significantly different between different ϕ at each undulation number ($F(1, 5) = 0.2, P = 0.64$ for undulation 2, $F(1, 19) = 0.03, P = 0.85$ for undulation 3 and $F(1, 4) = 5.3, P = 0.08$ for undulation 4). As in the previous analysis, individual was an insignificant factor influencing I_{rel}.

Mean speed (v_{seg}) also did not influence I_{rel} (Fig. 2.5, A) for undulation 2 and 4

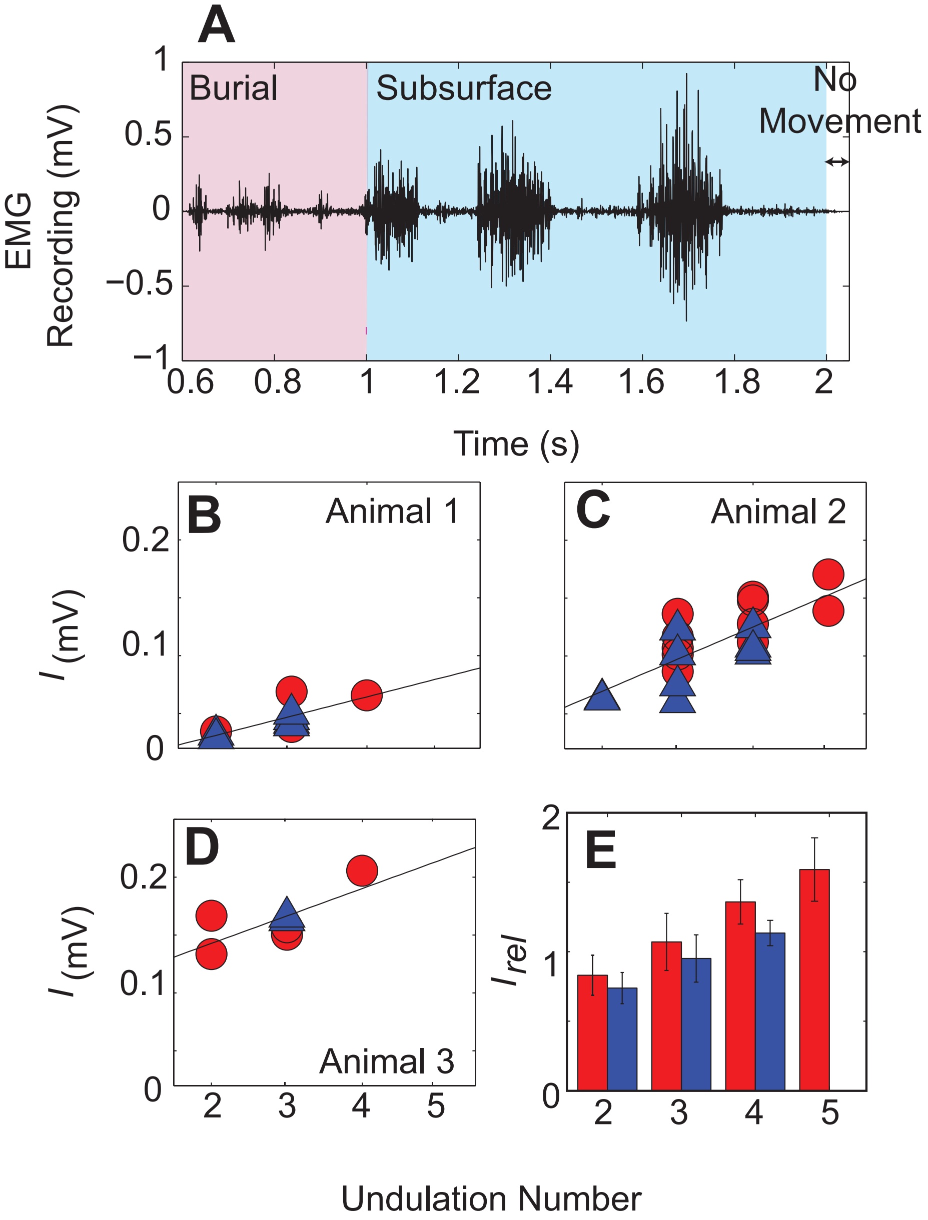

Figure 2.4: EMG intensity increases with swimming depth. (A)EMG recording for three subsurface undulations (2, 3, 4). Pink and blue regions indicate movement during burial and subsurface, respectively. (BD) Intensity (I) at 0.5 SVL site versus undulation number (which positively correlates with depth) for 3 representative individuals with the fitted line for all points in both LP (blue triangles) and CP (red triangles) treatments. I and undulation number have a positive correlation. (D) I_{rel} versus undulation number for all animals (N=5) in both LP (blue) and CP (red) treatments. The slope of CP and the slope of LP are statistically identical for the pooled data but the mean is higher for CP. However, the pooled data are dominated by data from animal 2.

$(F(1,5) = 1.2, P = 0.33$ and $F(1,4) = 6.9, P = 0.06$, respectively) but was calculated as a significant factor for undulation 3 $(F(1,19) = 7.0, P = 0.02)$. However, for undulation 3 the slope of the linear fit between I_{rel} and speed was small (0.15 s^{-1}) with a low coefficient of determination ($r^2 = 0.13$). Including spatial form in the analysis did not affect these results. v_{seg} was strongly correlated with undulation number, with a smaller v_{seg} for a larger undulation number $(F(3,16) = 10.8, P < 0.01$ for CP and $F(2,20) = 15.3, P < 0.01$ for LP). These trends were observed in each individual (Fig. 2.5, B, C, & D). In accord with previous work [11], v_{for}, v_{lat} and v_{seg} increased with undulation frequency.

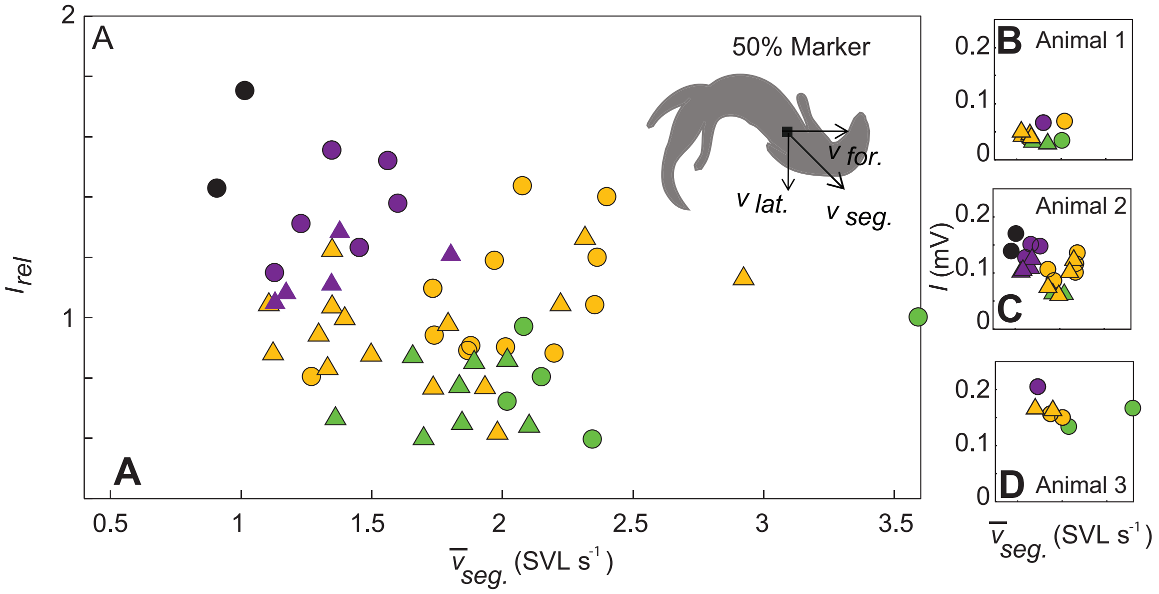

Figure 2.5: EMG intensity and its relationship to swimming speed. (A) Relative intensity, I_{rel}, is independent of mean segmental speed (v_{seg}) for a given undulation number (2, green; 3, yellow; 4, purple; 5, black) for all animals (N=5). I_{rel} is the intensity of the EMG at the 0.5 SVL marker normalized to the best fit I at undulation 3 (leading to a distribution of I_{rel} around 1 at undulation 3). (B-D) I versus v_{seg} for 3 representative animals shows similar patterns. Triangles represent LP trials and circles represent CP trials.

EMG onset at 0.3 SVL began after the muscle began to shorten (Fig. 2.6, C, magenta bar). The more posterior muscles (0.5-0.9 SVL) activated earlier relative to their muscle strain cycle (i.e. while the muscle was lengthening). The neuromechanical phase lags between EMG onset relative to curvature increased in the posterior direction for all animals statistically tested (N=4; $P < 0.01$). In two animals, there was a significant effect of both speed and ϕ of onset phasing (animal 3: $F(1,7) = 7.8, P = 0.03$ for speed and $F(1,7) =$

$10.2, P = 0.02$ for ϕ; animal 4: $F(1,7) = 7.7, P = 0.03$ for speed and $F(1,7) = 6.3, P = 0.04$ for ϕ). Tests show that, on average, phase shifted to the right (EMG onset occurs later in the strain cycle) when the animal moved at higher speeds, while there was a shift to the left when the animal moved through the higher ϕ. However, this was not significant for the other two animals, which had a higher number of overall trials (animal 1: $F(1,13) = 0.2, P = 0.69$ for speed and $F(1,13) = 1.0, P = 0.33$ for ϕ; animal 2: $F(1,25) = 4.2, P = 0.05$ for speed and $F(1,25) = 0.3, P = 0.59$ for ϕ). In accord with onset timing, EMG offset phase lags relative to curvature statistically increased in the posterior direction for animals 1, 2 and 3 ($P < 0.05$), but not for animal 4. Speed and ϕ were insignificant factors affecting offset phase lags for all animals tested except for animal 3 ($F(1,5) = 31.0, P < 0.01$ for speed and $F(1,5) = 33.8, P < 0.01$ for ϕ). As a result of the increasing neuromechanical phase lags along the body, the average wave speed of muscle activation (v_{EMG}) was greater than the average speed of the kinematic wave of bending (v_c) for almost all trials (Fig. 2.6, B), with a median ratio of $\frac{v_{EMG}}{v_c} = 1.24$. We report the median because the distribution is positively skewed. The lower quartile of the ratio is 1.13 and the upper quartile is 1.37.

EMG activity was detected for the majority of muscle shortening in all implantation sites sampled. The EMG duty cycle (EMG duration/EMG period) decreased in the posterior direction ($F(3,30) = 4.2, P = 0.01$ for CP and $F(3,34) = 4.2 and P = 0.03$ for LP) from 0.52 ± 0.07 at 0.3 SVL to 0.40 ± 0.06 at 0.9 SVL (Fig. 2.6, D) and showed no dependence on undulation number or individual. Burst duration was inversely correlated with undulation frequency but showed no correlation with I_{rel}, which supported the finding that I_{rel} was independent of speed.

2.5.4 Kinematics (Side View)

Subsurface side-view recordings revealed that markers near the dorsal surface of the sandfish followed a nearly linear trajectory (best linear fits had a mean $r^2 = 0.87 \pm 0.08$, Fig. **??**, A, B). The sandfish undulated within a plane with angle θ_d with respect to the horizontal. The animal did not pitch around its center of mass during descent into the media. The sandfish dived into the medium at a shallower θ_d (Fig. 2.7, C) in CP media (18.9 ± 4.3°, N=4 animals,

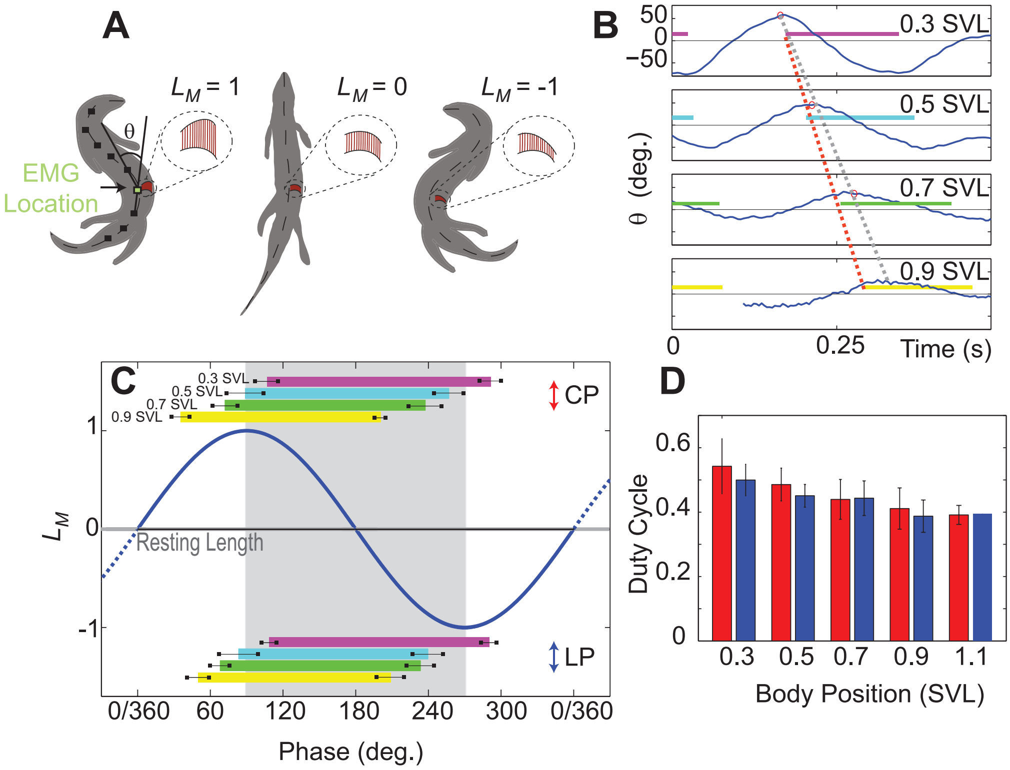

Figure 2.6: Muscle activation timing. (A) Normalized muscle length, L_M, is approximated by calculating the angle between consecutive markers relative to the EMG location. When the angle is maximal, we assume the muscle is maximally stretched ($L_M = 1$); when the angle is zero, we assume the muscle is at resting length ($L_M = 0$); when the angle is minimal, we assume the muscle is maximally shortened ($L_M = 1$). (B) Angle of a particular marker versus time compared with activation of the muscle at that location. The maximum angle and minimum angle are found and compared with onset of activation. (C) Timing of muscle activation relative to estimated L_M. Gray region shows the time in which the muscle shortens, where maximal convexity occurs at 90° and maximal concavity occurs at 270°. Onset of 0.3 SVL EMG burst (magenta) occurs after maximal convexity and onset at 0.5 SVL (cyan), 0.7 SVL (green) and 0.9 SVL (yellow) occurs before maximal convexity (when the muscle is still lengthening). Zero curvature (gray line) indicates resting length for a particular segment. Black horizontal bars show mean EMG onset and offset ± s.d. (D) Duty cycle decreases with marker position and does not differ between CP and LP trials.

n=18) than in LP media (26.1 ± 5°, N=4 animals, n=18, $F(1,28) = 18.0, P < 0.01$). The angle also varied significantly with individual ($F(2,28) = 5.9, P < 0.01$). The average depth between the surface level and 0.5 SVL dorsal marker at which the sandfish first stopped moving was significantly different between LP (3.01 ± 0.93 cm) and CP (1.85 ± 0.54 cm) media (Fig. 2.7, D, $P < 0.01$). Angles and depths reported previously [11] ($\theta_d = 22.2 \pm 3.7°$, depth $= 2.1 \pm 0.5$ cm for both LP and CP sand) fall within the ranges observed in this study. In both CP and LP media, the sandfish could dive to the bottom of the sand bed.

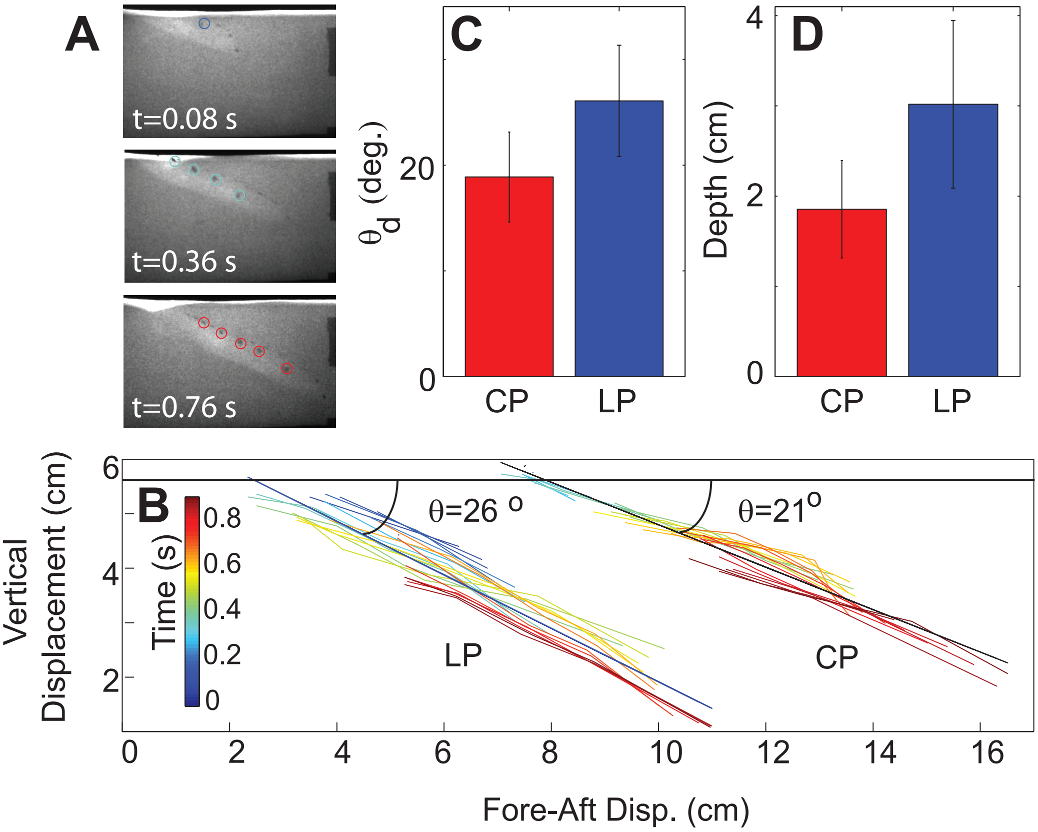

Figure 2.7: Sagittal sandfish kinematics. (A)X-ray images showing a representative trial of the sandfish diving at three different times. Colored circles indicated tracked markers. (B)Tracked trajectories of kinematic markers along the back in a representative LP and CP trial. The LP trial corresponds with the sandfish swim in A. The color of the lines indicates marker locations on the dorsal surface of the sandfish at different times (dark blue is time t = 0s and dark red is t = 0.96s). The black line is the best linear fit to all marker positions during the swim as measured from the surface of the sand. (C, D) In CP media (red), (C) the mean angle of descent is significantly lower than in LP (blue) and (D) the animal stops initially at a smaller mean depth. Values are means ± s.d.

2.6 Discussion

2.6.1 The Role of Epaxial Musculature in Lateral Undulation During Sand-Swimming

Above the surface, the sandfish exhibited minimal body undulation and no epaxial muscle activation; thrust was achieved through legsand interactions. The sandfish has prominent limbs (≈20% of total body length), suggesting that these appendages are important to sandfish movement strategies. In the sandfish, epaxial muscles are likely involved in lateral bending because epaxial activation coincided with large body undulations during burial and subsurface swimming. The use of epaxial musculature for bending in the sandfish resembles the case in other taxa [e.g. amphibians ([147]) and snakes ([160])] that use epaxial muscle for lateral bending. There is some evidence that epaxial muscle may be used during high-speed (> 3 SVL/s) above surface running, but further investigation is needed. More than half of the above surface trials recorded had an average speed of less than 0.5 SVL/s and all trials except one had average speeds <3 SVL/s. For the one trial that had an average above surface speed of 5.8 SVL/s, the animal exhibited some lateral bending and EMG activity was detected beyond the level of noise (I=0.036 mV). However, this intensity was much less than that recorded during subsurface swimming at lower speeds. Below 3 SVL/s sandfish did not show significant epaxial muscle activity.

Other studies have shown epaxial muscle activity in lizards (*Iguana iguana* [159] and *Varanus salvator* [161]) during walking at speeds less than 1.5 SVL/s. In these studies, the epaxial muscles were found to stabilize the trunk as they were active during the rear foot stance phase during normal walking. The difference in epaxial muscle use could arise from the difference in anatomy and body posture of the sandfish, which may lead to variation in ground reaction forces. The sandfish uses a sprawled gait with its body close to and occasionally touching the ground. The artificial setting of hard ground may differ from the natural above-ground movement that would occur on soft sand. Also, we could not confirm whether the hypaxial muscles were also being employed during movement because this layer of muscle is smaller than the epaxial musculature and difficult to implant with our current EMG electrodes. Future studies that investigate axial muscle use during running on sand over a range of speeds would help elucidate the role of the sandfish axial musculature in stabilization and/or bending.

2.6.2 Activation Pattern Influenced by Environmental Interaction

Jayne and Daggy [26] hypothesized that movement through loose, fluid-like sand could elicit an ancestral traveling wave axial activation pattern in lizards. In accord with this hypothesis, we found that the sandfish achieved forward propulsion by propagating an anterior-to-posterior traveling wave of activation along its epaxial musculature during burial and subsurface movement. This wave of muscle activation correlated with the kinematic wave of body undulation. Remarkably, we found that A/λ did not change with undulation number (depth), speed or ϕ. We previously hypothesized that the animal targeted this particular kinematic waveform. We thus predict that to maintain these kinematics as environmental conditions change, the activation strategy must change to accommodate the resistive demands from the environment. We argue that for sandfish-scale animals moving in highly resistive environments like granular media, external resistance dominates while effects of body and material inertia are small; previous studies [8,11] estimated that inertial forces at sandfish undulation frequencies were less than 10% of frictional forces. In addition, internal forces from deformation of elastic elements (like tendons) and friction from joint movement will influence muscle activation. However, with similar kinematics we assume that changes in internal forces are small compared with the change in external force due to differing depth and ϕ [162]. Thus, assuming muscle force scales with activation (a point we will return to) the change in activation should correlate with changes in external resistance when kinematics are similar. We therefore predict that resistance forces should give a qualitative indication of the intensity and timing of muscle activation, and we now discuss how depth, speed and volume fraction affect activation strategy.

2.6.2.1 Depth Dependence

From the top-view (dorsal) video and EMG measurements, we concluded that as the sandfish swam into the granular medium, I_{rel} increased with depth (characterized through undulation number) while A/λ did not. Rod drag experiments [11] revealed that for horizontal movement through a granular medium of a cylindrical steel intruder with coefficient of friction comparable to that of the sandfish and at comparable depths, drag force increased approximately linearly with depth by 1.32 ± 0.24 N/cm in CP media and by 0.86 ± 0.19 N/cm in LP media (Fig. 2.1, C). Also, resistive force in a granular medium and average muscle activation intensity were positively correlated. We hypothesize that for the sandfish, increased I generates larger muscle forces to accommodate the increase in granular force with depth and allows the animal to maintain similar kinematics. The increase in resistive force between estimated depths at undulation 2 and undulation 4 was 75% and 67% for CP and LP, respectively; the increase in I_{rel} was 63% and 54% for CP and LP, respectively. In contrast, during movement through water, resistance force remains approximately constant for changes in depth, and thus small changes in depth should not change muscle activation strategy for aquatic swimmers. Depth has only been considered for aquatic swimmers during large changes in depth ($\approx$800 m) such as in diving sperm whales [163].

Our results showing a change in EMG with depth are in accord with other studies of burrowing in soil [164]. For example, larval lamprey display an increase in EMG burst amplitude (difference between the maximum EMG burst height and the baseline) when moving from steady-state swimming to burrowing and then during initial stages of burial compared with the final stage. Changes in kinematics also occur between these three states (swimming, initial and final burrowing), so the increase cannot be solely attributed to environmental differences. However, these studies suggest depth of movement is a crucial factor for locomotion in a granular environment. It is interesting to contrast the data for sandfish with a recent study of razor clam digging. Winter and Hosoi recognized that increased depth leads to increased force in wet granular media and suggested that the Atlantic razor clam (*Ensis directus*) uses a movement strategy that diminishes this force dependence by fluidizing the media surrounding its shell [38].

Although A/λ did not change, we found that the sandfish decreased its undulation frequency as it moved deeper into the material. The animal slowed by 0.64 ± 0.4 SVL/s (n=21, N=5) for each undulation cycle. This deceleration is expected to have little effect on resistive force as inertia is negligible. A similar phenomenon was found in the nematode;

undulation frequency decreased with increasing external resistance as a result of increased viscosity [142, 165]. This change in frequency may act to limit muscle power expenditure. Korta and colleagues found that mechanosensory input may act to regulate this temporal frequency and allow gait adaptation in response to different surroundings [142]. Studies of our sandfish models [7, 78, 105] could be used to determine the extent of muscle power reduction as a result of decreasing frequency with depth for a sand-swimmer.

2.6.2.2 Speed Independence

Like other swimmers, the sandfish increased swimming speed by increasing burst frequency and, consequently, undulation frequency. However, unlike animals moving in water [138], I for the sandfish was insensitive to segmental speed (Fig. 2.5). We can understand this with the following argument: if the force to move is dominated by body inertia, then we expect that the force should scale like the undulation frequency squared. If, however, the force is dominated by the force to move the environment, then the force should scale like the environmental forces do with speed. Because during sand-swimming inertial forces are small and the granular resistive forces are insensitive to speed, muscle force in a granular medium can be predicted by environmental interaction forces. We note that sandfish decelerate as they move deeper into granular media (Fig. 2.5); this deceleration is not expected to affect resistive forces from the surrounding media because inertia is small. However, these accelerations may affect the EMGmuscle force relationship.

The above arguments rely on the assumption that muscle activation and force scale proportionally. This might not be true because muscle contractions with differing speed, muscle lengths or activation history may generate different forces for the same activation intensity. When moving at a higher speed, it is possible that the change in sandfish I is due to inherent muscle mechanics (e.g. contraction speed due to muscle force-velocity relationship). However, our findings, which show that muscle activation intensities are insensitive to speed, suggest that these effects may be small compared with the variation between trials. In contrast, in a study of the American eel (*Anguilla rostrata*) [138], which moves with speeds comparable to those of the sandfish, but in a fluid where resistive force increases with speed, muscle activation intensity increased and kinematics changed with increasing speed. This change could result from the changing resistive force imposed on the eel and/or from the muscle mechanics, which are speed dependent [e.g. Hill muscle model [166]].

2.6.2.3 Volume Fraction

Surprisingly, although changes of a few percent in ϕ led to relatively large charges in drag force, we did not observe a correspondingly large increase in I_{rel} for swimming in LP relative to CP. A few characteristics of the animal and the response of the granular medium could explain the smaller than expected changes in activation.

First, the similar activation level could result from the body interacting with disturbed material as the animal proceeds through the granular medium. As the sandfish swims, its anterior body elements shear nearby grains, which causes a CP medium to dilate and a LP medium to consolidate, both evolving toward an intermediate critical packing state ($\phi \approx 0.605$) [90,97]. The local volume fraction surrounding the bulk of the swimming animal might be similar in the two preparations despite different ϕ. Consequently, the resistive force could be similar for sandfish swimming in states with different initial ϕ.

Another explanation of the similar activation level could be the different angles of descent between LP (≈26°) and CP (≈19°) states. A given undulation number in LP occurs at slightly deeper depths than in CP because of the steeper descent angle in the former; for example, during undulation 3 it is estimated that LP trials are 0.34 cm deeper than CP trials as depth was not directly measured in top-view recordings. The confounding effects of depth may have shifted our results, increasing the average intensity of the LP trials at each undulation number. Thus, there may be a greater I_{rel} difference between LP and CP than reported because depth was not directly measured. Future work that uses models of both the sandfish and granular media [167] could better elucidate how internal forces change with changing parameters such as θ_d, ϕ and depth of sand-swimming. In addition, models could be used to analyze how ϕ changes within the media as a consequence of sandfish movement.

2.6.3 Activation Timing During Subsurface Swimming

In the swimming sandfish, the average speed of the traveling wave of activation was faster than the average speed of the curvature wave (median of $\frac{v_{EMG}}{v_c} \approx 1.2$). For undulatory swimmers moving in true fluids, this difference in average speeds has also been observed and the ratio is 2.4 for trout [126] and 1.4 for lamprey [126, 168]. The speed differences occur as a result of changing EMG timing relative to curvature. The phase lag between EMG onset and maximum curvature (neuromechanical phase lag) increases along the length of the animal. Many recent studies have reproduced the neuromechanical phase lags in simulation. For example, Tytell and colleagues simulated an undulatory swimmer and varied undulation frequency, muscle stiffness and fluid viscosity [144]. They found that increasing neuromechanical phase lags down the body resulted when average muscle forces were small compared with average fluid forces. A similar phenomenon could explain the phase lags found in sandfish. Other work has suggested that geometry and passive viscoelasticity may affect the extent of the changing phase lags [165, 168]. For the sandfish, muscle shortening begins in anterior locations before activation is detected. We have found similar results with our RFT model, which prescribes a kinematic waveform similar to the sandfish and couples it to a theoretical model of the granular media. We can use the RFT to predict required torque. We find that bending can start while the torque is produced in the opposite direction in anterior segments because of external forces exerted on the body. A more detailed description can be found in Chapter 3 (and [162]) which compares EMG timing in sandfish to torque generation in a model undulatory swimmer moving through granular media. Currently, our results are inconclusive regarding the effect of speed and resistive force on activation timing. The RFT model could be used to analyze the effect of these parameters on required torque and provide insight on how timing may change.

Similar to other undulatory animals moving through water [138], the EMG duty cycle decreased in the posterior direction (Fig. 2.6, D) from 0.52 ± 0.07 at 0.3 SVL to 0.40 ± 0.06 at 0.9 SVL. This decrease in duty cycle was small relative to that in some aquatic fish. Studies have shown that for elongate animals with uniform body shape, such as the eel [138] and lamprey [126, 169], EMG duration changes are small along the length of the body compared with those in fish with differing body diameter and shape [169, 170]. Also, the duty cycle in sandfish was comparable to that in other animals such as the terrestrial snake [≈0.45 in iliocostalis of *Nerodia fasciata* ([160])] and aquatic lamprey [≈0.5 ([126])], despite differences in environment. Currently, we do not understand what factors influence this timing and how the environment might play a role. In future studies, we will use models in order to investigate timing and duration as it relates to movement through different environments.

2.6.4 Template for Control

Many studies [20, 147, 171] have found a change in neuromuscular strategy with changing external resistance, suggesting sensory feedback is used to modulate gait during swimming (i.e. feedback control). We argue that the sandfish controls its spatial form to target a template to optimize escape into the granular medium. (1) EMG intensities increased with depth (and thus resistive force), which suggests that the sandfish is sensing changes in external environment. (2) No differences between A/λ at varying depth and ϕ were detected, suggesting that the change in neural strategy allowed the animal to maintain the waveform within a range. (3) RFT and computational models [7] of an undulatory swimmer in granular media suggest that within this range of A/λ, speed is maximized and mechanical cost of transport is minimized, and these parameters are insensitive to changes in $A/\lambda \approx 0.2$ (Fig. 2.8). Therefore, targeting this template can yield benefits in speed and energetics as well as sensitivity to changes in kinematics during escape. Mechanoreceptors within muscle, near the skin, and/or head, could be causing the change in muscle activation. Further work is needed in this area to identify the causes for the change. Furthermore, to confirm that this is a general template for undulatory locomotion through sand, kinematics in other sand-swimming animals must be assessed. We predict that sand-adapted subarenaceous animals (defined as animals that primarily live subsurface) with similar body shape should employ a similar waveform to achieve rapid burial. Promising candidates include *Sphenops sepsoides* and *Neoseps reynoldsi*.

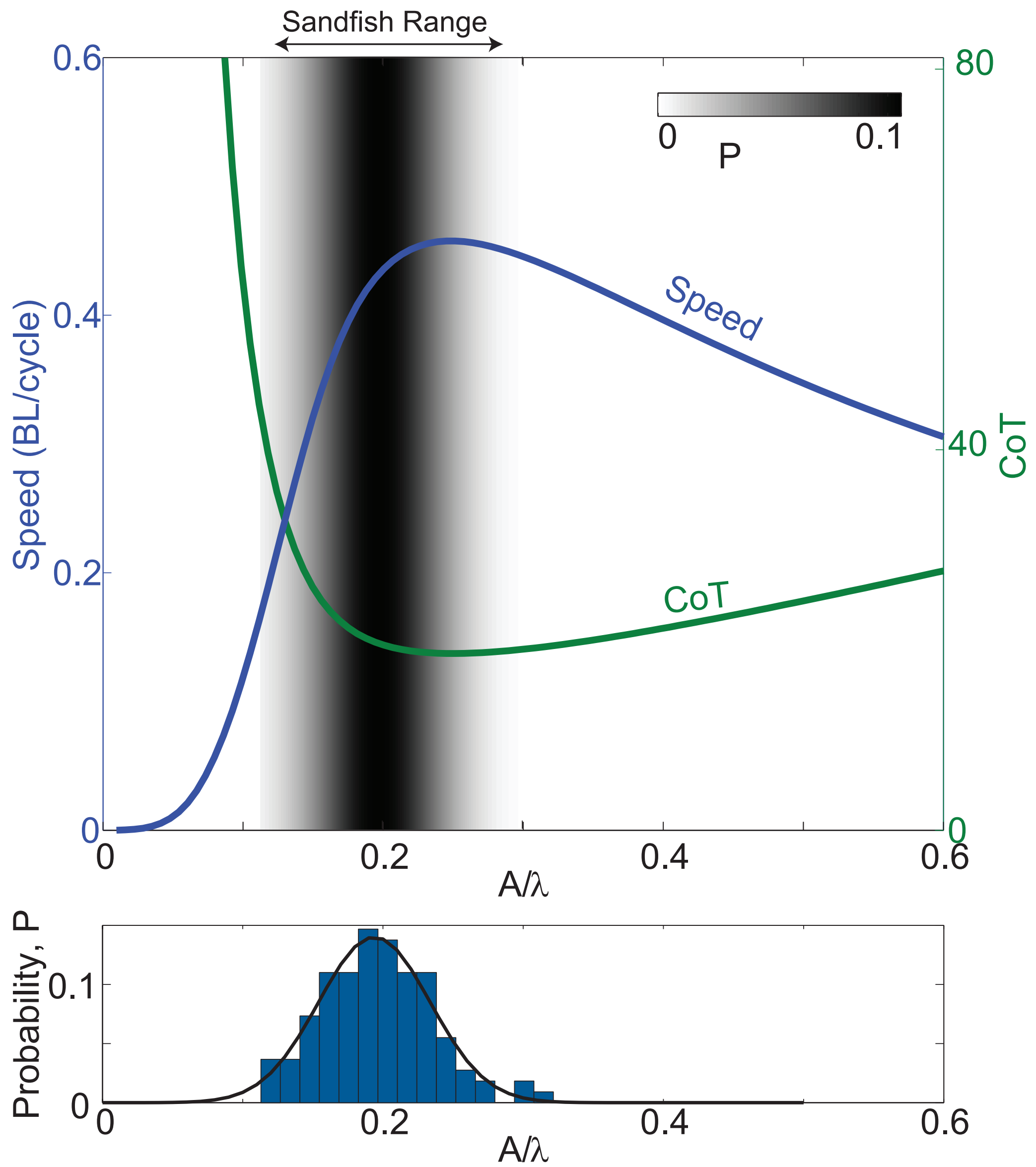

Figure 2.8: Benefits of a template for sand-swimming. (A) Resistive force theory (RFT) predictions of swimming speed normalized by total body length (snouttail length, STL) (blue, left axis) and weight-specific mechanical cost of transport (CoT; green, right axis) indicate that the kinematics used during swimming are in a range that models predict yield maximal speed and minimal mechanical CoT. Speed and CoT are also insensitive to changes in A/λ in this range. In the calculation, the material is 0.3 mm glass beads and the depth is 3.5 cm from the center of the swimmer to the surface. The black shaded region shows a probability distribution of A/λ calculated for sandfish from this study and a previous study [11] (N=17 animals, n=109 trials), where darker shading indicates more animals were observed operating with the corresponding spatial form. The best Gaussian fit to a probability distribution of A/λ (B) is shown in grayscale in A, where black indicates a probability of 0.1 and white indicates a probability of zero. (B) The discrete histogram of A/λ is binned in increments of $A/\lambda = 0.014$ in the range 0.12 0.32. The average spatial form is $A/\lambda = 0.2 \pm 0.04$.

2.6.5 Influence of Particle Properties

Unlike the spherical particles used in our experiments, some natural sands have irregular shapes. These irregularities can allow individual particles to interlock, effectively increasing particleparticle friction [94]. Consequently, volume fractions in natural sands can be lower [94, 95] than our laboratory LP state; however, the volume fractions we achieve are within the range of volume fractions found in nature. Also, the mechanical properties of spherical glass beads have similar characteristics as natural sands [88]: resistance force is insensitive to speed and increases with depth [11]. A previous study of sandfish showed that η is independent of particle size over an order of magnitude [7]. Also, simulation of sandfish has shown that graingrain friction has a small effect on sandfish η while bodygrain friction has a larger effect [?, 78]. Increasing particleparticle friction by 50% caused a 14% increase in η while increasing particlebody friction by 50% caused an 84% decrease in η. Thus, we expect that our laboratory granular media elicit similar η and template as those used during swimming in natural desert sand.

2.7 Conclusions

The sandfish lizard is a sand-swimmer, displaying both morphological adaptations [22,36,55] and kinematics that allow it to move effectively within granular media [7]. A diversity of animals live on and bury within granular substrates, such as the Namib desert mole [13], sand-swimming shovel-nose snake [21], ocellated skink [22], caecilian [14], worm [172], sand lance [39] and razor clam [38]. The techniques developed for the sandfish (like high-speed subsurface x-ray imaging, subsurface EMG, and substrate preparation using a fluidized bed) could also be used to quantify and compare kinematics for other species and determine whether the neuromechanical principles that govern sandfish movement are similar for other subsurface locomotors.

We found that the muscle activation pattern in the sandfish was correlated with drag forces in granular media, and surprisingly that the general features of muscle activation timing was similar to those of undulatory swimmers in water despite differences in environment. The discovery that muscle activation strategy changes with depth (Fig. 2.4) while spatial waveform remains similar in sandfish suggests that these kinematics are targeted and maintained using sensory feedback. This finding supports the hypothesis that operating with $A/\lambda \approx 0.2$ is a template for single period sinusoidal undulatory locomotion through sand and essential to attain a high-speed escape with a low cost of transport.

Finally, we note that the sandfish is an attractive animal model on which to test hypotheses and model neuromechanics of locomotion. First, the sandfish swims in granular media over a range of speeds and resistive force conditions while maintaining similar kinematics. Most studies have shown a change in neural activation and kinematics with differing environments [165] and speeds [138], which makes their coupled effect harder to interpret. In addition, the sandfish has similar wave amplitude along the length of its body (unlike most undulatory swimmers in fluids) and its shape during swimming can be described well with a sinusoidal wave. The granular environment in which the sandfish moves is also a controllable environment. The forces within the granular media can be tuned by changing surface pressure, compaction of the media, friction between grains and bead density. Weakening the material using airflow [173, 174] can allow the animal to move in a different regime where material inertia becomes important. Such manipulations could provide more insight into activation timing and sensory systems used during swimming.

In future studies, we will use both RFT and numerical simulation [7] of the sandfish and granular media to determine how internal forces in the animal body relate to the environment. Since it is difficult to estimate forces from EMG, such models can be used to estimate internal forces during sand-swimming due to external influences. In addition, our sandfish-inspired robotic model can be used to test neuromechanical control strategies in real-world granular environments [105]. For example, we can change morphology and passive stiffness to test how they would affect neuromechanical phase lags (see Chapter 3). Also, control systems that modify the robotic models motor output based on the resistive force can be implemented to optimally change gait with varying conditions. These biologically inspired activation strategies can also give insight into challenges associated with the movement of robots through complex terrain [7, 105, 175].

2.8 Appendix

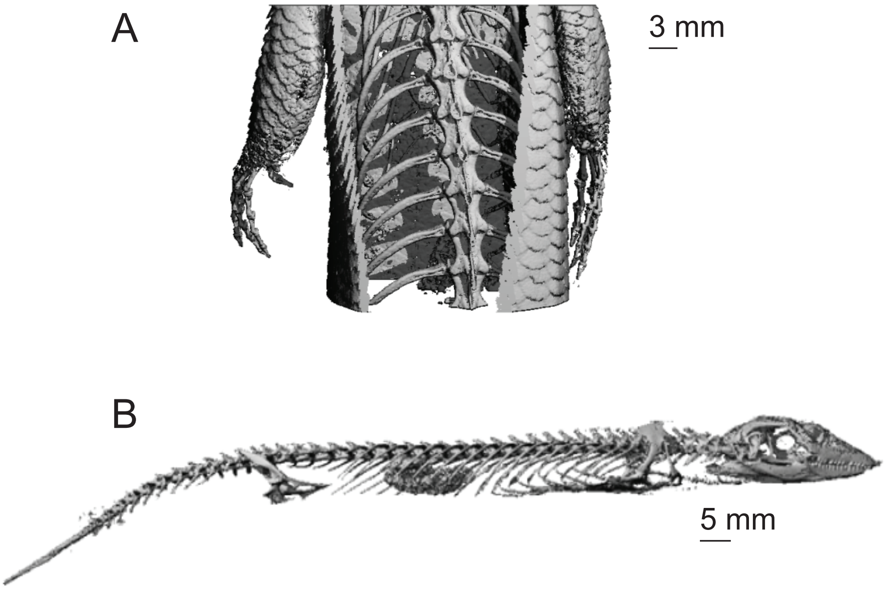

Figure 2.9: X-ray computed tomography (CT) scan showing (A) dorsal view of sandfish vertebrae, ribs, and scales and (B) sagittal view of the skeletal structure.

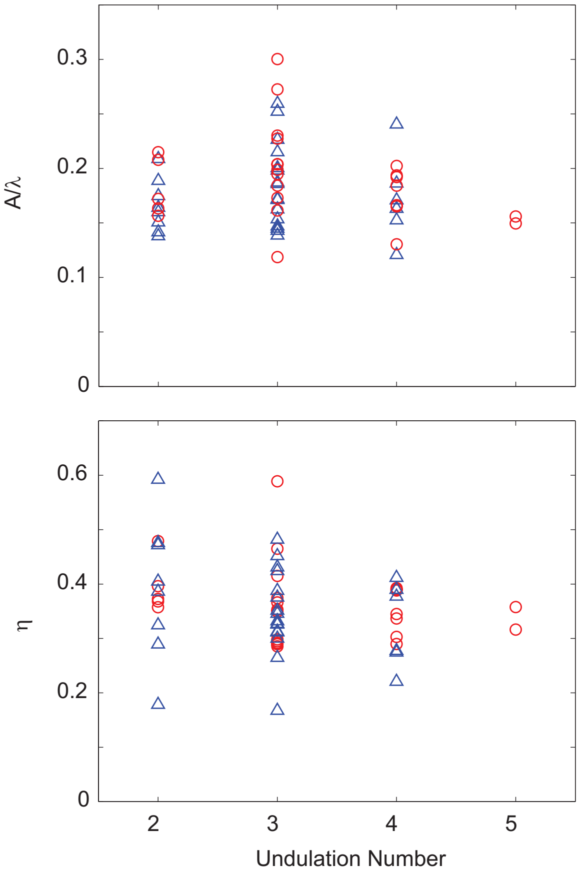

Figure 2.10: Spatial form, A/λ, and wave efficiency, η, do not vary with compaction (red circles, closely packed; blue triangles, loosely packed) or undulation number (N=5 animals, n=51 trials).

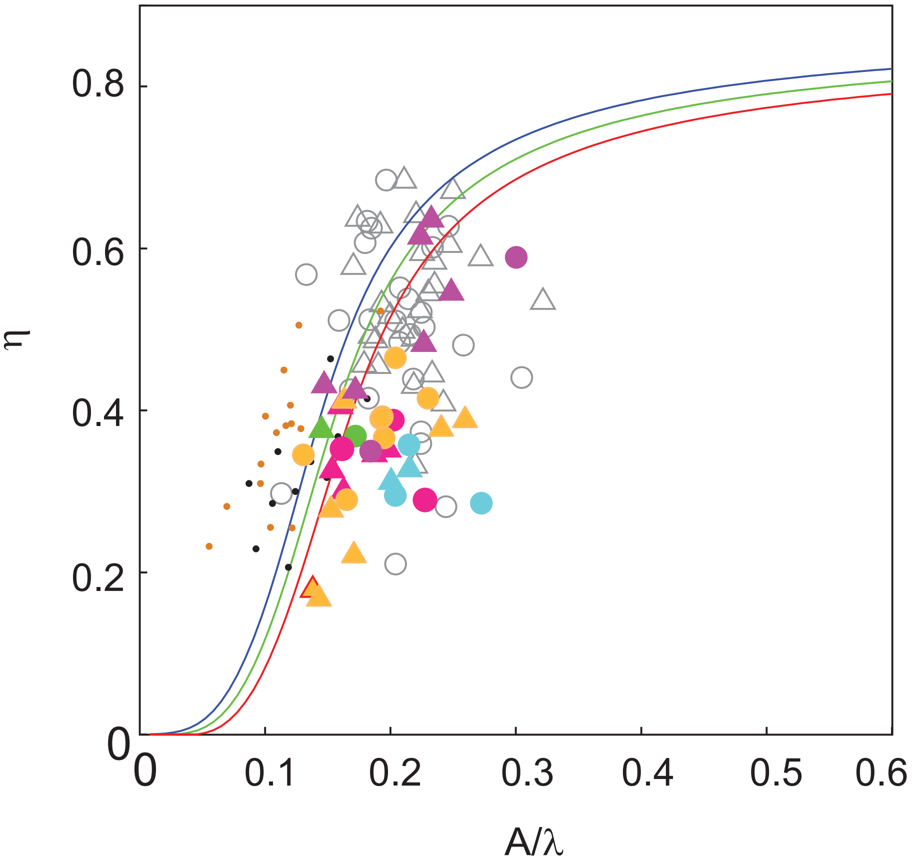

Figure 2.11: Wave efficiency, η, increases with spatial form, A/λ, and is in accord with predictions from resistive force theory (RFT). Filled markers (triangles for loosely packed, circles for closely packed) are data taken in animals implanted with EMG wires (N=5 animals; n=37 runs) where different colors indicate different individuals. Open markers are data from [11]. Brown points are data from animals tested without wires (N=15 runs; n=4 animals) and black points are data from the same animals tested with wires glued to their back (N=11; n=2 animals) in a loosely packed medium. The blue curve is a prediction of η versus A/λ from RFT with drag comparable to the sandfish without wires. The green and red curves are the RFT prediction with 20% and 40% increased drag on the head, respectively.

2.9 Contributions

All resistive force theory in this chapter (speed and CoT predictions in Fig. 2.8 and wave efficiency (η) prediction in Fig. 2.11) were calculated by Yang Ding. Mateo Garcia assisted with setup and collection of side-view kinematic data. Thomas J. Burkholder helped with sandfish dissection and Robert E. Guldberg's lab assisted with acquiring a CT scan of sandfish morphology and skeletal structure. Elizabeth A. Gozal provided the EMG analysis code (SpinalMOD).

CHAPTER III

NEUROMECHANICAL PHASE LAGS (NPL) EXPLAINED USING A SIMPLE MODEL: SANDFISH SWIMMING IN GRANULAR MEDIA

3.1 Summary

Undulatory locomotion, a gait in which thrust is produced in the opposite direction of a traveling wave of body bending, is a common mode of propulsion used by animals in fluids, on land, and even within sand. As such it has been an excellent system for discovery of neuromechanical principles of movement. In nearly all animals studied, the wave of muscle activation progresses faster than the wave of body bending, leading to an advancing phase of activation relative to the curvature towards the tail. This is referred to as “neuromechanical phase lags” (NPL). Several multi-parameter neuromechanical models have reproduced this phenomenon, but due to model complexity the origin of the NPL has proved difficult to identify. Here we use perhaps the simplest model of undulatory swimming to accurately predict the NPL during sand-swimming by the sandfish lizard, with no fitting parameters. The sinusoidal wave used in sandfish locomotion, the friction-dominated and non-inertial granular resistive force environment, and the simplicity of the model allow detailed analysis, and reveal the fundamental mechanism responsible for the phenomenon: the combination of synchronized torques from distant points on the body and local traveling torques. This general mechanism should help explain the NPL in organisms in other environments; we therefore propose that sand-swimming could be an excellent system to quantitatively generate and test other neuromechanical models of movement. Such a system can also provide

---

This chapter is a published paper by Yang Ding, Sarah S. Sharpe, Kurt Wiesenfeld, and Daniel I. Goldman, *Proceeding of the National Academy of Sciences*, 2013 [162]

*All theoretical analyses were developed and conducted by Yang Ding, see [132] for more details guidance for the design and control of robotic undulatory locomotors in complex environments.

3.2 Introduction

Animal movement emerges from the complex interplay of nervous and musculoskeletal systems with the environment. Much progress has been made for understanding the neural control patterns and motor systems responsible for effective locomotion ([18, 20, 176–180]). While the environment's influence on neural control is increasingly recognized [181, 182], challenges remain in understanding how environments shape the control strategy of locomotion. Particular behaviors, gaits and environments have revealed themselves to be amenable to detailed comparison of experiment and theory to elucidate neuromechanical principles of control [20, 144, 183, 184]. A form of locomotion where there has been much progress is *undulatory locomotion*, a movement strategy employed by numerous, phylogenetically diverse animals such as fish, snakes, worms and sandfish lizards (*Scincus scincus*) (see Fig. 3.1, A) [11, 133, 185–188] to traverse fluids, solids, and even sand.

In undulatory locomotion, a traveling wave of muscle activation (and curvature) propagates from head to tail resulting in forward movement. The forces produced on different "segments" of the body can be decomposed into thrust and drag, and integrating these over the body at any instant in time determines the propulsion of the animal. Many robots have also been built that use such a gait [189–191]. A feature of undulatory locomotion that is observed across a range of animal sizes and environments is that the wave of muscle activation travels faster than the wave of curvature [34, 126, 139, 169, 192]. Consequently, the relative phase of the muscle activation to the curvature advances along the body. Physically, this means that more posterior muscles begin activating earlier in the muscle strain cycle (i.e. while the muscle is lengthening) and produce more negative work than anterior muscles. The phenomenon of the advancing neuromechanical phase is often referred to as the "neuromechanical phase lags" (Fig. 3.1, C & D), or "NPL" for short.

Two complementary modeling approaches are used to understand movement principles. The "bottom-up" approach (referred to as "anchoring" in [148]) integrates realistic models of multiple bio-components and the complex interactions among them, as well as the with models of the environment. For example, a model (see [168]) might incorporate tens to hundreds of muscles, hundreds to thousands of neurons, chemical kinetics, and the nonlinear couplings among them. Further complexity could be added by coupling these models to fluids which are governed by complex partial differential equations. In contrast, the "top-down" approach (referred to as "templates" in [148]) identifies coordinated components as one single element to generate reduced models and seeks general principles of system behavior. Using the first approach, many multi-parameter neuromechanical models [144, 165, 168, 193–196] have been proposed to model undulatory locomotion. While such models qualitatively reproduce the NPL in undulatory swimming, due to uncertainties about the passive body properties and the hydrodynamical forces, as well as the model complexity and number of parameters, it remains a challenge to explain the origin of the phenomenon.

In this Chapter we show that what might seem to be a specialized and complex system, a lizard "swimming" in sand using an undulatory gait, facilitates *quantitative* comparison of experiment and theory, and helps explain the fundamental origin of the NPL in undulatory locomotion in other environments. We base the present work on our previous biological muscle activity measurements (see Chapter 2 and [34]) which revealed that the sandfish displays neuromechanical phase lags when targeting a particular behavior: escape. These neuromechanical phase lags were present regardless of depth, media compaction and swimming speed. Using a template approach–inputting kinematics of the lizard which confer swimming speed and energetic benefits [8] into a previously developed granular resistive force model of sand-swimming and abstracting the nervous system and musculoskeletal system as a "black box"– we are able to reproduce internal torque timing patterns (i.e. from muscle contractions) with no fitting parameters. The simple kinematics combined with the relatively simple rheological features of organism-fluidized sand allow us to analyze the model and thus make statements about general principles of neuromechanics in swimming, applicable to organisms and robots in other environments.

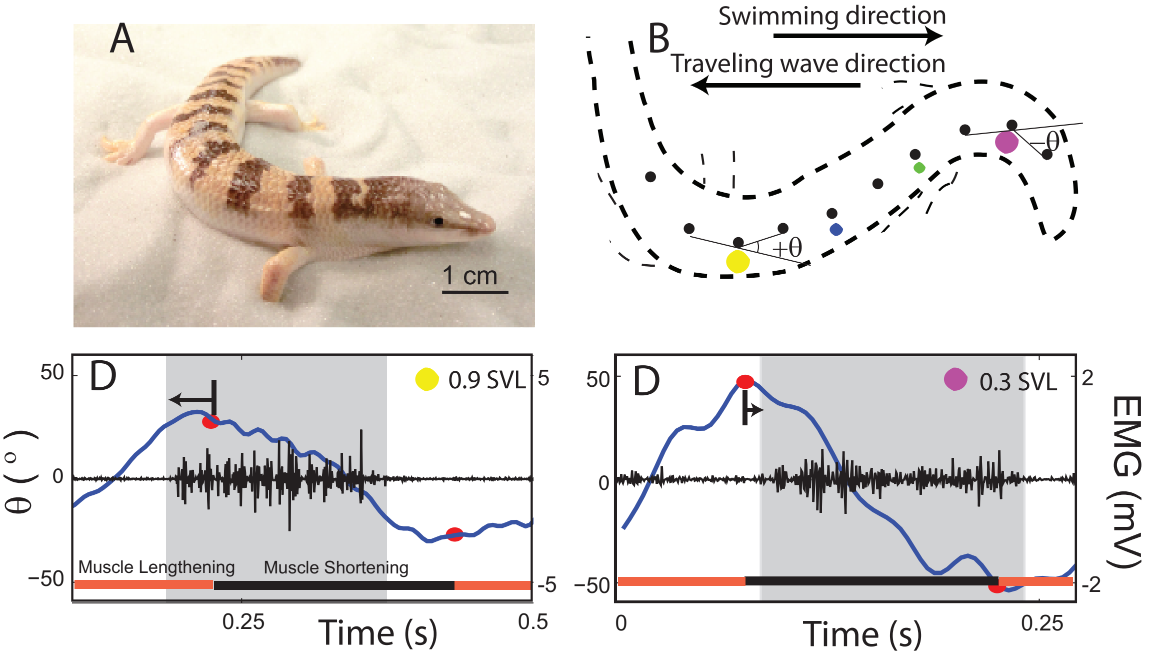

Figure 3.1: Neuromechanical phase lags of the sandfish during sand-swimming. (A) A sandfish lizard resting on 0.3 mm diameter glass particles. (B) A trace of an x-ray image of the sandfish during subsurface sand-swimming at time, $t = 0.21$ s in panels C and D. Opaque markers (black circles) are attached to the exterior midline to facilitate tracking. Electrodes are implanted in epaxial musculature on the right side of the body at 0.3 (magenta), 0.5 (green), 0.7 (blue), 0.9 (yellow) snout-vent length (SVL) locations (where the vent is just posterior to the pelvic girdle and the SVL is approximately 0.75 of the total body length). (C) & (D) EMG recordings at 0.9 and 0.3 SVL, respectively, during sand-swimming. Gray regions indicate time duration over which the rectified filter EMG is above a threshold (equal to the mean of the rectified-filtered signal) indicating muscle activation (see Chapter 2 and [34], Material and Methods for more details). The blue line shows the measured angle between consecutive markers (see panel B). The red circles show the maximum or minimum of the best 2nd order polynomial fit to the angle vs. time series for each half cycle. Arrows indicate the difference in time between the onset of muscle activation and maximal convexity. Note the different scales for EMG due to different electrode constructions.

3.3 Experimental Electromyogram (EMG) Recording Methods

Previous work [34] using a micro-CT scan of a single sandfish revealed 26 vertebrae in the trunk and more than 13 anterior caudal vertebrae in the tail. The iliocostalis musculature was targeted for implantation and is located on the dorso-lateral portion of the trunk. Dissection revealed qualitatively similar muscle morphology to that described for *Iguana iguana* [158, 159]; where iliocostalis musculature spanned approximately 1 vertebrae.

Electrodes were implanted in one side of the body at 0.3 (magenta), 0.5 (green), 0.7 (blue), 0.9 (yellow) snout-vent length (SVL)(Fig. 3.1, B) where the average SVL was 8.9 cm (N = 5 animals). EMG data used in this Chapter were taken from n=37 sandfish swimming trials. The EMG signal was filtered with a second-order Chebyshev filter and rectified in order to facilitate EMG burst detection. A burst threshold was set equal to the mean of this rectified-filtered EMG trace. Burst onset was defined as the time when the filtered EMG signal exceeded the threshold and afterwards remained above it for a minimum of 0.04s. EMG burst offset was defined as when the filtered EMG signal became lower than the threshold and remained below for at least 0.08 s [157]. This burst detection was necessary to exclude small voltage changes that did not constitute an EMG burst, such as noise due to movement artifact. See Chapter 2 or [34] for more details on the EMG recording and analysis technique.

3.4 Passive Body Properties

An inverse dynamics approach is used to predict internal torques generated in the sandfish (see Model section below). To compare internal torque with EMG timing we make two assumptions: (1) The lag between muscle activation and muscle force production is small compared to the undulation cycle period and approximately constant down the body and (2) sandfish passive body forces during swimming are are small compared to the force needed to move within granular media. To verify the second assumption we perform passive dynamic bending tests and pendulum ‘swing’ tests on anesthetized sandfish to get an approximate measure passive body properties.

3.4.1 Dynamic Bending Tests

3.4.1.1 Methods

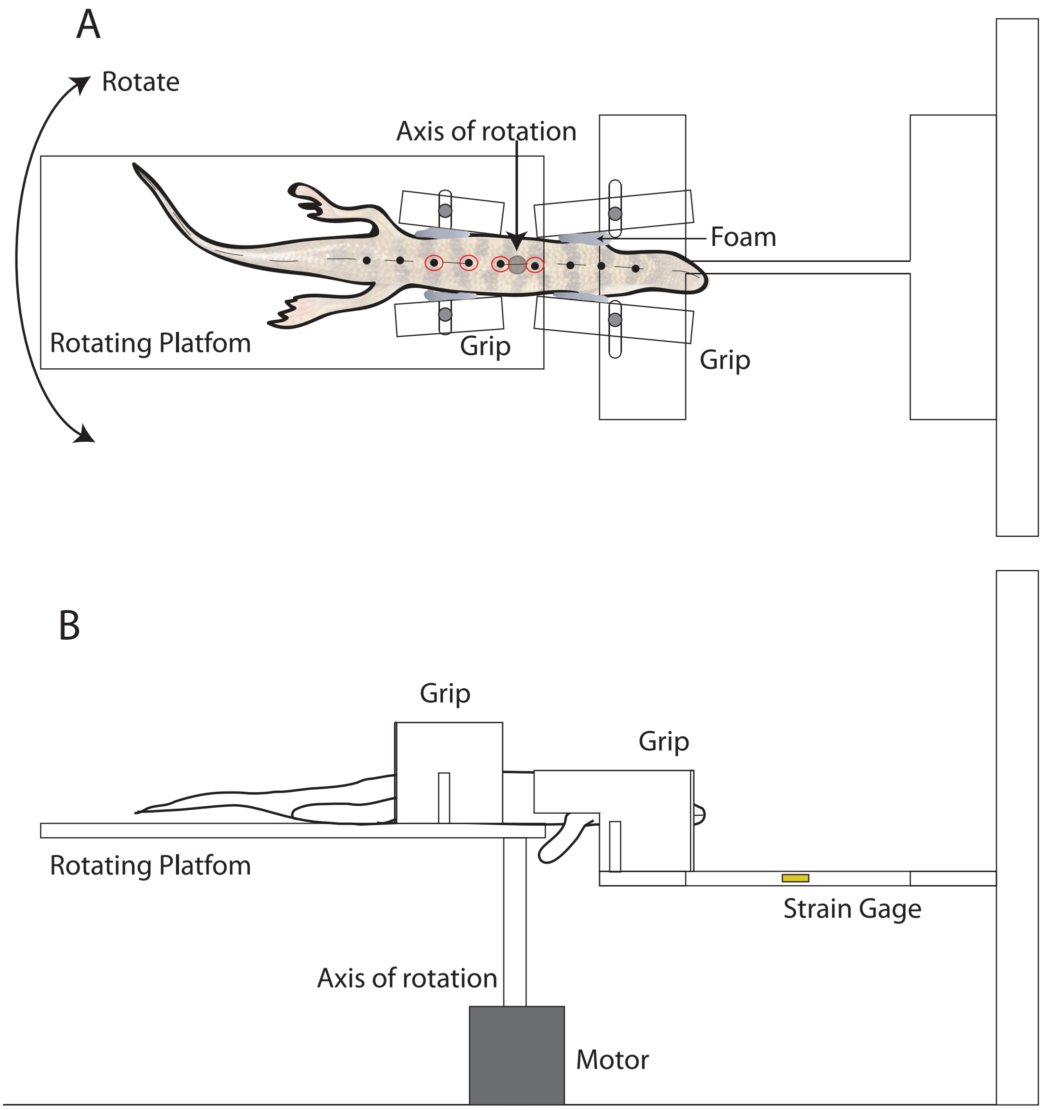

Figure 3.2: Elasticity experimentally measured by bending sandfish body and measuring resulting torque. (A) Top and (B) side view of experimental setup are shown. Adjustable grips hold animal at 0.5 and 0.6 SVL locations and are attached to a rigid platform and to a rotating platform, respectively. A motor rotates the anterior region of the sandfish through ±15° and resulting bending moment is measured with strain gauges. Black circle were marked on animal midline at increments of 0.1 SVL. The best fit line through the markers circled in red were used to calculate angle θ.

Three anesthetized sandfish (mass = 15, 16 and 25 g) (Table 3.1) were gently clamped at approximately 0.5 SVL and at 0.6 SVL (Fig. 3.2) with adjustable grips. The grips were attached to a rigid platform and to a rotating platform, respectively. A motor rotated the anterior region of the sandfish through ± 15° for 3 cycles at angular velocities of 1, 10 and 20°/s. The first and last half cycle were excluded from the analysis due to varying rotation velocities. The anterior end of the sandfish was clamped to a platform with two strain gages (Omega, KFG-3-120-C1-11L1M2R) used to record resulting torques. Signals were amplified (INA125P; Digi-Key) by 5000 before data acquisition and analyzed using custom software (LabVIEW, NI, Austin, TX, USA). Black points were marked on the animal midline at increments of 0.1 SVL. The best fit line through the markers circled in red were used to calculate the angle θ.

Torque from passive body properties was estimated by calculating elasticity and damping coefficients during work loop experiments. Body stiffness, K, was estimated using the slope of the best fit line through the torque-angular displacement curve (Fig. 3.3, A) for a single cycle (n=8 trials each). It is unknown whether body damping in the sandfish is better approximated by a viscous damping (which is speed dependent) or structural damping (which is displacement dependent, also known as hysteretic damping) [197], so both models are considered. Using a viscoelastic model (or Voigt model), the viscous damping coefficient, c, was approximated by quantifying the viscous torque (τ_v) at zero angular displacement during steady-state rotation and dividing by the angular speed ($\dot{\theta}$), (i.e. $c = \tau_v(\theta = 0)/\dot{\theta}$). For the hysteretic damping model, the structural damping coefficient h is proportional to angular displacement, θ and $\pi/2$ out phase. h was estimated by finding the torque at zero displacement during steady-state rotation and dividing by the maximum angular displacement: $h = \frac{\tau_h(\theta=0)}{\theta_{\max}}$. The loss factor was calculated as $\eta_{loss} = \frac{h}{K}$. The area contained within the work loop (E_{loss}) was determined using polynomial fits to the torque vs angle curves for increasing and decreasing angle.

To interrogate stiffness and damping coefficients at higher speeds, we repeated the experiment with one of the sandfish (animal 2,Table 3.1, Fig. 3.3) using angular speeds of 1, 10, 20, 50 and 100°/s and compared with previous results.

We substituted the values during sand-swimming (angular excursion of 30° and angular velocity of 240°/s) and the average calculated K and c at 20°/s into our viscous damping model to estimate torques during sand-swimming (Table 3.2). For hysteretic damping, we estimated the damping torque at 240°/s by extending the trend line between calculated torque from hysteretic damping and angular speed between 20 and 100°/s (note: this speed effect indicates that viscous damping may dominate during movement at high speeds and the Voigt model be be a better approximation).

Table 3.1: Mass and size of 3 sandfish used to estimate passive body properties (where SVL is snout-to-vent length and STL is snout-to-tail length). Note that sandfish 2 was used again for high speed rotation test.

Sandfish	Mass (g)	SVL (cm)	STL (cm)	Width (cm)	Height (cm)
1	25	10.1	15.7	1.6	1.2
2	16	8.6	14.5	1.5	1.1
3	15	8.2	13.4	1.5	1.1

3.4.1.2 Results

Torque versus angle work loops occurred in the clock-wise direction for all sandfish (N=3) indicating energy dissipation (Fig. 3.3, A). Elasticity changed between the animals tested and increased with speed within a range of $1 - 20°$/s (Table 3.2). Average elasticity across all animals at 1°/s was 0.12 N–cm/rad, at 10°/s was 0.17 N–cm/rad, and at 20°/s was 0.18 N–cm/rad. We found torque at zero displacement was constant between 1, 10 and 20°/s ($P > 0.05$), leading to a decreasing c with increasing speed (Table 3.2 and Fig. 3.13, B). For the hysteretic damping model, we found that h was independent of angular speed, between 1 and 20°/s ($P > 0.05$) resulting in a decreasing η_{loss} ($P < 0.0001$) due to the increasing K. Area enclosed by the hysteresis loop (E_{loss}) was constant between 1-20° (Fig. 3.13, C). Trends for estimated torque during swimming using calculated K and c are shown in Figures 3.3 & 3.13. Torque from hysteretic damping is proportional to torque from viscous damping (Fig. 3.13, B) and follows the same trends.

For the experiment in which a sandfish was rotated at 1, 10, 20, 50 and 100°/s (the maximum achievable value with our system) (Figs. 3.3 & 3.13, inset) we found similar results for rotations rates below 20°/s (i.e. the stiffness coefficient and the associated torque increased from 1 to 20°/s, while the torque from both viscous and hysteretic damping remain approximately constant). However, from 20 to 100 °/s the stiffness coefficient and

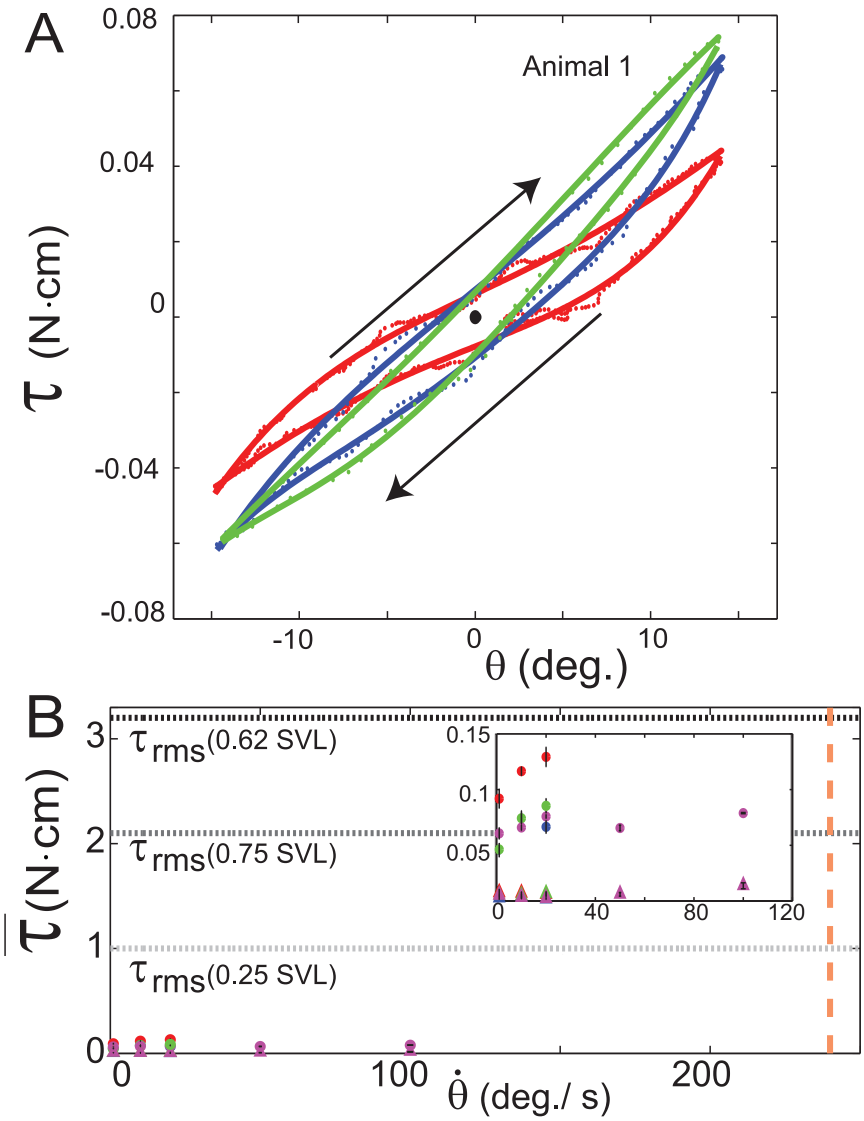

Figure 3.3: Experimental measurements of sandfish body elasticity and damping. (A) Representative work loop for Animal 1 with angular velocities of 1°/s (red), 10°/s (blue) and 20°/s (green). The direction is indicated by the arrows, where the angle is initially zero and increases to ≈ 0.26 rad. (15°) , decreases to ≈ -0.26 rad. (−15°), then returns to zero. Work loops are shown for constant angular velocity (i.e. the system has reached a steady state). Dotted trajectories represent the experimentally recorded force; solid curves are the best polynomial fits. (B) Estimated average torque using calculated elastic (circles) and damping (triangles) coefficients compared to the maximum τ_{rms} due to external forces calculated from discrete element simulation [8] (0.62 body length (BL))(dashed horizontal black line). Average τ_{rms} for 0.25 BL(light gray dashed line) and 0.75 BL (dark gray dashed line) are also shown. For animal 1 (red), 2 (blue) and 3 (green) coefficients were measured for 1, 10 and 20°/s. In animal 4 (magenta) coefficients were measured for 1, 10, 20, 50 and 100 °/s. The average angular speed the sandfish operates at is 240 °/s. Inset shows zoomed in region of data in the main figure (units are the same).

elastic torque remained constant, while both damping torques increased. This indicates that viscous damping may be a better model of the system at high angular velocities (while structural damping may be more dominate at low angular velocities).

The sandfish used an average angular velocity and angular excursion of 240 °/s and 30 °/s, respectively. Because stiffness coefficients and viscous damping coefficients did not change above 20 °/s, the torque during sand-swimming were approximated using these average values. We estimated that torque due to bending stiffness is 0.09 ± 0.03 N·cm and the torque due to viscous damping is 0.06 ± 0.034 N·cm. For comparison, we estimated the required torque the sandfish must generate during locomotion in a granular media. The torque varied over the undulation cycle with segment orientation, but the root mean square torque (τ_{rms}) was ≈1 at 0.25 SVL, ≈3.2 at 0.62 SVL, and ≈2.1 at 0.75 SVL (Fig. 3.3). This means that the passive body torques account for between 5–15% of the total required torque. Therefore, torque due to active muscle contraction is critical for movement in sand, and movement may stop quickly in a granular media after muscle activation ceases.

Table 3.2: Work loop parameters. One-way ANCOVA table testing effect of oscillation frequency and animal on stiffness K, viscous damping c, loss factor η_{loss} and area E_{loss} (left). Average values are shown and separated by speed and animal (right).

Variable	Source	d.f.	F	P	Animal #	Mean ± s.d.		
						1°/s	10°/s	20°/s
K (N-cm/rad.)	Frequency	1	151.7	<0.0001	sf 1	0.175 ± 0.017	0.222 ± 0.008	0.247 ± 0.017
	Animal	2	214.62	<0.0001	sf 2	0.084 ± 0.009	0.144 ± 0.011	0.127 ± 0.011
	Frequency × Animal	2	4.14	0.0203	sf 3	0.088 ± 0.011	0.142 ± 0.010	0.163 ± 0.012
	Error	66			**Overall**	**0.116 ± 0.045**	**0.170 ± 0.040**	**0.179 ± 0.053**
c (N-cm s/rad.)	Frequency	1	82.36	<0.0001	sf 1	0.418 ± 0.207	0.039 ± 0.008	0.017 ± 0.007
	Animal	2	5.48	0.0063	sf 2	0.151 ± 0.092	0.021 ± 0.010	0.005 ± 0.004
	Frequency × Animal	2	5.85	0.0046	sf 3	0.298 ± 0.072	0.027 ± 0.009	0.018 ± 0.005
	Error	66			**Overall**	**0.289 ± 0.172**	**0.029 ± 0.012**	**0.013 ± 0.008**
η_{loss}	Frequency	1	21.01	<0.0001	sf 1	0.157 ± 0.0718	0.117 ± 0.023	0.089 ± 0.037
	Animal	2	12.65	<0.0001	sf 2	0.123 ± 0.073	0.098 ± 0.044	0.050 ± 0.037
	Frequency × Animal	2	0.04	0.9593	sf 3	0.231 ± 0.078	0.128 ± 0.044	0.150 ± 0.04
	Error	66			**Overall**	**0.170 ± 0.085**	**0.115 ± 0.039**	**0.096 ± 0.057**
E_{loss} (N-cm rad.)	Frequency	1	0.39	0.5355	sf 1	0.006 ± 0.002	0.006 ± 0.002	0.007 ± 0.002
	Animal	2	19.7	<0.0001	sf 2	0.004 ± 0.001	0.004 ± 0.002	0.002 ± 0.002
	Frequency x Animal	2	2.22	0.1168	sf 3	0.005 ± 0.001	0.004 ± 0.001	0.006 ± 0.001
	Error	66			**Overall**	**0.005 ± 0.002**	**0.005 ± 0.002**	**0.005 ± 0.003**

3.4.2 Pendulum Swing Tests

3.4.2.1 Methods

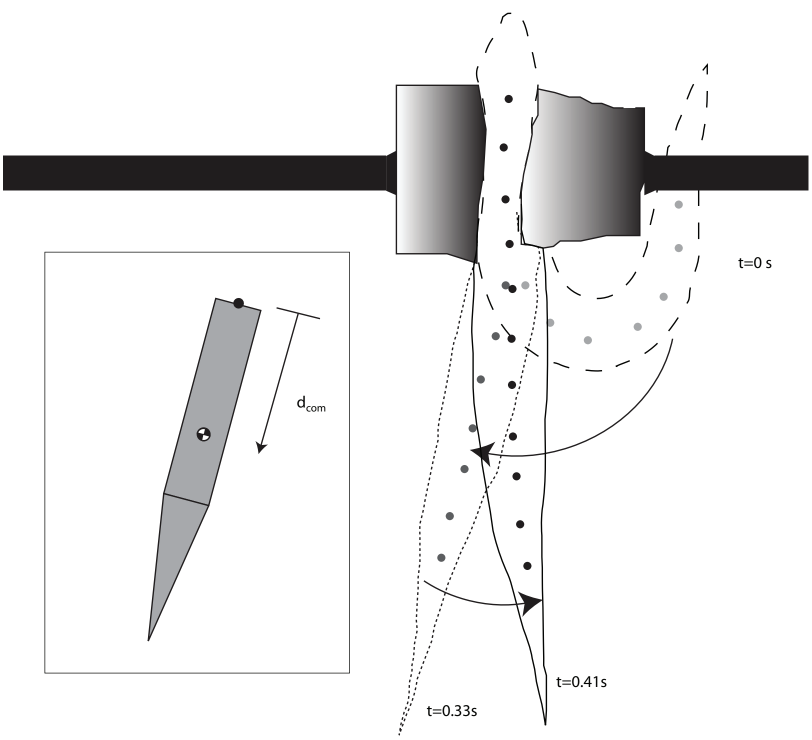

Figure 3.4: Swing test to measure passive body properties at natural frequencies. Sandfish were clamped with soft foam to restrict movement anterior to 0.5 SVL. The initial position is shown (dashed outline, t=0 s). Angle is calculated after the first half cycle (dotted outline, t=0.33 s) when the angle relative to 0.5 SVL and bending is smaller. Inset: Sandfish body is modeled as a cylinder and a cone with uniform density.

To verify the results from the bending test experiment, another technique was used in which sandfish were modeled as a physical pendulum and K, c and η_{loss} were estimated at higher angular frequencies. The same sandfish were used as in the previous experiment (Table 3.1). Animals were oriented vertically and clamped at approximately 0.5 SVL (Fig. 3.4). The tail of the sandfish was bent upward and released, allowing the body to swing freely. The sandfish body was modeled as a rigid cylinder and the tail as a cone with uniform density. The angular motion, θ was fit to a damped harmonic oscillator:

$$\mathrm{I}\ddot{\theta} + c\dot{\theta} + K\theta + mgd_{\mathrm{CoM}}\sin(\theta) = 0, \tag{3.1}$$

where d_{CoM} is the distance from the point of rotation to the center of mass, m is the mass of the unclamped portion of the sandfish, I is the moment of inertia, and $\ddot{\theta}$ is the angular acceleration. Angular motion during the first half cycle after the tail was released was neglected due to large angles and body bending. θ was measured between the 0.5 and 0.8 SVL body positions.

We also fit the motion using a hysteretic damping model:

$$\mathrm{I}\ddot{\theta} + (1 + i\eta_{loss})K\theta + mgd_{\mathrm{CoM}}\sin(\theta) = 0. \tag{3.2}$$

For both models, we used the small angle approximation $\sin(\theta) \approx \theta$. Best fit parameters were determined using minimization techniques (Matlab, Mathworks, Natick, MA, USA).

3.4.2.2 Results

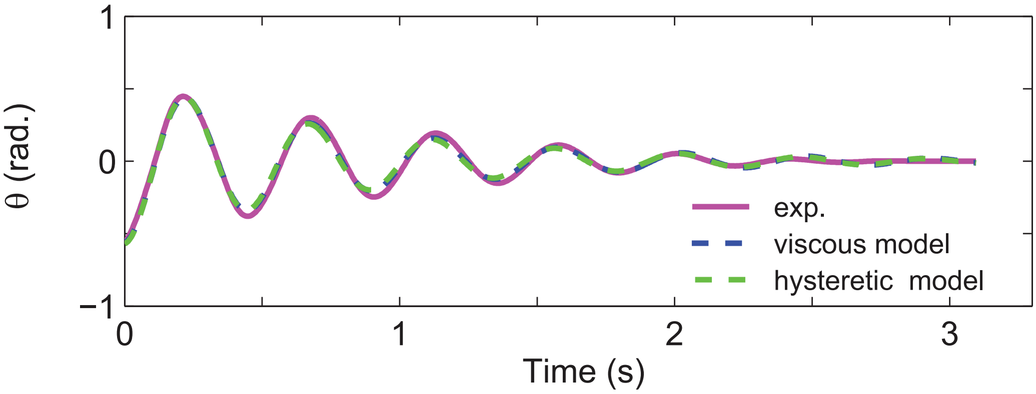

Figure 3.5: Representative angle vs. time trajectory for animal 1 during a pendulum swing test. Pink is experiment, blue dashed is the viscous model and green dashed is the hysteretic model with best fit parameters.

Both viscous and hysteretic models fit the angular displacement trajectory well ($r^2 <$ 0.9) (Fig. 3.5). Fitting a viscoelastic model and hysteretic model yielded small stiffness coefficients (K =0.006 ± 0.1) with some calculated values in the negative range (Table 3.3). We explain this because the torque due to gravity is large compared to the torque from passive elasticity during bending (on average 7% of the gravitational force) and, therefore is not beyond the error of approximation. However, this finding confirms that passive elasticity in sandfish is small.

The viscous damping coefficient (0.012 ± 0.006 N–cm s/rad.) was on the order as that measured in the bending test at 20°/s (Table 3.3). The loss factor also followed the pattern predicted by the bending test. η_{loss} was approximately 0.38 ± 0.22 N·cm/rad. Therefore, the average torque due to hysteretic damping is 0.009 ± 0.004 N·cm. Regardless of the model chosen, viscous or hysteretic, torque due to passive damping was small (between 1–4% of the required torque, τ_{rms}, along the body during swimming in a granular medium.

In conclusion, both swinging test and bending test show that passive stiffness and damping are small compared to the force due to the external load (combined <6%) and confirm the assumptions used in our model.

Table 3.3: Average parameter values (mean and s.d.) using viscous and hysteretic damping model for each sandfish and for all data (overall).

Animal #	Viscous Damping Model			Hysterestic Damping Model		
	Osc. Freq. ($^{-1}$)	K (N-cm/rad.)	c (N-cm-s/rad.)	Osc. Freq. (s^{-1})	K_v (N-cm/rad.)	η_{loss}
sf 1	2.21 ± 0.04	-0.115 ± 0.030	0.009 ± 0.002	2.20 ± 0.05	-.127 ± 0.016	0.183 ± 0.015
sf 2	2.70 ± 0.08	0.092 ± 0.035	0.020 ± 0.005	2.54 ± 0.02	-0.016 ± 0.007	0.698 ± 0.103
sf 3	2.73 ± 0.01	0.055 ± 0.037	0.009 ± 0.001	2.69 ± 0.08	0.039 ± 0.029	0.320 ± 0.025
Overall	**2.54 ± 0.26**	**0.006 ± 0.100**	**0.012 ± 0.006**	**2.47 ± 0.23**	**-0.036 ± 0.075**	**0.383 ± 0.224**

3.5 Model

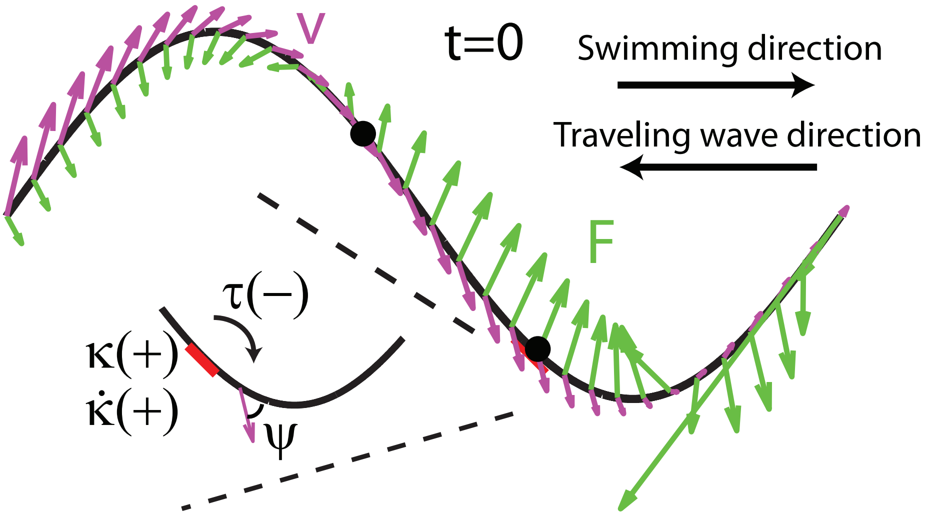

Figure 3.6: Diagram of the model. Magenta arrows represent velocity and green arrows represent forces from the medium. Inset shows the signs of the torque (τ), the curvature (κ), and the rate of change of curvature ($\dot{\kappa}$) at approximately 0.6 body length on the body. Negative τ corresponds to no muscle activation on the right side of the body (red thick line). ψ indicates the angle between the segment axis and its velocity.

3.5.1 Resistive Force Theory (RFT) Model

Previously we developed a granular resistive force theory (RFT) model and a numerical simulation that explained the swimming performance of the sandfish [7,8,11]. The models showed that the lizards swim within a self-generated "frictional fluid" where frictional forces between the granular particles dominate over both the body inertia and inertial forces from the environment. As before, we prescribe body kinematics (in the frame of the animal) based on the experimental observation that the body position of a sandfish in the body frame is approximately a single-period sinusoidal wave traveling posteriorly (Fig. 3.6):

$$y_b = A\sin[2\pi(\frac{x_b}{\lambda} + \frac{t}{T})], \tag{3.3}$$

where y_b is the lateral displacement from the midline of a straight animal, A is the amplitude, T is the period of undulation, λ is the wavelength, t is the time, and x_b is the distance along a line parallel to the direction of the traveling wave measured from the tail tip. Here, we

---

*Model development and torque calculation performed by Yang Ding, see [132] for more details normalize both the wavelength and period to 2π such that $\frac{2\pi}{\lambda} = \frac{2\pi}{T} = 1$. Since the trunk of the sandfish is quite uniform (with body width variations less than about 5% from 0.1 snout to vent length (SVL) to 1.0 SVL) and the diameter of the body decreases significantly after about 1.2 SVL, we used a uniform body shape and took the total arc length (L) in the model to be 1.2 times the average SVL (8.9 ± 0.3 cm) of the animal. Dissection revealed after 1.2 SVL the tail is composed of mostly adipose tissue and a small amount of muscle; therefore, both the external and internal torques on the tail should be minimal for the tail beyond 1.2 SVL. We neglected the variation of the horizontal position x_b of a segment within a cycle, so the normalized position on the animal body $s\frac{2\pi}{L}$ corresponded to the horizontal position x_b in the model, where s is the arc length from the tail end. When a smaller amplitude was used, the wavelength was kept as 2π.

For swimming in sand, the granular force $\vec{F}$ on any infinitesimal segment of the swimmer is independent of the segment speed (and thus undulation frequency), proportional to its depth, and is a function of the angle (ψ in Fig. 3.6) between the segment axis and its velocity direction. See Appendix for the empirically determined granular force $\vec{F}(\psi)$. The depth of a segment is calculated assuming the model sandfish swims with its center 3.5 cm below the horizontal plane and at an entry angle of 22 degrees (an average value for the sandfish [11, 34]). The entry angle is the angle between the horizontal plane and the plane in which the animal moves [34].

Since the estimated inertial force is negligible, the swimmer moves in a way such that net external force and torque are approximately zero. In this study, we consider all three degrees of freedom in a plane, namely the forward (the only degree of freedom in our previous RFT models), lateral and yaw motion ("recoil"), and determine the velocities of the three degrees of freedom by solving the force/torque balance equations at every instant of time. Since the motion of a point on the body is the superposition of the prescribed and center of mass (CoM) motions, the net external force $\vec{F}_{\text{net}}(\dot{\vec{R}}, \dot{\theta})$ and net external torque about the CoM $\vec{\tau}_{\text{net}}(\dot{\vec{R}}, \dot{\theta}) = (0, 0, \tau_{\text{net}})$ are functions of the center of mass velocity $\dot{\vec{R}}$ and rotation rate about the CoM $\dot{\theta}$. For the CoM movement, Newton's laws give

$$\begin{aligned}\vec{F}_{\text{net}}(\dot{\vec{R}}, \dot{\theta}) &= M\ddot{\vec{R}} \\ \vec{\tau}_{\text{net}}(\dot{\vec{R}}, \dot{\theta}) &= \dot{\vec{L}}\end{aligned} \tag{3.4}$$

where M is total mass and L is angular momentum. By setting the inertial terms on the right sides of these equations to zero, the center of mass velocities ($\dot{\vec{R}}$ and $\dot{\theta}$) can be numerically determined.

3.5.2 Torque Calculation in RFT

Because inertia is negligible, the net torque due to the granular force on a portion (e.g. $[x_b,\, 2\pi]$) of the sandfish body about any point of interest x_b is also approximately zero. From this we calculate the internal torque (i.e the torque generated by muscle) at x_b:

$$\begin{aligned}&\vec{\tau}_{\text{muscle}} + \int_{x_b}^{2\pi} \vec{r} \times \vec{f}\,\mathrm{d}s = \dot{\vec{L}} \approx 0 \\ &-\tau_{\text{muscle}} = \tau(x_b, t) \\ &= \int_{x_b}^{2\pi} \left\{(z - x_b) f_y(z,t) - [y(z,t) - y(x_b,t)] f_x(z,t)\right\} \sqrt{1 + y_b'^2}\,\mathrm{d}z.\end{aligned} \tag{3.5}$$

where $\vec{f}$ is the granular force per unit length. We assume the muscle must only overcome torque from resistive forces τ and thus internal passive body forces are small compared to external resistive forces. This assumption was verified in the above *in vivo* bending tests (see Passive Body Properties section above) on an anaesthetized animals and measuring stiffness and damping coefficients at varying rotation rates; we estimated that the maximal torques from elastic (0.094 ± 0.027 N·cm) and damping (0.055 ± 0.034 N·cm) forces are over an order of magnitude smaller than the maximal torque from resistive forces (4.1 N·cm). We also assume the time lag between neural activation and muscle force development is small compared to the sandfish undulation period (≈ 0.5 s). We thus assume activation timing approximately corresponds to "muscle" torque timing. Therefore, we use the sign of τ to predict muscle activation (Figs. 3.6 & 3.7): here positive τ (or negative τ_{muscle}) corresponds to muscle activation on the right side of the body.

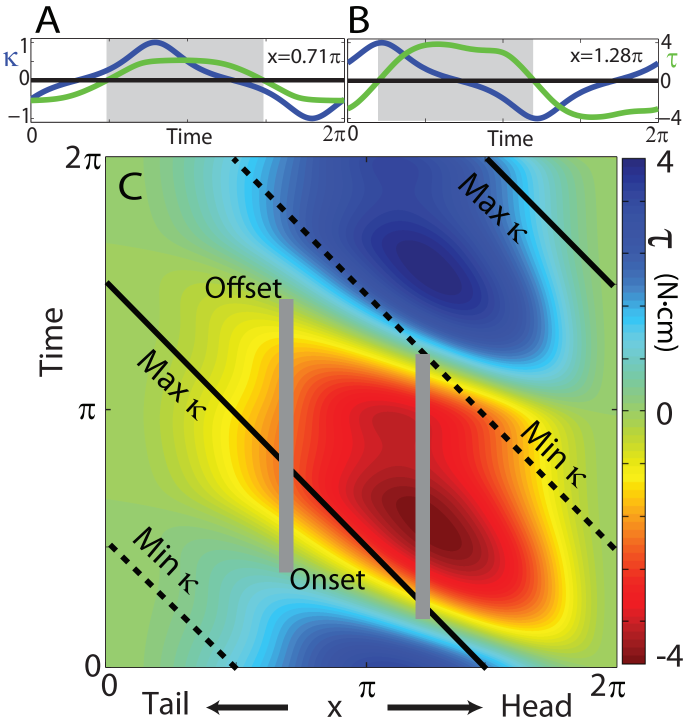

Figure 3.7: Neuromechanical phase lags in the model. (A) & (B) The curvature (blue lines), torque (green lines), and the predicted muscle activation (gray shaded region) from the RFT model at two representative points indicated by black dots in Figure 3.6 and gray vertical lines in (C). (C) Torque as a function of time and position along the body. Gray vertical bars indicate the predicted muscle activation durations at two representative points. Solid and dashed black lines represent the time when the maximal curvature and minimal curvature are reached, respectively.

3.6 Results and Discussion

3.6.1 Experimental and Model Agreement

We find that phase lags between internal torque and curvature in the model can explain the NPL between electromyogram (EMG) and curvature seen in experiments. τ displays a traveling wave pattern and positive τ occurs in a range close to that of measured EMG activation (Figs. 3.7 & 3.8). Without corrections from body passive forces or consideration of muscle physiology or body structure, the average phase difference between the beginning and ending of positive τ in the model compared to EMG onset and offset in experiments is less than 5%, where 2π is the range of possible phase lags. A large portion of the positive torque region overlaps with the region where the curvature decreases (negative $\dot{\kappa}$), but the positive τ region lags the negative $\dot{\kappa}$ region near the head and leads it near the tail. The agreement between experiment and theory is striking, particularly because our model has no fitting parameters; we posit this is largely a consequence of the simple movement and the relatively simple but strong environmental interaction.

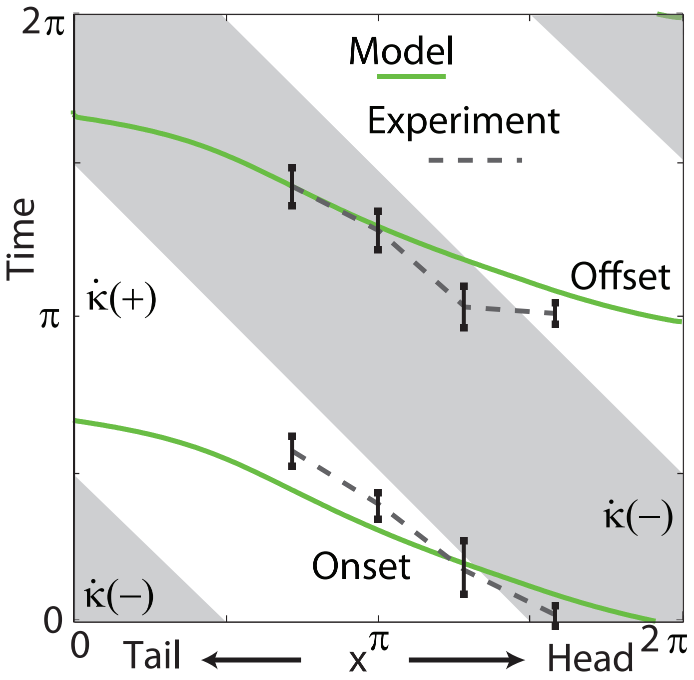

Figure 3.8: The predicted onset and offset of muscle activation from the model (green lines) compared to EMG measurements from the sandfish experiment (black error bars indicates standard deviation, adapted from [34]). Gray areas indicate the periods of negative $\dot{\kappa}$. $A/\lambda = 0.22$ and the model sandfish body is oriented at a downward entry angle of 22 degrees relative to the horizontal. The corresponding positions of the electrodes in the model are approximated based on the curvature phases.

3.6.2 Explaining the NPL

To gain more insight into how the phase lags arise due to torque contributions from different parts of the body, we consider a simplified case where amplitude is small, forward motion is negligible, and the resistive force is viscous. This makes analytical calculation of torque straightforward but does not change the results qualitatively. In this simpler case, the torque from the fore-aft forces is negligible, and only the lateral force (per unit length) $f_y(x,t) = -c\dot{y}(x,t) = -cA\cos(x+t)$ need be considered.

---

*Analytical calculation performed by Yang Ding, see [132] for more details

For simplicity and to separate the effects, we first neglect yaw motion. The torque can be calculated analytically from Equation 3.5: $\tau(x_0,t) = (2\pi - x_0)\sin(t) - \cos(x_0+t) + \cos(t)$. For example, if we take two points $x_1 = \pi$ and $x_2 = \pi - \Delta$ near the middle of the body, we obtain $\tau_1 = 3.7Ac\sin(t+\phi)$ and $\tau_2 = (3.7 + 1.7\Delta)Ac\sin(t + \phi - 0.29\Delta)$, where $\phi = 0.57$. The NPL is still captured since the phase difference between τ_2 and τ_1 is a fraction (0.29) of Δ, the phase difference between κ_1 and κ_2. The torque contribution can be approximately divided into three parts, as follows:

$$\begin{aligned}
\tau_1 &= \int_{x_1}^{2\pi} f_y(z,t)(z-x_1)\,\mathrm{d}z \\
&\approx \underbrace{\delta f_y(x_1,t)\delta/2}_{\text{local}} + \int_{x_1+\delta}^{2\pi-\delta} f_y(z,t)(z-x_1)\,\mathrm{d}z \\
&\quad + \underbrace{\delta f_y(2\pi,t)(2\pi-x_1)}_{\text{head}} \\
\tau_2 &= \int_{x_2}^{2\pi} f_y(z,t)(z-x_2)\,\mathrm{d}z \\
&\approx \underbrace{\delta f_y(x_2,t)\delta/2}_{\text{local}} + \int_{x_2+\delta}^{2\pi-\delta} f_y(z,t)(z-x_2)\,\mathrm{d}z \\
&\quad + \underbrace{\delta f_y(2\pi,t)(2\pi-x_2)}_{\text{head}}
\end{aligned} \tag{3.6}$$

where δ is a small length. The phase difference between the torque contributions from local forces for the two points is Δ, which is the same as the phase difference of other local variables (e.g. κ) on the traveling wave (Fig. 3.9). In contrast, the phase of the torque transmitted from a distant point on the body (e.g. the head) is the same for both points (even though the magnitude differs). This synchronized torque contribution can be thought of as either a standing wave or a traveling wave with infinite speed. Because of the combination of the torques from local and distant forces and the continuous force distribution, the net phase difference between τ_2 and τ_1 is less than Δ and the torque wave speed is greater than the curvature wave speed. A similar analysis can be performed if the integration is done on the posterior side of the body (toward the tail).

The balance of torque on the body leads to an overall yaw motion, whose phase is the same along the body. Superposition of yaw motion and lateral motion of the body results in variation of both the magnitude and phase of the lateral motion along the body in the lab frame (see Fig. 3.12 and derivation in Appendix). However, the overall speed of the lateral displacement in the lab frame is the same as the prescribed lateral displacement (sinusoidal wave) in the body frame. Therefore, the yaw motion only changes the relative phase between the curvature wave and the apparent displacement (or force) wave locally.

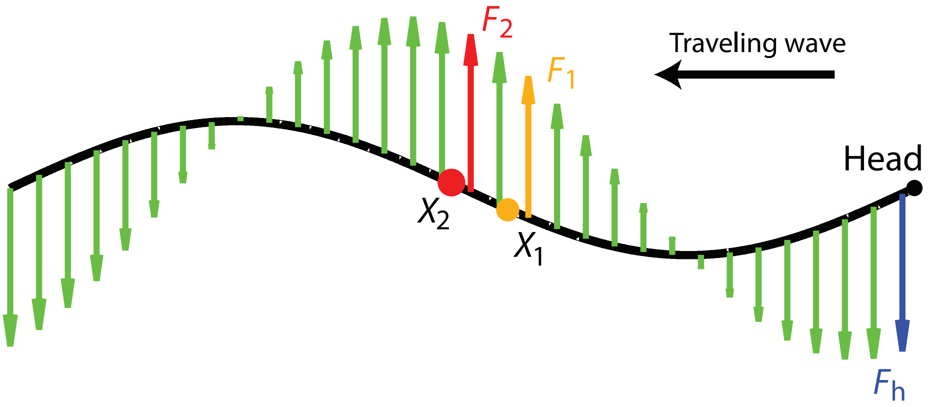

Figure 3.9: Local and distant forces contribute to the torque on two points near the middle of the body. Green arrows represent the forces on the body. The red and orange arrows indicate the force adjacent to x_2 and x_1, respectively. The blue arrow indicates the force at the head (F_h). Note that this is an analysis for a small amplitude case, and the lateral displacement is exaggerated in the figure for visibility.

3.6.3 Predicting NPL Under Other Conditions

Since the only requirement for this mechanism is a traveling wave pattern of force, it predicts the NPL are general for torques from distributed forces. As shown in Figure 3.10A, the localized elastic and damping forces by definition have constant phase differences with the curvature. In accord with previous studies [168,194], our calculations show that the relative phase between the torque from inertial forces and curvature advances in the posterior direction. However, the overall phase of the inertial torque advances by about 0.4π compared to the sandfish EMG phase. The phase lags persist if the granular resistive forces in the model are replaced with viscous resistive forces, which low Reynolds number swimmers like nematodes experience [185].

Although passive body forces are not responsible for the NPL, they can still influence

---

*Calculations performed by Yang Ding, see [132] for more details the observed pattern. For example, we find that the inclusion of viscous forces in the body shifts the phase of the torque in granular media toward the phase pattern produced from only viscous forces (dash-dotted red lines in Fig. 3.10a). That is, the phase difference between the torque and $\dot{\kappa}$ is smaller and the torque wave speed is smaller, in accord with previous studies in fluids [144, 193]. This suggests that the small internal viscous forces within the body may partially account for the phase differences we observe between the torque from resistive forces and EMG. For swimming in a high Reynolds number fluid, the muscle activation duration is in general smaller than those observed for the sandfish (≈ 0.5) [169]. Previous studies (e.g. [193]) suggest that the torque from external forces may be overcome by passive elements of the body. The nearly 0.5 duty factor of the muscle is evidence that resistive forces dominate in a granular environment and the slight decrease of the duty factor (a relatively larger decrease is typical during swimming in fluids [169]) implies passive forces play a small role for swimming of the sandfish.

Variations of locomotor kinematics also affect the timing of the torque (Fig. 3.10, B). For example, a downward entry angle (observed in the animal experiments [34]) advances the phase of the torque compared to the horizontal swimming case. This is because when the body is oriented downward, the head, which has a more advanced phase, contributes more to the overall torque due to the head's greater depth and correspondingly larger resistive forces. Also, a larger number of periods (longer body and smaller ratio of wave length to body length) both delays the phase of torque and reduces the torque wave speed. The phase shift is due to the contribution of the extra tail length, where the phase of the force lags that at anterior positions. The effect of period (body length) can be used to estimate the error in timing that may occur due to neglecting the tail after 1.2 SVL: The error should be a small fraction of the difference between the 1.2-period case and the control case. Further, we found that a smaller undulation amplitude reduced the variation in torque wave speed.

The time delay between EMG activation and force production ([154]) might affect the phase lag timing of EMG activation, but we argue that this delay is small compared to the typical period of undulation for the sandfish (minimum possible latency is $\approx$2 ms compared to $\approx$500 ms undulation period). If the time delay was significant and approximately

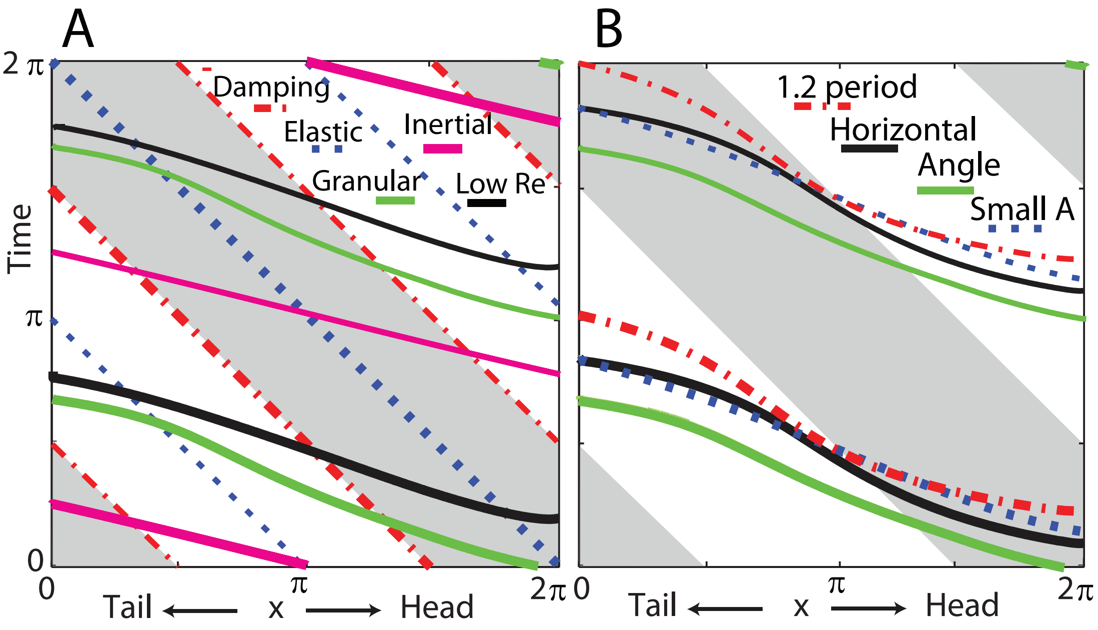

Figure 3.10: NPL for varying model parameters. (A) The starting (slightly thicker lines) and ending of positive torque generated by granular force (solid green lines), viscous fluid force (solid black lines), inertial force (solid magenta lines), damping force (dash-dotted red lines), and elastic force from the body (dotted blue lines). (B) The beginning and ending of positive torque when the model sandfish swims in a horizontal plane (solid black line, control case), at an entry angle of 22 degrees (solid green line), at a small amplitude $A/\lambda = 0.05$ (dotted blue line) , and with a 1.2 periods of wave on its body (dash-dotted red line). We aligned the head for the 1.2 period case and only the anterior portion (1 period of the wave) is shown in the figure. Gray areas indicate negative $\dot{\kappa}$.

constant, the EMG-curvature phase relation would change for different frequencies.

3.7 Conclusions

We developed a theory to explain the basic control signals needed to generate a particular undulatory movement pattern in a sand-swimming lizard. We abstracted the nervous/musculoskeletal system by assuming that passive body forces are small (which experiments reveal may be a valid assumption) and that internal torque is synchronized with neural activation timing; this abstraction revealed that the NPL is intrinsic to undulatory locomotion provided that distributed forces, such as resistive or inertial forces, play major roles. For undulatory locomotion in other environments, the principle of the simultaneous response to distant torques should also apply, though quantities such as the phase of the force will differ from the sandfish case. Building on this principle could help future studies explain other variations of the NPL.

Because we now have a system in which experiment and theory are in quantitative agreement, we can begin to develop more detailed models (i.e. anchors [148])which answer specific questions about nervous system control, muscle configuration, morphology, etc. For example, it has been established that the intersegmental coordination of neural oscillators along the body of swimmers is influenced by sensory feedback ([122]). Detailed models of central pattern generators (CPGs), sensory neurons and muscles can be used to understand how external torque and neural activation interact so that the intersegmental phase lags produce *single period* sinusoidal motion. As such, a hierarchy of anchors can be used to generate testable hypotheses and understand actuation timing for animals in a variety of environments.

More broadly, we have demonstrated that the seemingly specific and peculiar sand-swimming behavior could be an excellent system in which to develop quantitative models of neuromechanics. Due to relatively simple but dominant environmental interactions, the neuromechanical control pattern is greatly constrained by the environment. In addition, the granular RFT provides an excellent model for interaction with the substrate; this is in contrast to locomotion in true fluids in which more complex theories [198] are needed to quantitatively compare experiment and model. We hypothesize that by studying subarenaceous animals within dry and saturated granular substrates (like those on the bottom of the ocean floor), animal models with potentially fewer parameters can be analyzed in detail. This in turn can help provide guidance for the design and control of artificial undulatory locomotors in complex environments [199–201]. Better physical models can also improve our understanding of the biological systems.

3.8 Appendix

3.8.1 The Empirical Granular Force Laws in the Resistive Force Theory

To obtain the empirical force relationships for the forces acting on the sandfish, we dragged a stainless steel cylinder (radius = r =1.58 cm and length= l = 4 cm) in 0.3 mm glass beads at a constant velocity (10 cm/s) and measured the resulting perpendicular and parallel forces for angles ψ between the element and its displacement direction 3.11. The perpendicular $F_\perp$ and parallel $F_{||}$ components of the force on the cylindrical surface of the rod as a function of ψ are approximated as

$$\begin{aligned} F_\perp &= 2lr(C_s \sin\beta_0 + C_F \sin\psi) \\ F_{||} &= 2lrC_F \cos\psi, \end{aligned} \tag{3.7}$$

where $\tan\beta_0 = \cot\gamma_0 \sin\psi$, $C_S = 0.51\mathrm{N/m}^2{\times}10^{-4}$, $C_S = 0.28\mathrm{N/m}^2{\times}10^{-4}$, and $\gamma_0 = 13.84°$. See [11] for details of the empirical force laws.

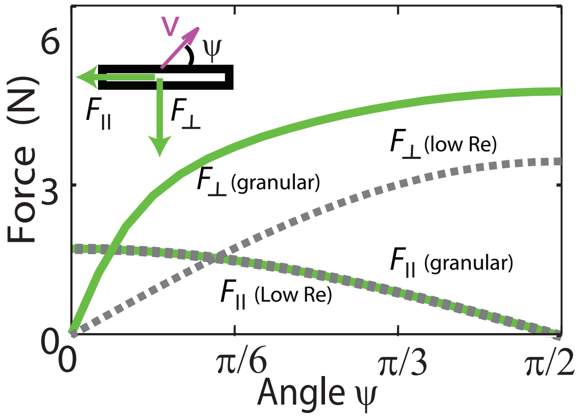

Figure 3.11: The empirical force laws used in the RFT model (adapted from [11]). Green solid lines represent the perpendicular ($F_\perp$) and parallel ($F_{||}$) components of the force. Dashed gray lines correspond to $F_\perp$ and $F_{||}$ calculated for an infinitely long slender ellipsoids in a low Re fluid by choosing a velocity that fits $F_{||}$ vs. ψ.

3.8.2 Small Amplitude Swimming in a Viscous Fluid

For the small (infinitesimal) amplitude, A, case, $\dot{x}_{\mathrm{CoM}} \to 0$ because previous studies (e.g. ref [133]) showed $\dot{x}_{\mathrm{CoM}} \propto A^2$ for swimming in a viscous fluid. Due to the symmetry of a sinusoidal wave in the lateral direction, $F_{\mathrm{net,y}} = 0$ and $\dot{y}_{\mathrm{CoM}} = 0$. The contribution to forward motion from small rotations is negligible, therefore the lateral position and velocity of the body in lab frame can be simplified as

$$\begin{aligned} y(x,t) &= (x-\pi)\theta + A\sin(x+t) \\ v_y(x,t) &= \dot{y}(x,t) = A\cos(x+t) + \dot{\theta}(t)(x-\pi), \end{aligned} \tag{3.8}$$

Using viscous resistive forces, the torque balance equation in Equation 2 (in the main text) becomes

$$\begin{aligned} &\tau_{\text{net}}(t) = 0 \\ &\int_0^{2\pi} -\dot{y}(x,t)(x - x_{\text{CoM}})\,\mathrm{d}x = 0 \\ &\theta(t) = \frac{3}{\pi^2} A \cos t \\ \Rightarrow &y(x,t) = A \sin(x+t) + \frac{3}{\pi^2} A \cos t (x - \pi). \end{aligned} \tag{3.9}$$

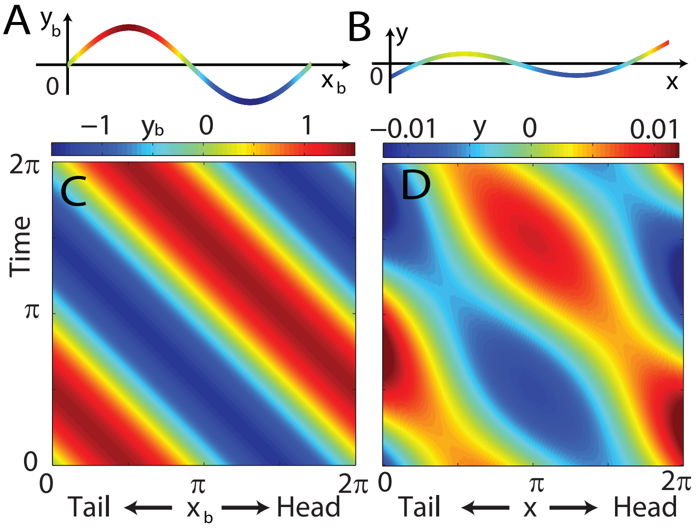

Figure 3.12: The lateral position of the swimmer in its (A) body frame and (B) lab frame. A & C: The position of the model swimmer in the body frame is a traveling sinusoidal wave with $A/\lambda = 0.22$. Color represents lateral displacement y_b. B & D: The position of a swimmer in a viscous fluid in the lab frame. The swimmer uses a sinusoidal wave with a small-amplitude ($A/\lambda = 0.01$ in this example). Color represents lateral displacement y. See Equation S3 for the analytical expression.

3.8.3 Torque from Body Elasticity and Damping Measured Using Bending Apparatus

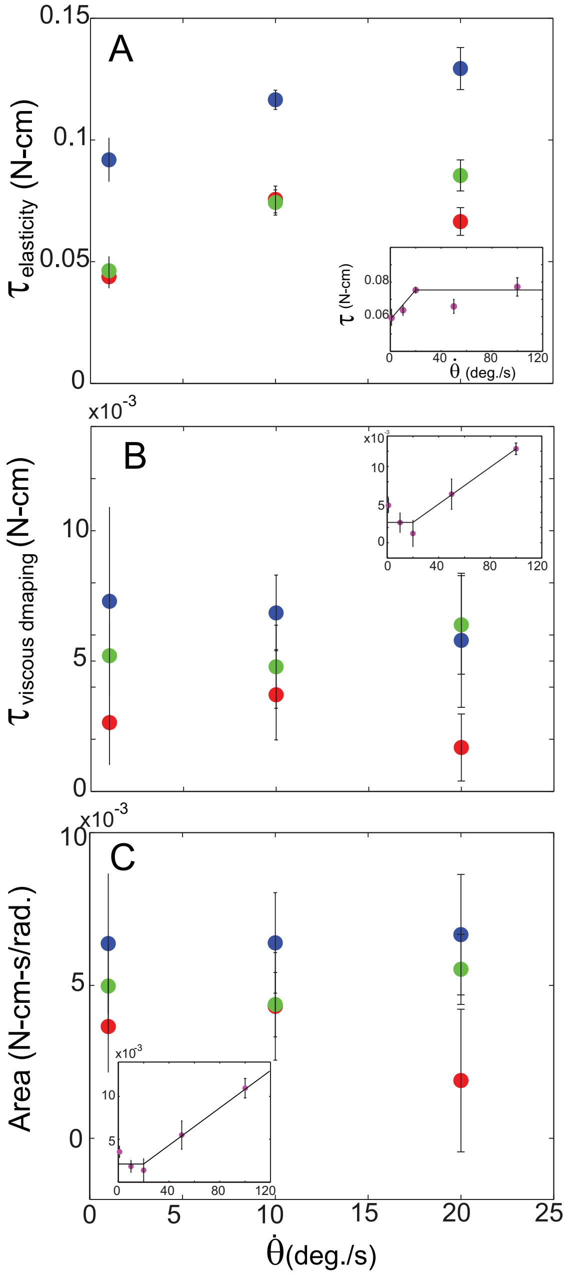

Figure 3.13: Estimated average torque using calculated elasticity and damping coefficients shown for animal 1 (blue), animal 2 (red) and animal 3 (green) (N = 8 trials each). Inset shows trends for experiment at higher speeds (magenta). (A) Torque slightly increases up to 20°/s then plateaus afterward. (B) Torque due to viscous damping remains constant up until 20° and increases afterward. (C) The area contained within the best fit curves between torque and angle is independent of speed before 20°.

3.9 Contributions

Sections 3.5, 3.6, 3.8.1 and 3.8.2 detail work performed by Yang Ding who developed the granular resistive force theory and performed all torque calculations (from RFT and from the small amplitude case). Humaira Taz built the bending apparatus used to measure passive torque vs. body angle. Elizabeth A. Gozal provided the EMG analysis code (SpinalMOD) used to detect onset and offset of EMG. Kurt Wiesenfeld assisted in the development of the analytical expression to calculate internal torques.

CHAPTER IV

LIMB USE IN THE SANDFISH LIZARD DURING RAPID BURIAL

4.1 Summary

Desert dwelling animals like the sandfish lizard (*Scincus scincus*) dive into sand to escape heat and predators. The sandfish swims subsurface using a traveling wave along its body with little limb movement. However, large lateral excursions of the limbs are observed above surface during initial burial into the substrate and burial occurred in approximately 0.5 s (≈2 body undulations). To investigate the role of limbs in burial, we tracked limb and body movements during submergence into 0.3 mm diameter glass particles using high-speed visible-light video and x-ray imaging. The sandfish used a stereotyped limb pattern and body undulation during burial. Just prior to submergence, the forelimbs were pressed against the body sequentially before each side of the body became convex and remained close the flanks during swimming. Approximately a half cycle later, hindlimbs retracted sequentially prior to maximal body convexity and also just before submergence. We hypothesized that since the hindlimbs were the last to retract, these limbs were more important than forelimbs for rapid burial. To test this hypothesis, we examined burial performance while restraining limbs using adhesive tape. Each animal was given 10 minutes to submerge subsurface with limb restraints, and trials were accepted when animals attempted to bury. Animals readily buried when hindlimbs were bound, but took a larger number of undulations (4 ± 2, $P < 0.01$) to submerge than unbound animals. When forelimbs were bound, animals buried in 6 of 14 trials (N = 5 animals) and burial took even longer (4-7.5 undulations). When all limbs were bound, burial occurred in only 1 of 15 trials.

This chapter is a paper in preparation by Sarah S. Sharpe, Andrew Masse, and Daniel I. Goldman

These results demonstrate that appropriately timed limb-ground interactions are critical to facilitate rapid burial.

4.2 Introduction

Desert dwelling animals often bury into the surrounding sand to avoid extreme climate or to conceal themselves from other animals. When moving above surface, the ability to *rapidly* bury can be vital for survival in order to escape predators. This behavior requires displacement of the surrounding grains which are dominated by friction and leads to a large penetration resistance on the animal during submergence. Gans [202] stated that with the exception of some snakes, all limbless tetropods are characterized as shelterers or burrowers in that they hide under loose debris or tunnel into the surrounding media. This may indicate that evolutionarily as reptiles become more inclined for burial and/or have more elongated bodies, limbs become less important. However, many small desert dwelling lizards which rapidly submerge into dry sand possess limbs that are large relative to their body length (such as those of the Genus *Uma* and *Scincus*) and field reports indicate that limbs aid in the burial process [11, 22, 26].

To investigate the role of limbs in rapid burial we study the sandfish, *Scincus scincus*, a sand-specialist lizard that inhabits the dry desert sands of northern Africa [11, 22, 70]. Sandfish have long fore- and hindlimbs (≈20% and ≈24% of their body length, respectively, measured from the body origin to the tip of the longest toe, Fig. 4.1) and they use these limbs to run rapidly of the surface. Sandfish also readily dive into granular media. They fully submerge in less than 0.5 s (≈2 body undulations). Sandfish move subsurface using large amplitude waves of body undulations that propagate from head to tail. A previous study which used x-ray imaging [11] revealed that the distance between limbs decreased during burial and remained small during subsurface swimming. However, little is known about how the limbs function during the burial process, or if they are necessary for submergence.

Recent work showed that an undulating ‘sandfish-like’ robot without limbs can swim downward into sand using propulsion from body undulations and by generating negative lift force with a downward tilted head [105]. However, burial was slow and took more than

5 body undulations for 75% of its body to submerge. We predict that limbs are important to facilitate the *rapid* submergence achieved by the sandfish during burial. Our objective in this chapter is to (1) characterize limb timing and kinematics during burial relative to body bending and submersion depth and (2) tease apart the relative contribution of the limbs by constraining limb movement.

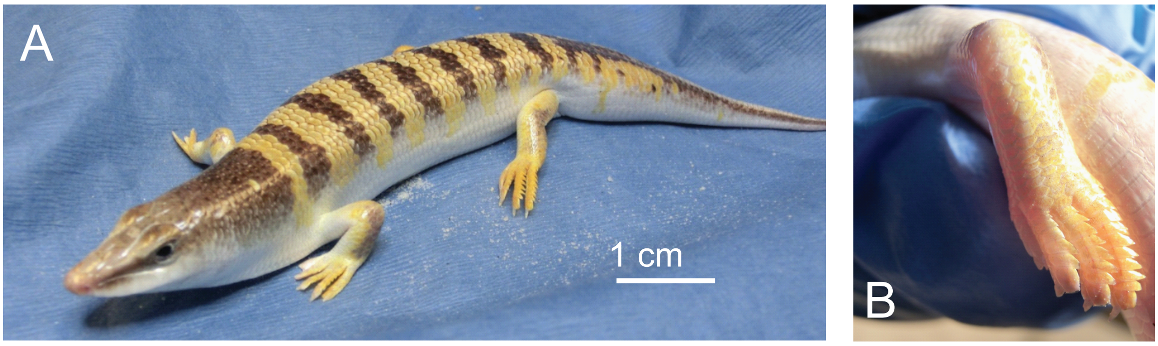

Figure 4.1: Sandfish have large limbs relative to their body size. (A) Sandfish and (B) zoomed in picture of the limbs showing paddle-like feet with toe fringes.

4.3 Material and Methods

Sandfish lizards, *Scincus scincus*, were purchased from a commercial vendor (LLL Reptile, Vista, CA, USA). Two animals were used to characterize normal burial patterns (Animal 1: n = 3 trials; Animal 2: n = 5 trials; see Table 4.1 for body length and mass). Five animals were used in the limb restraint study (Animal 1 - 5; Table 4.1) and at least 12 trials were analyzed for each binding condition. All animals were housed individually in large containers ($21 \times 43 \times 28$ cm^3) filled with sand to a depth of ≈ 15 cm. Animals were given mealworms coated in a supplemental calcium powder and allowed to eat *ad libitum*. The holding room was maintained on a 12h:12h light:dark cycle and the average temperature was 28°C during the day and 24°C during the night. Animals were provided with a heat lamp and a water dish to facilitate thermoregulation. All experimental procedures were conducted in accordance with the Georgia Institute of Technology IACUC protocol number (A11066) and Radiation Safety protocol (X-272).

Table 4.1: Sandfish length and mass

Sandfish #	SVL (cm)	STL (cm)	Mass (g)
1*	8.6	14.5	16
2*	8.7	13.8	14
3	9.5	14.5	16
4	10	15.5	18
5	10	15	17.1

* animals used in limb pattern characterization
SVL: snout-vent length, STL: snout-tail length

4.3.1 Burial Characterization

X-ray imaging (OEC 9000, Radiological Imaging Systems, Hamburg, PA, USA) and high-speed above surface video (AOS Technologies AG X-PRI, Baden Daettwil, Switzerland) were used to characterize the burial strategy in the sandfish. Both above surface and subsurface videos were recorded at 250 frames per second (fps). The x-ray was set to 85 kV and 20 mA and oriented with the horizontal plane (capturing the dorsal view of the sandfish during burial). For enhanced contrast in x-ray recordings, 10 small opaque lead markers ($\approx 1\ mm^2$ each, mass $\approx$ 0.01 g) were bonded to the sandfish midline at 0.1 SVL increments and two markers were bonded on each limb (Fig. 4.3, black squares). On the fore-/hindlimbs, one marker was placed halfway between the shoulder/hip joint and elbow/knee joint (proximal limb marker) and one marker was placed halfway between the elbow/knee joint and wrist/ankle joint (distal marker).

An air-fluidized bed (Fig. 2.1, B) filled with spherical glass particles (diameter = 0.27 ± 0.04 mm and density = 2.5 g/cm^3) was used to create repeatable loosely packed compactions. The size of the bed was 22.9 × 40.6 cm^2 and was filled with granular media to a height of 10 cm. An air flow created a fluidized state and a slow decrease in air flow to zero resulted in a loosely packed state ($\phi \approx 0.58$, where ϕ is the ratio of the volume of particles to the volume of occupied space).

Sandfish were placed on top of the prepared sand, unlike previous studies (in Chapter 2 or [34]) in which sandfish ran from a hard platform into the granular bed. Sandfish were placed away from the walls to prevent any interaction between limbs or body with a hard surface in order to replicate burial conditions more likely to occur in nature. The beginning of 'burial' was defined as the moment when a sandfish placed its snout into the granular media and began continuously moving. A stepping diagram was constructed by identifying protraction phases, when the limb moved in the anterior direction relative to the body, and retraction phases, when the limb moved in the posterior direction relative to the body (Fig. 4.2). The stepping diagram was shifted to compare timing across all trials by aligning the submergence time of the 0.3 SVL and 0.8 SVL markers; these markers were used because they were closest to the pectoral and pelvic girdle, respectively. Animals usually took 1-3 strides before submerging into the substrate.

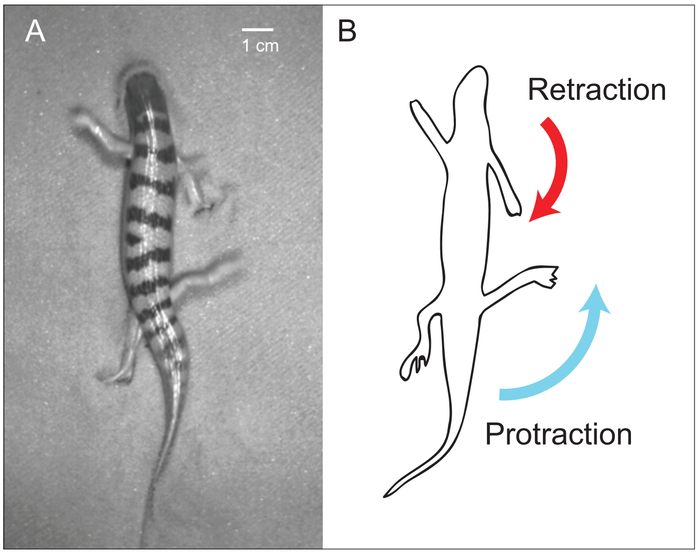

Figure 4.2: Characterization of limb movement. (A) Picture of a sandfish lizard during initial burial into 0.3 mm diameter glass particles. (B) Diagram explaining stepping characterization. During retraction (red arrow), limbs move in the posterior direction relative to the body, and during protraction (cyan arrow) limbs move in the anterior direction relative to the body.

To quantify above and below surface limb movement, the angles between limbs were measured with respect to the nearest local body segment (see Fig. 4.3). The vector connecting the proximal and distal markers on each limb was compared to the vector connecting the 0.3 SVL and 0.4 SVL markers for forelimbs, or 0.8 SVL and 0.9 SVL markers for hindlimbs. Body angle for a particular location was defined as the angle between the vectors connecting consecutive body markers (Fig. 4.3).

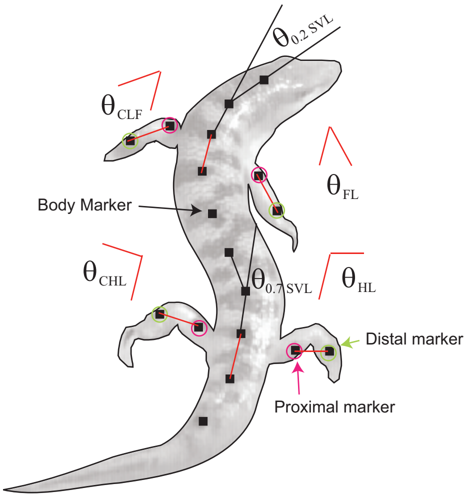

Figure 4.3: Diagram showing how body bending angles and limb angles were measured using marker locations. The angle between consecutive markers at 0.1 SVL locations were used to characterize body bending. Limb angles were quantified by comparing the vector connecting limb markers and the vector between the nearest consecutive body markers.

The fore-aft velocity (the velocity in the forward direction of movement) and the lateral velocity (the velocity in the direction perpendicular to forward movement) at the 0.3 and 0.8 SVL location were compared to the velocities of the distal markers on fore- and hindlimbs, respectively. The average speed of the distal marker on the limbs during retraction was computed for all animal trials to investigate if limbs were 'paddling' backward or stationary during burial.

4.3.2 Restrained Limb Experiments

To examine how limbs aid in submergence into granular media, sandfish burials were recorded for 5 different conditions (N=5 animals; Table 4.1): (1) no limb bindings (NB) in which animals buried into the media under normal conditions (n= 12 trials), (2) control (CONT) in which animals had tape wrapped around two body locations but limbs were not restrained (n = 15; Fig. 4.4, B), (3) hindlimbs were bound (HB) with restraints (n = 15), (4) forelimbs were bound (FB) with restraints (n = 14), and (5) all limbs were bound (AB) with restraints (n = 14; Fig. 4.4, A). Limbs were restrained using blue painter's tape (3M Scotch Blue, St. Paul, MN, USA). Tape was chosen because tying limbs together did not prevent all limb movement and foot ground interactions. Also, the blue painter's tape was relatively easy to place on the sandfish's body and could be removed with minimal animal distress.

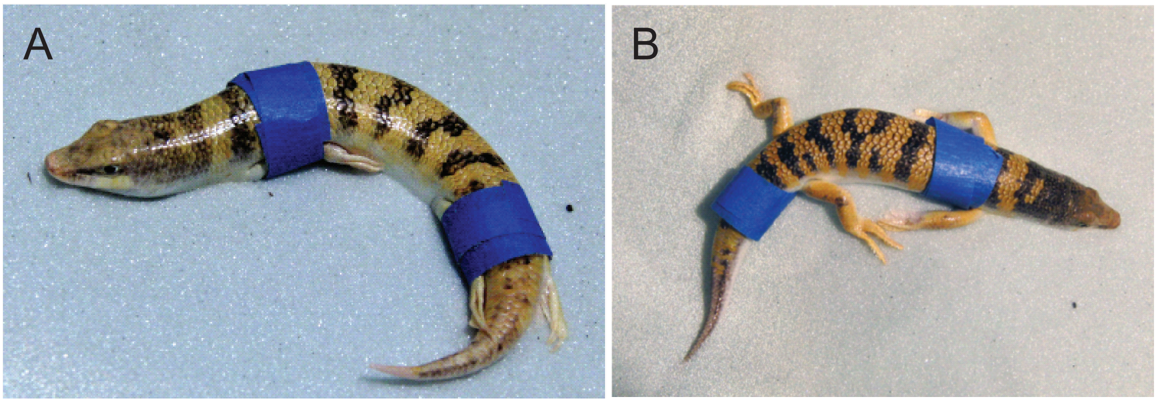

Figure 4.4: Restraints used to modified limb use during sandfish burial. Image of the sandfish with (A) all limbs bound and (B) no limbs bound, but with tape used as a control.

Each animal was placed on the surface of as-poured media ($\phi \approx 0.605$) away from walls and given 10 minutes to bury. If the sandfish did not immediately attempt to bury, then burial was initiated by light tail-squeezing or tapping. Burial initiation was defined as the moment when the sandfish placed its snout into the media and began undulating its body. The end of burial was defined as the moment when 1.2 snout-vent length (SVL) of the sandfish was underneath the substrate. The time duration and number of body undulations the sandfish used from burial start to finish was recorded for all successful submergences. The burial success rate for each condition was quantified as the ratio of the number of trials in which the animals submerged within the media to the total number of trials in which animals attempted to bury.

4.3.3 RFT Analysis

Granular resistive force theory (RFT) is a technique that has been used to explain features of sand-swimming (see [7, 11] and Chapter 1, RFT section for more details). Previous RFT studies that used a simplified model of the sandfish body kinematics (without limbs) coupled to an empirically based model of the environment, reproduced the wave efficiency (η; ratio of forward speed to the speed of the traveling wave) of the swimming sandfish. Here we used RFT to predict the wave efficiency of sandfish when a proportion of the body interacted with the modeled granular media. The modeled sandfish was assumed to have a uniform body, blunt head, and moved in 0.3 mm diameter glass particles. The swimmer was constrained to move in a horizontal plane at a depth of 4 cm. Forward locomotion occurred when the forward thrust from body segments exceeded the drag on the body segments and head. The forward speed of the body was obtained from the balance of thrust and drag in the forward direction. To simulate a proportion of body interaction, forces were integrated from the head to a percentage of the body length. η was calculated as a function of body proportion (where 0.5 indicates that forces were summed from the head to half of the body length, and 1 indicates that forces were summed across the entire body). This simulation provides insight into how much of the body must be submerged within granular media such that body-medium interactions alone are sufficient to generate forward locomotion without additional thrust from limbs.

4.4 Results

4.4.1 Limb Use During Normal Burial

All sandfish readily buried into the granular media after being placed on the surface of the substrate. During burial, the sandfish used a diagonal gait, in which the forelimb and contralateral hindlimb retracted and protracted at a similar phase in the cycle. During burial, a small-amplitude (body angle $\approx 20°$) wave of body undulation propagated from head to tail (Fig. 4.5, D). This wave increased in amplitude after submergence. Prior to submergence, the maximum limb angle was large ($\approx$120°) relative to the local body orientation. Afterward, limbs retracted and remained close to the body. The time at which each limb retracted (and remained retracted) for a representative trial is shown in Figure 4.5D by the white squares. This final retraction occurred in a stereotyped way for nearly all trials. The first forelimb would retract approximately 1/2 cycle before submergence, and the contralateral forelimb would retract 1/2 cycle later (during or just before submergence). During this time, hindlimbs underwent one more cycle of protraction. 1/2 cycle after the contralateral forelimb retracted, the final retraction of the contralateral hindlimb occured. Next, the ipsilateral hindlimb retracted 1/2 cycle later (again, during or just prior to submergence).

The average time separating the final limb retractions did not differ significantly (ANOVA, $F(2, 19) = 1.5, P > 0.05$) between limbs and was about 0.13 ± 0.03 s (where the undulation frequency was $\approx$ 4 Hz). Each limb retracted before their respective side of the body was maximally convex and the moment of final limb retraction occurred most commonly when the local body angle was small (typically $<15°$ except for the contralateral hindlimb (CHL) in which the body angle was slightly larger; see Fig. 4.5, B). After submergence, the limb angle of excursion oscillated between 0 and 40°. The maximum deviation occurred when the local body curvature was high indicating that subsurface limb movements might be passive.

Protraction and retraction times relative to submergence of the 0.3 SVL and 0.8 SVL marker are shown in Figure 4.6. In 7 of the 8 trials, time was scaled in order to align the submergence events across all trials (see Material and Methods). For the one trial that was not scaled, the time in seconds is shown in parenthesis. The average time between burial of the 0.3 SVL and 0.8 SVL marker was 0.27 ± 0.09 s and therefore the scaling was small between trials. Furthermore, animals would experience similar resistive forces upon entry for these different speeds due to the rate insensitive force response of the granular media. For all except one run, there was a gradual change in limb use. Both hindlimbs underwent one more cycle of protraction and retraction after the final retraction of the forelimbs. For the one run that did not follow this pattern, only 1 hindlimb went through an additional stepping cycle (i.e. the forelimb and contralateral hindlimb final retraction occurred at the same time). The mean and standard deviation of the times at which protraction and retraction started and stopped relative to submergence is shown in Figure 4.6. After the snout contacted the medium, the first forelimb protracted and retracted only once before submergence. It should be noted that the last ‘step’ taken by the ipsilateral hindlimb had a maximum angle of excursion that was similar to the maximum angle during subsurface swimming. However, from above surface video it was clear that this limb was actively protracted.

The position and speed of the distal markers on the fore- and hindlimbs were compared to the position and speed of the 0.3 SVL and 0.8 SVL markers, respectively (Fig. 4.7).

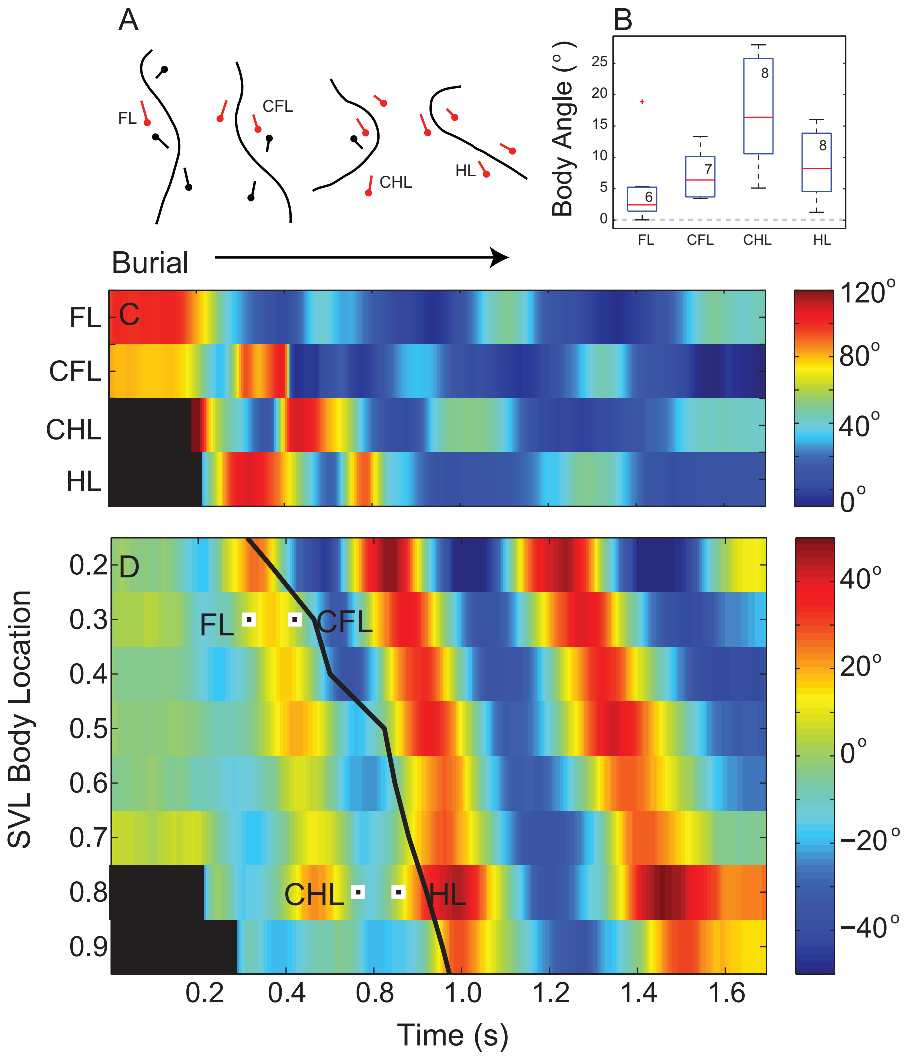

Figure 4.5: Limb and body angles for a representative trial during burial. (A) Sandfish midlines and limb vectors are shown at the moment when each limb retracted and remained retracted (time at which this occurs is shown in D). FL refers to the first forelimb that retracts, CFL is the contralateral forelimb, CHL is the contralateral hindlimb, and HL is the ipsilateral hindlimb. (B) Box plot showing median values of the local body angles (at 0.3 SVL for forelimbs and 0.8 SVL for hindlimbs) when final limb retraction occurs. The number in the top-right corner of the box shows the number of trials considered for each limb. (C) The angle between the limbs and the local body vector (see Fig. 4.3 for diagram) during burial and subsurface movement where the color corresponds to the magnitude of the angle (0° is dark blue and 120° is dark red). Black boxes indicate the time duration in which the limbs were not visible in the video. (D) The angle of the the body relative to consecutive markers for varying SVL locations and time during burial, where color corresponds to the angle (-50° is dark blue and 50° is dark red). Black boxes indicate that markers were not visible. Black lines connect the time at which that body location becomes submerged in the granular media. White boxes with black points show the moment of final limb retraction.

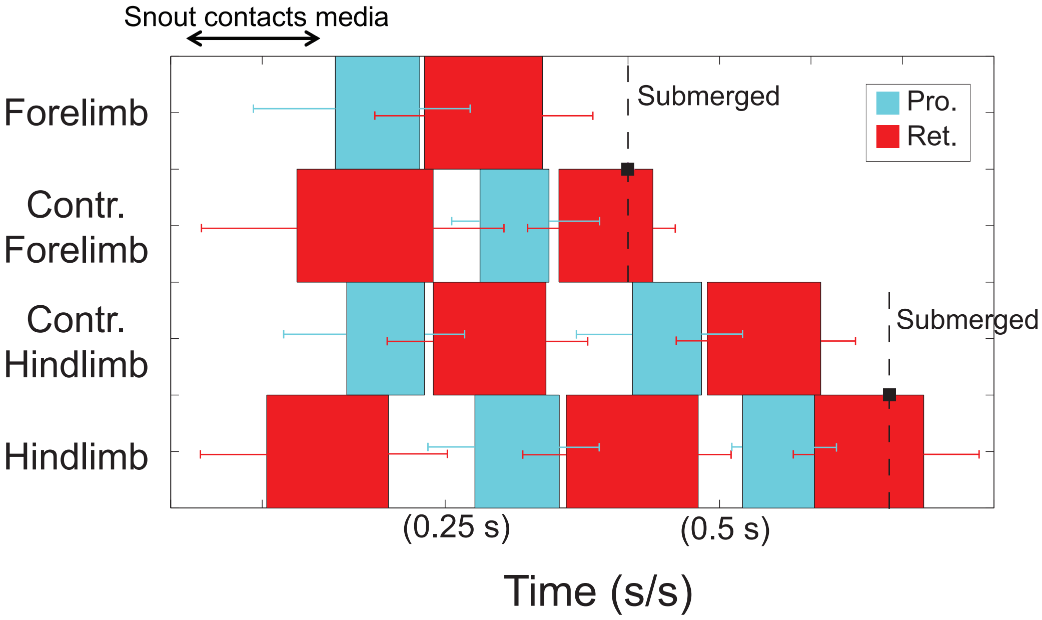

Figure 4.6: Stepping diagram showing the pattern of protraction and retraction during burial. Dotted vertical lines show the times at which the 0.3 SVL marker location submerged (top line) and the 0.8 SVL marker location submerged (bottom line). Time is scaled for 7 of 8 trials, but for the 1 unscaled trial, time in seconds is shown in parenthesis. The protraction time duration is shown by the cyan boxes and retraction is shown by the red boxes. Horizontal error bars show the standard deviation of the start and stop time of the protraction and retraction phases. In 7 out of the 8 runs, both hindlimbs stepped 1 more time before being placed near the animal's sides.

During retraction (red curves in Fig. 4.7, A), the hindlimbs moved toward the body midline and backward. The forelimbs had a similar pattern. The average speed of the limbs during retraction was 16 cm/s (Fig. 4.7, B) and did not differ significantly across different limbs (ANOVA, $F(7, 38) = 2.1, P = 0.12$). This indicates that limbs paddled backward within the media during thrust generation. The lateral velocity of the limbs during retraction and protraction was similar to the lateral velocity of the body (Fig. 4.7, C, D, G, & H). However, the fore-aft velocity of the limbs differed during retraction and protraction, compared to the body fore-aft velocity (Fig. 4.7, E, F, I, & J). After burial, the fore-aft velocity of the limbs was comparable to the body velocity.

4.4.2 Restraining Limb Use

All sandfish attempted to bury into media within the 10 minute time interval with or without limb restraints. For the control and hindlimbs bound condition, animals readily

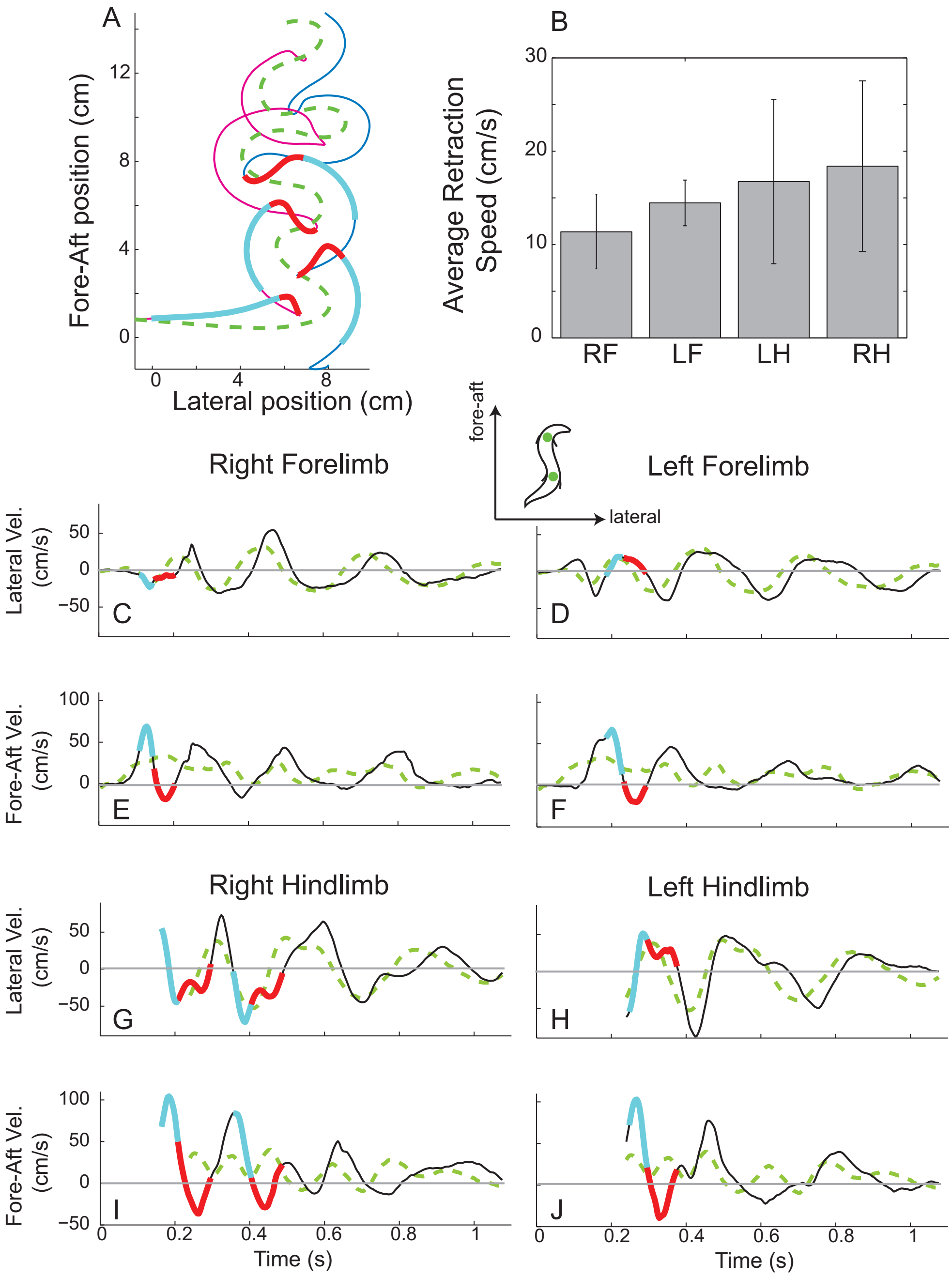

Figure 4.7: Velocity of limbs and body during burial. (A) Tracked position of the 0.8 SVL marker (green dashed curve), right hindlimb distal marker (blue curve) and left hindlimb distal marker (magenta curve) during burial. The larger red curve shows when limbs are protracting (cyan) and retracting (red). (B) Average speed of limbs during retraction. (C-J) Fore-aft and lateral velocity of each distal limb marker (black) compared to the velocity of the nearest body position (green dashed curve). The portion of the limb velocity that is highlighted by cyan and red indicates when that limb was protracting and retracting, respectively.

buried (Fig. 4.8, B). For the control condition, the number of body undulations the animal took to fully submerge was similar to the unbound condition (1.9 ± 0.5 and 1.9 ± 0.4, respectively; Fig. 4.8, D) but the undulation frequency was lower causing an overall higher burial time for the control compared to the natural condition (1.4 ± 0.3 s and 0.5 ± 0.2 s, respectively; Fig. 4.8, C). For the hindlimbs bound condition, animals took 4 ± 2 undulation cycles to bury, where the median burial time was 1.2 s, the shortest burial was 0.5 s, and the longest burial was 5.7 s.

The ability to bury was hindered when forelimbs were bound. Successful burial occurred in only 6 of the 14 trials analyzed. These successful burials occurred in 3 of the 5 animals tested, where 2 of the sandfish were never able to bury with forelimb restraints. Typically when forelimbs were bound, sandfish would attempt to bury, pause, then continue the burial process. Therefore, we were only able to record the entire burial process in 3 of the 6 successful trials (where the recording buffer was $\approx$ 39 seconds). For these 3 runs in which sandfish did not pause, the number of undulation cycles the animals took to fully submerge were 4, 5, and 7.5 and the time to burial was 2 s, 2.8 s and 4.5 s, respectively.

When all limbs were bound, only 1 successful burial occurred out of the 15 trials analyzed. During this burial the sandfish continually undulated, paused, then restarted undulation. Therefore the total burial time and number of undulations were not captured on the video.

4.5 Discussion

4.5.1 Limb Use During Burial

During initial burial, the sandfish used a diagonal gait with large angular excursions of the limbs and a smaller amplitude body undulation. There was a graded shift in limb use during burial, where forelimbs were the first to be placed by the sides followed by the hindlimbs. A similar transition between walking and swimming has been observed in the salamander [147, 203]. Like the sandfish, salamanders use a diagonal gait while walking on ground and use traveling wave axial undulations while swimming in water with the limbs held by its sides. Previous studies [204] have modeled the gait transition of salamanders by coupling limb and

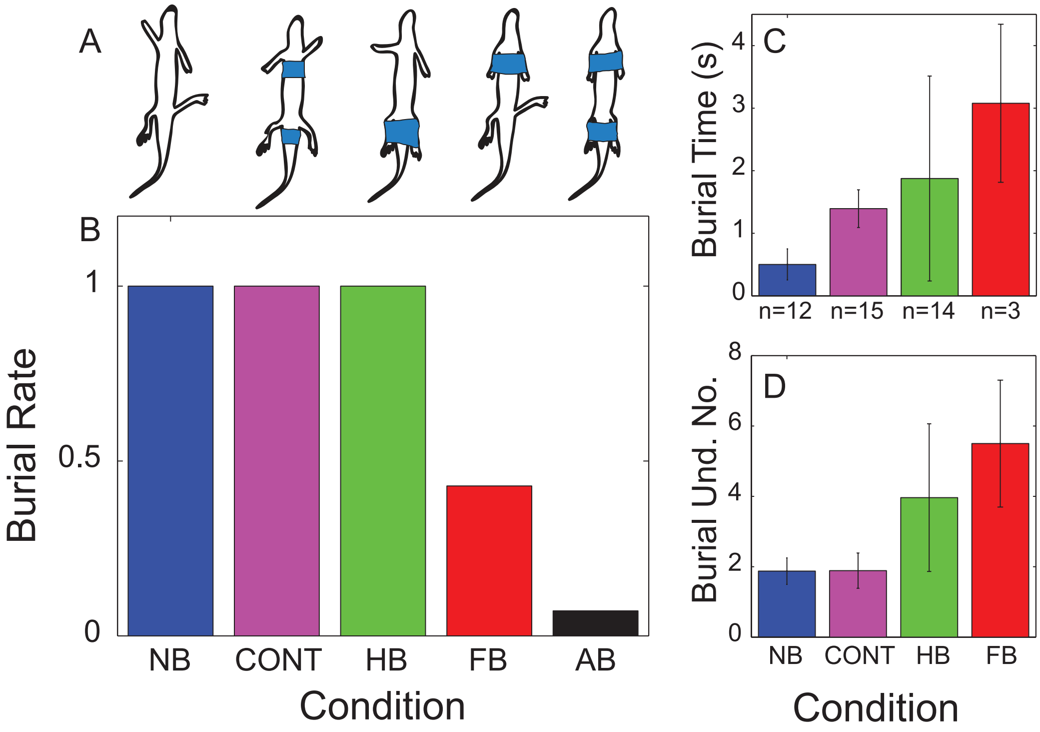

Figure 4.8: Burial ability with restraints. (A) Diagram of binding conditions. (B) Burial success rate for different limb binding conditions. (C) Time from the start of burial (moment when the snout contacted the media) to final submergence (>75% of body was covered by the media) for all successful burials. The number of trials are shown at the bottom of each bar (and also apply for D). (D) The number of burial undulations from the start of burial to final submergence. Error bars show ± s. d.

body central pattern generators (CPGs) based on electrophysiology studies [205] and have reproduced the swimming and walking kinematics observed in experiments [204]. In these models, a central drive produces a walking gait until a threshold is reached, beyond which there is an abrupt switch to a swimming pattern. This abrupt switch may not be reflective of the change between gaits that sometimes occur during gait transition [206]. Ashley-Ross [203] found that when California newts (*Taricha torosa*), a type of salamander, moved down a ramp into water the forelimbs were the first to lose contact with the surface and, therefore, the first to be placed by its sides. Meanwhile, the hindlimbs underwent one more cycle of protraction and retraction before being placed by its sides. The similarity between the limb-use transition in the salamander and sandfish may imply that the neural network couplings are similar between these two diverse species. Neural models that incorporate this gradual shift may help reproduce the sandfish and salamander kinematics during the gait transition.

Although limbs were held near the body during sandfish subsurface swimming, we cannot be certain that the sandfish was not activating limb muscles below ground since EMGs were not recorded. It is possible that sandfish are (1) activating muscles to hold limbs near their sides during swimming, (2) activating muscles but the torques generated at the joints are too low to overcome the resistance from the material causing smaller angular excursions, or (3) not activating muscles. It is interesting to note that many types of skinks use body undulations and hold limbs by their flanks when moving through closely packed objects such as when navigating through grass, rocks or other debris [22]. For example, the ocellated skink (*Chalcides ocellatus*) holds it hindlimbs near its sides well before it submerges into a granular medium (see Chapter 5). In the ocellated skink this appears to be an active process as hindlimb deviation from the body is small during subsurface swimming. Furthermore, the widespread use of this kinematic pattern by skinks in certain environments could suggest that a common ancestor of the Scincidae family may have used this locomotion mode. Therefore, this locomotor pattern could be an exaptation that skinks use under certain environmental pressures [22]. However, during subsurface movement, sandfish limbs deviated from the body midline direction by approximately 40°. This large angle of excursion may indicate that sandfish are not actively holding the limbs by its body. In addition, this maximum angular excursion occurred when the body was maximally concave. Because of the timing with body position, this movement could be due to the passive interactions with the granular medium. On occasion we noticed that when sandfish stopped swimming, a hindlimb would continue to protract. This may be a mechanism the sandfish uses to gain additional thrust upon restarting from a stopped position and indicates that the sandfish is capable of moving limbs forward while submerged in the granular substrate. Future studies which use EMG to measure neural activation could provide further insight into how limbs are actively used during above surface walking, burial and subsurface swimming. From kinematic data alone, it is clear that there is a transition in limb use that occurs near body submergence.

4.5.2 Restraining Limb Movement

Surprisingly, binding forelimbs had a greater effect on burial performance than hindlimb bindings. This was unexpected because forelimbs were placed toward the sides when 30% of the SVL was submerged while hindlimbs were placed near the body when 80% of the SVL was covered by granular media. This may indicate that additional thrust from forelimbs is most important during initial stages of burial. In addition, hindlimbs may act in more of a stabilization role.

Some terrestrial tetrapods possess a body plan in which they have well-developed forelimbs but completely lack hindlimbs. This body plan is rare and is only found in 3 lineages of squamates with elongated bodies: the Amphisbaenian of genus *Bipes*, and the Scincidaes of genus *Sirenoscincus* and genus *Jarujinia* [207]. All of these animals are fossorial and found in dry sandy areas. Therefore, this body plan may represent a convergent adaptation for animals that burrow into dry sand. In addition, we found that the ocellated skink, which possesses reduced fore- and hindlimbs, did not use hindlimbs during burial but did use forelimbs (see Chapter 5). Of the squamates, limb reduction has occurred most often in skinks and is typically accompanied by the addition of presacral vertebrae. However, limb reduction is typically more pronounced in the forelimbs of the skinks compared to the hindlimbs. Therefore, the absent hindlimbs in the *Bipes*, *Sirenoscincus*, and *Jarujinia* may represent the exception. However, the elongation of the body may change burial strategy and limb function. A more comprehensive examination of the body plans and burial kinematics of fossorial animals could help reveal how and when limb appendages aid in burial.

Although the presence of tape did not affect burial performance much in the control condition, we suspect that the tape did increase overall drag. It would be interesting to observe the burial ability of sandfish when using a paralytic on the limbs such as lidocaine. Furthermore, we found that when the sandfish had all limbs bound and was near a wall, the sandfish was more capable of burial. We attribute this increase in burial success rate to the additional thrust that the sandfish was able to generate by pushing its body off the wall and compensating for the lack of thrust generated from the limbs. We suspect that with the presence of rocks and other debris in a natural environment, animals may be able to gain more thrust during burial by pushing against these objects.

4.5.3 RFT Predictions

Resistive force theory, RFT, reproduces the wave efficiency (η, forward velocity divided by the velocity of the traveling wave) observed during sandfish subsurface locomotion (i.e. when the entire body is surrounded by the GM). This implies that thrust from limbs is not necessary for efficient subsurface sand-swimming. However, during burial only the anterior portion of the animal is surrounded by the media, whereas the posterior body is on the surface of the GM and has little substrate (or no substrate) to push against during lateral undulations. In collaboration with Yang Ding, we estimated the proportion of the body that must interact with the granular substrate to produce forward locomotion (Fig. 4.9) in a fully submerged animal. This is our first model to predict burial requirement. The body proportion was defined as the ratio between the anterior length of the animal that interacts with the GM to the total body length (or 1.2 SVL on the sandfish). For simplicity, we did not include an angle of entry which would result in different body segments of the animal encountering media with different resistive forces (due to differing depths). We expect that including an angle will decrease the overall η. The RFT revealed that more than 17% of the body must interact with the substrate to produce forward locomotion (i.e. $\eta > 0$). As more of the body interacted with the medium, wave efficiency increased. This analysis indicates that additional thrust is needed when only a small amount of the body interacts with the surrounding substrate. When the animal is submerged to a depth where body undulations are sufficient to produce forward motion but η is low, limb-ground interactions may act to aid in rapid burial by increasing η for a given undulation frequency.

The sandfish have paddle-like feet with toe fringes. Toe fringes occur in many sand-specialist lizards and the function of these fringes is currently unknown. Korff et al. [25] found that removal of toe fringes in *Uma scorparia* did not change running performance on sand. He hypothesized that fringes may aid during other processes, such as during burial. The toe fringes may act to 'expand' the foot area and increase thrust during backward paddling. Sandfish feet are approximately 1×1 cm^2 in area with fringes accounting for

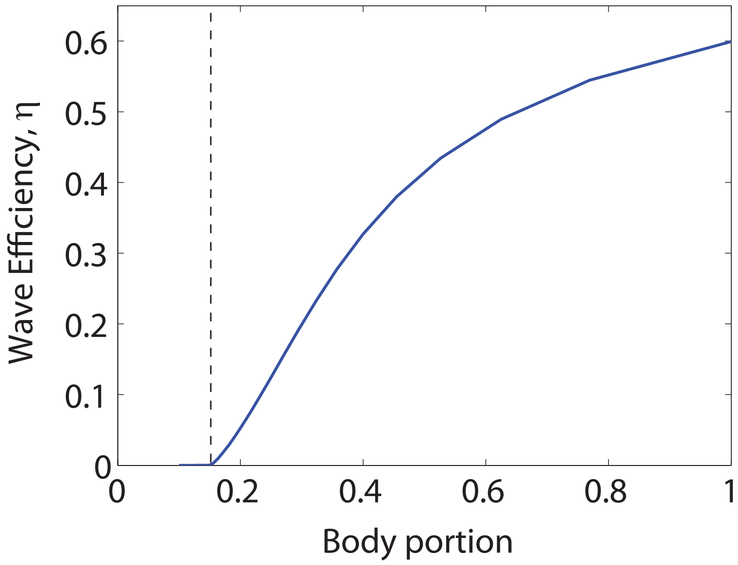

Figure 4.9: RFT estimate of wave efficiency, η as a function of body portion interacting with the granular media. For the RFT, the modeled sandfish swam in a horizontal plane at a depth of 4 cm with $A/\lambda = 0.22$. The forces were summed over the body from the head to a fraction of the body length (where 1 corresponds to integrating all forces from the head to the tail). Although orientation angle and belly drag were not considered, the results give a rough indication of the body proportion that needs to be submerged within the material to produce forward locomotion. In this calculation, forward motion is not possible unless >17% of the body is 'submerged'.

10-20% of that area. From plate drag experiments [208], we estimate that each foot could provide 0.04 N of thrust force. In addition, the limb shank could also provide additional thrust by pushing against the material.

4.6 Conclusions

The sandfish used a rapid burial strategy in which both limbs and body undulations contributed to thrust during submergence. There was a graded transition in limb use where the forelimbs were placed near the sandfish's body first and the hindlimbs underwent one more cycle of protraction and retraction. Even though hindlimbs were the last to retract, from limb restraint experiments we found that hindlimbs were not critical for sandfish burial. In contrast, the forelimbs contributed more to burial ability and rapid submergence and these limbs may aid particularly during the initial stages of burial. The sandfish was unable to bury without the use of all of its limbs in most trials revealing the importance of these appendages during burial.

Maladen et al. [105] found that a snake-like robot could bury into granular media when it had a downward tilted head. However, the number of undulations used to bury was much greater. This relatively heavy robot (mass = 1.3 g) moved within large (6 mm diameter) light weight (mass = 0.12 g) particles. The undulating robot body caused the robot to sink into the media and pushed material toward its sides. We hypothesize that this self-generated groove within the medium enabled the robot to push against the granular substrate during lateral undulations and provided thrust. This groove was not observed during sandfish undulation. It is possible that if the sandfish moved in larger particles with a lower density, then burial without limbs might be possible. We expect that the addition of limbs to the robot, capable of generating thrust above surface and that collapse toward the body when submerged, could enable faster robot burial. Future studies which investigate limbless and elongated burrowers such as the shovel-nosed snake (*Chionactis occipitalis*) or California limbless lizard (*Anniella pulchra*) could also shed light on how limbless burial is achieved in nature.

4.7 Contributions

Andrew Masse determined the material to be used in the limb restraint experiments (blue painter's tape) and performed preliminary limb restraint experiments inspiring further investigation of the role of limbs during burial. Yang Ding calculated the wave efficiency (η) as a function of the body portion interacting with the substrate using granular resistive force theory (Fig. 4.9).

CHAPTER V

THE EFFECT OF BODY LENGTH AND SLENDERNESS ON SAND-SWIMMING: COMPARING THE PERFORMANCE OF THE SANDFISH LIZARD AND THE SHOVEL-NOSED SNAKE

5.1 Summary

A variety of subterranean animals have developed techniques to live and move effectively within soil and dry sand. A few desert dwelling animals possess the ability to swim subsurface within sand and move by propagating anterior-to-posterior waves down their body. To investigate how body morphology affects swimming performance, we compare the movement strategies of two desert dwelling sand-swimmers exhibiting disparate body forms: the long-slender limbless shovel-nosed snake (*Chionactis occipitalis*) and the relatively shorter limbed sandfish lizard (*Scincus scincus*). The snake has an average body length to radius ratio (L/r) of 66.7 compared to the sandfish which has a L/r of 14.0. We hypothesize that a long slender body improves swimming performance. The snake also has a lower body friction (μ_s). X-ray imaging of subsurface kinematics revealed that the snake operated with a lower average slip factor ($\bar{S} = 6.0 \pm 1.6°$, defined as the average angle between velocity and tangent vectors along the body) compared to the sandfish ($\bar{S} = 21.6 \pm 3.7°$, $P < 0.01$); this implies that both animals caused local flow of the surrounding media but that the snake yielded the material less. The snake also used a higher number of waves along the body ($\xi = 3.5 \pm 0.7$) compared to the sandfish ($\xi = 1 \pm 0.1$, $P < 0.01$). We used a previously

---

This chapter is paper in preparation by Sarah S. Sharpe, Stephan A. Koehler, Robyn M. Kuckuk, Miguel Serrano, and Daniel I. Goldman developed model called granular resistive force theory, which assumes the snake swims in a frictional fluid, to predict how L/r, ξ, μ_s and the relative curvature ($\kappa\lambda_s$, local curvature at a bend multiplied by the arc length of the wave averaged over all visible undulations) affect $\bar{S}$ for the two animals. The model predicted the difference in L/r between the snake and sandfish had little effect on $\bar{S}$ alone. However, $\bar{S}$ decreased with increasing $\kappa\lambda_s$ and ξ. Therefore, the snake's long body may offer a functional advantage for low slip locomotion by allowing the snake to use a large number of waves along its body while maintaining a swimming waveform with higher curvature. The theory also revealed that the snake's lower body friction contributed to the difference between slip factors and implies that smooth bodied animals may be able to move more effectively underground.

5.2 Introduction

A variety of subterranean animals have developed techniques to live and move effectively within soil and dry sand. A subset of these animals are classified as "subarenaceous" sand-swimmers; they move underneath loose sand by propagating anterior-to-posterior waves down their body. Convergent body form and head shape are found for many subarenaceous reptiles, implying that these morphological features may offer a mechanical advantage for sand movement [55]. These animals typically have a counter-sunk jaw, wedge-shaped head, slender-uniform body, concave ventral surface, and reduced skin friction [55]. Yet few studies [105] have investigated how such features affect subsurface locomotor performance.

Body length, body width, and limb length can vary across different subarenaceous species. Sand-swimming reptiles range from the short thick-bodied lizards with prominent limbs (such as *Scincus scincus*, *Scincus mitranus*, and *Angolosaurus skoogi*), longer bodied skinks with reduced limbs (such as *Ophiomorus tridactylus* and *Sphenops sepsoides*), and even longer slender-bodied snakes and limbless lizards (such as *Chionactis occipitalis*, *Chilomeniscus stramineus*, and *Anniella pulchra*) [21, 22, 55, 56, 83, 209] (Figs. 5.1 & 5.2). We hypothesize that body-substrate interactions play a dominate role in determining swimming performance. To investigate how body morphology affects swimming, we compare the subsurface movement strategies of two desert dwelling sand-swimmers exhibiting disparate body forms: the long-slender limbless *Chionactis occipitalis* (or shovel-nosed snake, Fig. 5.2, A) and the relatively shorter limbed *Scincus scincus* (or sandfish lizard, Fig. 5.2, B).

Figure 5.1: Pictures of subarenaceous reptiles. (A) *Scincus Mitranus*; Credit: Richard Hornby. (Inset) Closer profile of the head; Credit: Michel Gunther-Biosphoto. (B) *Angolosaurus skoogi*; Credit: Paul Freed, freedsphotography.com. (C) *Ophiomorus tridactylus*; Credit: Barbod Safaei Mahroo, CalPhotos. (D) *Sphenops sepsoides*; Credit: Henrik Bringse, 1994. (E) *Chilomeniscus stramineus*; Credit: William Flaxington. (Inset) Closer profile of the head; Credit: Rob Schell, CalPhotos. (F) *Anniella pulchra*; Credit: William Flaxington. Scale bars in all images are 1 cm.

Recent work [7, 11] used high-speed x-ray imaging to investigate the kinematics of the

Figure 5.2: Photographs of two sand-swimming reptiles which exhibit some similar morphological features but have different lengths. (A) The long slender shovel-nosed snake in its natural environment. (B) The sandfish lizard resting on a bed of 0.3 mm diameter glass particles. Snake picture credit: drakeinteractive.com.

sandfish. The studies revealed that the sandfish dove into sand using a stereotyped swimming pattern. Once fully submerged, the sandfish propagated a single-period anterior-to-posterior traveling wave of body undulation to propel itself forward while limbs remained near its sides. The animal used high amplitude undulations, with an amplitude to wavelength ratio (A/λ) that was independent of swimming speed, compaction and depth [11,34]. Futhermore, the wave efficiency (η, defined as the ratio of the average forward speed of the animal to the speed of the kinematic traveling wave) was ≈0.5. This wave efficiency is higher than that of a nematode (≈0.2) moving through a low Reynold's number fluid [210], but lower than that of a snake moving on a terrestrial surface (≈0.9) [211] (Fig. 5.17). Models reveal that the sandfish swims within a self-generated localized frictional fluid in the granular media [7,8].

Compared to the sandfish, little is known about the subsurface locomotion of the shovel-nosed snake. These snakes are found in the Mojave and Sonoran deserts, typically near eolian sand dunes [21] (Fig. 5.3). On the surface of the media, shovel-nosed snakes move using lateral undulations and display little slip (i.e. all body locations move along the same path) [81]. The shovel-nosed snake moves only short distances on the surface of sand, in comparison to other snakes, and buries 'effortlessly' into granular media [21, 55, 82, 83]. This snake spends most of its day subsurface and has been found buried at depths between 2.5 cm to 60 cm beneath the ground [81]. However, the subsurface movement strategy and performance of these snakes are unknown. Previous work using mechanical models to investigate undulatory swimming within granular media revealed that forward locomotion

Figure 5.3: Shovel-nosed snakes are found in the Mojave and Sonoran deserts covering the southwestern United States and northwestern Mexico

occurs when thrust generated from the body exceeds drag on the head and body [8]. Ding et al. [8] posited that the overall locomotor ability depends on the ratio between body and head areas and, consequently, an animal with a more slender body (and head) may be able to achieve a higher swimming speed for a given undulation frequency.

Using x-ray imaging and high-speed above surface video, we investigate subsurface movement of the shovel-nosed snake in granular media with repeatable compactions and compare its performance to the sandfish. We measure performance by defining a new parameter called the slip, S, which we can calculate along the body during subsurface movement using the relation:

$$S = \arccos(1 - \hat{v} \cdot \hat{t}), \tag{5.1}$$

where $\hat{v}$ is the velocity vector and $\hat{t}$ is the tangent vector at a body location. We show that the average S along the body over 1 undulation cycle is inversely related to the wave efficiency (η). We examine how body properties and kinematics differ between the snake and sandfish by comparing body friction (μ_s), body morphology (L/r), number of waves along the body during swimming (ξ) and average relative curvature ($\overline{\kappa\lambda_s}$, local curvature at a bend multiplied by the arc length of the wave averaged over all visible undulations).

We also investigate how body morphology, skin friction and kinematics affect S using granular resistive force theory (RFT) [7, 8]. Granular RFT assumes the material around the swimmer is continuously deforming and has been used to reproduce the sandfish performance, η. We hypothesize that RFT can also be used to predict snake performance when kinematics and body parameters are similar to those measured in experiment.

5.3 Materials and Methods

Shovel-nosed snakes, *Chionactis occipitalis*, were collected in accordance with a scientific collection permit (#SP591773) approved by the Arizona Game and Fish Department. Snakes were acquired from Maricopa, Pima and Yuma counties in the Sonoran desert of southern Arizona. Morphological measurements were made on 4 snakes which had an average snout-tail length (STL) of 36 ± 3 cm and mass of 17 ± 3 g (see Table 5.1). Subsurface kinematics were recorded for 3 of these snakes (snake #107, #110, and #112); subsurface swimming in 3 closely packed (CP) and 3 loosely packed (LP) preparations were recorded for each snake with a total of 18 trials considered in the analysis. Animals were housed in large containers ($51 \times 26 \times 30$ cm^3) which were filled with sand to a depth of 2.5 - 3 cm. Snakes were given 2-3 crickets once a day and allowed to eat *ad libitum*. The holding room was maintained on a 12h:12h light:dark cycle and the average temperature was 28 °C during the day and 24 °C during the night. A water dish and a small plastic box filled with wet moss allowed snakes to regulate humidity conditions surrounding them which proved to be important for their survival in captivity. A heating lamp was placed above each aquarium toward one side of the container to facilitate thermoregulation. All experimental procedures were conducted in accordance with the Georgia Institute of Technology IACUC protocol number (A11066) and radiation safety protocol (X-272).

Kinematic sandfish data were utilized from previous studies [11, 34]. Trials from 6 different animals were considered for comparison with snake data. See Materials and Methods section of Chapter 2 or [34] for more information on acquisition, care, and protocol information for the sandfish.

5.3.1 Media Preparation

To control the compaction of the substrate, an air-fluidized bed was used to create repeatable initial compactions, characterized by volume fraction, ϕ, the ratio of the volume of the granular media to the volume of occupied space. The bed (Fig. 5.4) was filled with spherical glass beads that were similar in size (diameter = 0.27 ± 0.04 mm) and density ($\rho = 2.5$ g/cm^3) to particles found in sand dunes [95]. An air flow created a fluidized state and a slow decrease in air flow to zero resulted in a loosely packed (LP) state ($\phi = 0.588 \pm 0.006$). Closely packed (CP) states ($\phi = 0.617 \pm 0.012$) were created by applying a slight air flow below the onset of fluidization and subsequently vibrating the granular media using a motor with an off-axis mass that was attached to the side of the bed. The difference in compaction resulted in an increase in resistive force (≈ 25 %) between LP and CP preparations [11]. Air flow was off during all animal trials and ϕ was determined by measuring the height of the granular media after preparation.

Experiments took place in a room with an average temperature of 25°C and average humidity level of 41%. Lights heated the granular substrate for approximately 1 hour prior to experimentation and the temperature of the sand was measured prior to each animal trial. The average sand temperature for all runs was 32.5 ± 2.5°C. The bed was periodically fluidized which helped homogenize the distribution of temperatures within the bed and lights were turned off when necessary to keep a constant sand temperature.

A similar setup was used for the sandfish lizard experiments (see Material and Methods of Chapter 2 or [34]). The same granular bed and particles were used for snake and sandfish trials. However, the ϕ range achieved was larger (ϕ =0.584 ± 0.013 for LP experiments and ϕ = 0.635 ± 0.013 for CP) for the sandfish trials due to a slightly different shaking apparatus used to create CP preparations. Sand temperatures in the sandfish experiments ranged between 30 and 38°C, with the majority (>75%) conducted in the 34-38°C range.

5.3.2 Snake Kinematics

Shovel-nosed snakes were placed in a container resting just above the surface of the prepared sand (Fig. 5.4). A gate was used to separate the snake from the granular media. As the gate was lifted the bottom-rear section of the container also lifted via a string connection, causing the snake's orientation to angle downward toward the media. Transparent walls resting on the surface of the sand outside the holding container ensured burial at a desired location away from container walls and within the x-ray field of view.

Above surface visible light video was recorded at 63 frames per second (fps) using a high-speed camera (AOS Technologies AG X-PRI, Baden Daettwil, Switzerland) to characterize general features of above surface movement. Subsurface snake kinematics were recorded using an x-ray system (OEC 9000, Radiological Imaging Systems, Hamburg, PA, USA) coupled to a high-speed camera (Fastcam 1024 PCI, Photron, San Diego, CA, USA). Top-view (i.e. dorsal view) subsurface snake kinematics were recorded at 60 fps. Different frame rates were used in above surface video and x-ray imaging due to the camera constraints. The x-ray system was set to an energy of 85 kV and 20 mA. Snakes swam into a granular bed (22.9×40.6 cm^2) filled with glass particles to a height of 10 cm (Fig. 5.4). Due to the apparatus position and x-ray image intensifier size, the field of view within the container was constrained to a 20 cm diameter circle. Therefore, snakes often moved into and out of the field of view during the trial.

For enhanced contrast in x-ray videos, small opaque markers ($\approx 1\ mm^2$ each, mass $\approx$0.01 g) made from lead were bonded to the midline of the snake using cyanoacrylate glue. These markers were placed at 1 or 2 cm increments down the length of the snake's body. Markers were automatically tracked using custom code (Matlab, Mathworks, Natick, MA, USA) [212]. If a marker did not exist at every 1 cm location, that location was manually tracked over the course of the trial. A 3rd order basis spline (B-spline) was fit to the snake's body at every frame for all markers visible.

The B-spline is a fitting technique in which, given a number of points (called knots), a set of basis vectors are used to reproduce the best fit polynomial function [213]. The number of knots defined for each snake was equal to the number of markers along the body (between 26 and 35) and were equally spaced. We used 3rd order basis functions so that the 1st and 2nd order derivatives were continuous along the snake's body. The B-spline function is described by:

$$x(t) = \sum_{i=1}^{N_x} \alpha_i \phi_i(t) \tag{5.2}$$

where $\phi_i(t)$ are the basis functions center at the knots, N_x are the number of knots, and α_i

are the coefficients of the spline. α_i is solved for by minimizing the energy function:

$$E = \frac{1}{2}\|x(t) - \sum_{i=1}^{N_x} \alpha_i \phi_i(t)\|^2 + \frac{1}{2}\lambda_b \alpha^\top \nabla^2 \alpha \tag{5.3}$$

where λ_b is a penalization term that controls the smoothness of the fit (see [214] for more details). A high penalization term will minimize the distance of the curves between knots. This term was manually changed until the fits visually matched the animal's body. A regulation term of 0.001 was used for all snake and sandfish data. A good fit to the body was critical in accurately determining the tangent vectors at marker locations which were used to estimate slip.

Kinematics were characterized during subsurface movement only. The number of waves along the body, ξ, was measured for all animals during a time when most, if not all, of the body was within the field of view. When the full length of the snake was not within the field of view or subsurface, then the ξ was calculated as $\xi_{inside} + \xi_{outside}$. ξ_{inside} was directly measured by counting the number of waves within the field of view. $\xi_{outside}$ was estimated by using the known length of the snake outside of the field of view and the average wave arc length (λ_s). The length of body spanning each bend varied, so λ_s for each bend was calculated as $\lambda_{s/2} \times 2$, where $\lambda_{s/2}$ is the arc length of a half wave. The average curvature (κ) was calculated for all bends in the field of view by fitting a circle to the body near the point of maximal concavity or convexity; relative curvature ($\kappa\lambda_s$) was used for a non-dimensional comparison with the sandfish data (see Fig. 5.10 for curves with differing $\kappa\lambda_s$). The slip, S, (equation 5.1) was measured for every tracked point along the body at every instant in time. Tangent vectors, $\hat{t}$, at varying body locations were found by using the tangent to the B-spline fit. Velocity vectors, $\hat{v}$, were spatially filtered to remove noise associated with tracking markers. The average slip, $\bar{S}$, during a trial was calculated by averaging S over all points visible and during a minimum of a half cycle of undulation (with more time included in half cycle increments). The slip at the first and last marker locations were excluded from the average due to the increased error in the B-spline fit at the end points.

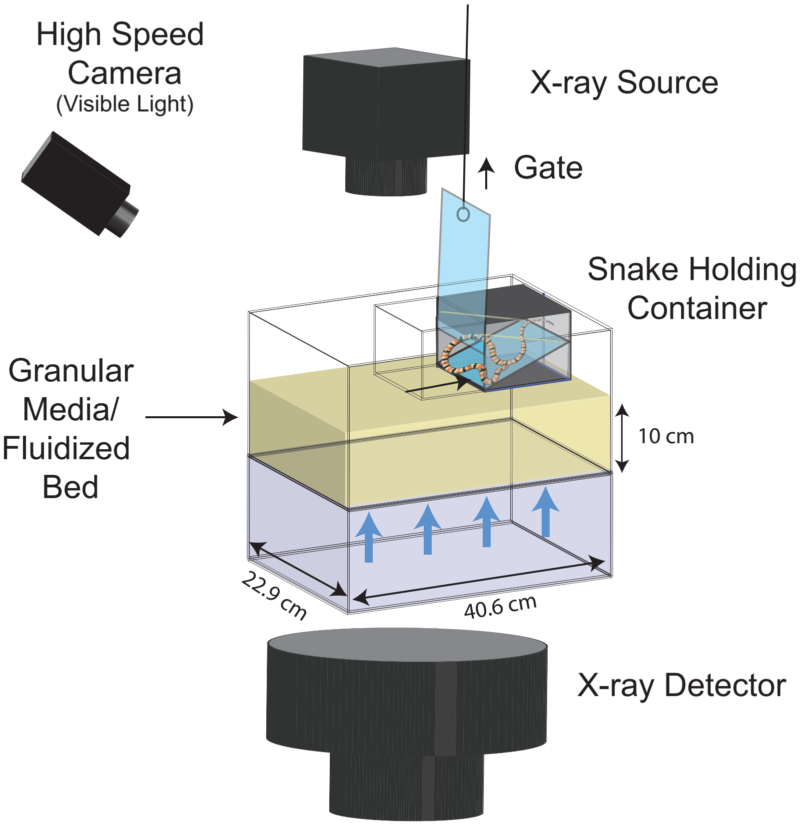

Figure 5.4: Experimental apparatus used to collect snake data.

5.3.3 Sandfish Kinematics

Sandfish were initially held in a container separated by the sand-filled bed by a gate. After the gate lifted, sandfish dove into the granular media. Above surface video and subsurface x-ray imaging recorded motion at 250 fps (the same cameras were used for snake and sandfish experiments). The x-ray system was set to 85 kV and 20 mA.

A maximum of 12 markers were glued to the sandfish midline at locations between 0.2 and 1.1 snout-to-vent length (SVL) in 0.1 SVL increments. A maximum of 2 markers were bonded to each limb. The markers were tracked using custom Matlab code [34]. B-splines were fit to the sandfish midline during a trial using the same fitting code [212] that was used in the snake analysis.

Only subsurface kinematics were considered for analysis. The sandfish was considered to be 'subsurface' when the sandfish's vent and hindlimbs were covered by granular media. Identical methods as described for the snake were used to estimate ξ, λ_s, κ and $\bar{S}$ for the sandfish. Because the sandfish had more than 9 markers on the body per undulation wave and was within the field of view for the entire trial, the slip error is estimated to be lower than that calculated for the snake (Fig. 5.6). See Chapter 2 or [34] for more details on sandfish experimental methods.

5.3.4 Slip Factor

Traditionally slip during locomotion has been quantified for undulatory animals by measuring $\frac{v_x}{v_w}$ (also called waved efficiency, η [11]), where v_x is the forward velocity, and v_w is the velocity of the wave. $v_w = f\lambda$, where f is the frequency of undulation, and λ is the body wavelength. Another closely related parameter that has been used is $\frac{v_x}{v_c}$ [215], where v_c is the velocity of the curvature wave and $v_c = f\lambda_s$, where λ_s is the arc length of one wave. However, for animals that change direction and/or change shape (i.e. λ) during movement these parameters can be challenging to estimate. Therefore we introduce a new parameter called the slip factor, S, that can also be used to analyze movement efficiency within materials.

The benefit of using S, which is the defined as angle between velocity and tangent body vectors (equation 5.1), is that this factor can be calculated for an animal that is (1) moving along any arbitrary path, (2) changing frequency or (3) changing shape during movement. In addition, this measure gives an instantaneous measure of slip along different body locations. The main disadvantage is that the slip value is dependent on body orientation with respect to velocity, and therefore, our trials must be averaged over the whole body and over at least a half undulation cycle for comparison between sandfish and snakes.

To investigate the reliability of the slip measurement using our tracking program and B-spline fitting analysis, we created a simulation of a 2-period sinusoidal wave that moved forward with a known wave efficiency (Fig. 5.5). The wave undulates twice. For varying η, we tracked 20 equally spaced markers along the wave (10 markers per wave) and fit the body using the B-spline technique [212] at each frame (Fig. 5.5, A, B, & C). We calculated slip at each marker location. Due to geometry, the slip was lowest near areas of maximal curvature (Fig. 5.5, D, E & F). Also slip on average was higher near the first and last marker due to B-spline fitting error near the end-points of the wave. The overall slip decreased as wave efficiency increased (see Fig. 5.15 in Results).

To investigate how the number of markers along the body affected the reliability of the slip measure, the average slip ($\bar{S}$) was calculated when η=1 (i.e. no slip condition) for differing marker densities along the simulated body (Fig. 5.6). In experiment, the number of markers per wave varied on the snake depending on the $\kappa\lambda_s$ of the bend but, in general, was between 5.5 and 12. The simulation revealed that if there were a low number of markers (less than 5 markers per wave) then the B-spline fit had difficulty reproducing the sinusoid, leading to a high error in slip (for 3 markers per wave there was a 18° error). As more markers were added, $\bar{S}$ was more reflective of the actual slip (≈3° error for the 10 markers per wave simulation). The slip error increased as a large number of markers were included due to the tracking program failing to identify marker locations correctly (i.e. tracker would jump from the correct marker to a nearby marker location).

For some snake trials, markers were placed at 2 cm increments on the posterior portion of the body. On occasion this caused as little as 3 markers per wave and the B-spline had difficulty reproducing the actual snake body midline. Consequently, body locations

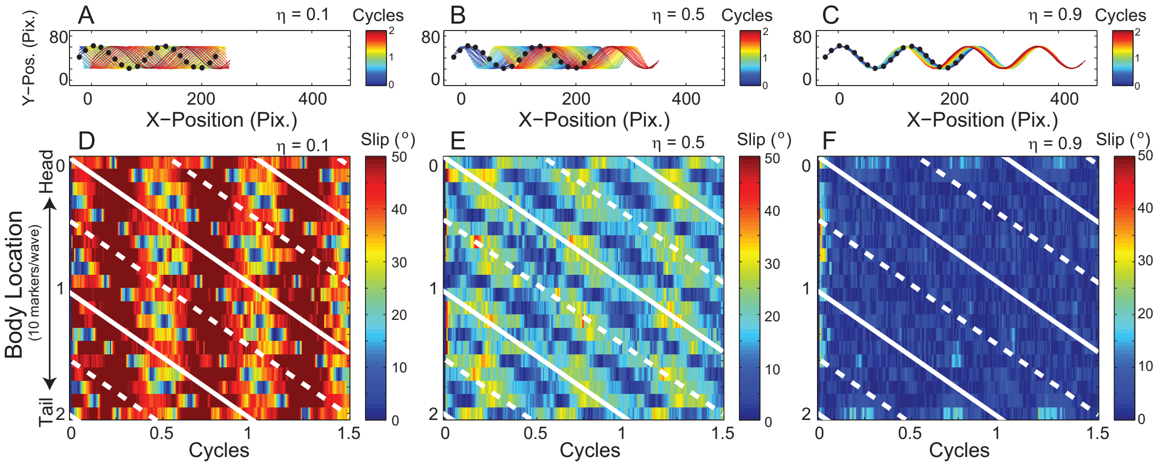

Figure 5.5: Slip factor reliability investigated using data with known wave efficiency (η). (A, B & C) A two period, sinusoidal wave ($A/\lambda = 0.2$ and $\kappa\lambda = 7.1 \pm 0.4$ (or 7.9, analytically)) simulated for 2 undulation cycles and constrained to move with varying η of 0.1, 0.5 and 0.9, respectively. 20 equally spaced locations along the waves arc length were defined (black points). These points were tracked and fit with B-splines using the same code used in the experimental data analysis. B-spline fits to the marker locations are shown for every 0.005 cycles (dark blue is time 0 (the initial starting position) and dark red is two cycles later). (C, D, & E) The slip angle (represented by color) calculated for all 20 points (along the 2 waves) during the simulated run (0 - 1.5 cycles) where a slip of 0° is dark blue and a slip of 50° is dark red. White solid and dashed lines show the propagation of zero curvature down the body.

were manually tracked for all snake trials such that a tracked point occurred at every 1 cm location. This increased the minimum marker density to at least 5.5 markers per wave. To investigate the error due to manually tracking we simulated a wave with only 3 points per wave then manually tracked locations resulting in 5.5 markers per wave (Fig. 5.6, magenta circle). Manually adding points decreased the overall error from 18° to 7°. However, this error was slightly higher compared to the case when there were the same number of markers but no manual tracking was done (5°).

5.3.5 Morphology and Body Friction Measurements

Morphological measurements were made on 4 anesthetized snakes and 9 anesthetized sandfish. We report average weight and length for animals that were measured more than once over the course of the study.

Body-particle friction measurements were made using 0.3 mm glass particles (the same media animals interact with in the kinematic studies) following techniques described in [186].

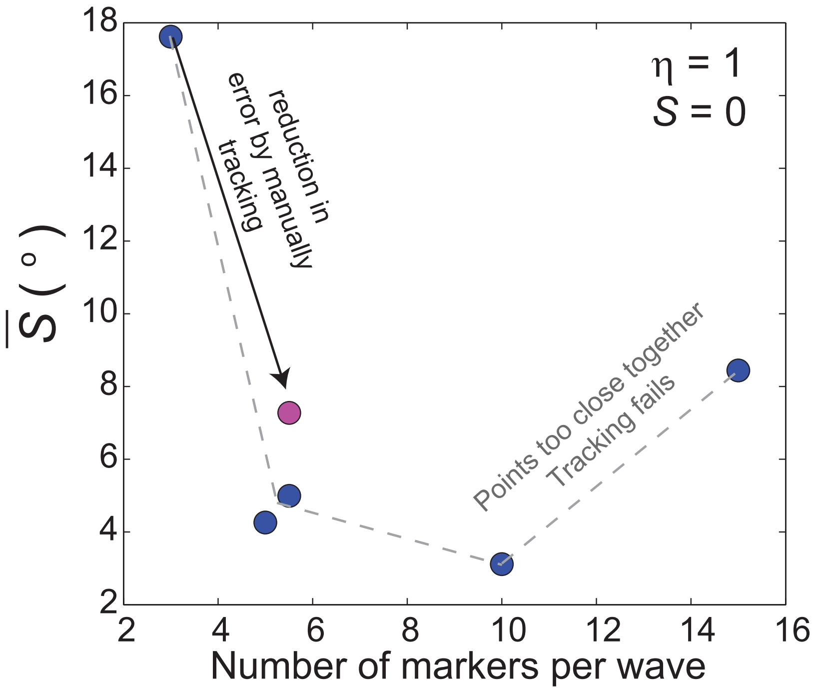

Figure 5.6: Simulated data shows that the number of markers per wave influences error in the average slip calculation. For the $\eta = 1$ case (ie. no slip) the number of markers along wave were varied between 3 and 15 (blue points). $\bar{S}$ was measured by averaging slip over 1 undulation cycle and excluding slip values of the first and last point. The magenta circle represents a trial where there were only 3 markers per wave and more points were manually added to raise the total number of tracked points to 5.5 per wave. Error is smallest ($\approx 3°$) when there are 10 markers per wave.

Snakes and sandfish lizards were sedated by gas induction with 5% isoflurane in medical grade oxygen and then anesthetized with an intramuscular injection of ketamine hydrochloride (200 mg/kg body mass). Anesthetized animals were placed on an inclined plane covered with a mono-layer of particles. Animals were placed so that either their ventral or dorsal surface was in contact with the particles, and their head was either oriented downward (causing “forward” sliding) or upward (causing “backward” sliding) relative to the sloping angle; in total, four orientations were tested. The edge of the plane was lifted by hand until an inclination angle (θ) was reached which caused animals to slide (Fig. 5.7). θ was measured using a level with an angle locator. The static coefficient of friction, μ_s, was calculated from the relation $\mu_s = \tan(\theta)$. Four friction measurements were made in each orientation for three different snakes and three sandfish lizards unless otherwise noted in Table 6.1.

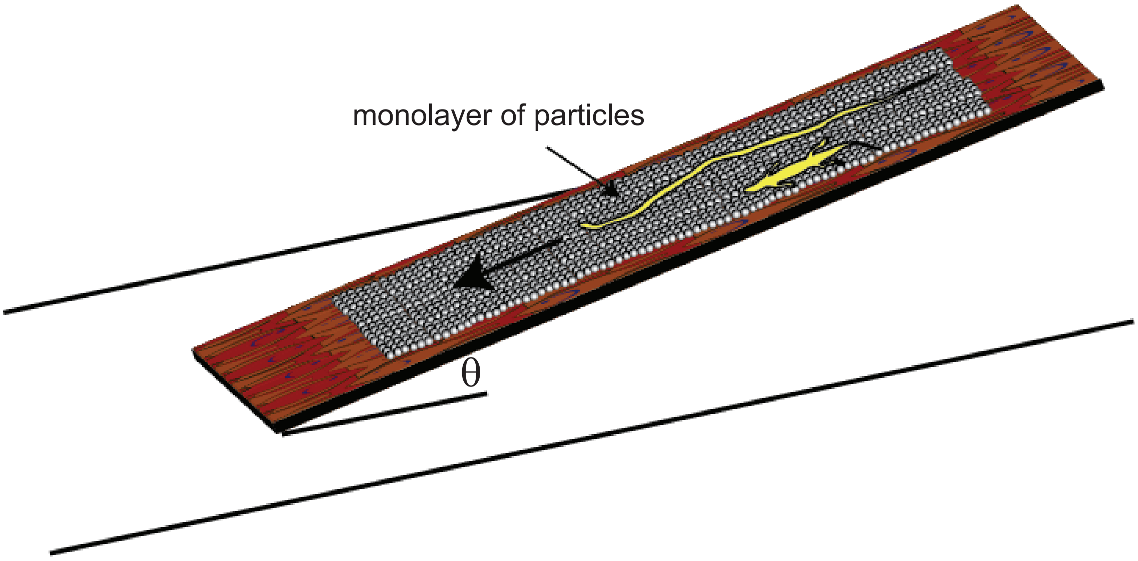

Figure 5.7: Diagram of apparatus used to measure the coefficient of static friction (μ_s) between the animal's body and particles by observing the angle (θ) at which the animal starts sliding. Here the snake and sandfish are shown in the "forward" orientation.

5.3.6 RFT Model

In collaboration with Dr. Stephan A. Koehler, we used our previously developed granular resistive force theory (RFT) model [7, 11] to compare sand-swimming for animals with different L/r, ξ, $\kappa\lambda_s$, and μ_s. The RFT used a simplified model of the snake and sandfish kinematics such that $\kappa\lambda_s$ for all bends along the modeled undulatory swimmer's body were the same and no turning occurred. The modeled animals had a uniform cylindrical body, blunt head, and propagated a serpentine wave from head to tail. A serpentine wave is described by:

$$\theta(t) = \theta_{max} \sin \frac{2\pi}{\lambda_s}(s + v_c t) \tag{5.4}$$

where t is time, s is the distance along the path, θ is the angle between the direction along the wave at position s and the forward direction [216, Chapter 4], θ_{max} is the maximum angle of deviation (or maximum θ), t is time, and v_c is the velocity of the curvature wave. $v_c = f\lambda_s$ where f is the cycle frequency. The forward position, X and the lateral distance from the midline Y are described by:

$$
\begin{aligned}
x(t) &= \int_0^s \cos(\theta(t))\mathrm{d}s \\
X(t) &= x(t) - \bar{x}(t) + \int_0^t v_x \mathrm{d}t \\
y(t) &= \int_0^s \sin(\theta(t))\mathrm{d}s \\
Y(t) &= y(t) - \bar{y}(t),
\end{aligned}
\tag{5.5}
$$

where $\bar{x}$ is the average x, $\bar{y}$ is the average y, and v_x is forward velocity.

The body of the modeled swimmer was divided into infinitesimal segments. For each segment, forces were calculated as functions of orientation angle with respect to the velocity direction (forces were speed independent) and empirically measured from rod drag experiments within a 0.3 mm diameter glass particle substrate [see Maladen et al. [7,11] for functional forms of the force laws]. The friction coefficient, μ_s, between the stainless steel rod and glass particles was ≈0.17. To simulate the lower friction value between the snake skin and particles, the the tangential forces obtained from the rod drag experiments were decreased by 50%. The forward speed of the body was then obtained from the balance of thrust and drag in the forward direction. The average slip, $\bar{S}$, was calculated along the body over one undulation cycle.

5.4 Experimental Results

5.4.1 Body Morphology

Snakes had a consistent body width of ≈1 cm (Table 5.1) and long bodies with an average snout-to-tail length (STL) of 36.6 ± 2.7 cm. The snake's body diameter decreased rapidly for the last 10% to 15% of its length (Fig. 5.8). To account for the changing diameter, we defined an effective snake length (L_{Eff}) which was equal to 0.87 × STL. On average L_{Eff} = 31.8 ± 2.4 cm for snakes. We estimated that the systematic error in our measurements was approximately ± 0.04 cm.

For sandfish the body width was ≈1.5 cm, 50% larger than the snakes' body width. However, the STL was 60% smaller than snakes' at 14.1 ± 0.8 cm. Interestingly, mass was similar between the snake and sandfish (17.4 ± 3.4 g and 17.6 ± 2.8 g, respectively). The body diameter of the sandfish decreased rapidly after the 1.2 snout-to-vent length (SVL) location (Fig. 5.8); therefore, the L_{Eff} was defined as 1.2 × SVL and was 10.6 ± 0.6 cm.

The body length to radius ratio, L/r, was calculated as $\frac{L_{Eff}}{w/2}$ for both animals, where w is the body width. L/r for the snake was approximately 5 times larger than the L/r for the sandfish (66.7 ± 4.9 and 14.0 ± 0.7, respectively). Morphological measurements were also made on awake animals used in kinematic experiments on the day of data collection. Because awake animals tended to bend their bodies and move during measurements, the measurements were subject to more error in accuracy. However, average L/r values were similar for these animals as those made on the anesthetized animals (71.1 ± 6.8 for the snakes and L/r= 14.6 ± 0.4 for sandfish).

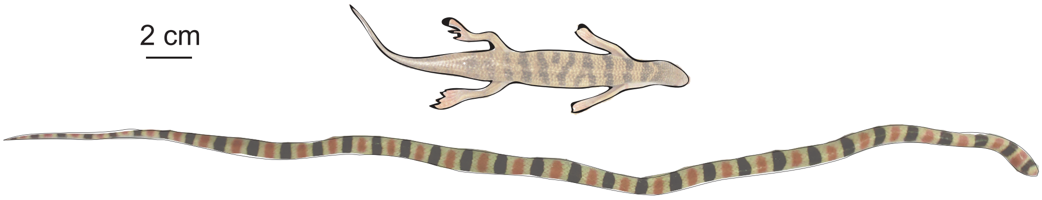

Figure 5.8: Dorsal views of the shovel-nosed snake (bottom) and the sandfish (top) on the same length scale.

5.4.2 Friction Measurements

Snake body-particle friction was lower than the sandfish body-particle friction on the ventral surface in the forward direction (snake ventral-forward: μ_s= 0.11 ± 0.02, sandfish ventral-forward: μ_s= 0.19 ± 0.02) and in the backward direction (snake ventral-backward: μ_s= 0.14 ± 0.02, sandfish ventral-backward: μ_s= 0.28 ± 0.03; Table 6.1; Fig. 5.7). However, friction was similar on the snake and sandfish on the dorsal surface in the forward direction (snake dorsal-forward: μ_s= 0.16 ± 0.03, sandfish dorsal-forward: μ_s= 0.18 ± 0.03) and backward direction (snake dorsal-backward: μ_s= 0.24 ± 0.03, sandfish dorsal-backward: μ_s= 0.23 ± 0.02). We expect that smoother ventral surface of the shovel-nosed may offer the snake a functional advantage.

Table 5.1: Snake and sandfish morphology

Animal	SVL (cm)	STL (cm)	L_{Eff} (cm)	Width (cm)	Mass (g)	L/r
Ch. occipitalis						
110		32.5	28.3	0.95	12.6	59.6
80		38.7	33.7	0.95	20	71.0
112		37.5	32.6	0.97	19.4	67.5
107		37.5	32.6	0.95	18	68.7
						66.7 ± 4.9
S. scincus						
46	8.7	14.2	10.4	1.5	16	13.9
36	9	14.0	10.8	1.4	18.8	15.1
29	9	12.5	10.8	1.7	19	12.7
73	8.3	13.6	10.0	1.4	15.8	14.2
75	8.8	14	10.6	1.4	14.5	15.1
74	10.0	15.7	12.0	1.7	24.1	14.3
103	9.1	15.1	10.9	1.6	18.1	13.3
102	8.3	13.4	10.0	1.5	14.2	13.3
98	8.8	14.4	10.5	1.5	16	14.5
97	9	14.6	10.8	1.6	18.1	13.5
96	8.5	14	10.2	1.5	18.5	13.6
						14.0 ± 0.7

Table 5.2: Snake and sandfish skin friction tests

Snake #	STL (*cm*)	SVL (*cm*)	Mass (*g*)	μ_s, Ventral Forward	μ_s, Ventral Backward	μ_s, Dorsal Forward	μ_s, Dorsal Backward
Ch. occipitalis							
80	38.7		20	0.112 ± 0.01	0.117 ± 0.003*	0.177 ± 0.003*	0.208 ± 0.006
110	33.7		15	0.123 ± 0.006*	0.142 ± 0.005*	0.179 ± 0.003*	0.247 ± 0.016**
112	41.4		22.9	0.092 ± 0.017	0.152 ± 0.009	0.127 ± 0.017	0.254 ± 0.023
Average				**0.109 ± 0.016**	**0.137 ± 0.018**	**0.161 ± 0.029**	**0.237 ± 0.025**
S. scincus							
96	14	8.5	18.5	0.212 ± 0.015	0.313 ± 0.04	0.183 ± 0.014	0.217 ± 0.017
98	14.6	8.8	16.1	0.17 ± 0.02	0.266 ± 0.009	0.147 ± 0.009	0.224 ± 0.042
74	15.4	9.9	24.5	0.201 ± 0.014	0.271 ± 0.036	0.208 ± 0.017	0.254 ± 0.022
Average				**0.194 ± 0.022**	**0.283 ± 0.026**	**0.179 ± 0.031**	**0.231 ± 0.019**

no notation indicates n=4 measurements, * n= 3 measurements, ** n= 2 measurements
± indicates s.d.

5.4.3 Snake Subsurface Kinematics

Prior to entry, snakes typically probed the granular media with their snout. Once begun, burial was fast and continuous. Snakes used lateral body undulations to move subsurface and the waveform was serpenoid (also referred to as a meandering curve), where the angular bending was sinusoidal. Snakes often turned during subsurface swimming; turning was characterized by a large amplitude bend followed by a smaller amplitude bend (or vice-versa). Figure 5.9 shows the above surface and subsurface images during a representative burial.

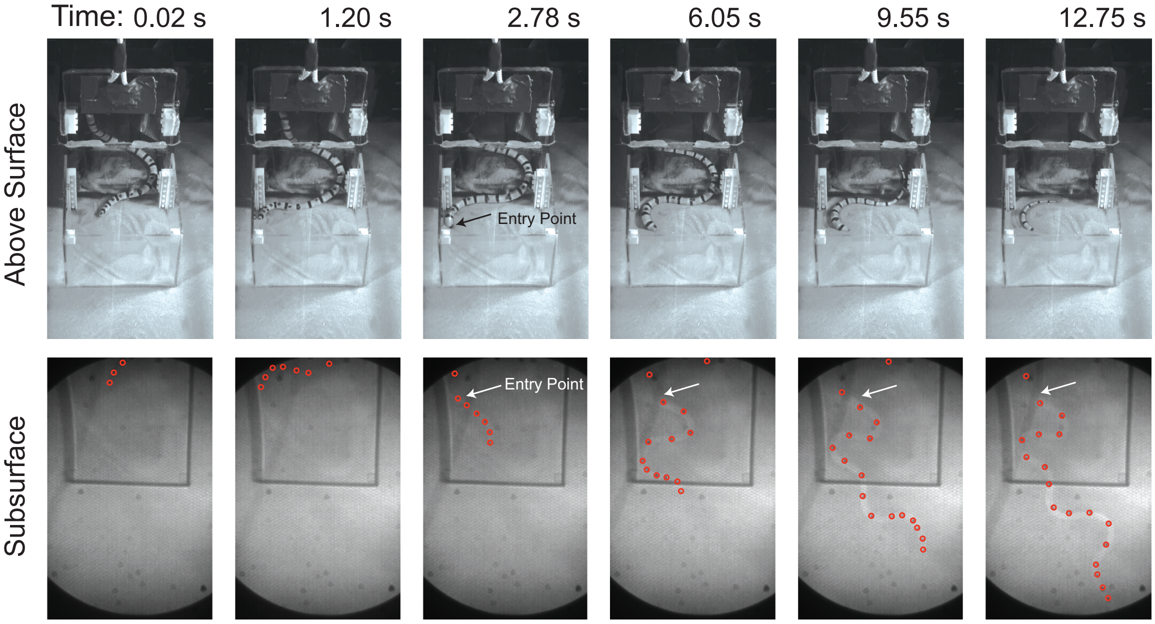

Figure 5.9: Above surface and subsurface images of a representative snake burial. Time is shown relative to the first image recorded. Burial starts at time = 1.2 s. Markers on the body are circled in red in the subsurface images. The point at which the snake starts moving subsurface is shown with the arrow. Markers visible in the subsurface video that occur before this location are moving above surface and are not considered in the analysis.

Traveling waves of curvature propagate at 3.7 ± 1.3 cm/s during steady-state snake swimming. On average $\kappa\lambda_s$ (Fig. 5.10) for each bend (or half-wave) statistically decreased as the snake moved farther into the media (Fig. 5.11, ANOVA, $F(7, 105) = 3.3, P < 0.01$ for all bends considered). Some of the high $\kappa\lambda_s$ that occurred later in the burial (at large bend numbers) were due to snake turning. The maximum $\kappa\lambda_s$ observed during straight movement decreased linearly with bend number. We did not record side-view x-ray video, but we used the known arc length between markers and the measured projected distance between markers acquired in the top-view x-ray to estimate entry angle. We calculated that snakes moved into media at an entry angle of 23 ± 10°. This average is similar to the angle of entry found in previous studies for the sandfish [34].

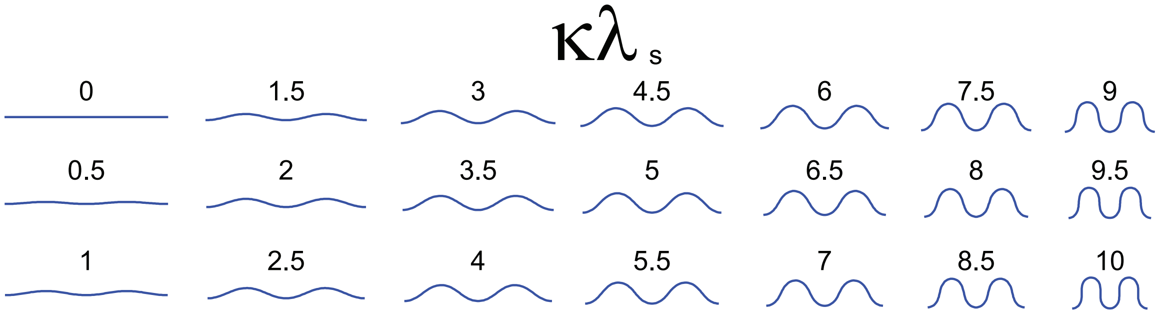

Figure 5.10: Waves with differing $\kappa\lambda_s$ and $\xi = 2$.

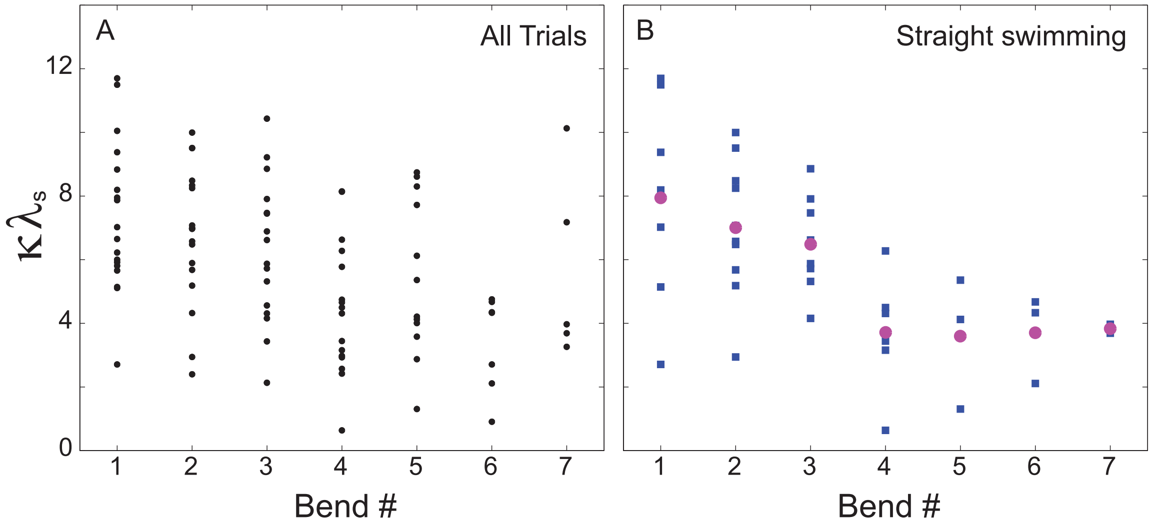

Figure 5.11: The relative curvature, $\kappa\lambda_s$, of each bend decreased ($P < 0.01$) as the snake moved farther (and presumably deeper) into the media. (A) $\kappa\lambda_s$ and corresponding bend number for all trials (both turning and straight). (B) $\kappa\lambda_s$ for bends during straight swimming *only*. Magenta circles show the average $\kappa\lambda_s$ at each bend for straight swimming. The maximum $\kappa\lambda_s$ decreased for straight swimming while the minimum stayed approximately constant with increasing bend number.

5.4.4 Kinematic Comparison with the Sandfish

5.4.4.1 Body Shape and Wave Number

Examples of snake body midlines are shown in Fig. 5.12A for an instant in time during subsurface sand-swimming in the 18 trials recorded (N=3 snakes). The portion of the body shown is within the field of view and subsurface. κ and λ_s varied not only between trials but along the body. Sandfish body midlines during sand-swimming tended to have a more consistent κ and λ_s between trials (Fig. 5.12, B; 30 of 45 trials shown, N= 6 sandfish).

The relative curvature, $\kappa\lambda_s$, of each bend along the body was calculated for all snake and sandfish trials at an instant in time when most (if not all) of the animal was within the field of view and for submerged body segments. $\kappa\lambda_s$ did not vary between LP and CP trials for each animal. The probability distribution shows that snakes have a broader distribution of $\kappa\lambda_s$ during swimming whereas the sandfish tends to remain closer to $\kappa\lambda_s \approx 8$ (where each $\kappa\lambda_s$ was considered an independent measurement; Fig. 5.12).

The mean $\kappa\lambda_s$ ($\overline{\kappa\lambda_s}$) for a single trial was calculated by averaging $\kappa\lambda_s$ over all bends visible along the body. On average, snake trials has a lower $\overline{\kappa\lambda_s}$ than sandfish trials ($\overline{\kappa\lambda_s}$= 6.1 ± 1.3 for snakes, and $\overline{\kappa\lambda_s} = 7.4 \pm 1.0$ for sandfish; ANOVA, $F(2, 73) = 20.3, P < 0.01$) and $\overline{\kappa\lambda_s}$ did not statistically vary with compaction.

The snake swam with a higher average number of waves along its body ($\xi = 3.5 \pm 0.7$) than the sandfish ($\xi = 1 \pm 0.1$, ANOVA, $F(2, 73) = 695, P < 0.01$) and ξ did not statistically vary with compaction for each animal.

5.4.4.2 Slip in GM

Snakes slipped during subsurface locomotion; all body points did not move through the same trajectory (Fig. 5.13, A & B). However, snake slip was significantly less compared to the sandfish slip (P <0.01, Fig. 5.13, C & D). The difference in slip was visible when viewing the subsurface body midline over time. For example, midlines are shown in Figure 5.13 for a representative snake and sandfish trial. By plotting one midline per undulation, it is clear that the snake advanced farther per undulation cycle relative to its wavelength than the sandfish. The snake's body midline moved backward ≈0.2 wavelengths during

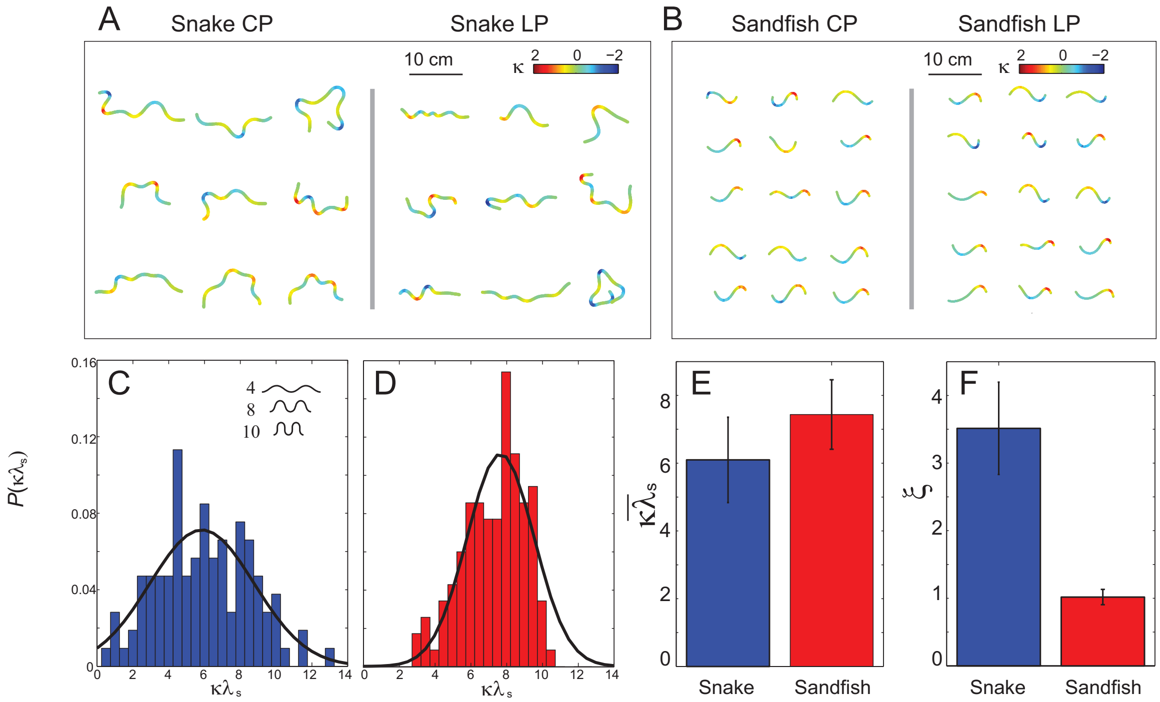

Figure 5.12: Body shape, relative curvature and wave number measurements for the snake and sandfish. (A) Body shapes and signed κ along the body during snake subsurface swimming in CP (left) and LP (right) media. Only the portion of the snake that is subsurface and within the field of view is shown. (B) Body shape and signed κ of sandfish during sand-swimming in CP (left) and LP (right) media. Because body shape and number of waves along the body did not change for different compactions, all trials were considered together in C-F. (C) Probability distribution of the absolute $\kappa\lambda_s$ measured for the snake trials and (D) the sandfish trials, where each measurement from a bend is considered independent. Black curves in C and D show a fitted gaussian distribution to the snake ($r^2 = 0.67$) and sandfish ($r^2 = 0.84$) data, respectively. (E) Average $\overline{\kappa\lambda_s}$ along the snake (blue) and sandfish (red) body for each trial. (F) Average number of waves along the snake (blue) and sandfish (red) body. If a portion of the snake's body was not visible, the number of waves outside the field of view were estimated using the known length and average λ_s. Error bars show ± s. d.

undulation 3 relative to the location during undulation 2. Between undulation 3 and 4 it only moved backward ≈0.1 wavelength. Although slip decreased during movement farther into the media for this trial, we did not find this decrease was consistent in other trials. For the sandfish, slip can be compared between cycles by extending the body midline during undulation 1 to where the midline trajectory would be if the sandfish had moved in a tube (Fig. 5.13, D, position 2'). Comparing the extended midline (2') to the actual position during undulation 2, the body is located ≈0.5 wavelengths behind tube movement, and therefore had greater slip than the snake. Because this analysis was difficult for a trial when a snake turned or changed shape (see Materials and Methods) we quantified the slip factor, S (Eq. 5.1), for quantitative comparison between snake trials (N = 3 snakes, n = 18 trials) and sandfish trials (N = 6 sandfish, n = 56 trials).

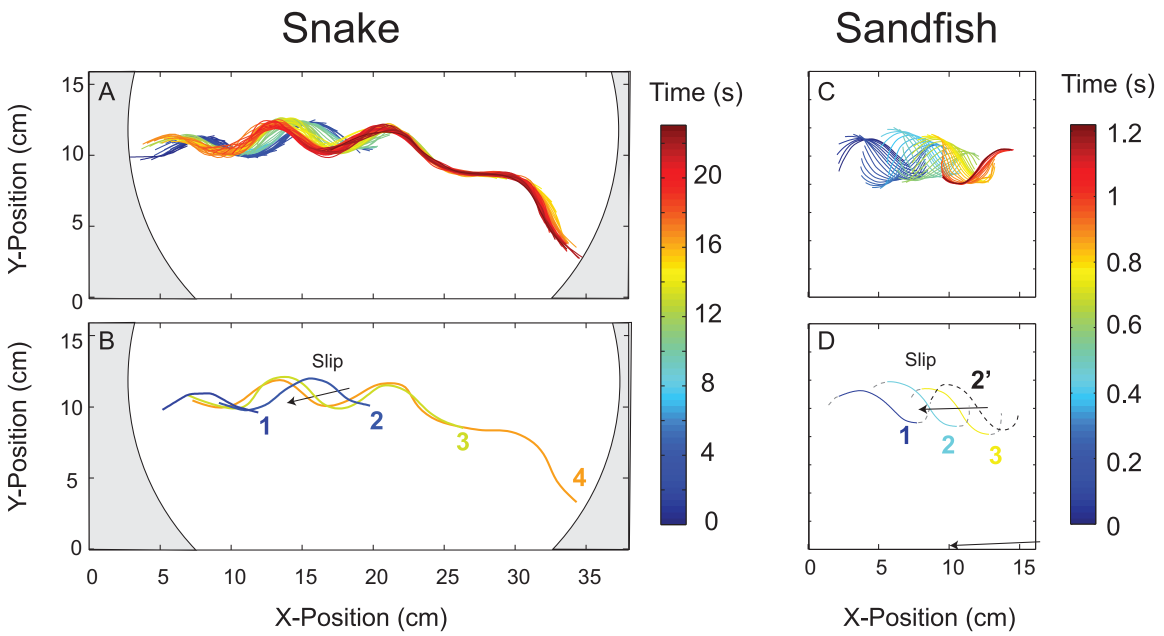

Figure 5.13: Comparison of subsurface tracks. (A) Shovel-nosed snake body position at different time instants, where time = 0 s is shown in dark blue and time = 23 s is shown in dark red. The body midlines are plotted in 0.17 s time increments (and the snake paused in this trial between 4 and 10 seconds). Gray regions are beyond the field of view. (B) Snake body position during the first, second, third and fourth undulation (indicated by numbers). Slip is clear when comparing undulation 2, 3 and 4. (C) Sandfish body during subsurface swimming at different time instants, where time = 0 s is dark blue and time = 1.2 s is dark red. A body midline is plotted every 0.02 s. (D) Undulation 1, 2 and 3 are shown. Slip is clear when comparing 2' and undulation 2, where 2' is an extension of the body midline during undulation 1 to the approximate location one cycle later if it were moving with no slip. Markers along the sandfish body extend from 0.3 SVL to 1.1 SVL and are shown by colored curves in C and D. Gray dotted lines extend from the head to 1.2 SVL location on the sandfish.

Deviations between velocity and tangent vectors at the tracked marker positions (Fig. 5.14, A & B) were larger during sandfish subsurface locomotion compared to snake locomotion. Figure 5.14, C & D, show the slip angle (S) at marker locations during snake and sandfish sand-swimming, respectively, for a representative trial. White lines show propagation of zero curvature. In the sandfish, there were large variations in slip with body orientation (≈50°).

The average slip, $\bar{S}$, was significantly smaller during snake sand-swimming ($\bar{S} = 6.4 \pm 1.4$) compared to sandfish sand-swimming ($\bar{S} = 21.3 \pm 4.1$, ANOVA, $F(2, 73) = 280, P < 0.01$). $\bar{S}$ did not depend on media compaction for either animal. See Materials and Methods for an analysis of the error in the calculated $\bar{S}$ using simulated data with known wave efficiency (η).

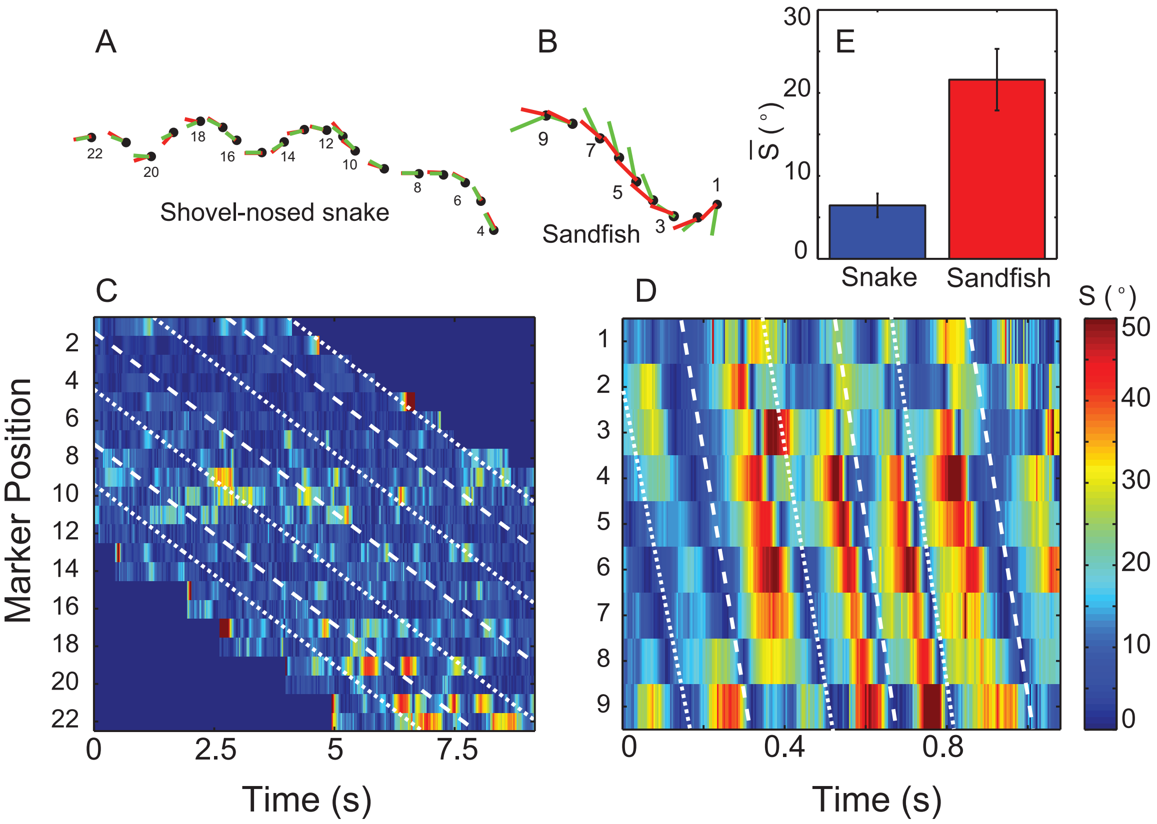

Figure 5.14: Slip comparison between shovel-nosed snake and sandfish. (A) Velocity vectors (green) and tangent vectors (red) at points along the body shown for a single time instant during the shovel-nosed snake subsurface movement from a representative run. (B) Velocity vectors and tangent vectors at tracked points along the body from a sandfish trial. (C) Slip angle (S) from a snake trial and (D) sandfish trial, where dark blue is $S = 0°$ and dark red is $S = 50°$. White dotted and dashed lines show when curvature is 0 along the body; curvature propagates from head to tail with increasing time. Dashed-to-dashed (or dotted-to-dotted) show 1 undulation cycle. The dark blue solid region in C is not considered in the analysis because markers are outside the field of view. (E) Average slip angle, $\bar{S}$, for all trials. The first marker and last marker were excluded from the averages because of error in the B-spine fit associated with the end-points. Error bars show ± s. d.

Slip values were compared to wave efficiency, η, using simulated data with 10 markers per wave (see Material and Methods, Fig. 5.5). The calculated average slip, maximum slip, and minimum slip (Fig. 5.15, black circle, green circles and red circle, respectively) calculated from the simulation are shown as a function of η. The average experimental slip calculated for the sandfish, corresponds to an η of ≈0.45, close to the value reported previously [11, 34]. The snake slip corresponds to a $\eta \approx 0.8$. In some trials there were a lower number of markers per wave than simulated data and manual tracking was done. Therefore, we expect that due to increased error, the actual η could range from 0.8 to 0.9. However, snake experimental trials with manual tracking showed similar calculated $\bar{S}$ as compared to trials without manual tracking indicating this error is low. Also, experimental body midlines of snakes during sand-swimming look similar to the simulated data tracks with a wave efficiency between 0.8 and 0.9 (Fig. 5.5, C).

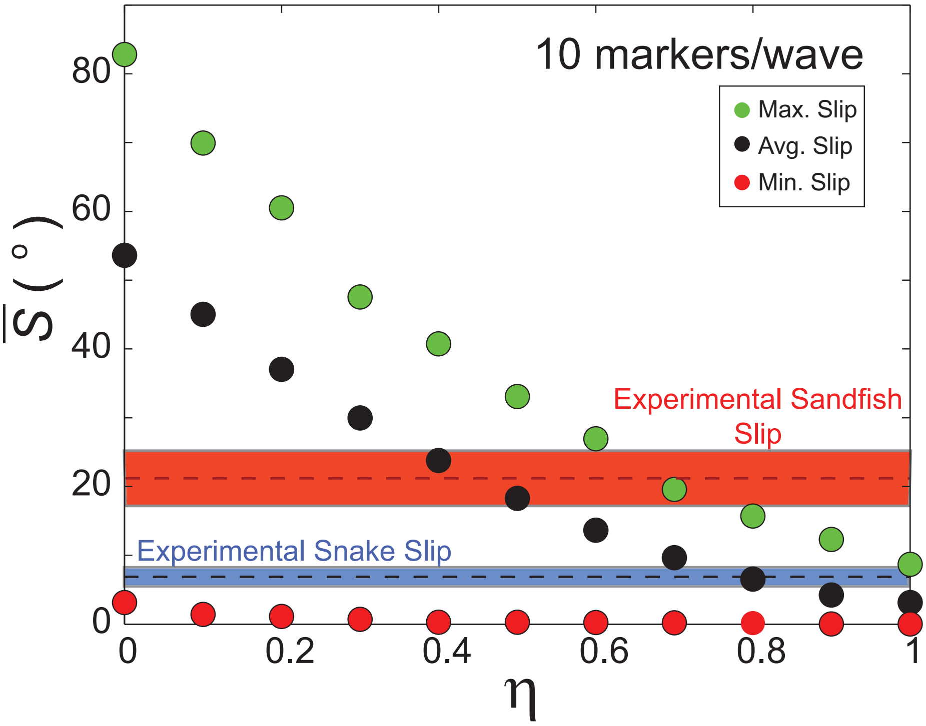

Figure 5.15: Slip factors for simulated data with known wave efficiency. The average slip factor (black points), the maximum slip factor (green points) and the minimum slip factor (red points) are shown over 1 undulation cycle for the case when there are 10 markers per wave. The mean experimental $\bar{S}$ (dashed line) and standard deviations (enclosed colored region) are plotted for the sandfish trials (red region) and snake trials (blue region).

5.5 RFT Comparison

When using similar body morphologies (L/r), wave numbers (ξ), and body-particle frictions (μ_s) as found for the sandfish and snake, resistive force theory (RFT) predictions of $\bar{S}$ were similar to experimentally measured $\bar{S}$ during the sandfish and snake locomotion (Fig. 5.16). Similar to previous studies [7], theory predicted that S decreased with increasing $\kappa\lambda_s$. Solid curves are for theoretical analyses with μ_s=0.17 and L/r= 14.1, similar to the parameters experimentally measured in the sandfish. $\bar{S}$ decreased as ξ increased for a given $\kappa\lambda_s$, but gave diminishing returns after ξ exceeded 1. In addition, due to the animal's finite length, increasing ξ decreased the maximum $\kappa\lambda_s$ achievable due to geometry. For example, for the sandfish morphology, it is not possible to have a wave number of 2 and $\kappa\lambda_s$ greater than 6. This is limited by the maximum 'winding number' which is defined as the maximum number of circles (or turns) that can be formed when bending the animal's body maximally. We estimate the maximum winding number is ≈2 in the sandfish and ≈10 in the snake. For the sandfish, which has a low winding number, increasing the number of waves along its body would constrain the animal to use lower $\kappa\lambda_s$ bends and could lead to higher overall slip.

Surprisingly, increasing L/r to 83.3 while holding ξ constant had little effect on the performance curve (Fig. 5.16, cyan solid curve compared to cyan dashed curve). However, higher L/r may offer an advantage for the animal by increasing maximum winding number (allowing either a higher curvature, longer body, or both) which would enable the use of a high ξ and $\kappa\lambda_s$. We simulated the snake's lower body friction by decreasing tangential forces acting on each segment by 50% in the RFT model. A L/r value of 83.3 was used since L/r measurements were large in the snake. The lower μ_s, higher ξ, and higher L/r predicted $\bar{S}$ values that were within the range of $\bar{S}$ experimentally measured during snake locomotion. It is interesting to note that the model predicted no differences between curves for $\xi > 4$, and the snake used an average $\xi = 3.5$. This may indicate the animal is targeting this maximum number of waves to optimize performance.

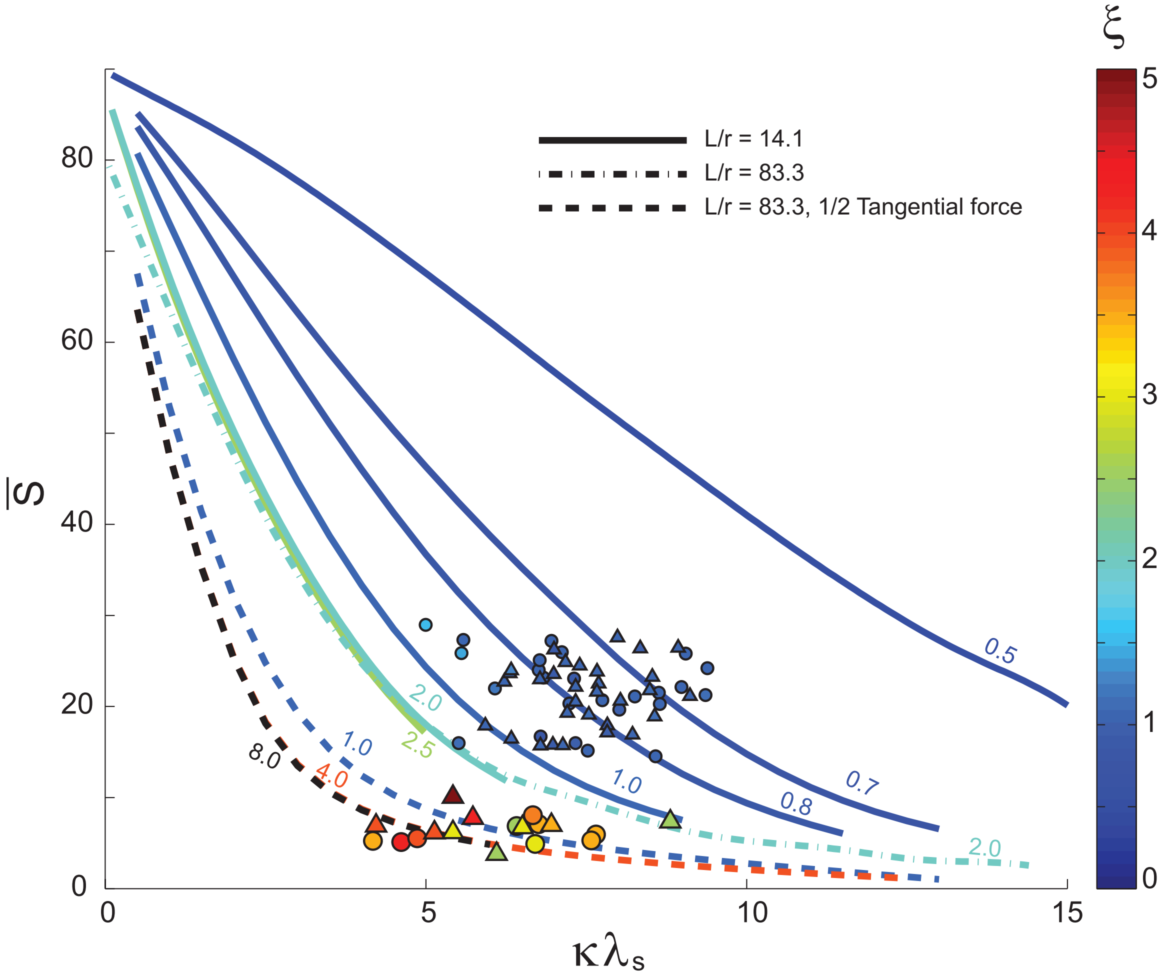

Figure 5.16: Granular resistive force theory predictions of average slip ($\bar{S}$) with changing relative curvature ($\kappa\lambda_s$), number of waves along the body (ξ), body length to radius ratio (L/r), and effective friction. The color of the curves corresponds to ξ (where dark blue is $\xi = 0$, dark red is $\xi = 5$ and black is $\xi = 8$). All solid curves are predictions for an undulatory swimmer with a $L/r = 14.1$ and body-particle friction, μ_s, of 0.17. The dotted-dashed curves show the theoretical predictions with $L/r = 83.3$ and $\mu_s = 0.17$. The dashed curves are the predictions for $L/r = 83.3$ and when tangential forces were decreased by 50% (simulating a lower body-particle friction). These values are closer to the experimentally measured snake values. Experimental data taken in CP media (circles) and LP media (triangles) are shown where the large symbols correspond to the snake data and the smaller symbols correspond to sandfish data. The color of the symbols corresponds to ξ.

5.6 Discussion

5.6.1 RFT Model Predicts Snake Performance

Previous studies have found that during subsurface locomotion the sandfish generates a localized region of moving granular media, or a ‘frictional’ fluid, around its body [7,8] (see appendix for DEM simulation of modeled surrounding media, Fig. 5.19). Although, the shovel-nosed snake yielded the material less during sand-swimming, we found that snakes also slipped during subsurface movement. Furthermore, the RFT model of a frictional fluid that incorporated the snake's body morphology and friction was able to predict the experimentally observed slip. This indicates that snakes also swim within a friction fluid during subsurface locomotion. To move in a 'tube' without slip, an animal would have to apply normal force on the medium that was less than the material yield strength. For example, Mazouchova et al. [208] found that sea turtle hatchlings moved on loose sand by inserting the flipper into the media and applying a thrust force that was under the media's yield stress but was sufficient to propel themselves forward. In this way, the turtle maintained a solid region around its flipper and was able to move with a performance that was comparable to movement on hard ground. We hypothesize that the snake must use a higher thrust force relative to the hatchlings because its body is surrounded by media causing the snake to experience a higher drag during movement. In addition, due to the snake's long body and low friction the slip is already low, and controlling force such that it does not exceed the material yield stress may not offer the snake much improvement in performance.

Tracks left by the shovel-nosed snake moving on the surface of sand in nature revealed that the snake moved with $S \approx 0$ [81]. This lower slip above surface could be due to decreased drag on the body. However, quantitative laboratory measurements are needed to make a more thorough comparison.

5.6.2 Body Length, Friction and High Relative Curvature Improves Performance

For a wave number (ξ) of 2, increasing body length relative to the radius (L/r) did not substantially change slip for a given swimming curvature. We expect that for more extreme changes in L/r, slip may be more affected. However, having a larger L/r may have an indirect advantage for the snakes by increasing the maximum winding number [217]. This increase in winding number allows the snakes to use a larger ξ ($\approx$3.5) while maintaining high relative curvature ($\kappa\lambda_s$) during swimming. In contrast, using a wave number greater than 2 would constrain sandfish to low $\kappa\lambda_s$ and increased slip.

Surprisingly, we found that the low snake skin friction ($\mu_s \approx 0.11$ on the ventral surface) may be largely responsible for the observed low subsurface slip compared to the sandfish ($\mu_s \approx 0.19$ on ventral surface). Previous reports on the ventral skin friction in snakes show variations ($\mu_s \approx$ 0.2-0.4 in the grass snake on a smooth dry surface [218]; $\mu_s \approx$ 0.15-0.2 in the Amazon tree boa on resin surfaces with different roughness [219]; $\mu_s \approx$ 0.11-0.14 in the Pueblan milk snake on a cloth surface and smooth fiberboard [186]). Because these experiments were conducted on a range of materials, it is hard to compare them directly to our measurements. While studies have anecdotally reported that fossorial animals have reduced skin friction [55], measurements which support this claim are lacking. However, our study suggests that having a lower skin friction would increase performance during subsurface movement and may imply that this adaptation in burrowers would be advantageous.

For these RFT simulations, $\kappa\lambda_s$ did not change along the simulated swimmer's body. However, we observed that the snake used a higher average $\kappa\lambda_s$ during initial burial compared to movement deeper within the substrate. Future work which uses models with differing $\kappa\lambda_s$ along the body could be used to explore if waves with high $\kappa\lambda_s$ can compensate for low $\kappa\lambda_s$ waves in order to maintain low slip with less lateral excursions.

5.7 Conclusions

Shovel-nosed snakes use a continuous motion of lateral body undulations to propel themselves within granular media similar to the sandfish. The snake and sandfish use a similar relative curvature during swimming, but the snake has a higher number of waves along its body, a phenomenon enabled by its long-slender body morphology. Resistive force theory predicted the lower slip of the snake when incorporating its lower skin friction and body morphology into the model. This indicates that the snake is also swimming within a frictional fluid and its higher performance is a result of its differing skin friction and winding number, which allows it to use a high ξ while maintaining a large $\kappa\lambda_s$.

5.8 Appendix

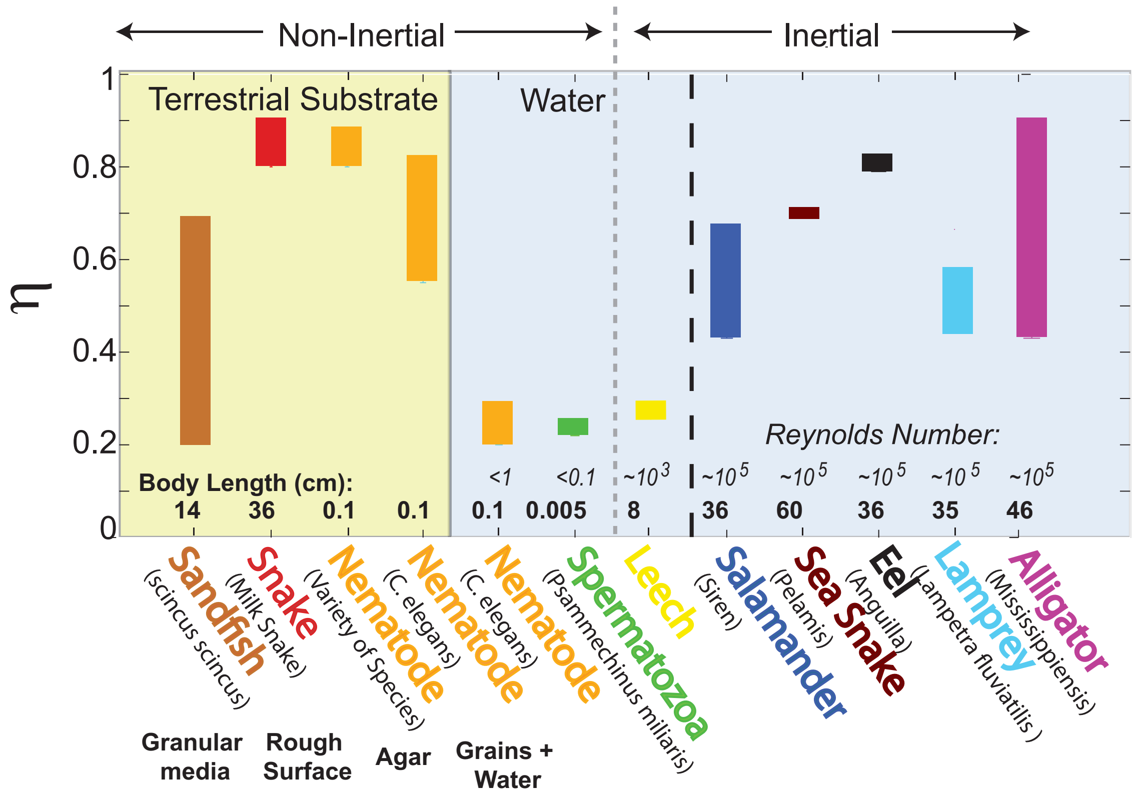

Figure 5.17: Wave efficiency (η, defined as the forward velocity over the velocity of the traveling wave) for a variety of undulatory animals in different environments. Animals moving in low-Reynold's number fluid tend to move with a low wave efficiency, while animals moving on the surface of a substrate tend to use a high wave efficiency. For animals moving in an inertial fluid, wave efficiency can vary and may be dependent on movement strategy. Sandfish lizard and nematodes that are surrounded by particles tend to use an intermediate wave efficiency. [11,33,34,126,133,210,211,220–222]

5.9 *Contributions*

Stephan A. Koehler performed the granular resistive force theory (RFT) calculations for the snake and sandfish body shape and friction (solid and dashed curves in Fig. 5.16). Robyn M. Kuckuk modified the experimental apparatus for snake trials and collected all kinematic snake data. Miguel Serrano provided automatic tracking program to identify marker locations on the snake midline over the course of a trial. He also wrote code to fit B-splines to the midline of snake kinematics.

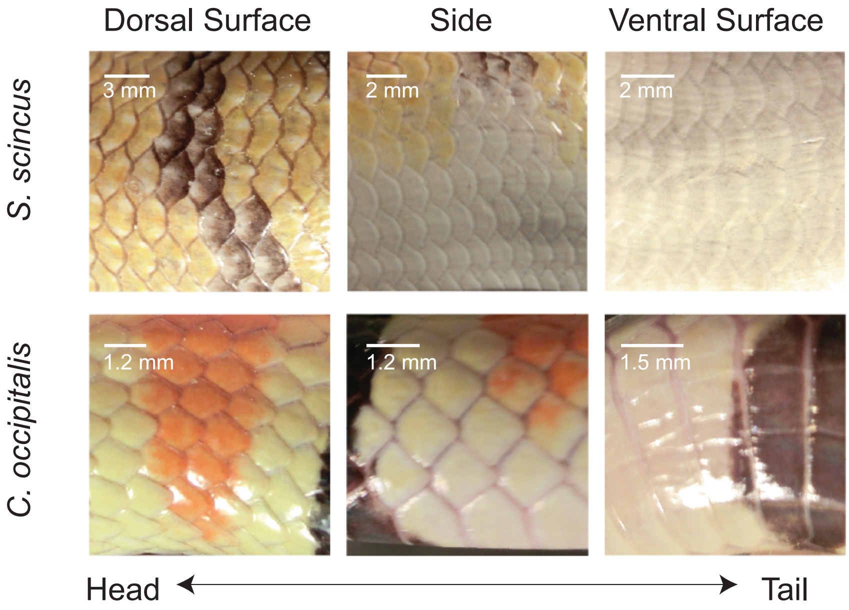

Figure 5.18: Picture showing the sandfish's scales (top) and shovel-nosed snake's scales (bottom). In each picture the head of the animal is toward the left and the tail is toward the right. For the pictures of the sides, the dorsal surface is toward the top of the image and the ventral is toward the bottom. A scale bar is shown on each image.

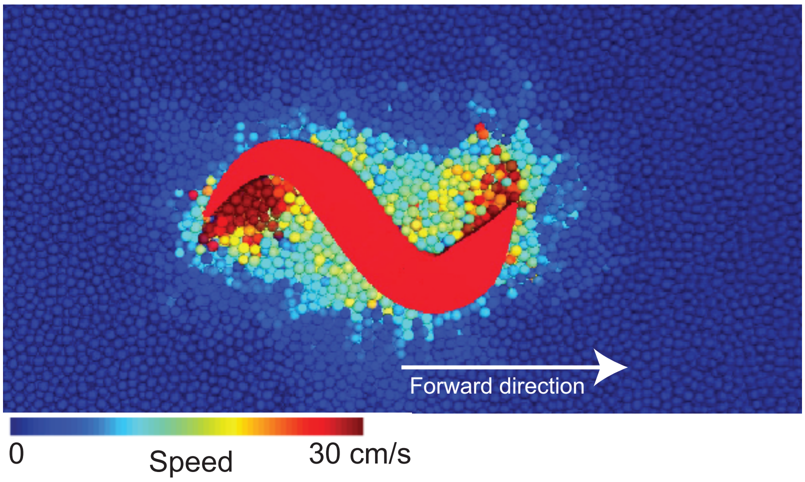

Figure 5.19: DEM simulation of moving sandfish in simulated 3 mm diameter particles. Particles are colored according to speed. The undulatory swimmer creates a localized fluid region around its body [7]. Figure courtesy of Yang Ding.

CHAPTER VI

OCELLATED SKINK (*CHALCIDES OCELLATUS*) BURIAL BEHAVIOR AND PERFORMANCE REVEALED USING NEW TECHNIQUE FOR CREATING HOMOGENOUS WET GRANULAR MEDIA

6.1 Summary

Granular media, such as agricultural soils and beach sands, are abundant in nature. The properties of such substrates can depend sensitively on water content and compaction, factors influenced by geographical location and weather variations. Numerous animals move on and within these substrates but little is known about how granular media wetness influences locomotion behaviors and mechanics. This is due in part to the challenges associated with creating large repeatable preparations of wet substrates in which wetness and compaction can be varied and accurately measured. To systematically study locomotion, we developed a novel technique such that large volume ($\approx$6500 cm^3) preparations of wet granular media are created that lack large voids and where compaction and water content can be independently varied. We found that a small addition of water to dry granular media increased resistive forces on a small cylindrical intruder that moved through the substrate by a factor of 4. Furthermore, increased compaction within the wet substrate doubled resistive forces. Using our technique, we explored the subsurface locomotion strategy of the ocellated skink (*Chalcides ocellatus*), a desert-generalist lizard that burrows into both wet and dry substrates. We compared the skink's burial performance in a dry and wet medium using high speed x-ray imaging to characterize head, body and limb kinematics. In both substrates,

---

This chapter is a paper in preparation by Sarah S. Sharpe, Robyn Kuckuk, and Daniel I. Goldman the ocellated skink maintained a curved body posture and moved using a start-stop motion. During forward movement, the head oscillated and the forelimb on the convex side of the body was used to push the animal forward. However, both speed and maximum head angular excursion were lower in the wet substrate compared to the dry, and the skink was unable to achieve large submersion depths in wet media. We attribute the differences in performance to the larger resistance forces experienced in the wet substrate and hypothesize that the animal may prefer pre-made burrows in wet soil during burial in nature.

6.2 Introduction

A diversity of animals live on and within granular media (GM), materials that can display both solid and fluid-like features. Dry granular media such as that found in sandy deserts, are collections of particles that interact through dissipative, repulsive contact forces [2]. Recent work has worked to understand locomotion in dry sand by studying animal movement on GM, such as sandfish (*Scincus scincus*) burial [11, 34] and zebra-tailed lizard (*Callisaurus draconoides*) running [25, 104, 223]. Theoretical, computational and robotic models have helped to elucidate how animals interact with the surrounding GM to generate successful forward locomotion [7, 8, 69, 78, 89, 105]. These studies have benefited from laboratory versions of the environment where parameters, like compaction and grain size, can be systematically varied, resistive forces can be measured, and animal studies can be compared with models that incorporate the same substrate properties.

Wet granular media make up an even larger proportion [224] of terrestrial substrates, occurring in rainforest soils, coastal regions, and agricultural lands (see Fig. 1.16 in Chapter 1). The addition of water to dry granular media can have large effects on the substrate physics, enabling the formation of sandcastle-like structures [106, 107, 225]. Despite the myriad of animals that walk, run, and burrow within wet terrestrial soils, few studies have explored these locomotion strategies [226–228] and even fewer animal studies have systematically varied water content and/or compaction [43] of the substrate. In this Chapter, we develop a technique to prepare wet granular substrates with repeatable compaction and water content and explore the burrowing strategy of the ocellated skink (*Chalcides ocellatus*), which is found on coastal regions and near vegetation where moist sand is common (Fig. 6.1).

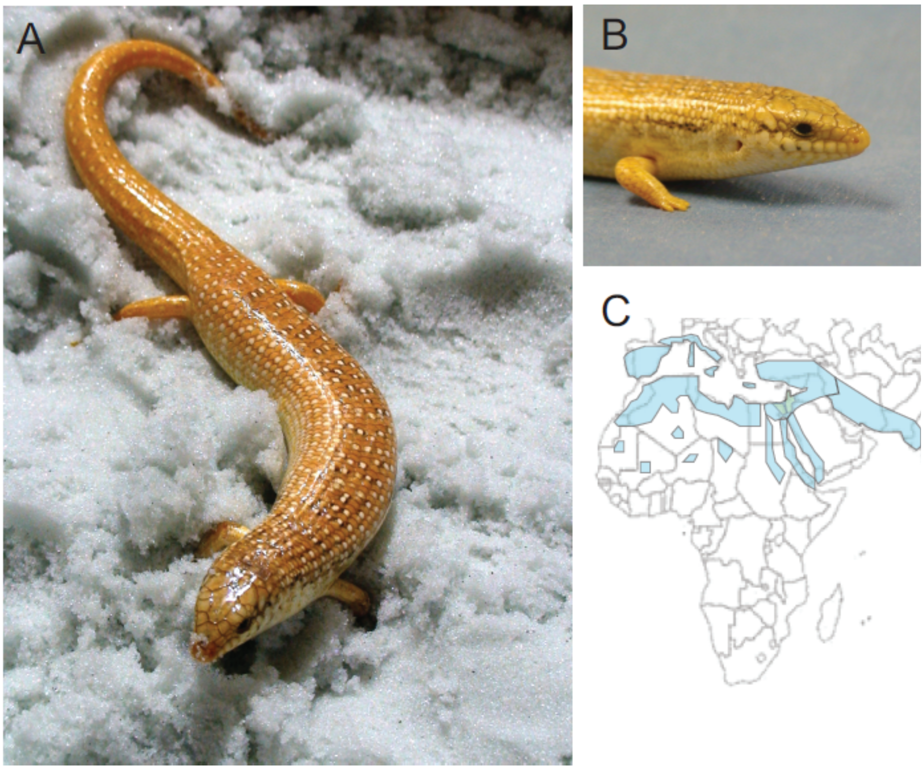

Figure 6.1: The ocellated skink (*Chalcides ocellatus*) is a habitat generalist and moves on and within both wet and dry media. (A) The ocellated skink resting on wet 0.3 mm diameter glass particles. (B) Side view of the ocellated skink head and forelimb. (C) Map showing locations that the ocellated skink has been found (blue regions) which include northern Africa, southern Europe, and western Asia (modified from [84]).

Ocellated skinks co-exist with sandfish lizards (Fig. 1.7) in the sand dunes of North Sinai, Egypt [70]. However, within this environment the ocellated skink occupies a different microhabitat. Ocellated skinks are commonly found near vegetation and 'harder' soil whereas the sandfish is found farther from vegetation on the dry, loose sands of the dunes. Recently, the sandfish burial and subsurface locomotion have been studied extensively [8,11,34]. The sandfish swims subsurface within dry substrates at high forward speeds ($\approx$4 cm/s or 0.9 SVL/s) using large amplitude body undulations while the limbs remain close to its sides. While this burial and swimming strategy is effective in dry media, sandfish in captivity either avoid wet media (as in nature) or use a limbed digging strategy to displace the wet sand (from personal observations). This may indicate that in wet sand the sandfish swimming strategy is ineffective. In contrast, ocellated skinks have been observed to burrow into both wet and dry substrates. The ocellated skink has a slender body with relatively reduced limbs [229] that lack toe fringes and, like the sandfish, has a wedge-shaped head. Fields observations have shown that the ocellated skink spends most of its time near cover and will bury into granular substrates to seek refuge from heat and predators [70]. In this chapter we will explore how ocellated skinks are able to submerge and move subsurface, and identify differences in the locomotion strategy between burial into wet and dry granular media.

Soil water content (W, defined as the ratio of the mass of the water to the mass of the dry sand) can vary with factors such as geographical location, weather conditions, time of day, or depth beneath the surface. Water induces cohesion between sand grains due to the surface tension of the fluid and capillary effects [106]. This increased cohesion results in an increased angle of stability for a granular pile, such that sandcastle structures and tunnels can be formed [106, 111], and can influence mechanical properties such as shear strength [110]. Wet granular media is usually grouped into 4 states: pendular—in which liquid bridges form between particle contacts; funicular—where the liquid fills the pore-space spanning multiple particles but some air-filled voids remain; capillary—where all pores are filled with liquid; and the slurry state—in which particles are completely immersed in the liquid and no capillary action occurs at the surface [106, 107] (Fig. 6.2). The top layer of soil found on the majority terrestrial surfaces are in the pendular or funicular state [224].

The compaction of a granular medium is characterized by the volume fraction, ϕ, defined as the ratio of the volume of dry granular media to the volume of the occupied space [2]. For dry granular substrates in nature, ϕ can range from 0.55 to 0.63 [95]. The compaction can be controlled in the laboratory setting by using an air-fluidized bed [69, 90] in which a combination of air-flow and shaking is used to generate different ϕ states. As little as a 4% increase in ϕ can increase resistance force by 50% [11]. Despite the well established literature on dry GM emphasizing the importance of ϕ in influencing the substrate behavior, compaction is typically not reported or controlled in wet granular experiments, especially

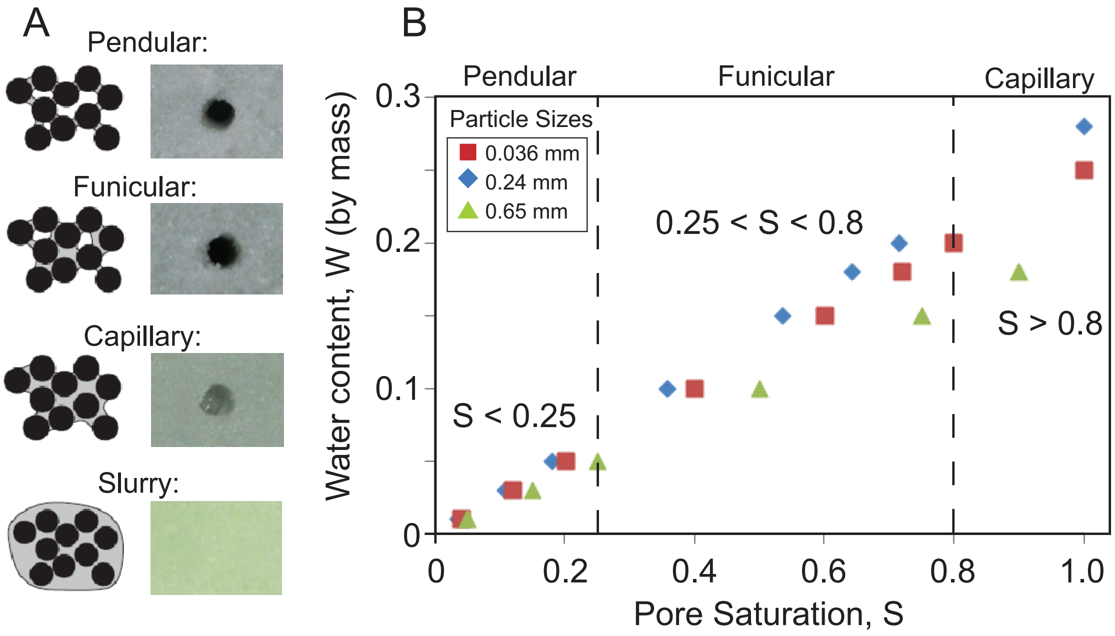

Figure 6.2: Description of the wetness states (A) (Left) Diagrammatic representation of the 4 wetness states. Figure reproduced from [106]. The black circles represent grains and the gray regions represent the liquid. At low water contents wet media is in the pendular state where liquid bridges form between individual particles. With increasing wetness content, liquid bridges begin to merge. In the capillary state all pores are filled with liquid but capillary action at the surface occurs. After saturation the slurry state occurs and no capillary action occurs at the surface. (Right) Images of granular media in the 4 states with a hole made in the media. In the slurry state the hole fills in completely. (B) Water content vs. pore saturation (where S=0 is dry media and S=1 is full saturated media) for different particle sizes (diameter = 0.036 ± 0.011 mm (red squares), 0.24 ± 0.03 mm (blue diamonds), and 0.65 ± 0.15 mm (green triangles)). Figure courtesy of Daria Monaenkova.

for animal locomotion studies. Furthermore, wet granular media can exhibit an even larger range of ϕ; lower ϕ can be achieved in wet GM compared to dry due to the stabilizing effect of the liquid bridges [106]. In a review of wet granular physics studies, Mitarai [106] stressed the importance of "careful preparation" of laboratory versions of wet GM in order to get reproducible results, and mentioned that compacting the wet media in a different way could generate different mechanical responses.

Currently, there is no well-established technique to create repeatable, homogenous preparations of wet granular media with controllable compaction and wetness. The techniques that have been used previously include: (1) Mixing the liquid and dry media, followed by slow pouring into a container [114]; (2) Vigorously shaking of the liquid-sand preparation to homogenously distribute the water [107,110]; (3) Constructing thin (2.5-5mm thick) layers of sand and using a fine jet to spray a known quantity of water onto each layer before another is added [115]; (4) Imbibition (a wetting process) in which water is allowed to percolate through the media [108]; (5) Use of a humidifier [116] to introduce water into the substrate; and (5) Drainage (a drying process) [108]. Studies that have attempted to control or alter the compaction do so by using a ram [117] or by tapping the material [107,113,116] to achieve higher ϕ states. While these methods are sufficient to achieve homogeneity for high ϕ states, either these methods do not produce low ϕ preparations or, if they do, these preparations may contain large voids which are variable depending on the trial.

We present a novel technique which uses a sieve apparatus to deposit mixed wet granular media into a container that results in an initially loose packed state and does not contain large voids. Additional shaking after the material has been deposited increases media compaction. We characterize and evaluate this system's capabilities for creating low water content preparations at 0.01, 0.03 and 0.05 W (i.e. pendular states) and show that both W and ϕ influence resistive forces exerted on an intruder moving through the medium. We then characterize the burrowing strategy of the ocellated skink in dry and wet (0.03 W) granular media which were prepared using the air-fluidization and sieving techniques, respectively, such that repeatable conditions were obtained across trials.

6.3 Materials and Methods

6.3.1 Dry Media Preparation

Loosely packed (LP) dry granular media preparations ($\phi = 0.58 \pm 0.01$) were created using an air-fluidized bed with an area of 22.9×40.6 cm^2 and filled with spherical glass particles to a height of 10 cm (see Chapter 2 and [11,34]). The particles were similar in size (diameter $= 0.27 \pm 0.04$ mm) and weight (density $= 2.5$ g/cm^3) to sand found in nature. An evenly distributed air flow was generated that moved upward through the grains; below a critical flow rate grains remained stationary and above the flow rate the grains moved relative to each other which is referred to as fluidization. To generate the LP states, the medium was fluidized followed by a slow decrease in flow rate to zero. Air flow was off during resistance force measurements and animal burial trials.

6.3.2 Wet Media Preparation

6.3.2.1 Wet Media Mixture

A high-speed hand mixer (Hamilton Beach/Proctor-Silex, Southern Pines, NC) was used to combine 14 kg of dry spherical glass particles (diameter = 0.27 ± 0.04 mm, density = 2.5 g/cm^3) with 0.14 kg, 0.42 kg and 0.7 kg of water, such that 0.01, 0.03 and 0.05 water content (W) preparations were achieved, respectively. The media were mixed for at least 3 minutes to distribute water evenly throughout the preparation. Media preparation and experimentation took place in a room with a humidity level of ≈41% and temperature of ≈25°C. The wet mediums were used in experiments for only two hours after preparation to limit changes in water content due to evaporation. We characterized water loss due to evaporation by preparing 0.01 W, 0.03 W and 0.05 W mixtures and weighing the substrates periodically. The substrates were stirred once every hour. These experiments revealed that W decreased by 0.0014± 0.0003 W after two hours for all starting W preparations.

6.3.2.2 Apparatus Development

A 'sieve' apparatus was constructed in order to deposit media homogenously into a testing container (Fig. 6.3). The sieve apparatus consisted of two polycarbonate boxes (30.5 × 30.5 × 19.5 cm^3) that were stacked vertically, a holding plate, and a vertical shaker. The top box was separated from the bottom container by a stainless steel woven mesh grid (wire diameter = 1.2 mm, opening area of 3 × 3 mm^2). The wet media was poured into the top container of the sieve apparatus. The cohesion between grains prevented the media from falling through the mesh when the apparatus was stationary. The stacked boxes fit securely into a holding plate and were secured using straps which prevented relative motion between the boxes and plate during shaking (Fig. 6.3, A). Sinusoidal vertical vibrations, with a frequency of 60 Hz and average amplitude of 1.75 mm, were applied to the holding plate via the electromagnetic shaker (VTS, Auroa, OH). Media readily fell through the mesh when these vibration parameters were used (Fig. 6.3, B). The shaker was controlled using custom software (LabVIEW, National Instruments, Austin, TX) and a power amplifier

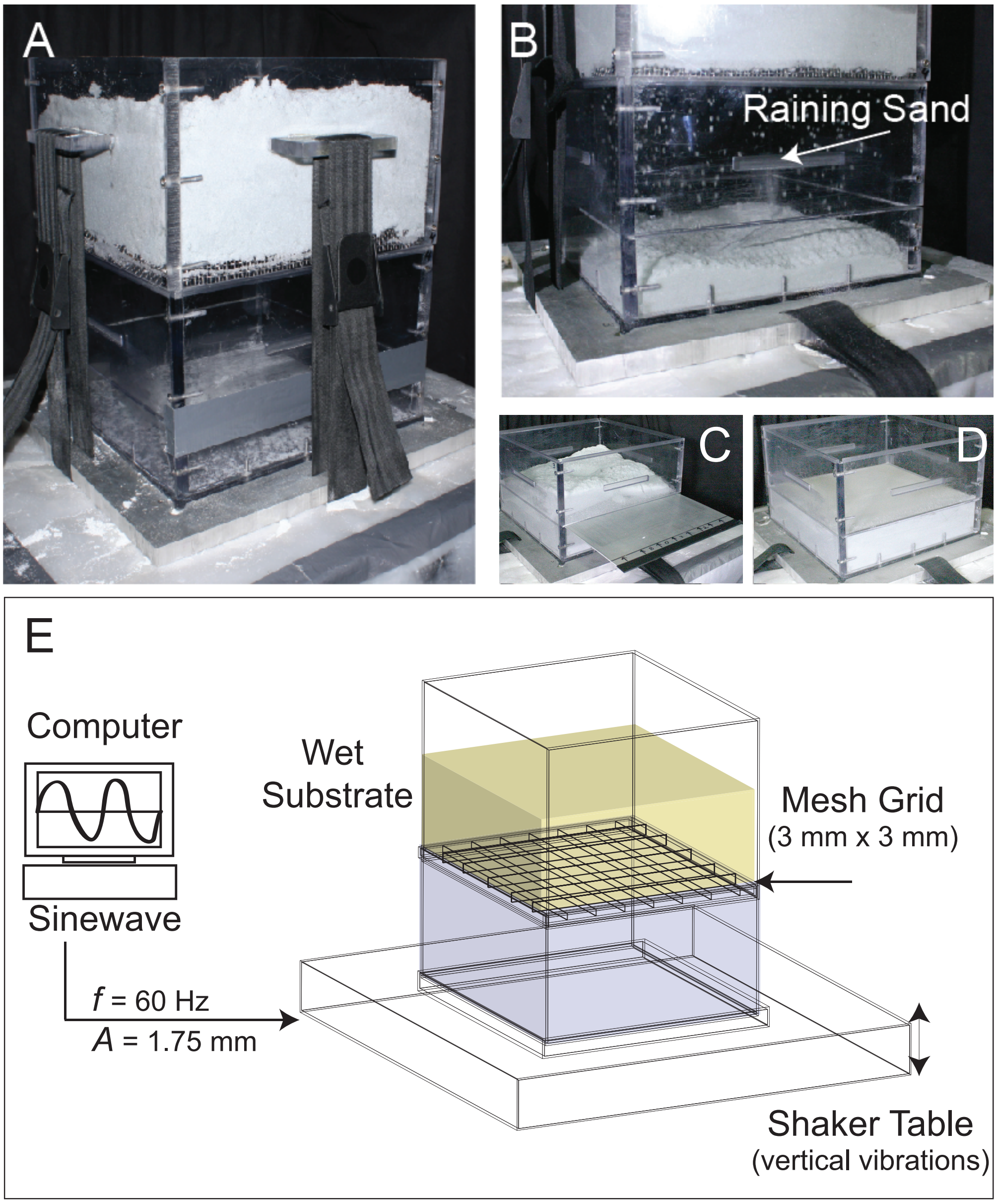

Figure 6.3: Wet media sieve apparatus. (A) Apparatus with the wet media loaded into top container prior to shaking. (B) Agglomerates of wet grains fall through the mesh due to vertical vibrations and accumulate in the lower container. (C) The leveling sheet slices through the media separating the media at a desired height. (D) Leveled preparation used for experiments, with the final volume of 30.5 × 30.5 × 6.9 cm^3. (E) Schematic of the sieve apparatus and shaking parameters.

(Model # 7550, Techron, Elkhart, IN). Vibrations were monitored using an accelerometer (PCB Piezotronics, Depew, NY) that was attached to the holding plate. The software monitored the shaking and maintained the desired shaking paramters using a PID controller. Changing the amplitude and/or frequency of the vibrations changed the shaker efficacy of inducing media deposition. Analysis of how these parameters affect the final medium compaction is beyond the scope of the present study.

Shaking was stopped after the sieved material in the lower container exceeded a height of 7 cm. A slit and groove located at 7.06 ± 0.16 cm in the lower box allowed a thin aluminum plate to slide into the container separating the granular media into two sections (Fig. 6.3, C). The top media above the thin plate was removed leaving a volume of wet media ($30.5 \times 30.5 \times 6.9$ cm^3) with a level surface which was used for experiments (Fig. 6.3, D). The volume fraction, ϕ, was determined by weighing the wet media. Due to the leveling technique, the volume of the space occupied remained constant across trials. The volume of the dry granular media was determined from the relation $V_{GM} = \frac{M_{wet}}{\rho_{GM}(1+W)}$, where ρ_{GM} is the density of the granular media, M_{wet} is the mass of the wet media and W is the water content. Due to the error in the volume and W measurements, we estimate a systematic error in the ϕ calculation of ± 0.007.

6.3.2.3 Technique Characterization and Capabilities

Homogeneity-

We evaluated the homogeneity of a sieved wet media preparation (W = 0.01, ϕ = 0.575) using x-ray imaging (source: OEC-9000, Radiological Imaging, Hamburg, PA, USA; detector: Varian flat panel 25250V Csl, Palo Alto, CA, USA) (Fig. 6.4, A). The x-ray was set to an energy of 20 mA and 60 kV. Variations within the substrate were detected by examining the pixel intensity (on a 0-255 grayscale) where higher intensities (appearing more white) indicate areas containing voids and darker areas (appearing more black) have a higher concentration of media. The sieved preparation was compared to wet media (W = 0.01) that was mixed then compacted by 'hand' by dropping the media container from a height between 5-8 cm multiple times to remove large voids (Fig. 6.4, A). Fluctuations in the hand preparation were higher ($\approx$50 grayscales, Fig. 6.4, B) compared to the fluctuation in the sieve preparation ($\approx$10 grayscales, Fig. 6.4, B).

Compaction-

The media deposition process lasted a minimum of 70 s to achieve $>$ 7 cm (in height) of

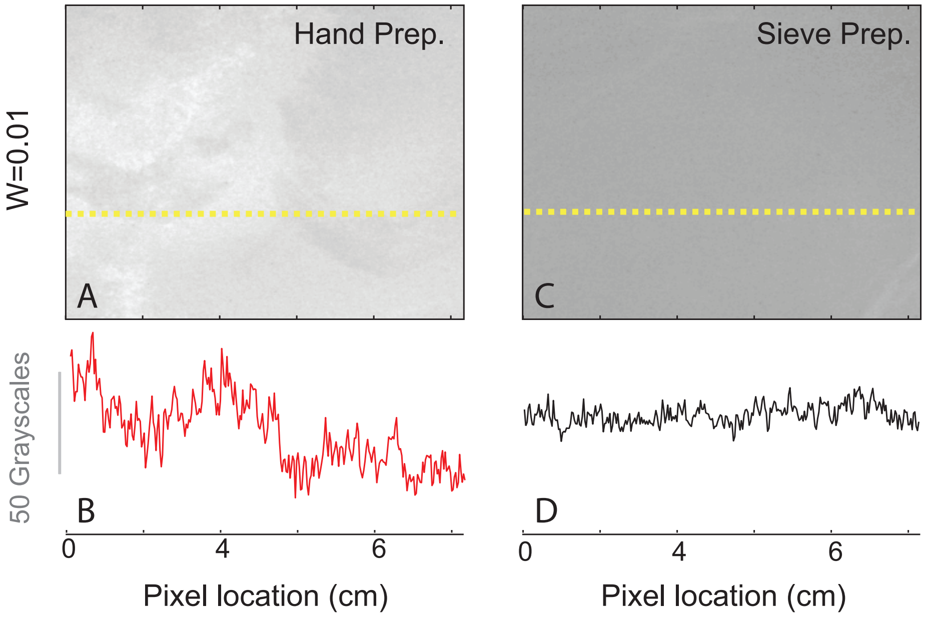

Figure 6.4: Comparison between a preparation that was mixed then dropped in order to clear large voids and a preparation in which the sieve technique was used. (A) X-ray image of a 0.01 W GM prepared with the mixer and by dropping and (B) pixel intensity (in grayscales) across a randomly chosen horizontal line (dashed yellow line in A). (C) X-ray image of the 0.01 W GM prepared using the sieve technique ($\phi = 0.575$) and (D) pixel intensity across a horizontal line in the image (dashed yellow line in C).

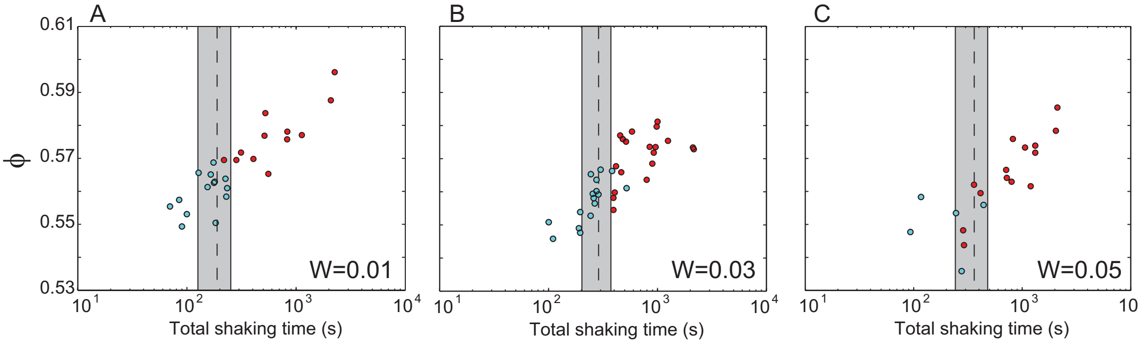

Figure 6.5: ϕ increases logarithmically with shaking time during the first 37.5 minutes of vibrations. The dashed vertical line shows the average time that it took the entire wet media preparation (14 kg dry sand + water) to shake through the sieve (gray bar shows ± s.d). Light blue points indicate that the shaking stopped at or before all material had fallen through the sieve. Red circles indicate trials in which shaking was continued after all the media had fallen through the mesh.

media in the bottom container. The average time for all wet media (≈14 kg) to fall through the mesh increased with wetness content (188.5 ± 62.6 s for 0.01 W, 287.9 ± 84.8 s for 0.03 W, and 316.4 ± 119.7 s for 0.05 W; Fig. 6.5). The total shaking time was varied between

70 s and 2250 s to achieve varying compactions.

Depending on shaking time, compaction varied between ϕ = 0.53-0.60 (Fig. 6.5). As expected due to the stabilizing effect of liquid bridges, the minimum ϕ obtained in wet media was lower than the minimum ϕ achieved in dry media (ϕ= 0.58) using the air-fluidization technique. Compactions higher than ϕ = 0.60 were never produced within the 40 minutes of shaking which was the maximum time used in these experiments. For all wet media preparations, the compaction of the media increased logarithmically with shaking time. Fiscina et al. [113] found that ϕ as large as 0.62 could be achieved in water-granular media mixtures. Since we did not observe an asymptote in compaction with increased shaking time, we expect that higher compactions are possible for shaking times >40 minutes.

6.3.3 Force Measurements

To measure penetration resistance and drag force in wet and dry granular media, a robotic arm (CRS robotics, Burlington, Ontario, Canada) with 6 degrees of freedom was used to drive a stainless steel cylindrical rod (diameter = 1.6 cm and length = 3.81 cm) through the media. A support rod (diameter = 0.63 cm) and nut (height = 0.55 cm, corner-to-corner width = 1.25 cm) were used to attach the cylindrical intruder to a force sensor (ATI industrial, Apex, NC, USA), accurate to 0.06 N, located on the robot end effector. The cylinder was submerged 3.2 cm into the granular media (measured from its center axis to the surface of the substrate), and the cylinder was dragged 12.7 cm where its long axis was oriented perpendicular to the direction of motion (Fig 6.6, A). Speed during penetration and drag was 10 cm/s (where force is insensitive to speed in dry granular media below 50 cm/s [11, 34] and preliminary studies indicate the same force insensitivity in wet media). The total projected area of the cylinder, submerged support rod and nut during drag was 8.4 cm^2. The instantaneous force periodically fluctuated due to material fracturing that occurred during movement within the substrate (see results, Fig 6.6, B); consequently, the average drag force was calculated during steady state movement from the start of one oscillation to the start of another oscillation.

To quantify the average drag force as a function of depth on an intruder with the same projected area (6.1 cm^2), the drag force on the support rod and nut was subtracted from the drag force of the cylinder + support rod and nut. Force as a function of depth was quantified in dry media ($\phi \approx 0.58$) and in 0.03 W wet media ($53.2 \leq \phi \leq 55.7$).

6.3.4 Ocellated Skink Experiments

Ocellated skinks, *Chalcides ocellatus*, (Fig. 6.1) were purchased from commercial vendors (East Bay Vivarium, Berkeley, California, USA and Ocean Pro Aquatics, Chino Hills, CA, USA). The 4 animals used in this study had an average snout-vent length (SVL) of 10.9 ± 1.3 cm, snout-tail length (STL) of 18.6 ± 3.2 cm and mass of 21.5 ± 6.8 g. All animals were housed individually in large containers ($21 \times 43 \times 28$ cm^3) filled with moist sand to a depth of 15 cm and were provided with a water dish and moss for hiding. Ocellated skinks were given 6 mealworms coated in a supplemental calcium powder twice a week and allowed to eat *ad libitum.* The holding room was maintained on a 12 h:12 h light:dark cycle. All experimental procedures were conducted in accordance with the Georgia Institute of Technology IACUC protocol numbers (A08012, A11066) and Radiation Safety protocol (X-272).

We compared the burial strategy of the ocellated skink on loosely packed ($\phi = 0.56 \pm 0.01$) 0.03 W wet granular media to the strategy used on loosely packed dry granular media ($\phi = 0.58 \pm 0.01$). Loosely packed (LP) wet media was used because ocellated skinks did not bury as readily into closely packed (CP) wet media. Ocellated skinks were placed on top of the media preparation inside of a 14.5 cm diameter hollow plastic cylinder resting on the surface of the substrate which induced burial at a desired location. For enhanced contrast, a minimum of 11 lead markers (≈ 1 mm^2 each, mass ≈ 0.01 g) were placed on the skink's midline at 0.1 SVL increments and one marker was placed on each limb. Above surface visible light video recorded at 63 frames per second (fps) using a high speed camera (AOS Technologies AG X-PRI, Baden Daettwil, Switzerland) to characterize general features of above surface movement such as time to burial and limb use. Top-view subsurface kinematics were recorded using an x-ray system (OEC 9000, Radiological Imaging Systems, Hamburg, PA, USA) coupled to a high speed camera (Fastcam 1024 PCI, Photron, San Diego, CA, USA) which recorded at 60 fps. The different above surface and subsurface video frame rates were set due to camera constraints. For dry granular media preparations, the x-ray system was set to 85 kV at 20 mA, and for wet preparations, to 73 kV and 20 mA. Ocellated skink burial time was determined from above surface video as the time it took for the animal to submerge such that the head to vent was covered by the substrate. When the anterior portion of the animal was buried prior to the start of the above surface recording, then the time to burial was calculated as the the time it takes for the above surface fraction of the SVL to submerge divided by the proportion of the SVL above surface at the beginning of the recording.

To determine angle of entry and final depth of burial in wet and dry granular media, biplanar x-ray was acquired. The OEC-9000 x-ray system was again used to record top view images. An additional x-ray system (source: Spellman XRB502 Monoblock, Hauppauge, NY, USA; flat panel detector: Varian 25250V Csl, Palo Alto, CA) was oriented 90° with respect to the top view x-ray such that side view images of the subsurface locomotion were simultaneously obtained. The flat panel detector captured images at 30 fps. The width of the wet granular media container was decreased to ≈17 cm by using foam inserts. Decreasing the width was necessary to enhance contrast between the ocellated skink and surrounding media during side view imaging. Opaque lead markers were placed on the dorsal midline, and along the animal's side closer to the ventral surface to enable visualization of the ocellated skink in both top and side view images. 3-D reconstructions were made using custom software (Matlab, Mathworks, Natick, MA, USA).

6.4 Results

6.4.1 Penetration and Drag Forces in a Wet Substrate

Instantaneous force during drag (Fig. 6.6, B) and penetration (Fig. 6.6, C & D) revealed a large increase (≈ 4 times greater) in force between dry and wet media preparations. During penetration, force increased with depth (Fig. 6.6, C) for both dry and wet substrates. During withdrawal, there was a slight negative force in all substrates. We attribute this negative force due to the weight of the material on top of the rod and the shearing forces that

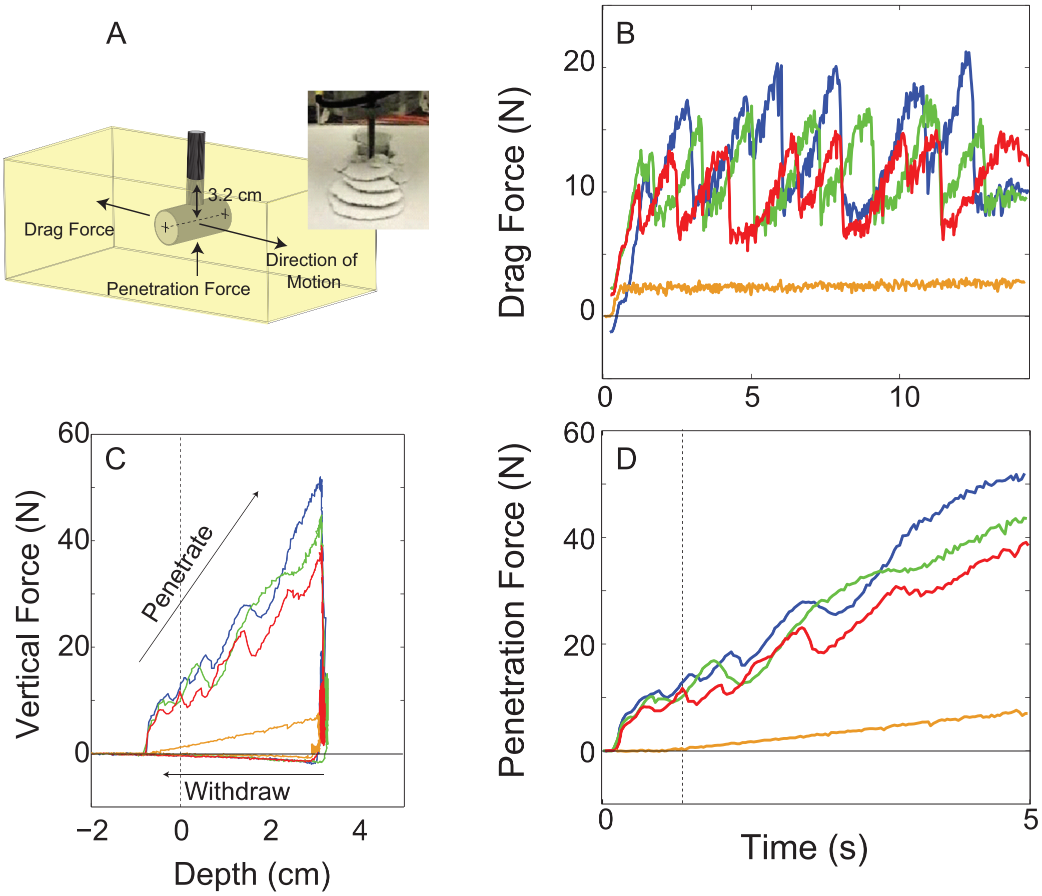

Figure 6.6: Rod drag and penetration force in granular media with varying water contents. (A) Force was obtained by dragging a stainless steel cylinder (diameter = 1.6 cm, length = 3.81 cm) and a support rod (diameter = 0.64 cm) at a depth of 3.18 cm measured from the center of the cylinder to the surface. (Inset) Material fracturing in wet media corresponding with force fluctuations in B. (B) Representative instantaneous drag force at varying water contents (orange is 0 W (ie. dry), red is 0.01 W, green is 0.03 W and blue is 0.05 W). Compactions in these representative trials are between $\phi = 0.55$ - 0.59. (C) Representative instantaneous vertical force on the cylinder during penetration and withdraw as a function of depth. (D) Vertical force during penetration (same as in C) as a function of time at varying water contents. The dotted lines in C and D indicate when the center of the cylinder was level with the surface (i.e. depth = 0 cm).

occur between the grains. Force fluctuations occurred in wet substrates during penetration and drag which corresponded to material fracturing visible at the surface (Fig. 6.6, A, inset). These large force fluctuations resemble shear band formation and fracturing during drag in CP dry media [90]. The mechanism by which these bands occur in wet media has not been investigated and is beyond the scope of this work. In agreement with previous studies [11,90], these large force fluctuations were not present during drag in LP dry media.

Average drag in 0.01 W wet media ($\phi = 0.58$) was ≈4 times larger than the average drag force in dry media (0 W , $\phi = 0.58$; Fig. 6.7). The average force continued to increase with increasing wetness content, from 0.01 to 0.05 W (ANCOVA, $F(5, 59) = 32.0, P < 0.001$), but by a smaller amount (≈1 N per 0.01 W increase). Resistance forces increased with compaction in 0.01, 0.03, and 0.05 W preparations (Fig. 6.8, ANCOVA, $F(5, 59) = 7.5, P < 0.01$). Force changes were large with small changes in ϕ; for example, force increased by 50% in 0.03 W media from approximately 8.0 N at $\phi = 0.53$ to 11.8 N at $\phi = 0.58$.

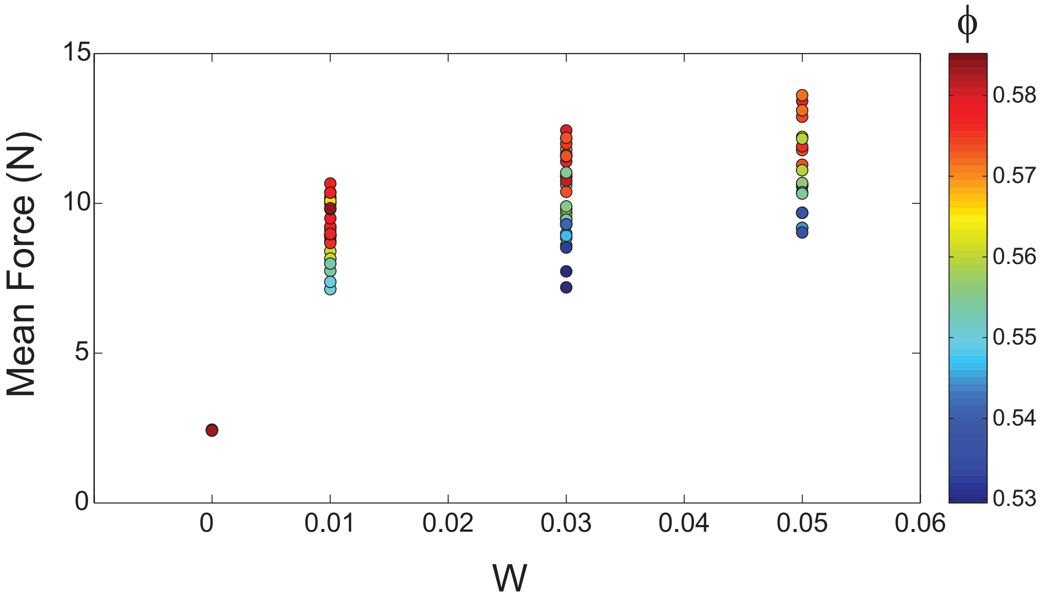

Figure 6.7: Average resistance force measurements at varying water contents and compactions (shown by color). Resistance force sharply increased from 0 W to 0.01 W, then gradually rose from 0.01 W to 0.05. For a single water content, a high ϕ state (dark red) had a 50% higher resistance force compared to the low ϕ state (dark blue).

6.4.2 Ocellated Skink Burial in Wet and Dry Media

After placement on the 0.03 W wet media, ocellated skinks took between 1 and 30 minutes before initiating burial. Light tail squeezing or tail tapping occasionally induced burial more quickly. Ocellated skinks rarely buried into substrate preparations above $\phi > 0.58$ and so loosely packed preparations of wet granular media ($\phi \leq 0.56$) were used in all experimental trials. Initiation of burial took less time in dry granular media (between 1 and 15 minutes).

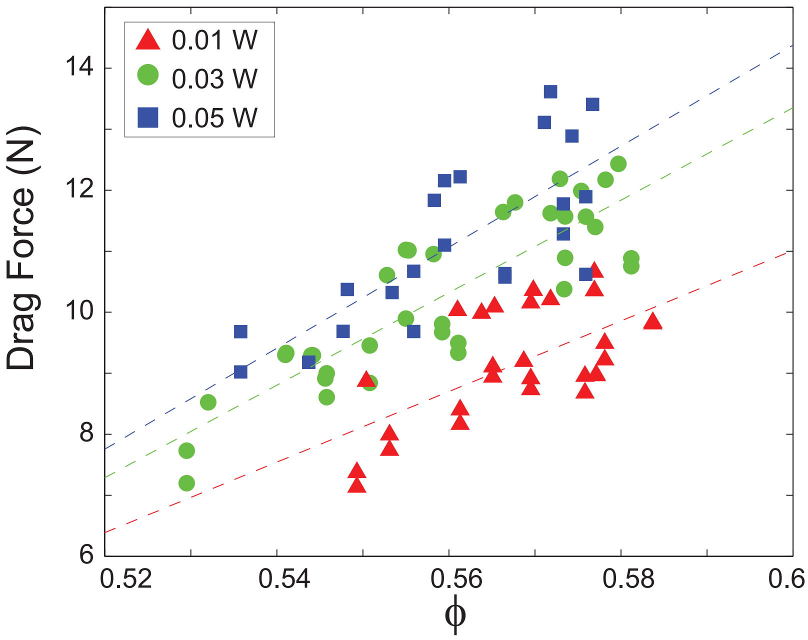

Figure 6.8: Average drag force with changing compaction for 0.01 W (red), 0.03 W (green) and 0.05 W (blue). The dashed lines show the best linear fits to the data.

After initiation, ocellated skink burial was slow relative to sandfish burial. Burial time was moderately smaller in dry media (22.9 ± 13.4 s) compared to wet media (29.4 ± 9 s, ANOVA, $F(7, 36) = 4.5, P < 0.05$) and differed slightly among animals tested (ANOVA, $F(7, 36) = 3.0, P < 0.05$, N = 4 animals). In contrast, the sandfish lizard submerged into sand in ≈0.5 s (see Chapter 4). This slow burial was in part a consequence of the start-stop locomotion strategy that the ocellated skink used during burial (Fig. 6.10). Figure 6.10A shows the movement of the 5th marker (at the 0.4 SVL location) on the ocellated skink for a representative trial, where the movement (M) is the integrated path length from the beginning of the trial. The plateaus (pink regions) indicate that the skink paused while the green regions correspond to progression. Ocellated skinks moved for 0.8 ± 0.5 s in both wet and dry media before pausing (N = 3 animals, n = 3-4 runs each). The average subsurface speed of the 0.4 SVL location during movement was higher in dry media (0.10 ± 0.02 SVL/s) compared to in wet media (0.07 ± 0.02 SVL/s, T-test, $P < 0.01$; Fig. 6.10). This speed is smaller in comparison to the sandfish, where the speed of the 0.5 SVL location during sand-swimming is ≈ 2 SVL/s [34].

Most ocellated skinks placed their hindlimbs near their sides prior to limb submergence

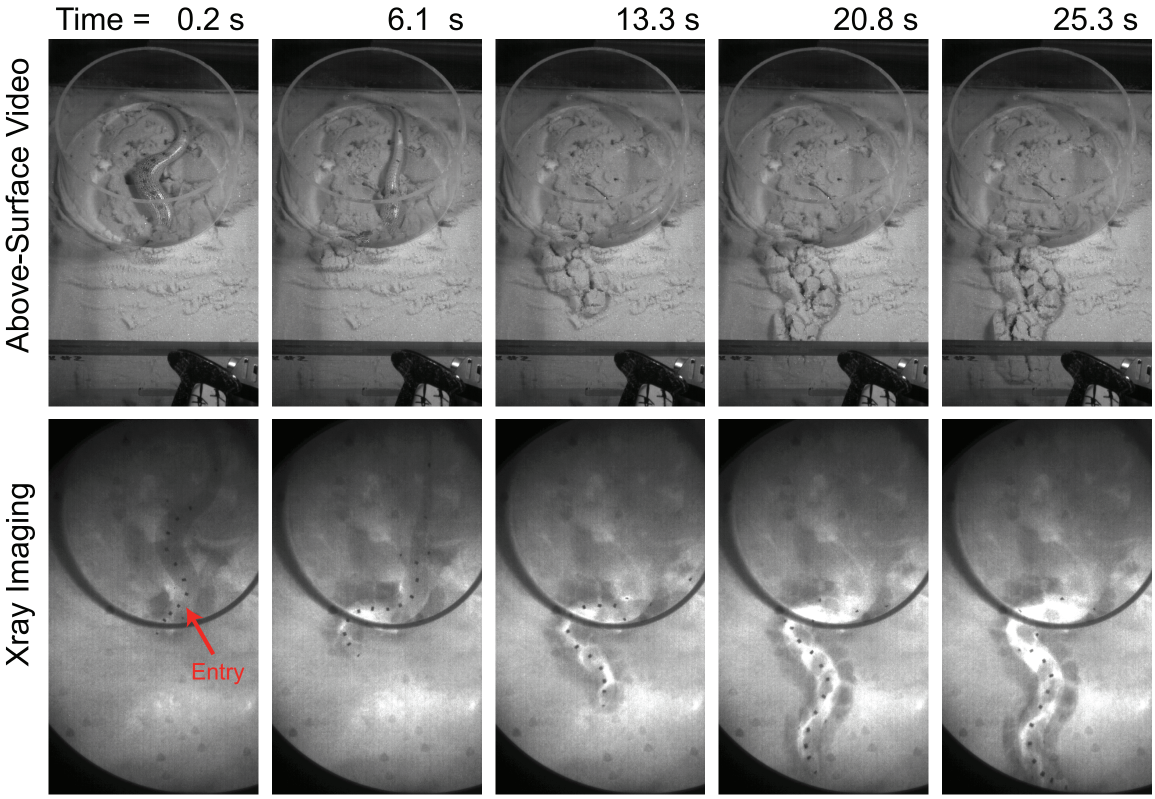

Figure 6.9: Ocellated skink during burial. Above surface images (top) and subsurface images (bottom) at synchronized times during burial into 0.03 W media with $\phi = 0.56$. This animal remained close to surface during the entire burial. Animals started from within the hollow cylinder that was placed on top of the substrate which contained burial to a desired location.

(Fig. 6.18). This occurred when 0.8 ± 0.2 of the SVL was submerged in the media for both wet and dry substrates and across all animals tested (ANOVA, $P > 0.05$). In both wet and dry media, ocellated skinks had a curved body posture during burial resembling a serpentine curve with $\approx$1.5 waves along the body (Fig. 6.9) and the subsurface slip was low (i.e. all body locations followed a similar trajectory, Fig. 6.11). While the hindlimbs were placed by the animal's sides before burial, the skink continued to use its forelimbs during subsurface locomotion. Protraction and retraction of the forelimb on the convex side of the body was observed during forward progression and the forelimb on the concave side was held near the body.

The head rotated from side to side (oscillated) during forward locomotion at $\approx$ 2 - 4 Hz. Figure 6.12A shows the trajectory of different markers along the body. The side to side motion is clearly visible in the trajectory of the snout marker (blue trajectory), while

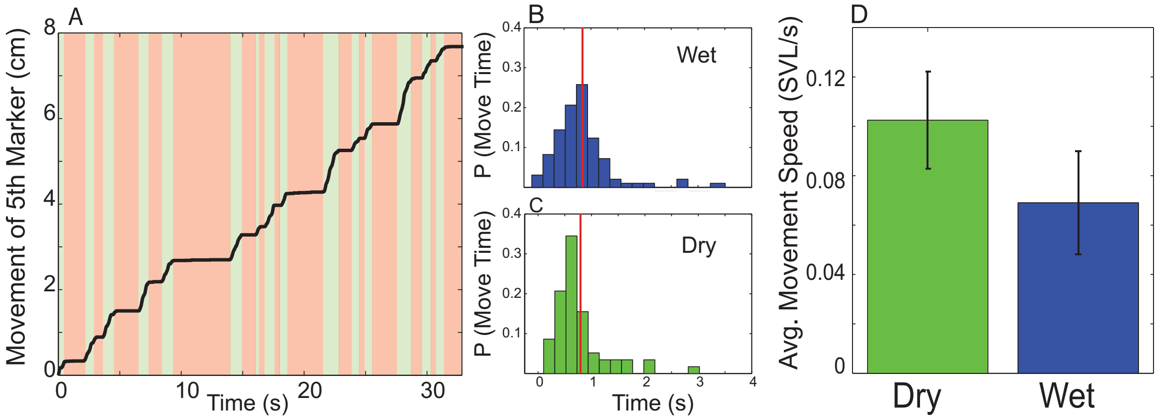

Figure 6.10: Start-stop motion of the ocellated skink. (A) Total displacement of the 0.4 SVL marker on the ocellated skink during burial. Pink horizontal bars indicate the duration that the ocellated skink was stationary and green regions indicate movement. A histogram of the amount of time that the ocellated skink moves before stopping in (B) wet media and (C) dry media. The mean move time is 0.8 ± 0.51 s in wet media and 0.77 ± 0.54 s in dry media. (D) The tangential speed during movement is higher in dry media (0.1 SVL/s) than wet media (0.07 SVL/s).

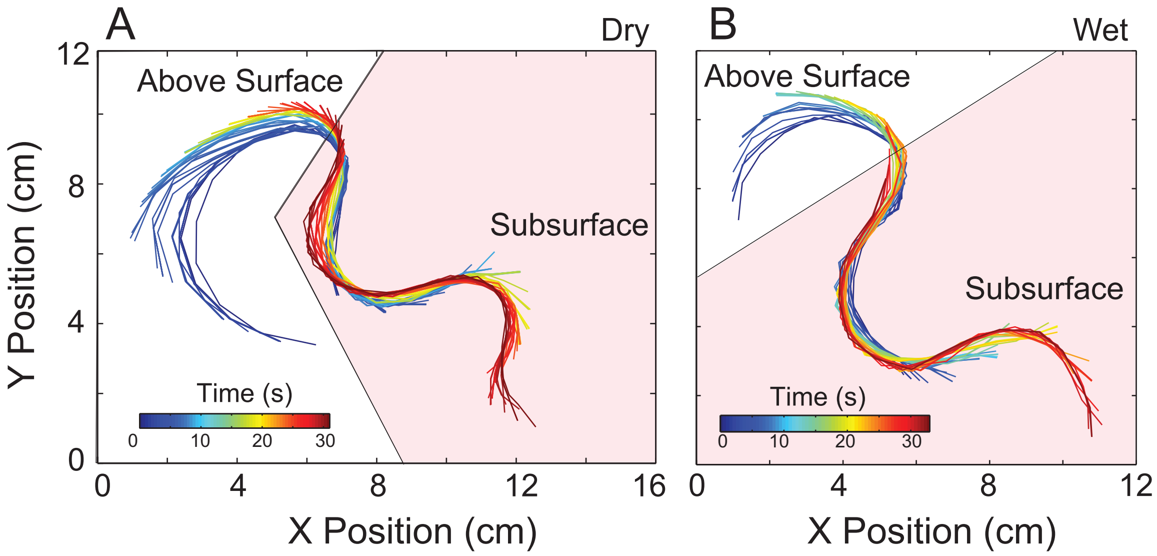

Figure 6.11: Subsurface body midlines during burial in (A) dry media and (B) wet media. The color of the curves correspond to the time in seconds, where dark blue is time = 0 s and dark red is time = 30 s in A and time = 33 s in B. The white region indicates the portion of the body that is above surface and the pink shows the subsurface region. In both trials, slip was low.

other markers follow along its mean path. There was a lower amplitude deviation in the 2nd and 3rd marker as well, meaning that the pivot point was between the 0.2 and 0.3 SVL locations. The head angle of excursion was determined by filtering the position of the snout

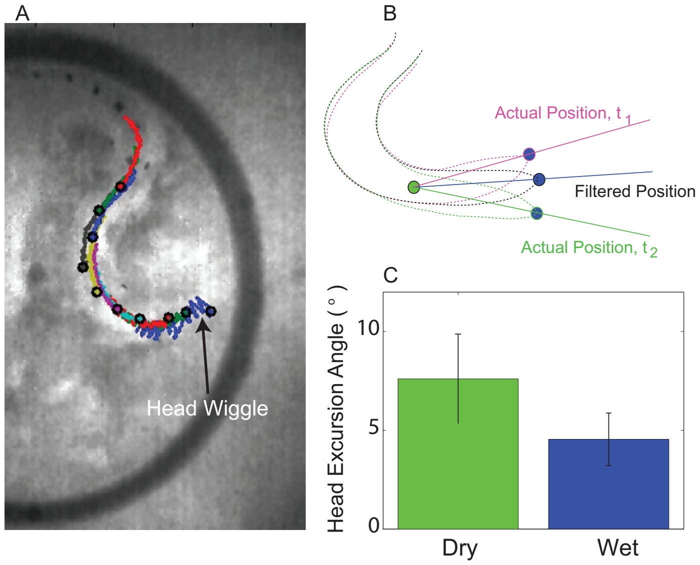

Figure 6.12: Head lateral excursion. (A) Trajectory of markers along the body during subsurface movement. (B) Angle of excursion was calculated by comparing the filtered snout positions to the actual snout positions. (C) The average maximum angle of excursion during movement in dry media is greater than in wet media.

(1st) marker, and comparing the vector between the filtered 1st marker position and the 4th marker position with the vector between the actual 1st marker position and 4th marker position (Fig. 6.12, B). The maximum angle of excursion in dry media (7.6 ± 2.3°, n = 10 trials, N = 3 animals) was higher than the maximum angle in wet media (4.5 ± 1.3°, n = 9 trials, N = 3 animals; ANOVA, $F(2, 18) = 10.3, P < 0.01$) and did not statistically vary across animals.

There was a large difference in the burrowing angle between wet and dry substrates. Ocellated skinks in dry media burrowed at an average angle of 21.2 ± 4.9°, while in wet media the angle was smaller 5.4 ± 4.2° (Fig. 6.13, C). Depth of burial was assessed by measuring the height from the surface to the ventral midpoint (≈0.5-0.6 SVL) along the body (Fig. 6.13, A) at the animal's final resting position. The average depth of burial in dry media (5.1 ± 1.2 cm) was twice as large as the depth of burial into wet media (2.5 ± 0.6 cm; Fig. 6.13,B). We attribute the lower angle and depth of burial to the higher resistance forces in wet granular media (Fig. 6.13, D).

6.5 Discussion

6.5.1 Preparation Method

The new sieve method created large homogenous preparations of wet granular media (i.e. no large voids) with variable compactions that depended on shaking time. Low ϕ states

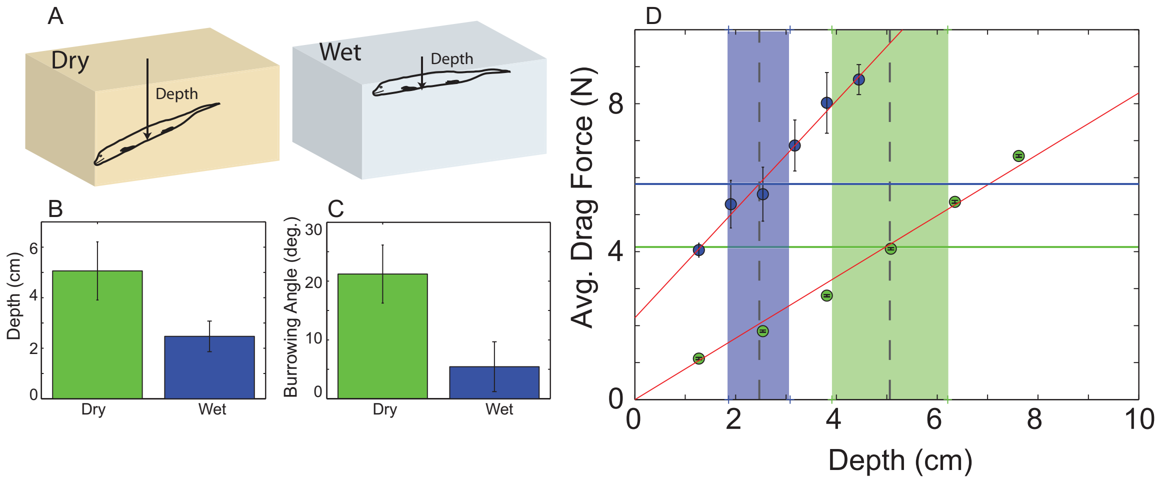

Figure 6.13: Difference in entry angle and depth during movement in wet and dry media. (A) Diagrammatic representation of the different orientations of ocellated in dry and wet media, where burial depth was measured from the surface of the substrate to the ventral midpoint of the animal. (B) Ocellated skinks buried themselves to an average depth of 5.1 cm in dry (green) media and 2.5 cm in wet (blue) media. (C) Burrowing angle was on average 21° in dry media (green) and 5° in wet (blue). (D) Average drag force (n = 3 trials per point) on a cylinder in LP dry media (green) and 0.03 W media (blue). The mean compaction in the wet substrates was 0.549 ± 0.006. Note that the standard deviation bars are within the marker size for dry media. Red lines show the best linear fits to the dry (slope = 0.83 N/cm) and wet (slope = 1.47 N/cm) data. Vertical dashed lines show the average burial depth in experiment and the standard deviations are shown by the colored regions for wet (blue) and dry (green) media. Blue and green horizontal lines show the estimated drag force around the midpoint of the body at the final burial depths in wet and dry media, respectively.

were achieved by stopping the vibrations soon after media deposition, while high ϕ states were achieve by prolonged shaking. We hypothesize that even lower compactions ($\phi < 0.53$) could be achieved by shaking the top container only. In our system, both the top and bottom containers were shaken simultaneously during the deposition process. Therefore, the media that was deposited into the lower container near the onset of shaking may be at a slightly higher compaction. However, we were unable to distinguish a compaction gradient within the material using x-ray imaging. Applying vertical vibrations to the top container alone would help to remove the compaction gradient, if it exists, and create an overall lower ϕ. The highest compaction achieved (≈0.6) occurred after 40 minutes of shaking. Furthermore, we did not observe a plateau in compaction with increased shaking time (as observed in other experiments [113]) so we suspect that prolonged shaking > 40 minutes would produce even more compacted states. However, for animal experimentation this may be impractical since the media preparation time would be inconvenient.

Vertical vibrations were applied at 60 Hz and 1.75 mm due to our observations that media readily fell through the 3 × 3 mm^2 mesh grid using these parameters. A systematic study which uses different mesh sizes, shaking frequencies and shaking amplitudes is needed to further characterize the capabilities of this system.

6.5.2 Resistance Forces

We found that resistance force increased with wetness (400% increase from dry to 0.01 W media) and with compaction (50% increase between LP and CP in 0.03 W media). These results emphasize the importance of controlling and reporting both W and ϕ when performing animal and robotic locomotion studies in wet GM since changes in resistance force could influence locomotion strategy and/or kinematics. The average drag force in the wet media preparations had larger standard deviations among different trials in comparison to the dry force measurements. We attribute this deviation to differences in the large force fluctuations during drag. Although we measured mean force from the start of one fluctuation to the start of another, changes in the fluctuations (such as the frequency and/or minimums) may have skewed mean values (see Fig. 6.6, B). A more in depth study which examines these force fluctuations with water content could lead to more consistent results and reveal principles of wet media behavior.

6.5.3 Burial Behavior

We were surprised at the low performance (speed) of the ocellated in dry media and even lower performance in wet media where the animals remained close to the surface during burial. Attum et al. [70] reported that ocellated skinks were more inclined to run toward vegetation to escape predators in the wild whereas sandfish preferred burial into granular media during escape. This difference in preference may be due to ocellated skink's inability to rapidly submerge. Also, we noticed during kinematic recordings in which the media had been disturbed and large voids were present, the ocellated skink tended to move toward the voids during subsurface locomotion. Although this was not investigated in detail, these preliminary findings could indicate that the head oscillation may be used to sense less resistance and attract the ocellated to that area. In nature, we suspect that ocellated skinks may use the pre-made burrows which exist in wet substrates to decrease resistance force acting on their bodies and improve performance.

This study has revealed an interesting pattern of subsurface locomotion which is different from the sandfish lizard. The ocellated skink uses a start-stop motion, head oscillations, and forelimbs to move subsurface with low slip. The function of the head oscillation is still unknown. The head oscillation could serve as a (1) force sensing mechanism (as described above) to steer motion toward low resistance regions, (2) propulsion mechanisms by push against the surrounding substrate and (3) force reduction mechanism to 'crack' granular media and reduce resistance to intrusion similar the activity of the annelid worm *Nereis virens* which burrows into mud by extending cracks [172]. To investigate whether the head oscillation could reduce resistance force during forward progression, we performed a simple experiment in which we submerged a cylindrical intruder into granular media and rotated the intruder by +20° and -20° prior to dragging it through the granular substrate (see Fig. 6.14, B; n = 3 trials). We found that in wet media, the yield force was reduced by ≈45% (Fig. 6.14, C) in comparison to drag without the rotation (Fig. 6.14, A & C). After 5 cm of horizontal movement, the forces in the rotated condition matched the forces in the non-rotated condition. In dry media, the forces were similar throughout the entire horizontal drag in both conditions, indicating that the rotation was not advantageous. Unlike these experiments, the head oscillation in the ocellated skink occurs *during* forward locomotion. This may indicate that the head is pulling the animal forward and acting as a propulsion mechanism. Even still, the oscillation could still act to reduce forces in wet media prior to the next movement. Future work using computational models may help to reveal the purpose of the head oscillation during forward motion. It is interesting to note that the maximum head angle of excursion is higher in dry media compared to wet (even though there is little force reduction in a dry substrate). We attribute the higher head angle to the lower resistance force in dry media. This may imply that the kinematic pattern is an open loop strategy in which the animal generates a constant torque at the head and kinematics change based on environmental conditions.

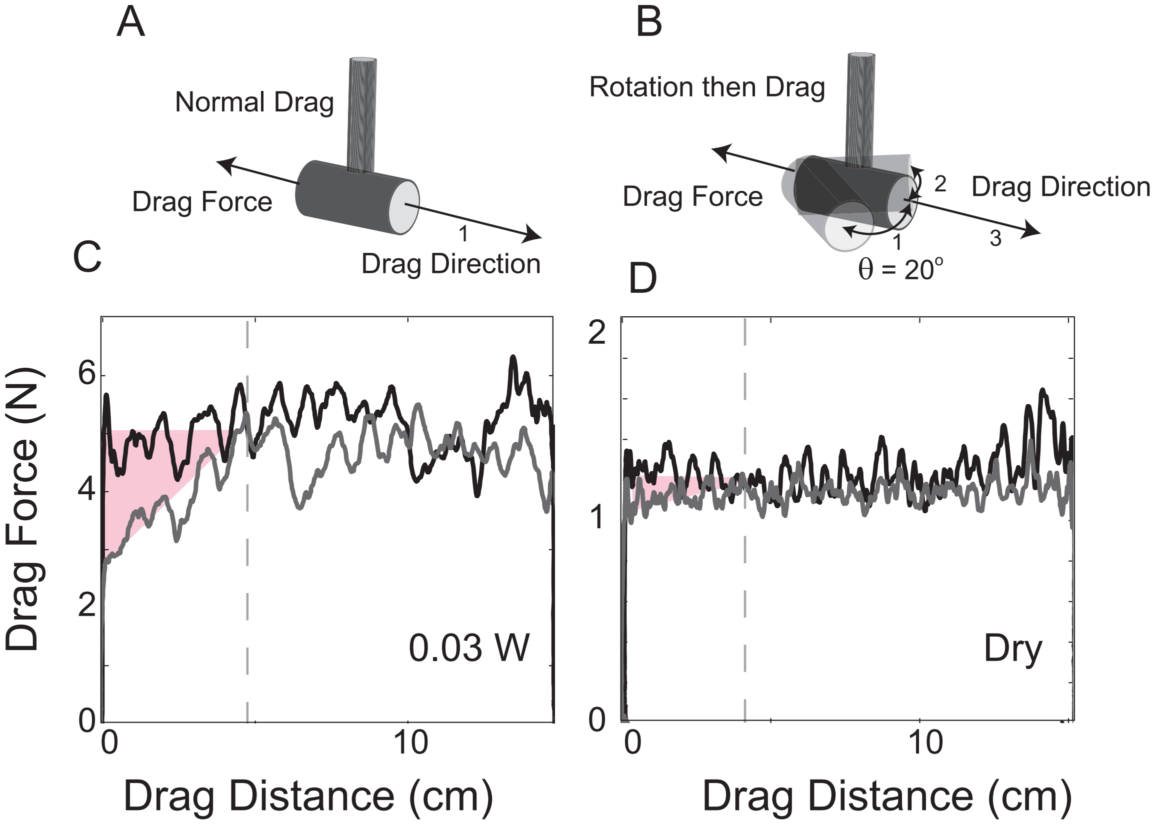

Figure 6.14: Exploring force reduction by rotation prior to forward drag. (A) In the normal drag condition, a cylindrical rod (diameter = 1.6 cm, length = 3.81 cm) moved 15.2 cm in granular media submerged to a depth of 3.81 cm. The rod was oriented such that its long axis was parallel to the direction of drag. (B) In the rotated condition, the cylinder rotated about the support rod clockwise 20° (step 1 in B), then rotated 40° counter-clockwise (step 2), then 20° clockwise to the original orientation. The cylinder was then moved forward 15.2 cm (step 3). (C) The force in wet media for the normal drag condition (black) and rotated condition (gray) for a representative trial. Yield force was reduced by 45% for the rotated condition and the mean drag forces were similar after ≈ 5 cm of movement. (D) Drag force in LP granular media for the normal drag condition (black) and rotated condition (gray). The reduction in yield force was minimal < 15%.

Ocellated skinks possess elongated bodies and reduced limbs in comparison to the sandfish. The forelimb movement on the convex side of the body reveals that limbs aid in propulsion subsurface. We received one animal that was missing nearly all of one of its forelimbs. In subsurface movement tests in dry granular media (poppy seeds) we found that the animal was still able to move forward when the side with the missing limb was convex (i.e. no limb movements occurred during this period). The animal was able to move forward using a head oscillation and serpentine body motion. This may indicate that although these limbs aid in forward propulsion, the head oscillation and body bendings are sufficient to produce forward thrust subsurface. More rigorous experiments which constrain limbs during subsurface locomotion in dry and wet substrates are needed to further investigate the role of limbs.

6.5.4 Targeting a Resistive Force Condition

During burial, both the sandfish and ocellated skink employed a locomotion strategy in which body bending was used to enter the substrate. The sandfish avoided burial into wet media, but the ocellated skink was capable of burial into both wet and dry substrates. However, the ocellated skink remained near the surface of the substrate during burial into loosely packed wet media. Empirically measured resistances forces on a cylindrical intruder revealed that at the ocellated skink's final burial depth in wet media, the resistance forces were higher on average (≈ 6 N) than the resistance forces at the final burial depth in dry media (≈ 4 N). We hypothesize that using body bending as the main form of propulsion is force limited and that the ocellated skink may not be able to move within material with resistances much greater than 7 N of force. This would indicate that the ocellated is capable of generating forces that are 35 times greater than its own body weight. This force relation is in agreement with previous estimates that show that for animals in a variety of behaviors the maximum force (normalized by body weight) they are capable of producing is between $0.5\times$body mass$^{-1/3}$ and $20\times$body mass$^{-1/3}$ [230] (Fig. 6.15). In contrast to the skinks, organisms such as the earthworm [231] and razor clam [109] can bury vertically downward into wet media and move to large submersion depths. The razor clam can produce 10 N of force [232] to pull itself into saturated granular media (which also falls within the maximum normalized force vs. body mass relation, Fig. 6.15). Although the organism's strength should only allow it to burrow a few centimeters in soil, it can submerge to depths greater than 70 cm [109]. Winter et al. [109] found that its unique valve movements fluidizes the surrounding media and reduces the energy required to reach these large depths. The earthworm also obeys this relationship and generates a maximum force of 3.2 N using longitudinal muscles in any one segment [231], but it too can submerge to deep within the ground (≈ 50 cm [233]). To cope with larger forces at larger depths or in compacted soils, earthworms may switch burial strategy and ingest soil to move through the medium. These varying techniques may have also developed to deal with the higher resistance that occurs when moving in wet materials. For subarenaceous animals that have a similar body plan as the ocellated skink, these animals may be limited due to their their evolutionary history. In the ocellated skink the head oscillation and use of limbs may have developed to add additional thrust when moving in these highly resistive regimes.

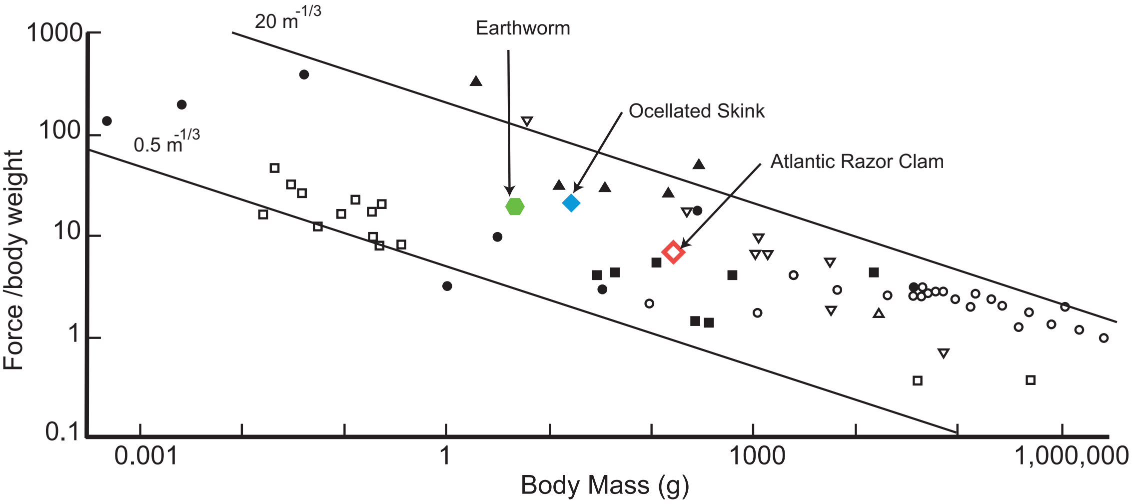

Figure 6.15: Maximum forces exerted by various animals on the environment during different activities. Open circles are for running, closed circles are for jumping, open squares are for pushing and pulling, closed squares are for swimming, open triangles are for flight, closed triangles are for nipping, and the upside down open triangles are for biting. This figure is modified from [230]. The maximum resistance force in which the ocellated skink has been observed to move (blue diamond), the maximum pulling force of the Atlantic razor clam (red open diamond) [232], and the maximum radial force of the earthworm (green hexagon) [233] during burial.

6.6 Conclusions

Ocellated skinks bury into ground using a different locomotor strategy than the sandfish. During periodic movement, the ocellated skink uses body bending, the forelimb on the convex side, and head oscillation. Although burial speeds were much slower than the sandfish, the general burial strategy enabled the ocellated skink to burrow into both wet and dry media preparations. The slow strategy may indicate that burial is not an effective method for predator evasion and corroborates the work by Attum et al. [70] that showed that the ocellated skink prefers to run toward vegetation to hide, although burial was also observed. We expect that this burial capability is vital for the ocellated skink's survival in nature, because it allows thermoregulation and conceals the skink from other animals.

The use of a homogenous wet granular preparation with controllable compaction allowed us to discover that the ocellated skink more readily buries in to LP wet substrate than CP which may be due to the higher resistance forces in CP media. This may also indicate that in nature, ocellated preferentially bury into looser substrates. Conducting experiments in a substrate without voids allowed us to test the limits of burial and quantify the forces acting on the animal during submergence. We found that the ocellated skink usually remained at depths in which resistance force was less than 7 N. Therefore, we hypothesize that the ocellated skink is force limited and may use pre-made burrows in wet substrates in nature to reduce force requirements.

The use of the sieve apparatus has many applications, such as in understanding subsurface nesting behaviors of fire ants (*Solenopsis*) in media with varying water contents or in robotic studies of motion in wet substrates (see Appendix). The homogeneity and repeatability will also aid in direct comparison with computational and theoretical models which can be used to generate hypotheses and increase understanding of biological principles.

6.7 Appendix

Other applications which have used sieve technique

The wet sieve technique can be used in a multitude of other biological and robotic applications where large preparations of homogenous wet media with controllable material properties are needed. Below we show two applications which have utilized this technique: fire ant nesting studies and bipedal robot footprint formation studies.

Fire ant tunneling-Work by Daria Monaenkova

The sieve apparatus was used to create consistent wet granular media to study nest

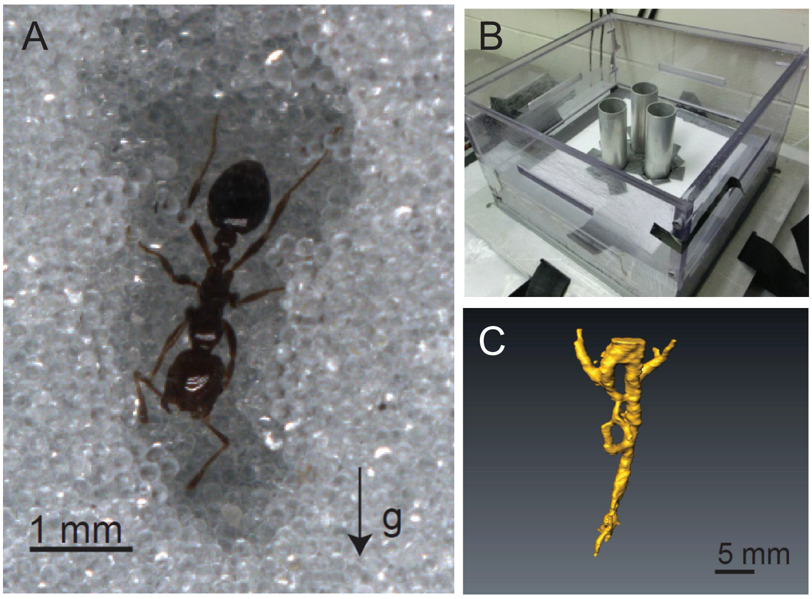

Figure 6.16: Fire ant tunneling networks were studied with varying water content and bead size. (A) Fire ant excavating a tunnel. (B) Setup showing bottom container with ant tubes. The sieve apparatus was used to deposit wet media into the tubes and prolonged shaking produced repeatable compactions. (C) 3D tunnel reconstruction using x-ray imaging.

construction by red imported fire ants, *Solenopsis invicta*, (Fig. 6.16) in simulated soils (glass beads: Jaygo Inc., Union NJ, USA; Surface Preparation, Morrow, GA, USA). The goal of the experiment was to discover how water content and grain size affect nest construction rates and nest morphology. Three grain sizes (0.036 ± 0.011 mm, 0.24 ± 0.03 mm and 0.65 ± 0.15 mm) and 7 wetness contents (0.01 W, 0.03 W, 0.05 W, 0.1 W, 0.15 W, 0.18 W and 0.2 W) were tested in experiment. Nine digging trials were performed for every size-wetness combination.

To create repeatable preparations, the media was deposited into hollow aluminum cylinders (inner diameter = 3.5 cm, height = 14.5 cm) which were fixed into the bottom container of sieving apparatus using a Styrofoam insert (Fig. 6.16, B). Sinusoidal vertical vibrations at a frequency of 60 Hz and amplitude 1.75 mm were sufficient to induce media deposition for all conditions. Depending on wetness and grain size, the time that it took to fill the tubes with media took between 5-20 minutes. To achieve consistent compactions, the tubes with wet media were shaken for a total of 10 minutes ($\phi = 0.6 \pm 0.025$). The soil surface was flattened and fire ants (N =100 ± 10) were placed on top of the media within the sand cylinders. Ants tunneled *ad libitum* for a total of 20 hours. Each cylinder was mounted on a rotary stage (Lin Engineering, Morgan Hill, CA, USA) and 400 projections of the excavated networks (i.e. every 0.9°) were acquired using an x-ray system (Philips, Andover,

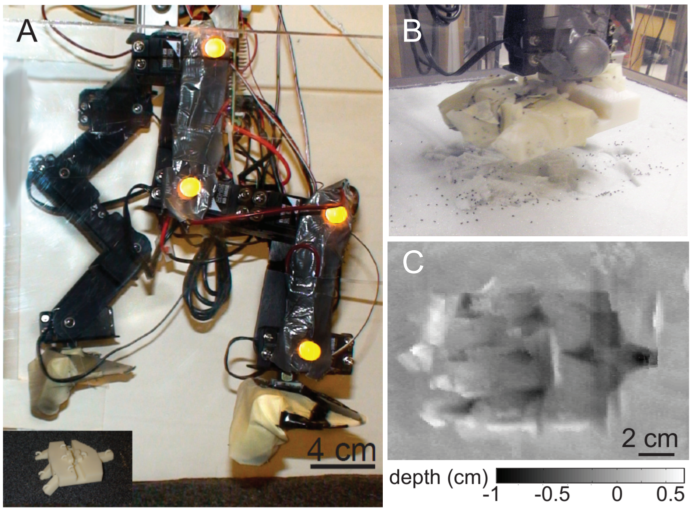

Figure 6.17: Bipedal robot used to study footprints as a function of material properties. (A) Bipedal robot shown with circular foot and single toe. (Inset) Trydactyl foot model with 3 moveable anterior toes and 1 posterior toe. (B) Robot footprint left in sieved media during walking. (C) Footprint reconstruction where color corresponds to imprint depth (white indicates media has risen 0.5 cm and black indicates an indentation of 1 cm).

MA, USA, 110 kVp, 3 mA) and high-speed camera (Phantom v210, Vision Research Inc., Wayne, NJ, USA). The 3-D tunnels were reconstructed using an open source reconstruction tool (OSCaR, Nargol Rezvani) based on Feldkamp-Davis-Kress algorithm and visualized and analyzed with Avizo 8.0 software (FEI Visualization Sciences Group) (Fig. 6.16, C). These x-ray computed tomography (CT) scans were performed to characterize nest morphology after 5, 10 and 20 hours of excavation. Results indicate that grain size and wetness content both influence tunnel morphology and digging rate.

Bipedal Robot footprint- Work done in collaboration with Mark Kingsbury

The sieve technique was used to prepare a substrate to characterize a footprint made in wet sand by a bipedal robot (Fig. 6.17). Each robot leg was composed of 4 servo motors connected by segments (Fig. 6.17, A) which mimic avian morphology. Iterative joint angle commands were sent to the motors to produce motion. The feet of the robot were inspired by the avian tridactyl feet and 3D printed with ABS plastic (Fig. 6.17, A, inset). The robot was planarized using two custom air bearings (Nelson Air, NH), constraining motion to only vertical and fore-aft directions. The robot otherwise supported its own weight and produced its motion.

The sieve apparatus was used to create a wet granular state. The sand was deposited into the container such that the final height was level with the height of the sand container. The container was placed such that the robot took a single step into the prepared wet media (Fig. 6.17, B). We used laser line profilometry [90] to characterize the surface profile and the indentation left by the foot (Fig. 6.17, C).

With this method it is possible to discover the relationship between the kinematics of a body moving over wet granular media and the tracks that it leaves behind. This work can provide greater insight into footprint formation and its relationship to material properties and kinematics. Creating repeatable wet substrates is critical for analyzing how resistance forces influence the footprint profile. In future studies, the changes in the footprint will be analyzed as a function of wet granular substrate properties (i.e. wetness content, compaction, particle size and particle density).

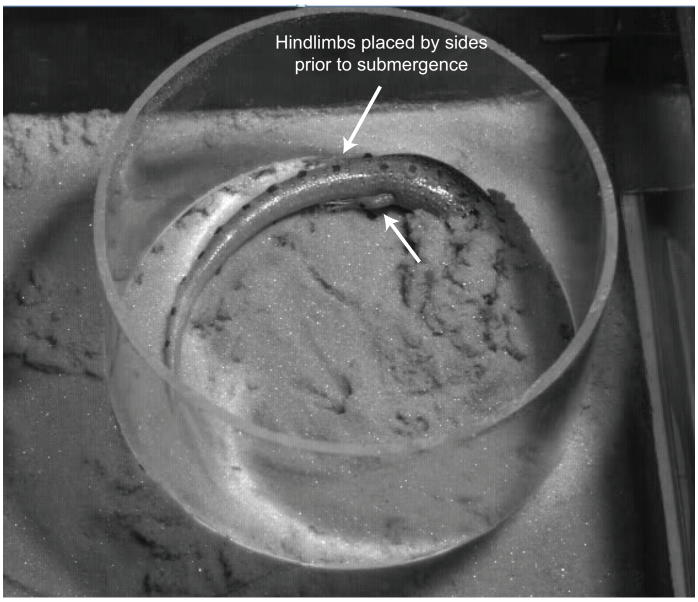

Figure 6.18: Hindlimbs are placed by the flanks prior to entry. On average this occurs when $\approx$0.8 SVL is submerged within the medium.

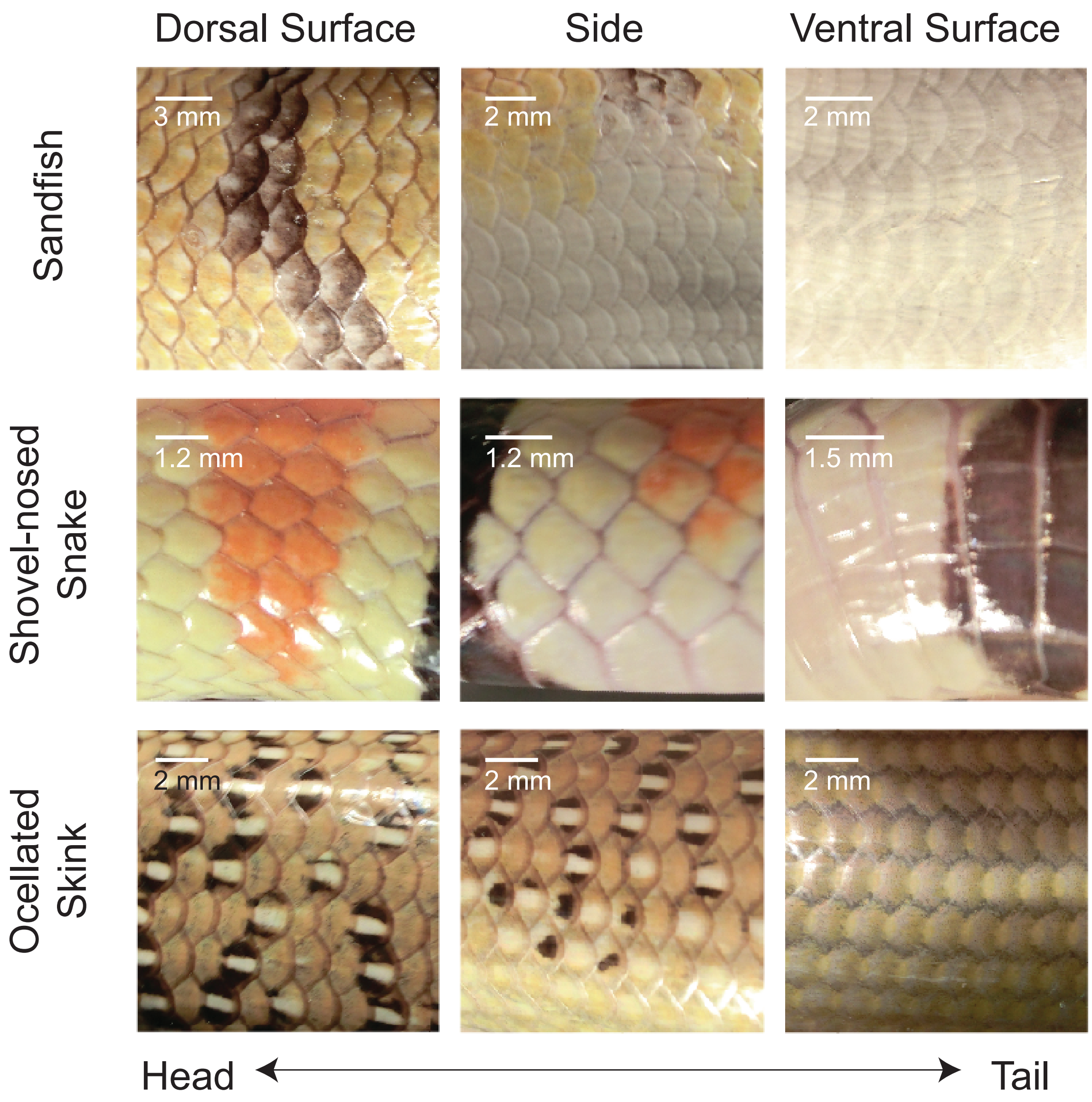

Figure 6.19: Close-up picture of sandfish (top), shovel-nosed snake (middle), and ocellated skink scales (bottom). In each picture the head of the animal is to the right and the tail is toward the left. For the pictures of the sides, the dorsal surface is toward the top of the image and the ventral is toward the bottom.

Table 6.1: Sandfish, shovel-nosed snake and ocellated skink skin friction tests

Snake #	STL (*cm*)	SVL (*cm*)	Mass (*g*)	μ_s, Ventral Forward	μ_s, Ventral Backward	μ_s, Dorsal Forward	μ_s, Dorsal Backward
S. scincus							
96	14	8.5	18.5	0.212 ± 0.015	0.313 ± 0.04	0.183 ± 0.014	0.217 ± 0.017
98	14.6	8.8	16.1	0.17 ± 0.02	0.266 ± 0.009	0.147 ± 0.009	0.224 ± 0.042
74	15.4	9.9	24.5	0.201 ± 0.014	0.271 ± 0.036	0.208 ± 0.017	0.254 ± 0.022
Average				**0.194 ± 0.022**	**0.283 ± 0.026**	**0.179 ± 0.031**	**0.231 ± 0.019**
Ch. occipitalis							
80	38.7		20	0.112 ± 0.01	0.117 ± 0.003*	0.177 ± 0.003*	0.208 ± 0.006
110	33.7		15	0.123 ± 0.006*	0.142 ± 0.005*	0.179 ± 0.003*	0.247 ± 0.016**
112	41.4		22.9	0.092 ± 0.017	0.152 ± 0.009	0.127 ± 0.017	0.254 ± 0.023
Average				**0.109 ± 0.016**	**0.137 ± 0.018**	**0.161 ± 0.029**	**0.237 ± 0.025**
Ch. ocellatus							
114	17.4	9.9	22.9	0.127 ± 0.011	0.181 ± 0.027	0.123 ± 0.013	0.217 ± 0.017
118	20.5	13	35.8	0.154 ± 0.009	0.161 ± 0.018	0.123 ± 0.014	0.136 ± 0.009
119	17	10.5	20.9	0.154 ± 0.031	0.167 ± 0.023	0.132 ± 0.010	0.147 ± 0.009
Average				**0.145 ± 0.015**	**0.17 ± 0.01**	**0.126 ± 0.005**	**0.182 ± 0.049**

no notation indicates n=4 measurements, * n= 3 measurements, ** n= 2 measurements
± indicates s.d.

6.8 Contributions

Tamunodiepriye George started kinematic work with the ocellated skinks and inspired further investigation of these animal's subsurface kinematics. Kevin Daffon assisted with the investigation of techniques to prepare repeatable wet granular states. Robyn Kuckuk helped with development of the "sieve" apparatus. Robyn also assisted in collecting compaction and resistive force data within media prepared by the sieve apparatus. Robyn helped with collection of the ocellated skink data in wet and dry mediums.

CHAPTER VII

CONCLUSION

7.1 General Remarks

Animal locomotion on and within granular media is ubiquitous in nature. In this dissertation, we have explored the burial and subsurface movement strategies of three animals in order to gain a broader perspective on biomechanical principles and control strategies utilized in granular environments. Using a combination of subsurface x-ray imaging, muscle activation recordings, resistive force measurements, and theoretical models we have discovered a template for movement in dry sand (**Chapter 2**), the fundamental mechanism behind neuromechanical phase lags in undulatory swimmers (**Chapter 3**), how body morphology and body friction influence subsurface performance (**Chapter 4**), and a general movement strategy for burial into wet and dry substrates that is force limited (**Chapter 5**). These studies emphasize the importance of considering neural control, body mechanics and morphology, *and* substrate interactions to discover how effective locomotion is generated. Furthermore, use of laboratory techniques which generate repeatable conditions and allow systematic variations of properties (such as compaction) can provide insight into how such properties influence locomotion strategies. Field biologists can then use these studies for comparison to measurements made in natural environments (e.g. media compaction and animal burial depth) which may promote evolutionary and ecological discoveries. Robotic designs which incorporate these principles of control and mechanics may have enhanced capability of moving on and within granular terrains.

7.2 Specific Accomplishments

By studying three burrowing animals, we were able to gain insight into how animals use neural control, kinematics, and body mechanics to bury and move effectively subsurface. We found that depth of movement and water content had large effects on locomotor strategy and locomotor ability and that animals target optimal kinematics to achieve improved performance. Our results were enabled by the use of repeatable substrate preparations that ensured consistent resistance forces across trials, and by x-ray imaging which enabled visualization through opaque material. Below we highlight the specific accomplishments achieved in this dissertation:

Neuromechanics:

- Simultaneous recordings of sandfish kinematics and epaxial EMGs revealed a traveling wave pattern of muscle activation during subsurface sand-swimming and little to no activation during above surface walking.
- We found that the sandfish EMG activation intensity was independent of speed and increased with submergence depth. These findings corresponded with resistance force measurements which were speed insensitive and increased linearly with depth. We found that changing the media compaction resulted in similar EMG intensities which we hypothesize is due to the similar compaction of the localized fluid region surrounding the animal's body during swimming.
- We discovered a template for sand-swimming, which corroborated previous findings by Maladen and Ding, by revealing that the sandfish was modulating muscle activation with increasing resistive forces while maintaining an optimal waveform (i.e. amplitude to wavelength ratio) which maximized speed and minimized mechanical cost of transport.
- We used the simplicity of the sandfish system (low passive body forces, consistent kinematics, and 'simple' environment where inertial forces are negligible and interactions can be described using resistive force theory) to explain the neuromechanical phase lag phenomenon, the advancing phase of EMG onset relative to curvature along the body, that occurs in all undulatory swimmers. We found torque timing must change relative to curvature along the body due to the different integration lengths, and therefore, advancing EMG timing is an emergent phenomenon that occurs due to mechanics.

Limbs aid in rapid burial:

- We used x-ray and above surface video to characterize protraction and retraction of the sandfish limbs during above surface walking, burial and subsurface swimming. The studies revealed a gradual shift in limb use during the burial transition, where limbs were placed near the body sequentially and the forelimbs were the first to retract and remain retracted.
- By restraining limbs, we found limb use was necessary for burial, but that forelimbs were more critical. When restraining forelimbs, we found a decreased burial ability and performance (speed), whereas when hindlimbs were restrained, burial ability was not hindered and performance was minimally affected.

The influence of body morphology and body properties on subsurface swimming performance:

- X-ray imaging revealed that the shovel-nosed snake uses a traveling wave of axial undulations to propel itself subsurface and moves subsurface with low slip.
- We found that the shovel-nosed snake's long-slender body morphology enabled the snake to use a higher number of waves along its body during swimming (≈3.5) in comparison to the sandfish (≈1), but both animals used a similar relative body curvature. The snake also had lower skin friction ($\mu_s = 0.11$) compared to the sandfish ($\mu_s = 0.19$).
- Resistive force theory (RFT) showed that having a higher length to body radius ratio did not influence the subsurface slip, but predicted that having a larger number of waves (to a certain extent) while maintaining a higher relative curvature would enable lower slip locomotion. RFT also predicted lower slip for an animal with decreased body-particle friction. The ability of the RFT to predict both the sandfish and snake's slip when incorporating their different body properties and morphology indicates that a frictional fluid model of the environment is a good approximation for both animals.

Burial strategy of a desert generalist

- We developed a new technique to create repeatable, homogenous wet granular media states with controllable compaction. Using this technique, we found that resistance force in a wet granular medium was 4 times higher than the resistance force in a dry granular medium and that increased compaction can increase resistance force by 50%.
- We characterized the burial strategy of the ocellated skink in wet and dry media. We found a similar locomotor strategy in both substrates in which the animals employed a start-stop motion, body bending, forelimb use, and head oscillations to move subsurface.
- We found a decrease in speed and head oscillation angle during movement in wet media compared to dry media and that animals remained at shallow depth during movement in wet substrates. We attribute these changes to the greater resistance forces in wet media and hypothesize that the ocellated skink is force limited and may be incapable of deeper burial in a wet substrate.

7.3 Future Directions

Other studies can build upon this work to establish a neuromechanics framework for locomotion in complex environments. Below we highlight some of the future directions in which this research could go.

Exploration of the neural control and kinematics in other subarenaceous animals to verify a "template" for sand-swimming

Our work exploring the muscle activation strategy in the sandfish lizard (Chapter 2) suggests that the sandfish is targeting an optimal shape (i.e. optimal curvature) which increases speed and decreases mechanical cost of transport. We suggest this waveform is a "template" for sand-swimming. However, to verify its generality among sand-swimmers we would need to examine this strategy for a multitude of subarenaceous species. In agreement with our hypothesis, the shovel-nosed snake uses a similar relative curvature along its body compared to the sandfish during sand-swimming (Chapter 5) which provides further evidence that this waveform is utilized by a number of species. EMG in the shovel-nosed snake along with investigation of the locomotor strategy of other subarenaceous species, such as the *Angolosaurus skoogi* and *Sphenops sepsoides*, would help to confirm (or refute) that this is indeed a general template.

Sandfish electrophysiology

The sandfish lizard is a good model organism when studying subsurface locomotion in sand in part due to its stereotyped behavior and simple undulatory kinematics. Our work measured EMG in epaxial musculature (where the iliocostalis muscle was targeted for implantation) during above surface walking and subsurface swimming (Chapter 2). However, a more detailed characterization of the neural control strategy and how it compares with other animals (such as the salamander or lamprey) is needed. For example, EMG measurements in other muscle groups (such as the hypaxial musculature) could provide further insight into how axial muscles generate subsurface movement.

We found no detectable activation in epaxial muscles during above surface walking. Studies on the iguana have suggested that hypaxial muscles provide stabilization [158] during walking. Measurements in these muscles for the sandfish during walking may show that activation is needed in order to prevent bending. Furthermore, we found for a single trial when the sandfish was running at a high speed above surface there was epaxial activation. Further investigation that explores above surface muscle activation as a function of speed could help identify how the axial musculature is used.

EMG measurements in limbs could help verify whether limbs are passive or active during above surface movement. If activation is detected, then the timings and intensity of the EMG could be used to identify if activation changes in the limbs between above surface, burial and subsurface movement.

Similar electrophysiology studies, such as that performed on the salamander [205] which induce fictive locomotion due to stimulation of the mesencephalic locomotor region (MLR) in the brain, could be used to characterize the neural networks which drive locomotion in the sandfish. Because the sandfish has a gradual transition from above surface walking to subsurface swimming it would be interesting to see if different levels of stimulation could reproduce all three modes (as it does the two modes of salamander movement: walking and swimming).

Burial and limb function

Our findings revealed that the limbs aid in the burial of the small sandfish lizard (Chapter 4). The mechanisms by which fossorial snakes and limbless lizards bury into substrates is unknown. Because body elongation and reduction of the limbs often occur simultaneously, this may indicate that limbs become less important while body substrate interactions (above surface) become more important as bodies increases in length. Future investigations are needed that investigate that above surface to subsurface transition in elongated and limbless burrowers.

The use of a robot and/or simulation could also be used to further investigate the role of the limbs by allowing modification of parameters such as limb orientation, shape and timing. We hypothesize that appropriately timed limb-substrate interactions would enable faster burial of our sandfish-like robot that currently buries using body undulations only.

Evolutionary adaptations to enhance subsurface performance

In our comparison of the shovel-nosed snake and sandfish lizard we found that an elongated body and low skin friction improved subsurface performance (Chapter 5). While studies have anecdotally reported that fossorial animals have reduced skin friction, comparison of friction values is needed to support these claims. Furthermore, by studying the low friction skin of these animals we may be able to develop biologically inspired materials (such as the shark-skin inspired fabrics) that can be used on future subsurface robots and contribute to higher performance.

Force generating capacity

In our studies we have estimated the force produced by the sandfish limbs during burial (Chapter 4) and estimated the force producing capacity of the ocellated skink by observing the limits of burial depth in wet and dry substrates (Chapter 6). Future studies which quantify body forces with the use of strain gauges or tendon buckles could help determine the forces produced by the body during subsurface movement. For the ocellated skink, the maximal bending force could be measured by using the body bending apparatus used to measure passive forces in the sandfish (see Chapter 3).

Daily subsurface activity

The behaviors observed in the sandfish, ocellated skink and shovel-nosed snake were primarily those of escape, where animals submerge lower into the media until they eventually come to rest (i.e. during locomotion trials, all animals studied had a negative angle with respect to the horizontal). Investigation exploring how these animals move during non-escape subsurface activity or during emergence from the media has never been observed using x-ray. A system which triggers the x-ray automatically in order to observe steady-state behavior could help investigators capture motion during activity. Furthermore, factors such as metabolic energy minimization which may not be important during escape could become a critical factor during other activities and different locomotion strategies could be discovered.

Ocellated skink muscle activation

We found that the ocellated skink's kinematics changed when moving in a wet vs. a dry substrate (Chapter 6). These changes could be explained from the larger resistance forces in the environment. Unlike the sandfish which changes activation to maintain its kinematics, we hypothesize that the ocellated skink may be using similar neural control (and torques) in both environments. To test if this is an open-loop strategy and activation does not change, EMG activation measurements can be made (similar to those in Chapter 2). EMG will help to identify whether the ocellated skink is using a general locomotor pattern that is sufficient for burial in both wet and dry substrates, or if activation is modulated with resistance forces (as in the sandfish).

7.4 Final Thoughts

Environmental pressures can lead to adaptations and exaptations which allow more effective locomotor ability and thus enhance the probability of survival. Studying the body plans, properties and control strategies of these biological organisms alone is not enough. We must consider and incorporate the environmental interactions which influence these factors. Investigating both environmental interaction and biological control together could lead to novel robotic developments and may provide evolutionary and ecological insights.

REFERENCES

[1] H. M. Jaeger, S. R. Nagel, and R. P. Behringer, "Granular solids, liquids, and gases," *Reviews of Modern Physics* **68**, 1259 (1996).

[2] R. Nedderman, *Statics and kinematics of granular materials* (Cambridge Univ Pr, 1992).

[3] J. Matson, "Unfree Spirit: NASA's Mars Rover Appears Stuck for Good," *Scientific American* **302**, 16 (2010).

[4] R. Temam, *Navier–Stokes Equations* (AMC Chelsea Publishing, 1984).

[5] J. Carling, T. Williams, and G. Bowtell, "Self-propelled anguilliform swimming: simultaneous solution of the two-dimensional Navier-Stokes equations and Newton's laws of motion," *Journal of Experimental Biology* **201**, 3143 (1998).

[6] G. V. Lauder and E. G. Drucker, "Forces, fishes, and fluids: hydrodynamic mechanisms of aquatic locomotion," *Physiology* **17**, 235 (2002).

[7] R. D. Maladen, Y. Ding, P. B. Umbanhowar, A. Kamor, and D. I. Goldman, "Mechanical models of sandfish locomotion reveal principles of high performance subsurface sand-swimming," *Journal of the Royal Society Interface* **8**, 1332 (2011).

[8] Y. Ding, S. S. Sharpe, A. Masse, and D. I. Goldman, "Mechanics of undulatory swimming in a frictional fluid," *PLoS Computational Biology* **8**, e1002810 (2012).

[9] Y. Ding, N. Gravish, and D. Goldman, "Drag induced lift in granular media," *Physical Review Letters* **106**, 28001 (2011).

[10] J. Lee and H. J. Herrmann, "Angle of repose and angle of marginal stability: molecular dynamics of granular particles," *Journal of Physics A: Mathematical and General* **26**, 373 (1993).

[11] R. D. Maladen, Y. Ding, C. Li, and D. I. Goldman, "Undulatory Swimming in Sand: subsurface locomotion of the sandfish lizard," *Science* **325**, 314 (2009).

[12] R. Gaymer, "New method of locomotion in limbless terrestrial vertebrates," *Nature* (1971).

[13] J. P. Gasc, F. K. Jouffroy, S. Renous, and F. V. Blottnitz, "Morphofunctional study of the digging system of the Namib Desert golden mole (*Eremitalpa granti namibensis*): cinefluorographical and anatomical analysis," *Journal of Zoology* **208**, 9 (1986).

[14] A. P. Summers and J. C. O'Reilly, "A comparative study of locomotion in the caecilians *Dermophis mexicanus* and *Typhlonectes natans* (Amphibia: Gymnophiona)," *Zoological Journal of the Linnean Society* **121**, 65 (1997).

[15] W. Baumgartner, F. Saxe, A. Weth, D. Hajas, D. Sigumonrong, J. Emmerlich, M. Singheiser, W. Boehme, and J. Schneider, "The sandfish's skin: morphology, chemistry and reconstruction," *Journal of Bionic Engineering* **4**, 1 (2007).

[16] R. Blickhan and R. J. Full, "Similarity in multilegged locomotion: bouncing like a monopode," *J. Comp. Physiol. A* **173**, 509 (1993).

[17] R. Dudley, *The biomechanics of insect flight: form, function, evolution* (Princeton University Press, 2002).

[18] R. M. Alexander, *Principles of Animal Locomotion* (Princeton University Press, Princeton, USA, 2003).

[19] G. V. Lauder and E. D. Tytell, "Hydrodynamics of Undulatory Propulsion," *Fish Physiology* **23**, 425 (2006).

[20] K. Nishikawa *et al.*, "Neuromechanics: an integrative approach for understanding motor control," *Integrative and Comparative Biology* **47**, 16 (2007).

[21] K. S. Norris and J. L. Kavanau, "The burrowing of the western shovel-nosed snake, *Chionactis occipitalis Hallowell*, and the undersand environment," *Copeia* **1966**, 650 (1966).

[22] E. N. Arnold, "Identifying the effects of history on adaptation: origins of different sand-diving techniques in lizards," *Journal of Zoology* **235**, 351 (1995).

[23] D. J. Irschick and B. C. Jayne, "Effects of incline on speed, acceleration, body posture and hindlimb kinematics in two species of lizard *Callisaurus draconoides* and *Uma scoparia*," *Journal of Experimental Biology* **201**, 273 (1998).

[24] A. Herrel, H. F. Choi, E. Dumont, N. De Schepper, B. Vanhooydonck, P. Aerts, and D. Adriaens, "Burrowing and subsurface locomotion in anguilliform fish: behavioral specializations and mechanical constraints," *The Journal of Experimental Biology* **214**, 1379 (2011).

[25] W. L. Korff and M. J. McHenry, "Environmental differences in substrate mechanics do not affect sprinting performance in sand lizards (*Uma scoparia* and *Callisaurus draconoides*)," *The Journal of Experimental Biology* **214**, 122 (2011).

[26] B. C. Jayne and M. W. Daggy, "The effects of temperature on the burial performance and axial motor pattern of the sand-swimming of the Mojave fringe-toed lizard *Uma scoparia*," *Journal of Experimental Biology* **203**, 1241 (2000).

[27] M. G. Paoletti and M. Hassall, "Woodlice (Isopoda: Oniscidea): their potential for assessing sustainability and use as bioindicators," *Agriculture Ecosystems and Environment* **74**, 157 (1999).

[28] N. Gravish, M. Garcia, N. Mazouchova, L. Levy, P. B. Umbanhowar, M. A. D. Goodisman, and D. I. Goldman, "Effects of worker size on the dynamics of fire ant tunnel construction," *Journal of the Royal Society Interface* **9**, 3312 (2012).

[29] R. S. Seymour, P. C. Withers, and W. W. Weathers, "Energetics of burrowing, running, and free-living in the Namib Desert golden mole (*Eremitalpa namibensis*)," *Journal of Zoology* **244**, 107 (1998).

[30] K. M. Dorgan, S. R. Arwade, and P. A. Jumars, "Burrowing in marine muds by crack propagation: kinematics and forces," *Journal of Experimental Biology* **210**, 4198 (2007).

[31] C. Darwin, *The Formation of Vegetable Mould Through the Action of Worms With Observation of Their Habits* (John Murray, London, 1892).

[32] F. J. R. Meysman, J. J. Middelburg, and C. H. R. Heip, "Bioturbation: a fresh look at Darwin's last idea," *Trends in Ecology & Evolution* **21**, 688 (2006).

[33] S. Jung, "*Caenorhabditis elegans* swimming in a saturated particulate system," *Physics of Fluids* **22**, 031903 (2010).

[34] S. S. Sharpe, Y. Ding, and D. I. Goldman, "Environmental interaction influences muscle activation strategy during sand-swimming in the sandfish lizard *Scincus scincus*," *The Journal of experimental biology* **216**, 260 (2012).

[35] H. Heatwole and E. Davison, "A Review of Caudal Luring in Snakes with Notes on Its Occurrence in the Saharan Sand Viper, *Cerastes vipera*," *Herpetologica* (1976).

[36] H. H. Schleich, W. Kästle, and K. Kabisch, *Amphibians and Reptiles of North Africa: Biology, Systematics, Field Guide* (Koeltz Scientific Books, 1996).

[37] S. Jung, A. G. Winter, and A. E. Hosoi, "Dynamics of digging in wet soil," *International Journal of Non-Linear Mechanics* **46**, 602 (2011).

[38] A. G. Winter and A. E. Hosoi, "Identification and evaluation of the Atlantic razor clam (*Ensis directus*) for biologically inspired subsea burrowing systems," *Integrative and Comparative Biology* **51**, 151 (2011).

[39] N. J. Gidmark, J. A. Strother, J. M. Horton, A. P. Summers, and E. L. Brainerd, "Locomotory transition from water to sand and its effects on undulatory kinematics in sand lances (Ammodytidae)," *Journal of Experimental Biology* **214**, 657 (2011).

[40] D. W. Wolfe, *Tales from the Underground: A natural history of subterranean life* (Basic Books, MA, USA, 2001).

[41] J. Gibert and L. Deharveng, "Subterranean Ecosystems: A Truncated Functional Biodiversity," *BioScience* **52**, 473 (2002).

[42] C. Juan and B. C. Emerson, "Evolution underground: shedding light on the diversification of subterranean insects," *Journal of Biology* **9**, 1 (2010).

[43] P. K. Ducey, D. R. Formanowicz Jr, L. Boyet, J. Mailloux, and R. A. Nussbaum, "Experimental examination of burrowing behavior in caecilians (Amphibia: Gymnophiona): effects of soil compaction on burrowing ability of four species," *Herpetologica* **49**, 450 (1993).

[44] H. Heatwole, "Burrowing Ability and Behavioral Responses to Desiccation of the Salamander, *Plethodon Cinereus*," *Ecology* **41**, pp. 661 (1960).

[45] R. D. Semlitsch, "Burrowing ability and behavior of salamanders of the genus *Ambystoma*," *Canadian Journal of Zoology* **61**, 616 (1983).

[46] J. G. K. Williams, A. R. Kubelik, K. J. Livak, J. A. Rafalski, and S. V. Tingey, "Movements and habitat use by the giant burrowing frog, *Heleioporus australiacus*," *Amphibia-Reptilia* **24**, 207 (2003).

[47] M. Kearney and B. L. Stuart, "Repeated evolution of limblessness and digging heads in worm lizards revealed by DNA from old bones," *Proceedings- Royal Society of London B* **271**, 1677 (2004).

[48] R. A. How and R. Shine, "Ecological traits and conservation biology of five fossorial 'sand-swimming' snake species (*Simoselaps*: Elapidae) in south-western Australia," *Journal of Zoology* **249**, 269 (1999).

[49] J. D. Willson and M. E. Dorcas, "Aspects of the ecology of small fossorial snakes in the western piedmont of North Carolina," *Southeastern Naturalist* **3**, 1 (2004).

[50] E. Nevo, "Adaptive convergence and divergence of subterranean mammals," *Annual Review of Ecology and Systematics* **10**, 269 (1979).

[51] G. Kaufman, S. Kocher, and D. Kaufman, "Distribution of carnivore burrows in a prairie landscape," *Great Plains Research* **15**.

[52] M. H. Posey, B. R. Dumbauld, and D. A. Armstrong, "Effects of a burrowing mud shrimp,*Upogebia pugettensis* (Dana), on abundances of macro-infauna," *Journal of Experimental Marine Biology and Ecology* **148**, 283 (1991).

[53] J. Wyneken, "Sea turtle locomotion: mechanisms, behavior, and energetics," *The Biology of Sea Turtles* **1**, 165 (1997).

[54] P. Charbonneau, L. Hare, and R. Carignan, "Use of X-ray images and a contrasting agent to study the behavior of animals in soft sediments," *Limnology and Oceanography* **42**, 1823 (1997).

[55] W. Mosauer, "Adaptive convergence in the sand reptiles of the Sahara and of California: a study in structure and behavior," *Copeia* , 72 (1932).

[56] F. H. Pough, "The burrowing ecology of the sand lizard, *Uma notata*," *Copeia* , 145 (1970).

[57] C. A. Navas, M. M. Antoniazzi, J. E. Carvalho, J. G. Chaui-Berlink, R. S. James, C. Jared, T. Kohlsdorf, M. Dal Pai-Silva, and R. S. Wilson, "Morphological and physiological specialization for digging in amphisbaenians, an ancient lineage of fossorial vertebrates," *Journal of Experimental Biology* **207**, 2433 (2004).

[58] D. S. Shafer, M. H. Young, S. F. Zitzer, T. G. Caldwell, and E. V. McDonald, "Impacts of interrelated biotic and abiotic processes during the past 125000 years of landscape evolution in the northern Mojave Desert, Nevada, USA," *Journal of Arid Environments* **69**, 633 (2007).

[59] K. Autumn, Y. A. Liang, S. T. Hsieh, W. Zesch, W. P. Chan, T. W. Kenny, R. Fearing, and R. J. Full, "Adhesive force of a single gecko foot-hair," *Nature* **405**, 681 (2000).

[60] K. Autumn, M. Sitti, Y. A. Liang, A. M. Peattie, W. R. Hansen, S. Sponberg, T. W. Kenny, R. Fearing, J. N. Israelachvili, and R. J. Full, "Evidence for van der Waals adhesion in gecko setae," *Proceedings of the National Academy of Sciences* **99**, 12252 (2002).

[61] Y. Tian, N. Pesika, H. Zeng, K. Rosenberg, B. Zhao, P. McGuiggan, K. Autumn, and J. Israelachvili, "Adhesion and friction in gecko toe attachment and detachment," *Proceedings of the National Academy of Sciences* **103**, 19320 (2006).

[62] S. Kim, M. Spenko, S. Trujillo, B. Heyneman, V. Mattoli, and M. R. Cutkosky, "Whole body adhesion: hierarchical, directional and distributed control of adhesive forces for a climbing robot," in *Robotics and Automation, 2007 IEEE International Conference on* pp. 1268–1273 IEEE 2007.

[63] D. Santos, M. Spenko, A. Parness, S. Kim, and M. Cutkosky, "Directional adhesion for climbing: theoretical and practical considerations," *Journal of Adhesion Science and Technology* **21**, 1317 (2007).

[64] S. Marras and M. Porfiri, "Fish and robots swimming together: attraction towards the robot demands biomimetic locomotion," *Journal of The Royal Society Interface* **9**, 1856 (2012).

[65] H. Hu, "Biologically inspired design of autonomous robotic fish at Essex," in *IEEE SMC UK-RI Chapter Conference, on Advances in Cybernetic Systems* pp. 3–8 Citeseer 2006.

[66] G. C. H. E. De Croon, K. M. E. De Clercq, R. Ruijsink, B. Remes, and C. De Wagter, "Design, aerodynamics, and vision-based control of the DelFly," *International Journal of Micro Air Vehicles* **1**, 71 (2009).

[67] A. M. Hoover, E. Steltz, and R. S. Fearing, "RoACH: An autonomous 2.4 g crawling hexapod robot," in *Intelligent Robots and Systems, 2008. IROS 2008. IEEE/RSJ International Conference on* pp. 26–33 IEEE 2008.

[68] D. Santos, S. Kim, M. Spenko, A. Parness, and M. Cutkosky, "Directional adhesive structures for controlled climbing on smooth vertical surfaces," in *Robotics and Automation, 2007 IEEE International Conference on* pp. 1262–1267 IEEE 2007.

[69] C. Li, P. B. Umbanhowar, H. Komsuoglu, D. E. Koditschek, and D. I. Goldman, "Sensitive dependence of the motion of a legged robot on granular media," *Proceedings of the National Academy of Sciences* **106**, 3029 (2009).

[70] O. Attum, P. Eason, and G. Cobbs, "Morphology, niche segregation, and escape tactics in a sand dune lizard community," *Journal of Arid Environments* **68**, 564 (2007).

[71] S. Carranza, E. N. Arnold, P. Geniez, J. Roca, and J. A. Mateo, "Radiation, multiple dispersal and parallelism in the skinks, *Chalcides* and *Sphenops* (Squamata: Scincidae), with comments on *Scincus* and *Scincopus* and the age of the Sahara Desert," *Molecular Phylogenetics and Evolution* **46**, 1071 (2008).

[72] C. Linnaeus *et al.*, "Systema naturae," *Salvii, Holmiae* **1**.

[73] M. F. Hussein, N. Badir, R. El Ridi, and S. El Deeb, "Effect of seasonal variation on immune system of the lizard, *Scincus scincus*," *Journal of Experimental Zoology* **209**, 91 (1979).

[74] T. E. Hetherington, "Use of vibratory cues for detection of insect prey by the sandswimming lizard *Scincus scincus*," *Animal Behaviour* **37**, 290 (1989).

[75] T. E. Hetherington, "Behavioural use of seismic cues by the sandswimming lizard *Scincus scincus*," *Ethology Ecology & Evolution* **4**, 5 (1992).

[76] I. Rechenberg and A. El Khyari, "Reibung und Verschlei am Sandfisch der Sahara," 2004.

[77] W. Baumgartner, F. Fidler, A. Weth, M. Habbecke, P. Jakob, C. Butenweg, and W. Böhme, "Investigating the Locomotion of the Sandfish in Desert Sand Using NMR-Imaging," *PLoS ONE* **3**, e3309:1 (2008).

[78] R. D. Maladen, Y. Ding, P. B. Umbanhowar, and D. I. Goldman, "Undulatory swimming in sand: experimental and simulation studies of a robotic sandfish," *The International Journal of Robotics Research* **30**, 793 (2011).

[79] D. W. Elvin, "Variation and distribution of the shovel-nosed snakes (*Chionactis occipitalis*) in the northern Mojave Desert, California and Nevada," *Herpetologica* **19**, 73 (1963).

[80] J. W. Warren, "Notes on the behavior of *Chionactis occipitalis*," *Herpetologica* **9**, 121 (1953).

[81] R. B. Cowles, "Observations on the winter activities of desert reptiles," *Ecology* **22**, 125 (1941).

[82] W. Mosauer, "Locomotion and diurnal range of *Sonora occipitalis*, *Crotalus cerastes*, and *Crotalus atrox* as seen from their tracks," *Copeia* **1933**, 14 (1933).

[83] W. Mosauer, "The reptilian fauna of sand dune areas of the Vizcaino desert and of north-western lower California," *Occasional papers of the museum of zoology, University of Michigan* **329**, 1 (1936).

[84] P. Kornilios, P. Kyriazi, N. Poulakakis, Y. Kumlutaş, Ç. Ilgaz, M. Mylonas, and P. Lymberakis, "Phylogeography of the ocellated skink *Chalcides ocellatus* (Squamata, Scincidae), with the use of mtDNA sequences: A hitch-hikers guide to the Mediterranean," *Molecular Phylogenetics and Evolution* **54**, 445 (2010).

[85] P. G. de Gennes, "Granular matter: a tentative view," *Reviews of Modern Physics* **71**, S374 (1999).

[86] R. Albert, I. Albert, D. Hornbaker, P. Schiffer, and A. L. Barabási, "Maximum angle of stability in wet and dry spherical granular media," *Physical Review E* **56**, R6271 (1997).

[87] M. P. Ciamarra, A. H. Lara, A. T. Lee, D. I. Goldman, I. Vishik, and H. L. Swinney, "Dynamics of Drag and Force Distributions for Projectile Impact in a Granular Medium," *Phys. Rev. Lett* **92**, 194301 (2004).

[88] D. I. Goldman and P. B. Umbanhowar, "Scaling and dynamics of sphere and disk impact into granular media," *Physical Review E* **77**, 21308 (2008).

[89] C. Li, T. Zhang, and D. I. Goldman, "A terradynamics of legged locomotion on granular media," *Science* **339**, 1408 (2013).

[90] N. Gravish, P. B. Umbanhowar, and D. I. Goldman, "Force and flow transition in plowed granular media," *Physical Review Letters* **105**, 128301 (2010).

[91] R. Albert, M. A. Pfeifer, A. L. Barbási, and P. Schiffer, "Slow Drag in a Granular Medium," *Physical Review Letters* **82**, 205 (1999).

[92] R. A. Bagnold, *The Physics of Blown Sand and Desert Dunes* (Methuen and Co. Ltd., 1954).

[93] E. Ezcurra, *Global Deserts Outlook* (United Nations Educational, 2006).

[94] G. C. Cho, J. Dodds, and J. C. Santamarina, "Particle shape effects on packing density, stiffness, and strength: natural and crushed sands," *Journal of Geotechnical and Geoenvironmental Engineering* **132**, 591 (2006).

[95] W. W. Dickinson and J. D. Ward, "Low Depositional Porosity in Eolian Sands and Sandstones, Namib Desert," *Journal of Sedimentary Research* **64**, 226 (1994).

[96] J. Duran, *Sands, powders, and grains* (Springer, 2000).

[97] P. B. Umbanhowar and D. I. Goldman, "Granular impact and the critical packing state," *Physical Review E* **82**, 4 (2010).

[98] J. B. Knight, C. G. Fandrich, C. N. Lau, H. M. Jaeger, and S. R. Nagel, "Density relaxation in a vibrated granular material," *Physical Review E* **51**, 3957 (1995).

[99] K. Wieghardt, "Experiments in granular flow," *Annual Review of Fluid Mechanics* **7**, 89 (1975).

[100] G. Hill, S. Yeung, and S. A. Koehler, "Scaling vertical drag forces in granular media," *EPL (Europhysics Letters)* **72**, 137 (2005).

[101] I. Albert, J. G. Sample, A. J. Morss, S. Rajagopalan, A. L. Barabási, and P. Schiffer, "Granular drag on a discrete object: Shape effects on jamming," *Physical Review E* **64**, 61303 (2001).

[102] I. Albert, P. Tegzes, R. Albert, J. G. Sample, A. L. Barabási, T. Vicsek, B. Kahng, and P. Schiffer, "Stick-slip fluctuations in granular drag," *Physical Review E* **64**, 1 (2001).

[103] C. Li, *Biological, robotic, and physics studies to discover principles of legged locomotion on granular media*, PhD dissertation Georgia Institute of Technology 2011.

[104] C. Li, S. T. Hsieh, and D. I. Goldman, "Multi-functional foot use during running in the zebra-tailed lizard (*Callisaurus draconoides*)," *The Journal of Experimental Biology* **215**, 3293 (2012).

[105] R. D. Maladen, P. B. Umbanhowar, Y. Ding, A. Masse, and D. I. Goldman, "Granular lift forces predict vertical motion of a sand-swimming robot," in *Robotics and Automation (ICRA), 2011 IEEE International Conference on* pp. 1398–1403 IEEE 2011.

[106] N. Mitarai and F. Nori, "Wet granular materials," *Advances in Physics* **55**, 1 (2006).

[107] Z. Fournier *et al.*, "Mechanical properties of wet granular materials," *Journal of Physics: Condensed Matter* **17**, S477 (2005).

[108] H. Schubert, W. Herrmann, and H. Rumpf, "Deformation behaviour of agglomerates under tensile stress," *Powder technology* **11**, 121 (1975).

[109] A. G. Winter, R. L. H. Deits, and A. E. Hosoi, "Localized fluidization burrowing mechanics of *Ensis directus*," *Journal of Experimental Biology* **215**, 2072 (2012).

[110] V. Richefeu, M. S. El Youssoufi, and F. Radjai, "Shear strength properties of wet granular materials," *Physical Review E* **73**, 051304 (2006).

[111] M. Scheel, R. Seemann, M. Brinkmann, M. Di Michiel, A. Sheppard, B. Breidenbach, and S. Herminghaus, "Morphological clues to wet granular pile stability," *Nature Materials* **7**, 189 (2008).

[112] D. J. Hornbaker, R. Albert, I. Albert, A. L. Barabási, and P. Schiffer, "What keeps sandcastles standing?," *Nature* **387**, 765 (1997).

[113] J. E. Fiscina, G. Lumay, F. Ludewig, and N. Vandewalle, "Compaction dynamics of wet granular assemblies," *Physical Review Letters* **105**, 048001 (2010).

[114] J. O. Marston, I. U. Vakarelski, and S. T. Thoroddsen, "Sphere impact and penetration into wet sand," *Physical Review E* **86**, 020301 (2012).

[115] S. J. Jackson, M. A. Whyte, and M. Romano, "Laboratory-controlled simulations of dinosaur footprints in sand: a key to understanding vertebrate track formation and preservation," *Palaios* **24**, 222 (2009).

[116] N. Vandewalle, G. Lumay, F. Ludewig, and J. E. Fiscina, "How relative humidity affects random packing experiments," *Physical Review E* **85**, 031309 (2012).

[117] G. Gioia, A. M. Cuitiño, S. Zheng, and T. Uribe, "Two-phase densification of cohesive granular aggregates," *Physical Review Letters* **88**, 204302 (2002).

[118] S. Collins, A. Ruina, R. Tedrake, and M. Wisse, "Efficient bipedal robots based on passive-dynamic walkers," *Science* **307**, 1082 (2005).

[119] E. Marder and D. Bucher, "Central pattern generators and the control of rhythmic movements," *Current Biology* **11**, R986 (2001).

[120] W. Otto Friesen, "Reciprocal inhibition: a mechanism underlying oscillatory animal movements," *Neuroscience & Biobehavioral Reviews* **18**, 547 (1995).

[121] W. O. Friesen and R. A. Pearce, "Mechanisms of intersegmental coordination in leech locomotion," in *Seminars in Neuroscience* volume 5 pp. 41–47 Elsevier 1993.

[122] E. Marder, D. Bucher, D. J. Schulz, and A. L. Taylor, "Invertebrate central pattern generation moves along," *Current Biology* **15**, R685 (2005).

[123] A. D. McClellan and S. Grillner, "Activation of 'fictive swimming' by electrical microstimulation of brainstem locomotor regions in an in vitro preparation of the lamprey central nervous system," *Brain research* **300**, 357 (1984).

[124] P. Wallen and T. L. Williams, "Fictive locomotion in the lamprey spinal cord in vitro compared with swimming in the intact and spinal animal.," *The Journal of Physiology* **347**, 225 (1984).

[125] P. Wallen and S. Grillner, "N-methyl-D-aspartate receptor-induced, inherent oscillatory activity in neurons active during fictive locomotion in the lamprey," *The Journal of Neuroscience* **7**, 2745 (1987).

[126] L. Williams, S. Grillner, V. V. Smoljaninov, P. W. Allen, S. Kashin, and S. Rossignol, "Locomotion in lamprey and trout: the relative timing of activation and movement," *Journal of Experimental Biology* **143**, 559 (1989).

[127] C. Koch and G. Laurent, "Complexity and the nervous system," *Science* **284**, 96 (1999).

[128] G. E. Loeb and G. Carl, *Electromyography for experimentalists* (University of Chicago Press, 1986).

[129] E. R. Kandel, J. H. Schwartz, and T. M. Jessell, *Principles of Neural Science* (McGraw-Hill, NY, USA, 2000).

[130] S. Sponberg and R. J. Full, "Neuromechanical response of musculo-skeletal structures in cockroaches during rapid running on rough terrain," *Journal of Experimental Biology* **211**, 433 (2008).

[131] X. Ren, X. Hu, Z. Wang, and Z. Yan, "MUAP extraction and classification based on wavelet transform and ICA for EMG decomposition," *Medical and Biological Engineering and Computing* **44**, 371 (2006).

[132] Y. Ding, *Simulation and theoretical study of swimming and resisitive forces within granular media*, PhD dissertation Georgia Institute of Technology 2011.

[133] J. Gray and G. J. Hancock, "The propulsion of sea-urchin spermatozoa," *Journal of Experimental Biology* **32**, 802 (1955).

[134] I. E. Brown and G. E. Loeb, *A reductionist approach to creating and using neuromusculoskeletal models* (Springer, 2000), pp. 148–163.

[135] J. C. Spagna, D. I. Goldman, P.-C. Lin, D. E. Koditschek, and R. J. Full, "Distributed mechanical feedback in arthropods and robots simplifies control of rapid running on challenging terrain," *Bioinspiration and Biomimetics* **2**, 9 (2007).

[136] A. A. Biewener and G. B. Gillis, "Dynamics of muscle function during locomotion: accommodating variable conditions," *Journal of Experimental Biology* **202**, 3387 (1999).

[137] N. J. Cowan, J. Lee, and R. J. Full, "Task-level control of rapid wall following in the American cockroach," *Journal of Experimental Biology* **209**, 1617 (2006).

[138] G. B. Gillis, "Neuromuscular control of anguilliform locomotion: patterns of red and white muscle activity during swimming in the American eel *Anguilla rostrata*," *Journal of Experimental Biology* **201**, 3245 (1998).

[139] G. B. Gillis, "Environmental effects on undulatory locomotion in the American eel *Anguilla rostrata*: kinematics in water and on land," *Journal of Experimental Biology* **201**, 949 (1998).

[140] A. A. Biewener and W. R. Corning, "Dynamics of mallard (*Anas platyrynchos*) gastrocnemius function during swimming versus terrestrial locomotion," *Journal of Experimental Biology* **204**, 1745 (2001).

[141] G. B. Gillis and R. W. Blob, "How muscles accommodate movement in different physical environments: aquatic vs. terrestrial locomotion in vertebrates," *Comparative Biochemistry and Physiology-Part A: Molecular & Integrative Physiology* **131**, 61 (2001).

[142] J. Korta, D. A. Clark, C. V. Gabel, L. Mahadevan, and A. D. T. Samuel, "Mechanosensation and mechanical load modulate the locomotory gait of swimming *C. elegans*," *Journal of Experimental Biology* **210**, 2383 (2007).

[143] A. M. Horner and B. C. Jayne, "The effects of viscosity on the axial motor pattern and kinematics of the African lungfish (*Protopterus annectens*) during lateral undulatory swimming," *Journal of Experimental Biology* **211**, 1612 (2008).

[144] E. D. Tytell, C. Y. Hsu, T. L. Williams, A. H. Cohen, and L. J. Fauci, "Interactions between internal forces, body stiffness, and fluid environment in a neuromechanical model of lamprey swimming," *Proceedings of the National Academy of Sciences* **107**, 19832 (2010).

[145] D. J. Ellerby, I. L. Y. Spierts, and J. D. Altringham, "Fast muscle function in the European eel (*Anguilla anguilla L.*) during aquatic and terrestrial locomotion," *Journal of Experimental Biology* **204**, 2231 (2001).

[146] M. Ashley-Ross, "Hindlimb kinematics during terrestrial locomotion in a salamander (*Dicamptodon tenebrosus*)," *Journal of experimental biology* **193**, 255 (1994).

[147] L. M. Frolich and A. A. Biewener, "Kinematic and Electromyographic Analysis of the functional role of the body axis during Terrestrial and Aquatic Locomotion in the Salamander *Ambystoma Tigrinum*," *Journal of Experimental Biology* **162**, 107 (1992).

[148] R. J. Full and D. E. Koditschek, "Templates and Anchors: Neuromechanical Hypotheses of Legged Locomotion on Land," *Journal of Experimental Biology* **202**, 3325 (1999).

[149] G. A. Cavagna, N. C. Heglund, and C. R. Taylor, "Mechanical work in terrestrial locomotion: two basic mechanisms for minimizing energy-expenditure," *American Journal of Physiology* **233**, R243 (1977).

[150] R. J. Full and M. S. Tu, "Mechanics of a rapid running insect: Two-,four- and six-legged locomotion," *Journal of Experimental Biology* **156**, 215 (1991).

[151] J. Schmitt, M. Garcia, R. C. Razo, P. Holmes, and R. J. Full, "Dynamics and stability of legged locomotion in the horizontal plane: a test case using insects," *Biological Cybernetics* **86**, 343 (2002).

[152] C. T. Farley and T. C. Ko, "Mechanics of locomotion in lizards," *Journal of Experimental Biology* **200**, 2177 (1997).

[153] A. N. Schofield and C. P. Wroth, *Critical State Soil Mechanics* (McGraw-Hill, London, 1968).

[154] M. A. Daley and A. A. Biewener, "Muscle force-length dynamics during level versus incline locomotion: a comparison of *in vivo* performance of two guinea fowl ankle extensors," *Journal of Experimental Biology* **206**, 2941 (2003).

[155] A. A. Biewener, R. Blickhan, A. K. Perry, N. C. Heglund, and C. Taylor, "Muscle forces during locomotion in kangaroo rats: force platform and tendon buckle measurements compared," *Journal of Experimental Biology* **137**, 191 (1988).

[156] E. A. Gozal, *Trace amines as novel modulators of spinal motor function*, PhD dissertation Georgia Institute of Technology 2010.

[157] S. Hochman, E. A. Gozal, H. B. Hayes, J. T. Anderson, S. P. DeWeerth, and Y. H. Chang, "Enabling techniques for in vitro studies on mammalian spinal locomotor mechanisms.," *Frontiers in Bioscience: a Journal and Virtual Library* **17**, 2158 (2012).

[158] D. Carrier, "Activity of the hypaxial muscles during walking in the lizard *Iguana iguana*," *J. Exp. Biol.* **152**, 453 (1990).

[159] D. Ritter, "Axial muscle function during lizard locomotion," *Journal of Experimental Biology* **199**, 2499 (1996).

[160] B. C. Jayne, "Muscular mechanisms of snake locomotion: an electromyographic study of the sidewinding and concertina modes of *Crotalus cerastes*, *Nerodia fasciata* and *Elaphe obsoleta*," *The Journal of Experimental Biology* **140**, 1 (1988).

[161] D. Ritter, "Epaxial muscle function during locomotion in a lizard (*Varanus salvator*) and the proposal of a key innovation in the vertebrate axial musculoskeletal system," *The Journal of Experimental Biology* **198**, 2477 (1995).

[162] Y. Ding, S. S. Sharpe, K. Wiesenfeld, and D. I. Goldman, "Emergence of the advancing neuromechanical phase in a resistive force dominated medium," *Proceedings of the National Academy of Sciences* **110**, 10123 (2013).

[163] P. J. O. Miller, M. P. Johnson, P. L. Tyack, and E. A. Terray, "Swimming gaits, passive drag and buoyancy of diving sperm whales *Physeter macrocephalus*," *Journal of Experimental Biology* **207**, 1953 (2004).

[164] K. C. Paggett, V. Gupta, and A. D. McClellan, "Adaptive variations of undulatory behaviors in larval lamprey: comparison of swimming and burrowing," *Experimental Brain Research* **119**, 213 (1998).

[165] C. Fang-Yen, M. Wyart, J. Xie, R. Kawai, T. Kodger, S. Chen, Q. Wen, and A. D. T. Samuel, "Biomechanical analysis of gait adaptation in the nematode *Caenorhabditis elegans*," *Proceedings of the National Academy of Sciences* **107**, 20323 (2010).

[166] A. V. Hill, "The heat of shortening and the dynamic constants of muscle," *Proceedings of the Royal Society of London. Series B, Biological Sciences* **126**, 136 (1938).

[167] D. C. Rapaport, *The art of molecular dynamics simulation* (Cambridge University Press, Cambridge, UK, 2004).

[168] T. McMillen, T. Williams, and P. Holmes, "Nonlinear muscles, passive viscoelasticity and body taper conspire to create neuromechanical phase lags in anguilliform swimmers," *PLoS Computational Biology* **4**, e1000157 (2008).

[169] C. Wardle, J. Videler, and J. Altringham, "Tuning in to fish swimming waves: body form, swimming mode and muscle function," *Journal of Experimental Biology* **198**, 1629 (1995).

[170] J. D. Altringham and D. J. Ellerby, "Fish swimming: patterns in muscle function," *Journal of Experimental Biology* **202**, 3397 (1999).

[171] A. A. Biewener and G. B. Gillis, "Dynamics of muscle function during locomotion: Accommodating variable conditions," *Journal of Experimental Biology* **202**, 3387 (1999).

[172] K. M. Dorgan, P. A. Jumars, B. Johnson, B. P. Boudreau, and E. Landis, "Burrowing mechanics: burrow extension by crack propagation.," *Nature* **433**, 475 (2005).

[173] A. R. Abate and D. J. Durian, "Partition of energy for air-fluidized grains," *Physical Review E* **72**, 031305 (2005).

[174] L. J. Daniels, Y. Park, T. C. Lubensky, and D. J. Durian, "Dynamics of gas-fluidized granular rods," *Physical Review E* **79**, 041301 (2009).

[175] H. M. Choset, *Principles of robot motion: theory, algorithms, and implementations* (MIT press, 2005).

[176] P. Holmes, R. J. Full, D. Koditschek, and J. Guckenheimer, "The dynamics of legged locomotion: Models, analyses, and challenges," *SIAM Review* **48**, 207 (2006).

[177] A. J. Ijspeert, "Central pattern generators for locomotion control in animals and robots: a review," *Neural Networks* **21**, 642 (2008).

[178] G. N. Orlovsky, T. G. Deliagina, and S. Grillner, *Neuronal control of locomotion: from mollusc to man* (Oxford University Press, New York, USA, 1999).

[179] R. K. Josephson, "The mechanical power output of a tettigoniid wing muscle during singing and flight," *Journal of Experimental Biology* **117**, 357 (1985).

[180] A. L. Hof, "EMG and muscle force: an introduction," *Human Movement Science* **3**, 119 (1984).

[181] E. D. Tytell, P. Holmes, and A. H. Cohen, "Spikes alone do not behavior make: why neuroscience needs biomechanics," *Current Opinion in Neurobiology* **21**, 816 (2011).

[182] H. J. Chiel, L. H. Ting, Ö. Ekeberg, and M. J. Z. Hartmann, "The brain in its body: motor control and sensing in a biomechanical context," *The Journal of Neuroscience* **29**, 12807 (2009).

[183] M. H. Dickinson, C. T. Farley, R. J. Full, M. A. R. Koehl, R. Kram, and S. Lehman, "How Animals Move: An Integrative View," *Science* **288**, 100 (2000).

[184] J. Schmitt and P. Holmes, "Mechanical models for insect locomotion: dynamics and stability in the horizontal plane - II. Application," *Biological Cybernetics* **83**, 517 (2000).

[185] N. Cohen and J. H. Boyle, "Swimming at low Reynolds number: a beginners guide to undulatory locomotion," *Contemporary Physics* **51**, 103 (2010).

[186] D. L. Hu, J. Nirody, T. Scott, and M. J. Shelley, "The mechanics of slithering locomotion," *Proceedings of the National Academy of Sciences* **106**, 10081 (2009).

[187] B. C. Jayne and G. V. Lauder, "Speed effects on midline kinematics during steady undulatory swimming of largemouth bass, *Micropterus salmoides*," *Journal of Experimental Biology* **198**, 585 (1995).

[188] M. Sfakiotakis, D. M. Lane, and J. B. C. Davies, "Review of fish swimming modes for aquatic locomotion," *IEEE Journal of Oceanic Engineering* **24**, 237 (1999).

[189] C. Wright, A. Johnson, A. Peck, Z. McCord, A. Naaktgeboren, P. Gianfortoni, M. Gonzalez-Rivero, R. Hatton, and H. Choset, "Design of a Modular Snake Robot," in *Proceedings of the IEEE International Conference on Intelligent Robots and Systems* pp. 2609–2614 IEEE 2007.

[190] A. Crespi and A. J. Ijspeert, "Online optimization of swimming and crawling in an amphibious snake robot," *IEEE Transactions on Robotics* **24**, 75 (2008).

[191] H. M. Choset, J. E. Luntz, E. Shammas, T. Rached, D. Hull, and C. C. Dent, "Design and motion planning for serpentine robots," in *Proceedings of SPIE* volume 3990 p. 148 2000.

[192] B. C. Jayne and G. V. Lauder, "Red muscle motor patterns during steady swimming in largemouth bass: effects of speed and correlations with axial kinematics," *Journal of Experimental Biology* **198**, 1575 (1995).

[193] J. Y. Cheng, T. J. Pedley, and J. D. Altringham, "A continuous dynamic beam model for swimming fish," *Philosophical Transactions of the Royal Society of London. Series B: Biological Sciences* **353**, 981 (1998).

[194] G. Bowtell and T. L. Williams, "Anguilliform body dynamics: modelling the interaction between muscle activation and body curvature," *Philosophical Transactions of the Royal Society of London. Series B: Biological Sciences* **334**, 385 (1991).

[195] J. Chen, W. O. Friesen, and T. Iwasaki, "Mechanisms underlying rhythmic locomotion: body–fluid interaction in undulatory swimming," *Journal of Experimental Biology* **214**, 561 (2011).

[196] T. J. Pedley and S. J. Hill, "Large-amplitude undulatory fish swimming: fluid mechanics coupled to internal mechanics," *Journal of Experimental Biology* **202**, 3431 (1999).

[197] D. M. Dudek and R. J. Full, "Passive mechanical properties of legs from running insects," *The Journal of Experimental Biology* **209**, 1502 (2006).

[198] B. Rodenborn, C.-H. Chen, H. L. Swinney, B. Liu, and H. P. Zhang, "Propulsion of microorganisms by a helical flagellum," *Proceedings of the National Academy of Sciences* **110**, E338 (2013).

[199] S. Hirose, *Biologically Inspired Robots: Serpentile Locomotors and Manipulators* (Oxford University Press, 1993).

[200] D. T. Roper, S. Sharma, R. Sutton, and P. Culverhouse, "A review of developments towards biologically inspired propulsion systems for autonomous underwater vehicles," *Proceedings of the Institution of Mechanical Engineers, Part M: Journal of Engineering for the Maritime Environment* **225**, 77 (2011).

[201] J. E. Colgate and K. M. Lynch, "Mechanics and control of swimming: a review," *Oceanic Engineering, IEEE Journal of* **29**, 660 (2004).

[202] C. Gans, "Tetrapod limblessness: evolution and functional corollaries," *Integrative and Comparative Biology* **15**, 455 (1975).

[203] M. A. Ashley-Ross and B. F. Bechtel, "Kinematics of the transition between aquatic and terrestrial locomotion in the newt *Taricha torosa*," *Journal of Experimental Biology* **207**, 461 (2004).

[204] A. J. Ijspeert, A. Crespi, D. Ryczko, and J. M. Cabelguen, "From swimming to walking with a salamander robot driven by a spinal cord model," *Science* **315**, 1416 (2007).

[205] J. M. Cabelguen, C. Bourcier-Lucas, and R. Dubuc, "Bimodal locomotion elicited by electrical stimulation of the midbrain in the salamander *Notophthalmus viridescens*," *The Journal of Neuroscience* **23**, 2434 (2003).

[206] F. S. Labini, Y. P. Ivanenko, G. Cappellini, S. Gravano, and F. Lacquaniti, "Smooth changes in the EMG patterns during gait transitions under body weight unloading," *Journal of Neurophysiology* **106**, 1525 (2011).

[207] A. Miralles, M. Anjeriniaina, C. A. Hipsley, J. Müller, F. Glaw, and M. Vences, "Variations on a bauplan: description of a new Malagasy mermaid skink with flipper-like forelimbs only (Scincidae, Sirenoscincus Sakata & Hikida, 2003)," *Zoosystema* **34**, 701 (2012).

[208] N. Mazouchova, N. Gravish, A. Savu, and D. I. Goldman, "Utilization of granular solidification during terrestrial locomotion of hatchling sea turtles," *Biology letters* **6**, 398 (2010).

[209] K. A. Nagy, B. C. Clarke, M. K. Seely, D. Mitchell, and J. R. B. Lighton, "Water and energy balance in Namibian desert sand-dune lizards Angolosaurus skoogi (Andersson, 1916)," *Functional Ecology* , 731 (1991).

[210] J. Gray and H. W. Lissmann, "The locomotion of nematodes," *Journal of Experimental Biology* **41**, 135 (1964).

[211] D. I. Goldman and D. L. Hu, "Wiggling through the world," *American Scientist* **98**, 314 (2010).

[212] M. Serrano, S. S. Sharpe, D. I. Goldman, and P. A. Vela, "What's going on under there? Tracking subsurface animal locomotion through granular media," (In Prep).

[213] A. S. Umar, J. Wu, M. R. Strayer, and C. Bottcher, "Basis-spline collocation method for the lattice solution of boundary value problems," *Journal of Computational Physics* **93**, 426 (1991).

[214] P. H. C. Eilers and B. D. Marx, "Splines, knots, and penalties," *Wiley Interdisciplinary Reviews: Computational Statistics* **2**, 637 (2010).

[215] G. B. Gillis, "Anguilliform locomotion in an elongate salamander (*Siren intermedia*): effects of speed on axial undulatory movements," *Journal of Experimental Biology* **200**, 767 (1997).

[216] L. B. Leopold, *A View of the River* (Harvard University Press, 1994).

[217] S. A. Koehler and B. S. Tilley, "Optimizing waveforms for finite-length undulating filaments," (In prep).

[218] J. Gray and H. W. Lissmann, "The kinetics of locomotion of the grass–snake," *Journal of Experimental Biology* **26**, 354 (1950).

[219] R. A. Berthé, G. Westhoff, H. Bleckmann, and S. N. Gorb, "Surface structure and frictional properties of the skin of the Amazon tree boa *Corallus hortulanus* (Squamata, Boidae)," *Journal of Comparative Physiology A* **195**, 311 (2009).

[220] G. B. Gillis, "Undulatory locomotion in elongate aquatic vertebrates: Anguilliform swimming since Sir James Gray," *Integrative and Comparative Biology* **36**, 656 (1996).

[221] F. E. Fish, "Kinematics of undulatory swimming in the American Alligator," *Copeia* **4**, 839 (1984).

[222] G. Taylor, "Analysis of the swimming of long and narrow animals," *Proceedings of the Royal Society of London. Series A. Mathematical and Physical Sciences* **214**, 158 (1952).

[223] D. J. Irschick and B. C. Jayne, "A field study of the effects of incline on the escape locomotion of a bipedal lizard, *Callisaurus draconoides*," *Physiological and Biochemical Zoology* **72**, 44 (1999).

[224] European-Environmental-Agency, "Global surface soil moisture content based on remote sensing data," 2012.

[225] S. Herminghaus, "Dynamics of wet granular matter," *Advances in Physics* **54**, 221 (2005).

[226] S. Jung, "*Caenorhabditis elegans* swimming in a saturated particulate system," *Physics of Fluids* **22**, 031903 (2010).

[227] E. R. Trueman, "The mechanism of burrowing of the mole crab, *Emerita*," *Journal of Experimental Biology* **53**, 701 (1970).

[228] G. Juarez, K. Lu, J. Sznitman, and P. E. Arratia, “Motility of small nematodes in wet granular media,” *Europhysics Letters* **92**, 44002 (2010).

[229] A. E. Greer, V. Caputo, B. Lanza, and R. Palmieri, “Observations on limb reduction in the scincid lizard genus *Chalcides*,” *Journal of Herpetology* , 244 (1998).

[230] R. M. Alexander, “The maximum forces exerted by animals,” *Journal of Experimental Biology* **115**, 231 (1985).

[231] B. McKenzie and A. Dexter, “Radial pressures generated by the earthworm Aporrectodea rosea,” *Biology and fertility of soils* **5**, 328 (1988).

[232] E. R. Trueman, “The dynamics of burrowing in *Ensis* (Bivalvia),” *Proceedings of the Royal Society of London. Series B. Biological Sciences* **166**, 459 (1967).

[233] M. Joschko, H. Diestel, and O. Larink, “Assessment of earthworm burrowing efficiency in compacted soil with a combination of morphological and soil physical measurements,” *Biology and Fertility of Soils* **8**, 191 (1989).

VITA

Sarah Sharpe was born to Daniel L. Steinmetz and Debra Jahns-Nelsen on October 14, 1983 in Orange Park, FL. She was also raised and influenced by her step-mother, Karen Steinmetz. She has 4 siblings (Nick, Christen, Kelly and Eric). Sarah attended the University of Central Florida and graduated *magna cum laude* with a B.S. in Mechanical Engineering in 2007. During her last two years, she worked in the Robotics and Autonomous Controls Laboratory under the supervision of Alexander Leonessa. She then joined the Interdisciplinary Bioengineering Graduate Program (home-school of Biomedical Engineering) at the Georgia Institute of Technology. She entered with a two-year Integrative Graduate Education and Research Traineeship (IGERT) from the the National Science Foundation (NSF) that focused on integrating living neural tissue with engineered components. She joined Daniel Goldman's Complex Rheology and Biomechanics (CRAB) lab in 2008. Sarah was awarded 2nd place for the best student paper in the Comparative Biomechanics Division at the 2013 Society of Integrative and Comparative Biology meeting for her work on sandfish limb function. She also won Georgia Tech's 2012 best student publication award for her work on muscle activation in swimming sandfish. Sarah married her long-term boyfriend, Jeffrey Sharpe, in 2011. In the future, Sarah hopes to pursue a career in injury biomechanics.